Prepared by:
GEER Association
geerassociation.org
Kumamoto Earthquakes
Version 1.0
July 2016

Geotechnical Aspects of the 2016 $\mathbf{M_W}$ 6.2, $\mathbf{M_W}$ 6.0, and $\mathbf{M_W}$ 7.0 Kumamoto Earthquakes

Prepared by:
GEER Association
geerassociation.org
Kumamoto Earthquakes
Version 1.0
July 2016

Geotechnical Aspects of the 2016 $\mathbf{M_W}$ 6.2, $\mathbf{M_W}$ 6.0, and $\mathbf{M_W}$ 7.0 Kumamoto Earthquakes

Geotechnical Extreme Events Reconnaissance Association
Version 1.0
July 2016

Prepared By:

Robert Kayen, Shideh Dashti, Takaji Kokusho, Hemanta Hazarika, Kevin Franke, Nicolas Oettle, Brad Wham, Jenny Ramirez Calderon, Dallin Briggs, Samantha Guillies, Katherine Cheng, Yutaka Tanoue, Katsuji Takematsu , Daisuke Matsumoto , Takayuki Morinaga, Hideo Furuichi, Yuuta Kitano, Masanori Tajiri, Babloo Chaudhary, Kengo Nishimura, Chu Chu.

Contents

List of Appendices

List of Tables

List of Figures

Executive Summary

The 2016 Kumamoto earthquakes are a series of events that began with an earthquake of moment magnitude 6.2 on the Hinagu Fault on April 14, 2016, followed by another foreshock of moment magnitude 6.0 on the Hinagu Fault on April 15, 2016, and a larger moment magnitude 7.0 event on the Futagawa Fault on April 16, 2016 beneath Kumamoto City, Kumamoto Prefecture on Kyushu, Japan. These events are the strongest earthquakes recorded in Kyushu during the modern instrumental era. The earthquakes resulted in substantial damage to infrastructure, buildings, cultural heritage of Kumamoto Castle, roads and highways, slopes, and river embankments due to earthquake-induced landsliding and debris flows. Surface fault rupture produced offset and damage to roads, buildings, river levees, and an agricultural dam. Surprisingly, given the extremely intense earthquake motions, liquefaction occurred only in a few districts of Kumamoto City and in the port areas indicating that the volcanic soils were less susceptible to liquefying than expected given the intensity of earthquake shaking, a significant finding from this event.

Significant Case Histories: The primary objective of the GEER reconnaissance effort is the identification of important case histories that will likely be targets for future investigations that help develop methodologies to mitigate damage in future earthquakes. Important case histories identified by the participants from this earthquake are discussed in Chapter 9. Here they are briefly described:

Surface Rupture: Oh-Kirihata Dam

An approximately 0.5-km long by 0.25-km wide water reservoir was ruptured by the main strand of the Futagawa Fault. The fault crossed the reservoir in two places, along the western flank of the reservoir, where the fault first crossed, and through the intersection of the spillway and the spillway outlet channel, on the northern side of the reservoir (Figure 9-1). Around nearly the entire reservoir bench, slope movements of 0.2 m to 0.5 m occurred. Complete slope failures of the reservoir bench and underlying slope occurred at two locations: just to the east of the spillway and on the eastern flank of the reservoir. The reservoir's gatehouse was significantly back tilted, rendering it inoperable.

The bench itself was highly distorted at the fault crossing, and the reservoir side slope below the bench was relatively intact, except that the riprap was disturbed (i.e., "dilated") as a result of shearing. The location at which the Futagawa Fault exited the reservoir was approximately between the spillway and the spillway outlet channel. Disturbance caused by the fault could be noted in the slopes below the spillway, again due to dilated riprap. The fault movement apparently caused failure of one of the spillway training walls. A secondary rupture apparently went through the right side of the spillway based on offsets recorded there.

Surface Rupture: Aso Caldera Depression Zone

The Futagawa surface fault rupture extended northeast into the southwestern corner of the Aso Caldera, a region of active volcanism. An approximately 10-km-long section of graben-structure ground movement, herein call the "depression zone", occurred coseismically, roughly projecting out from the point at which the Futagawa Fault ruptured into the caldera, up and to the northwestern end of the caldera. This depression zone ranged from 36-m to 106-m wide through the zone captured with LIDAR with near vertical offsets as large as 2.5 m at each end of the depression zone. Our

interpretation is that this depression zone is likely caused by nearly vertical normal faulting on the caldera's ring fault, with a secondary fault (and hence the zone of depression) created as a result of the deep, soft soil profile in the caldera or as a result of underlying interaction with a ring dike or other deeper geological structure. Borings conducted by others prior to the earthquake in the caldera indicate deep lake deposits, with very soft clay, reaching a void ratio of 5 to 7, and ranging in thickness between about 20 m to 70 m.

Surface Rupture: Shimojin-Cho River Canal

One site of importance as a case history was the Futagawa Fault rupture through a river levee and embankment at Shimojin District. At this site, two separate strands of the Futagawa Fault converged and ruptured through a canal. The northeastern trending strand of the Futagawa Fault that ruptured through the canal had the typical right-lateral strike-slip movement of this earthquake. The second strand was a left-lateral strike slip fault. This second strand appeared to be a link between a northern strand of the Futagawa Fault that was about 0.6 km north of the canal site and the strand of the Futagawa that ruptured through here.

Zero-Displacement Lateral Spread

Of particular interest to the engineering community would be a location where liquefaction is believed to have triggered, but no horizontal deformations occurred. These types of case histories have been referred to as zero-displacement lateral spread (Youd et al. 2009), and are generally lacking from most of the current empirical lateral spread databases.

We believe that a zero-displacement lateral spread may have occurred at the large highway bridge on Route 501 crossing the southern tributary of the Midorikawa River near Minamihashirikami (32.69389° N 130.64776° E). No evidence of lateral spread was visible in the free-field around the bridge, but the existence of sand boils and minor cracking near the northern abutment suggests that at least one soil layer liquefied during the Kumamoto earthquake sequence. This bridge is located approximately 12 kilometers to the southwest of the epicenter of the main shock.

Paucity of Liquefaction and Lateral Spread Features

Ground motions from both the April 14 event on the Hinagu fault and the April 16 7.0 event on the Futagawa fault exceeded 1g in Mashiki town and central Kumamoto. One important observation was the surprising lack of widespread and pervasive liquefaction and lateral spread failure of the ground given the intensity of these motions. Soil borings indicate that much of the alluvial plane is underlain by volcanic sand deposits. Why these did not liquefy in abundance is worthy of further investigation to understand what aspect of the soil structure has resisted liquefaction susceptibility and consequences in terms of excessive deformation. The regional source material for alluvium is the volcanic debris shed from Aso san caldera. It may be that a combination of grain angularity of the volcanic rock and shards, and the prevalence of highly plastic weathered clay from volcanic ash in the void space of the sands has produced a low-susceptibility soil for liquefaction. Soil borings inside Aso san indicate deep accumulations of high void ratio (Smectite) clays. Erosion of these materials and re-deposition in the Kumamoto plane may lead to depositions of dirty sands with a high plasticity fines fraction. A campaign of soil sampling with reliable SPT/CPT data where liquefaction was not observed would be warranted to better understand why the geo-spatial extent of liquefaction was limited.

Acknowledgments

The GEER reconnaissance was led by Shideh Dashti (University of Colorado Boulder) and Robert Kayen (United States Geological Survey & University of California, Los Angeles) and included, alphabetically, team members Dallin Briggs (Brigham Young University), Jenny Ramirez Calderon (University of Colorado Boulder), Kevin Franke (Brigham Young University), Samantha Guillies (University of Colorado Boulder), Nicolas Oettle (AECOM), and Brad Wham (Cornell University). The Japanese team was led by Takaji Kokusho (Prof. Emeritus, Chuo University) and Hemanta Hazarika (Kyushu University), and included Yutaka Tanoue (Kiso-Jiban Consultants Co., Ltd.), Katsuji Takematsu (Japan Foundation Engineering Co., Ltd.), Daisuke Matsumoto (Japan Foundation Engineering Co., Ltd.), Takayuki Morinaga (Japan Foundation Engineering Co., Ltd.), Hideo Furuichi (Giken Co., Ltd.), Yuuta Kitano (Giken Co., Ltd.), Masanori Tajiri (Professional Engineering Office), Babloo Chaudhary (Kyushu University), Kengo Nishimura (Kyushu University), and Chu Chu (Kyushu University). Katherine Cheng (University of California, Berkeley) and Jenny Blonquist (Brigham Young University) participated on the reconnaissance data processing remotely from the US.

The authors of this report would like to thank Professor Ishihara (Chuo University), Professor Tokimatsu (Tokyo Institute of Technology), Professor Konagai (Yokohama National University), Professor Yasuda (Tokyo Denki University), Dr. Kuraoka (JSCE), the Japanese Society of Civil Engineering (JSCE) and the Japanese Geotechnical Society (JGS) for assisting in the planning of this reconnaissance effort. Thanks are extended to Yasunori Kimura (Japan Water Works Association) and Kumamoto City Waterworks and Sewage Bureau representatives Hirofumi Nakashima and Hitoshi Fujimoto for providing valued information about municipal utility damage and recovery efforts. Colleagues at Kubota Corp, including Toshio Toshima, Satoshi Suenaga, Takeshi Hara, Mitsuo Hayashi, and Kohei Ikeda, are acknowledged for providing valuable guidance and information before, during, and after the reconnaissance mission.

The work of the GEER Association, in general, is based upon work supported in part by the National Foundation through the Geotechnical Engineering Program under Grant No. CMMI-1266418. Support for the participation of students (Ms. Jenny Ramirez Calderon and Ms. Samantha Guillies) in the reconnaissance effort was provided by the National Science Foundation through Grant No. 1454431. The GEER Association is made possible by the vision and support of the NSF Geotechnical Engineering Program Directors: Dr. Richard Fragaszy and the late Dr. Cliff Astill. GEER members also donate their time, talent, and resources to collect time-sensitive field observations of the effects of extreme events. Any opinions, findings, and conclusions or recommendations expressed in this material are those of the authors and do not necessarily reflect the views of the NSF.

1.0 Introduction

The 2016 Kumamoto earthquakes are a series of events that began with an earthquake of moment magnitude 6.2 on the Hinagu Fault at 21:26 JST on April 14, 2016, at an epicentral depth of about 11 kilometers, followed by another foreshock of moment magnitude 6.0 on the Hinagu Fault at 0:03 JST on April 15, 2016, and a larger moment magnitude 7.0 event on the Futagawa Fault, which struck at 01:25 JST on April 16, 2016 beneath Kumamoto City, Kumamoto Prefecture on Kyushu, Japan, at an epicentral depth of about 10 kilometers. These events are the strongest earthquakes recorded in Kyushu during the modern instrumental era. The earthquakes resulted in substantial damage to infrastructure, buildings, cultural heritage of Kumamoto Castle, roads and highways, slopes, and river embankments due to earthquake-induced landsliding and debris flows. Surface fault rupture produced offset and damage to roads, buildings, river levees, and an agricultural dam. Surprisingly, given the extremely intense earthquake motions, liquefaction occurred only in a few districts of Kumamoto City and in the port areas indicating that the volcanic soils were less susceptible to liquefying than expected given the intensity of earthquake shaking, a significant finding from this event.

The motivation for organizing and fielding the Kumamoto event reconnaissance rapidly was to document engineering and scientific effects of an unusual event that produced almost 40 kilometers of surface rupture in order to advance research and practice in designing and constructing in this environment. The GEER Kumamoto field team's main goal is to quantify the spatial extent and characteristics of that surface rupture as well as geotechnical failures and non-failures (e.g., damage from the Kumamoto and Aso San Caldera area due to soil-foundation-structural failures, ground failures, soil liquefaction, landslides, and damage to bridges, piers, ports and harbors, lifeline systems, earth dams, levees, and other critical facilities). It is important to document poor ground performance, but also surprisingly good performance of ground in the Kumamoto region with regard to liquefaction effects. Due to the necessary follow-on recovery and reconstruction activities, much of the critically important observable damage is perishable. Toward that end, GEER fielded a team within three weeks after the event, and soon after the initial humanitarian response phase had ended. The primary duties of the Kumamoto GEER reconnaissance team are to identify critical case histories, report our findings rapidly on the GEER website through PDFs, web pages, Google Earth kml files, and animations of UAV and LIDAR data. Experienced participants also have the responsibility to train new participants in the key-elements of reconnaissance fieldwork.

The authors conducted the GEER reconnaissance survey from May 11th to 13th. GPS tracklogs of the movement of the reconnaissance team were recorded and are presented in Figure 1-1. The entire team worked together the first day in the field visiting liquefaction sites in Kumamoto City and the port of Kumamoto. During the second and third days, the team worked in two or more groups to characterize damage in the lowland and upland region of Aso San and the alluvial plane of Kumamoto City and Mashiki town. On the second day, Drs. Brad Wham and Shideh Dashti also met with engineers from Kumamoto City Waterworks and Sewage Bureau Deputy and Satoshi Suenaga of Kubota Corp on May 12th, 2016 to discuss overall performance of lifelines during the Kumamoto earthquake series. This report summarizes the observations of the GEER team.

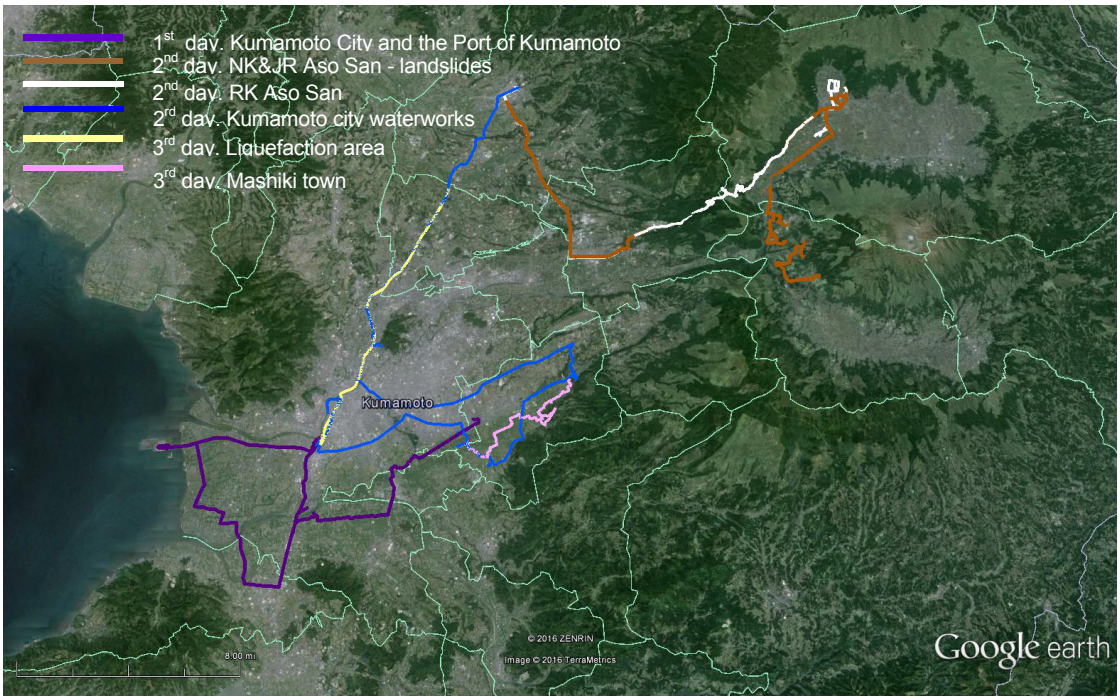

Figure 1-1. Tracklog of GEER team movements in the Kumamoto region in Japan.

2.0 Regional Geology

2.1 Framework Geology

The Kumamoto-Aso San region of Kyushu Island is a complex structure of Paleozoic and Mesozoic rocks associated with Island arc plutonism/volcanism, accretionary tectonics metamorphism, and the filling of backarc and forearc basin. The Geologic Survey of Japan (GSJ) has published a map of the Kumamoto Quadrange (Hoshizumi, 2004) that shows this complex structure of Paleozoic, Mesozoic, Cenozoic, and Neogene rocks. Of the Paleozoic, Kyushu is underlain by a suite of arc-tectonics-related igneous and metamorphic terrain including the mafic/ultramafic Permian Yamaga Metagabbro, Late Permian Mizukoshi Formation, and the Mississipian & Pennsylvanian to Permian Sangun-Renge Metamorphic Rocks.

Mesozoic structures also indicate arc-volcanism with preservation of more felsic igneous rocks than preserved from the Paleozoic and arc-sedimentary basins structures including the Triassic-to-Jurassic Suō Metamorphic Rocks, the Cretaceous Higo Metamorphic Rocks, the Cretaceous marine and non-marine sedimentary of the Mifune and Himenoura Groups, and Cretaceous granitic rocks.

Paleocene, Neogene and Quaternary rocks are associated with arc-volcanics and sedimentary structures shed from these volcanics rocks including Miocene basalts and andesites, Pliocene basalts, andesites, and rhyolites. Significant volumes of Quaternary volcanics the source of as Unzen crater, Aso San Caldera, and the Mt. Kimbo and Mt. Tara volcanoes. Eocene to Oligocene sedimentary rocks are Ginsui and Hokonoko Formations, Ōmuta, Isahaya, Manda, Ochi and Kishima Groups. Neogene Quaternary volcanoclastic sediment form the Kumamoto basin and Shimabara Bay depocenter.

2.2 Tectonics

Kyushu is unusual for Japan in that a rift extending from the central Aso San region to Okinawa is a NW-SE has led to an extensional region associated of normal faulting and active volcanism. Aso San caldera and the Beppu-Haneyama graben define the eastern end of this rift zone, and towards the southwest the Unzen volcano and graben extends to the southern edge of Kyushu and continues down to the Okinawa trough (Okumura, 2016).

The extensional rift zone of central and western Kyushu transitions to a transform mechanism defined by the strike-slip Quaternary Median tectonic line, starting in Beppu Bay and crossing Shikkoku Island and Wakayama peninsula. This transform relieves compressional E-W stresses from Philippine plate.

Futagawa and Hinagu fault zones are the southern boundary of the extensional graben/rift zone to the north. Motion along these faults is a combination of right-lateral slip and normal-down-to-the-north-slip resulting in oblique displacement. The basin formed by the long-term normal motion to the north of the faults has filled the Kumamoto basin with Neogene and Quaternary volcanics and volcanoclastic sediment. To the south of the Futagawa and Hinagu faults, the uplifted Mesozoic subduction-related sediment have been dragged toward the southwest, extending the Kagoshima peninsula in that direction and creating the upland Kyushu Mountain region and southern boundary to the Kumamoto basin. Normal displacement along the Futagawa and Hinagu system represents southern boundary of the extensional rift zone of Central Kyushu, and the right-lateral strike-slip component of motion represents a continuation of compressional stresses driven by Quaternary Median tectonic transform.

Structurally, Futagawa and Hinagu faults strike NE and dip NW at angles of 60 to 80 degrees (Okumura, 2016).

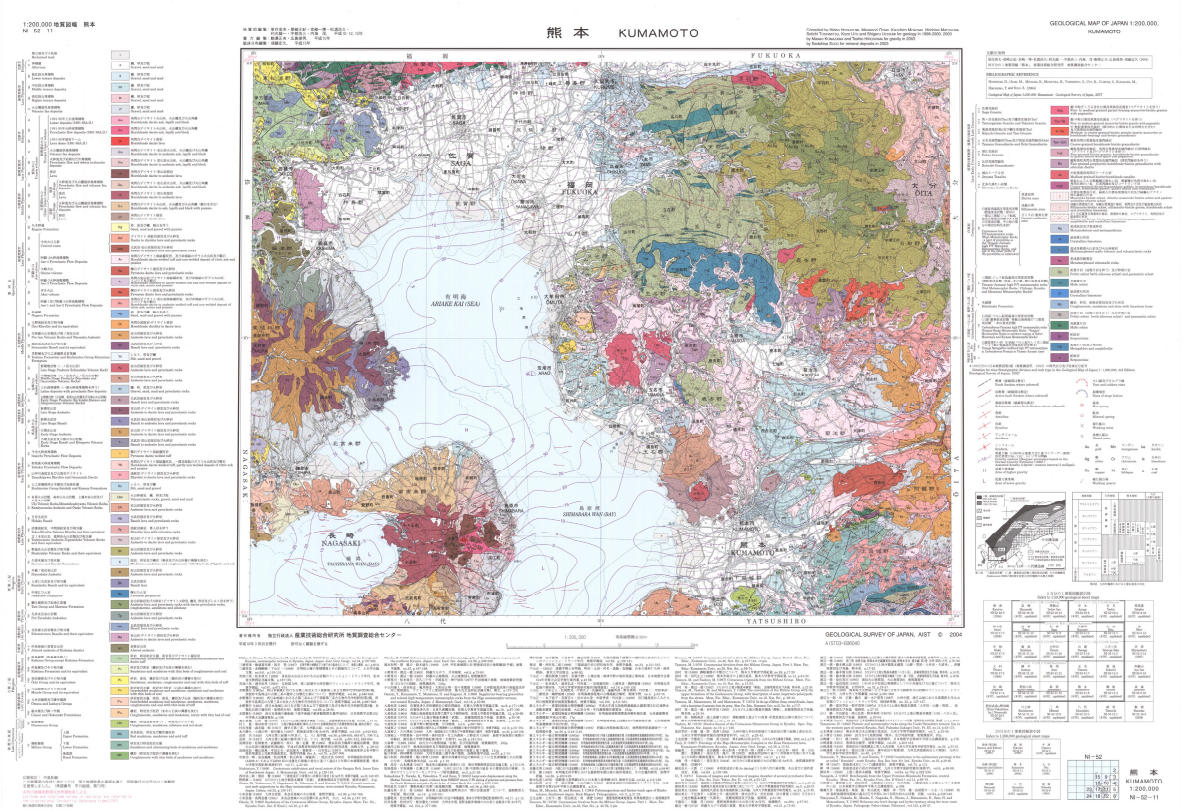

Figure 2-1. Geologic units of the Central Kyushu region (Hoshizumi et al. 2004). Red and pink units represent volcanic and pyroclastic origin, white, grey and earth tone units represent sedimentary environments. Larger version is presented in Appendix A.

2.3 Sedimentary Structures of the Kumamoto – Aso San Region

The sedimentary structures of the Kumamoto region are presented on the seam-less geologic map of the Geological Survey of Japan (2016d) and divided into the southern Pleistocene and Holocene alluvial plane called the Heiya (Unit 1), and elevated Pleistocene fluvial terraces (Units 170-171). A pyroclastic flow of late Pleistocene age (Unit 83 and 95) also provides elevated ground to the north. Kumamoto City, Mashiki-Mura and most of the urban developed areas of the Kumamoto basin are founded on the elevated fluvial terraces and pyroclastic flows. The Futagawa fault cuts the lava plateau of Unit 83 and to the southwest is the boundary between the Heiya (Heiya1) and Mesazoic accretionary sedimentary rocks. The Hinagu fault also cuts through the Heiya and mesazoic bedrock and merges with the Futagawa fault east of Mashiki-mura.

Subsidence of the Kumamoto Heiya has been estimated to have rates of a rate of 0.90 mm/yr near the coast and 0.45 mm/yr in south of Kumamoto city (Okumura, 2016). Thus, since the last (Sangamon) interglacial transgressive sea level high stand,120-126 k.y.a., approximately 100 m of subsidence has occurred at the coast and perhaps 50 m along the southern city boundary of Kumamoto. This plain now resides in equilibrium slightly above sea level (Ishizaka et al. 1975). Soft wet soil of the Heiya is associated with poor foundation conditions and agricultural land, and so there

was minor rural development in the region where site amplification would be predicted to be greatest. Where structures did cross the Heiya, for example the Kumamoto highway, damage was severe.

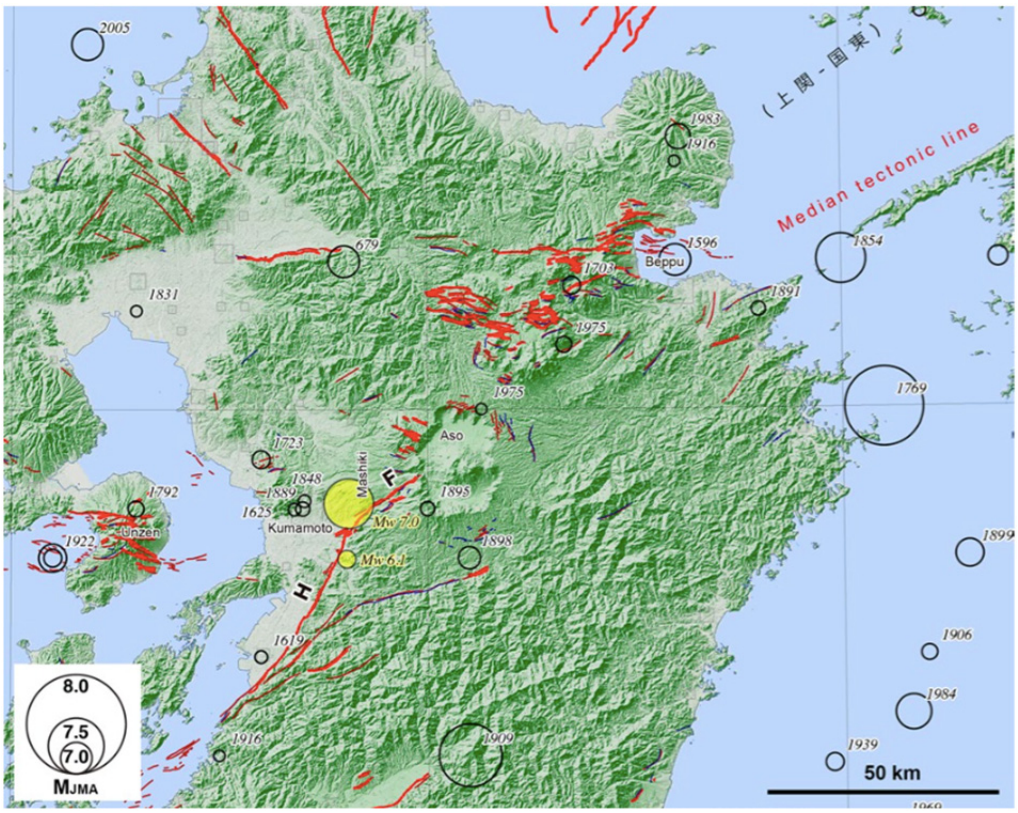

Figure 2-2. Quaternary faults and earthquakes in Northern Kyushu Quaternary faults: Nakata and Imaizumi eds. (2002), Research Group for Active Faults of Japan (1995) Historic earthquakes: Usami (1996).

The urban area of greatest damage, Mashiki-Mura is located on the south-facing slope above the alluvial plain and below the Pleistocene fluvial terrace deposits and pyroclastic flows. Ground shaking during the April 14 and 16 events (JST) exceeded 1.0g and Intensity 7 at Mashiki Town. A manifestation of the volcanic classic origin of sediment underlying Kumamoto City is seen in the sand as a boil material that came to the surface as a result of the earthquake shaking of April 14 and April 16. With the exception to fill deposits, all of the observed sand boils were dark, seemingly mafic granular material. Inspection of this material found that it was composed of pumice and coherent granular volcanically derived material. The volcanic origin and dark coloration is in stark contrast to typical liquefaction surficial materials derived from the weathering of sedimentary, metamorphic, or plutonic rocks. It was also observed that there was a general lack of abundant liquefaction given the strong level of earthquake shaking. Although soil borings are needed to verify, the GEER team believes that this lack of abundance is probably associated with high plastic fines content associated with hydrous clays (smectite, etc.) that are daughter products of weathering of volcanic terrain.

Volcanic soil also is highly angular compared with spherical quartz grains. This angularity may be associated with denser packing materials and lower liquefaction susceptibility.

2.4 Soil Conditions in the Aso Caldera

Aso San Caldera formed 95 kya and as a result, a crater lake filled in with many tens of meters of fine-grained high void ration sediment. A soil boring near the Aso San depression zone indicates nearly 70 meters of fine sediment with void ratios ranging from 5 to 7. The central cone of the caldera broke through this crater lake and deposited upwards of 10 meters of additional pyroclastic sediment near the modern surface. A late Pleistocene/Holocene outburst event(s) drained the crater lake through a western passage dissecting the Aso Caldera rim wall, flooding the Kumamoto plain. Formation of the sedimentary fault-graben Aso and likely site amplification are associated with this high void ratio sediment of volcanic origin. These void ratios are most likely due to an abundance of hydrophilic clays (Montmorillinite, Smectite).

Figure 2-3. Dark sand boils were typical of liquefaction sites in Mashiki town and southern Kumamoto City.

3.0 Seismological Information and Recorded Ground Motions

Two strong foreshocks (moment magnitude M_w 6.2 and 6.0; Japan local magnitude M_J 6.5 and 6.4) on April 14th and April 15th, respectively, and a mainshock (M_w 7.0; M_J 7.3) on April 16th, 2016 (Japan Standard Time, JST) caused strong levels of shaking in the region and damaged buildings and parts of the infrastructure. These earthquakes were shallow (hypocentral distance of approximately 11 and 12 km, according to the Japan Meteorological Agency) under the city of Kumamoto. Building collapse due to strong shaking or landslides as well as damage to roads and lifelines were observed.

The plate tectonic map in Figure 3-1 shows the Pacific, Philippine, and the Eurasian plates and their rates of movement. The Philippine Plate continues subducting beneath the Eurasian plate at a rate of approximately 55 mm/year. Figure 3-2 (Iris, 2016) shows the historic seismicity in the area and that the April 16th, 2016 main event occurred on a crustal fault within the Eurasian plate. The earthquakes were distributed along the Futagawa and Hinagu faults. The focal mechanism for the earthquake has been identified as primarily a strike-slip right lateral mechanism in the northeast direction (fault plane movement shown in Figure 3-3).

Figure 3-4 and Figure 3-5 show the shaking intensity map and the distribution of PGA and PGVs recorded during the main shock. Significant shaking was observed and recorded in the region. Figure 3-6 and Table 3-1 show the location and properties of ground motions recorded at the KiK-net and K-NET strong motion stations within a distance of 40 km from the epicenter of the main event. Some of the strong motion stations appear to have been placed on soil as opposed to outcropping rock. A few examples of recordings and soil profiles near the epicenter are provided in Figure 3-7 through Figure 3-12. PGAs as high as 1.2g and 0.9g were recorded during the main event in the horizontal and vertical directions, respectively (e.g., at the KMMH16 station).

Generally, despite significant depths of saturated sandy soils that could be liquefiable with SPT blow counts of less than 10 (KMMH5 and 8), there was no clear evidence of soil liquefaction in the surface recordings (e.g., the shape of acceleration time histories or their frequency content). The available boring logs (Appendix B) do not provide information on the fines content and plasticity of different soil layers. It is hypothesized that the granular soils in this region contained a significant clay content that increased soil's resistance to liquefaction. This observation was consistent throughout the region.

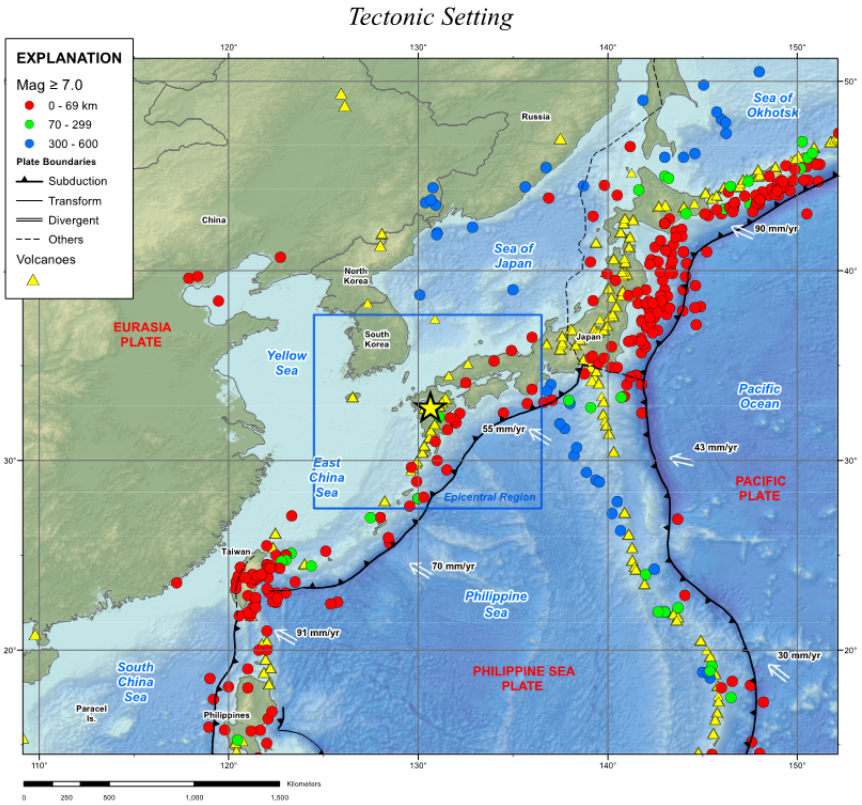

Figure 3-1. Plate tectonic map in the Kyushu region of Japan, courtesy of IRIS, 2016

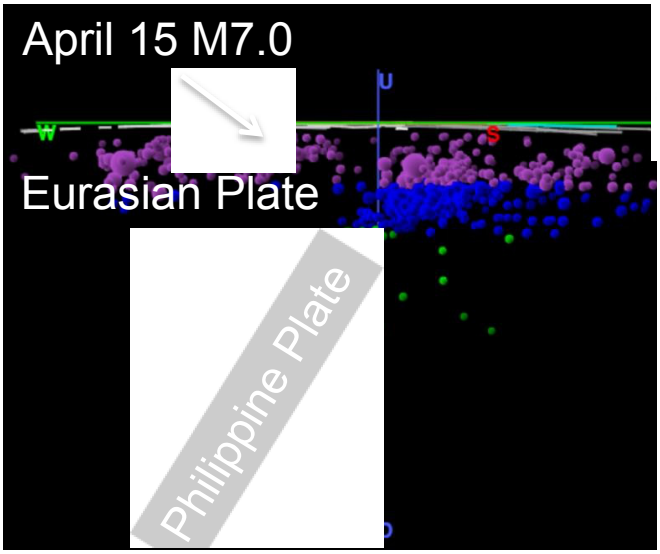

Figure 3-2. Historic seismicity shown in the Kyushu region of Japan and the Philippine Plate subducting below the Eurasian plate, courtesy of IRIS Interactive Earthquake Browser.

Figure 3-3. Right-lateral fault movement observed by the GEER team.

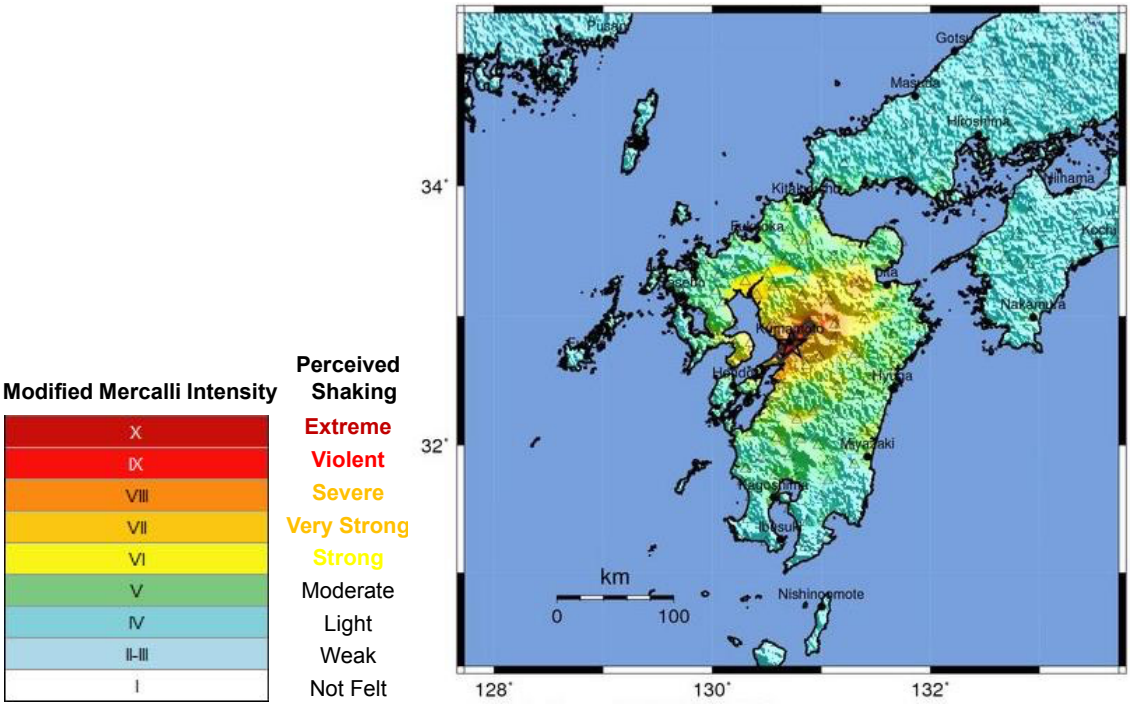

Figure 3-4. Shaking Intensity Map during the M_W 7.0 Kumamoto Earthquake in Japan Courtesy of the USGS.

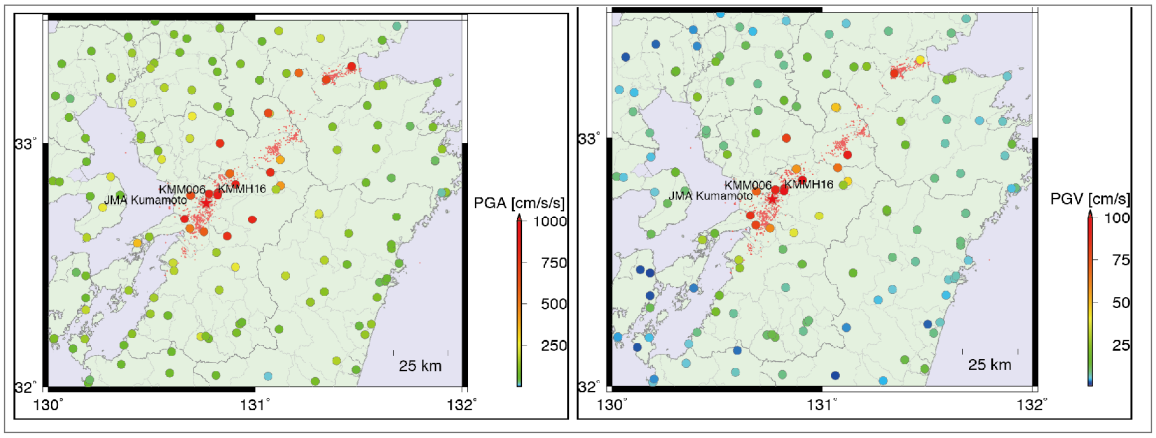

Figure 3-5. Distribution of PGAs and PGVs recorded during the main M_W 7.0 earthquake (Goto, 2016).

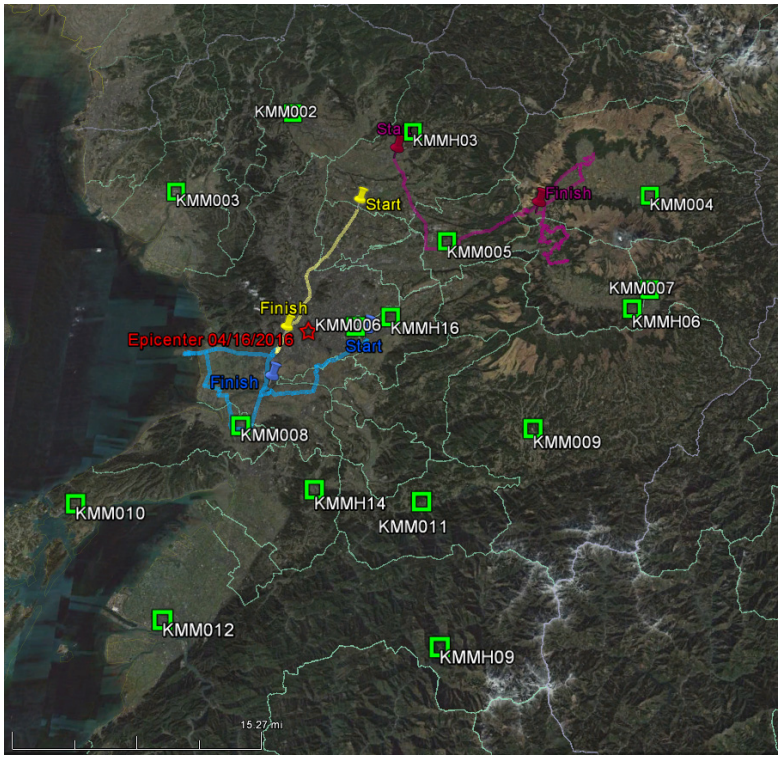

Figure 3-6. Map of strong motion stations within an epicentral distance of 40 km and the reconnaissance paths taken by the GEER team.

Table 3-1. Location and intensity of motions recorded at strong motion stations within an epicentral distance of 40 km.

Station	Latitude	Longitude	PGA (g) dir. NS	PGA (g) dir. EW	PGA (g) dir. UD	Altitude (m)
KMM002	33.0185	130.6846	0.16	0.20	0.15	+30
KMM003	32.9336	130.5477	0.15	0.18	0.08	+14
KMM004	32.9320	131.1214	0.26	0.32	0.26	+556
KMM005	32.8761	130.8774	0.36	0.43	0.42	+124
KMM006	32.7934	130.7772	0.85	0.47	0.54	+34
KMM007	32.8267	131.1226	0.22	0.43	0.28	+548
KMM008	32.6878	130.6582	0.66	0.78	0.44	+4
KMM009	32.6858	130.9856	0.79	0.58	0.19	+443
KMM010	32.6136	130.4874	0.09	0.11	0.07	+2
KMM011	32.6167	130.8652	0.60	0.62	0.27	+142
KMM012	32.5078	130.6024	0.19	0.17	0.14	+3
KMMH03	32.9984	130.8301	0.03 0.44	0.08 0.23	0.04 0.39	-22 +178
KMMH06	32.8114	131.101	0.03 0.12	0.03 0.19	0.09 0.11	+381 +492
KMMH09	32.4901	130.9046	0.08 0.19	0.08 0.19	0.01 0.09	+420 +520
KMMH14	32.6345	130.7521	0.11 0.32	0.11 0.36	0.13 0.53	-40 +70
KMMH16	32.7967	130.8199	0.19 0.64	0.28 1.18	0.19 0.90	-197 +55

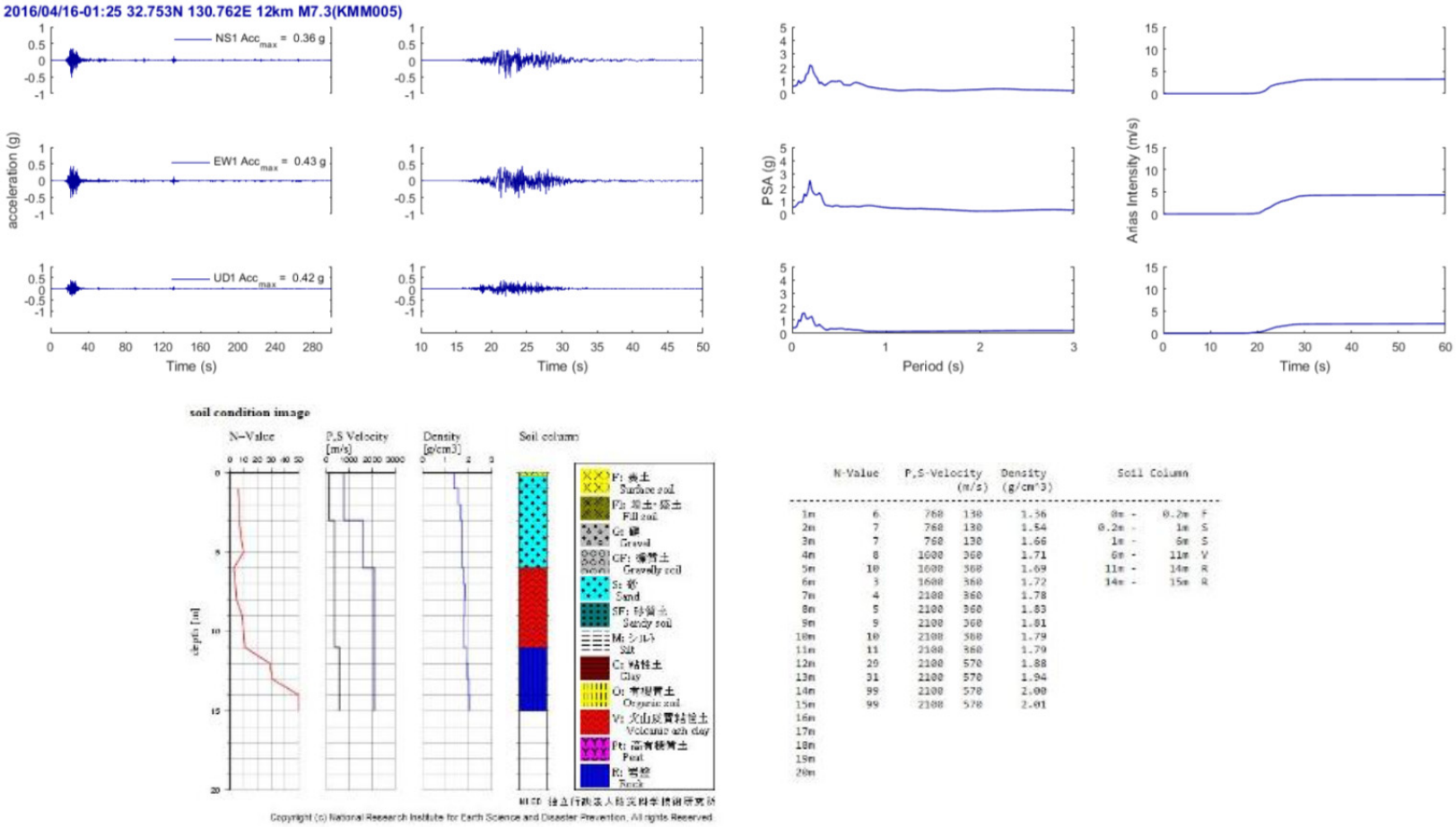

	N-Value	P,S-Velocity (m/s)		Density (g/cm^3)	Soil Column		
1m	6	760	130	1.56	0m -	0.2m	F
2m	7	760	130	1.54	0.2m -	1m	S
3m	7	760	130	1.66	1m -	6m	S
4m	8	1600	360	1.71	6m -	11m	V
5m	10	1600	360	1.69	11m -	14m	R
6m	3	1600	360	1.72	14m -	15m	R
7m	4	2100	360	1.78			
8m	5	2100	360	1.83			
9m	9	2100	360	1.81			
10m	10	2100	360	1.79			
11m	11	2100	360	1.79			
12m	20	2100	570	1.88			
13m	31	2100	570	1.94			
14m	99	2100	570	2.00			
15m	99	2100	570	2.01			
16m							
17m							
18m							
19m							
20m							

Figure 3-7.Three components of acceleration recorded at the soil surface at station KMM005.

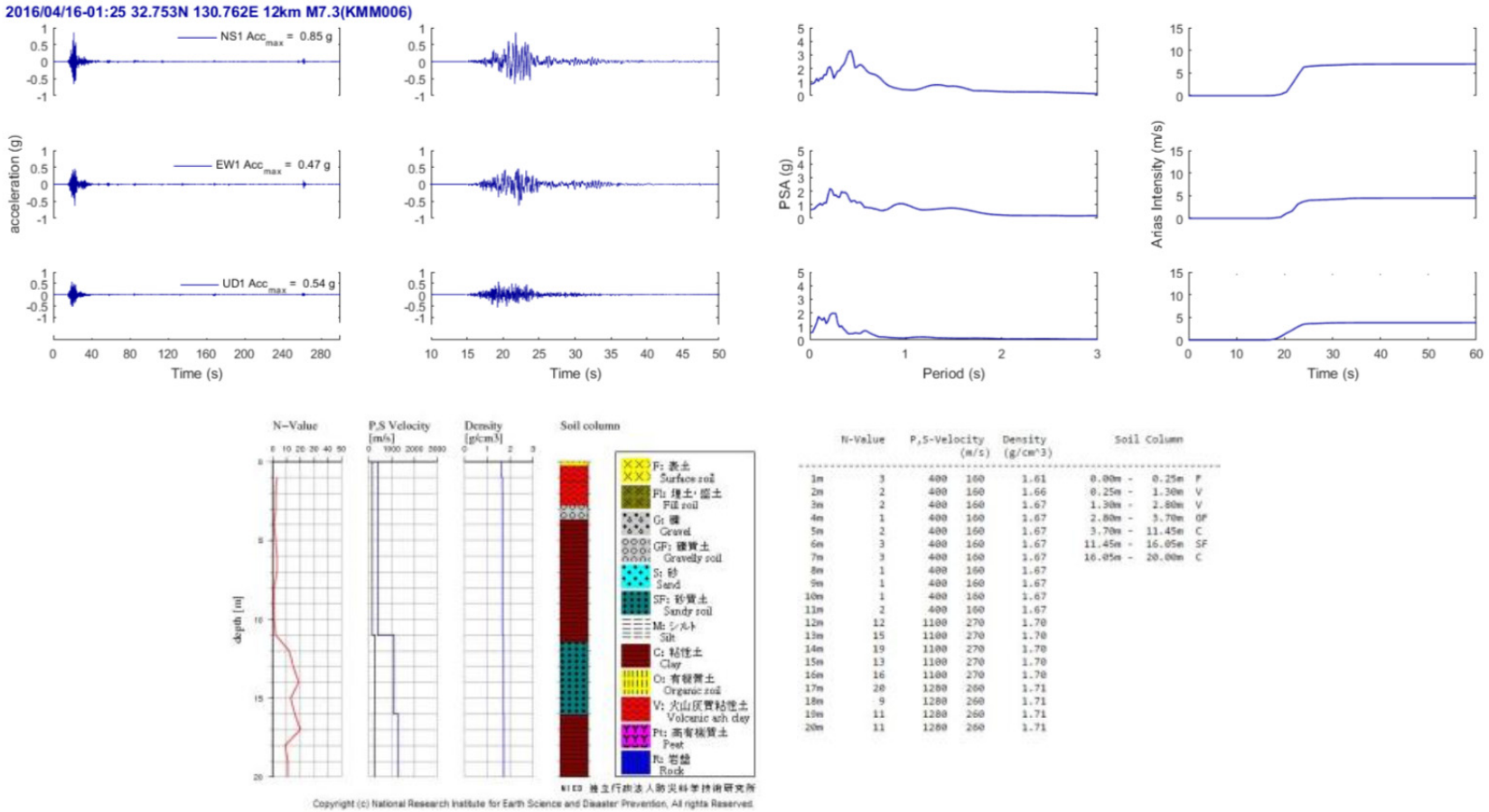

	N-Value	P,S-Velocity (m/s)		Density (g/cm^3)	Soil Column	
1m	3	400	160	1.61	0.00m - 0.25m	F
2m	2	400	160	1.66	0.25m - 1.30m	V
3m	2	400	160	1.67	1.30m - 2.80m	V
4m	1	400	160	1.67	2.80m - 3.70m	OF
5m	2	400	160	1.67	3.70m - 11.45m	C
6m	3	400	160	1.67	11.45m - 16.05m	SF
7m	3	400	160	1.67	16.05m - 20.00m	C
8m	1	400	160	1.67		
9m	1	400	160	1.67		
10m	1	400	160	1.67		
11m	2	400	160	1.67		
12m	12	1100	270	1.70		
13m	15	1100	270	1.70		
14m	19	1100	270	1.70		
15m	13	1100	270	1.70		
16m	16	1100	270	1.70		
17m	20	1280	260	1.71		
18m	9	1280	260	1.71		
19m	11	1280	260	1.71		
20m	11	1280	260	1.71		

Figure 3-8. Three components of acceleration recorded at the soil surface at station KMM006.

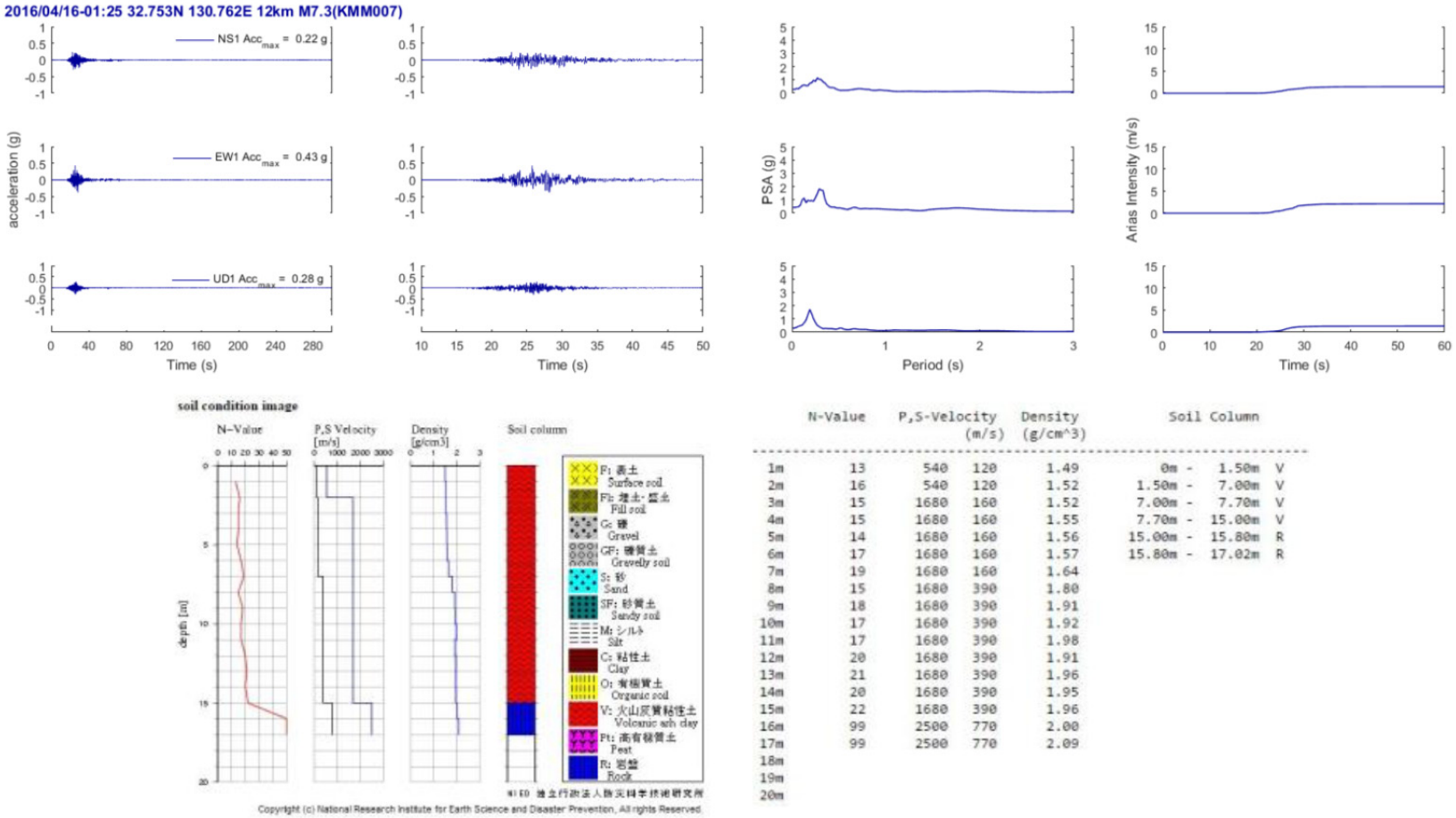

	N-Value	P,S-Velocity (m/s)		Density (g/cm^3)	Soil Column		
1m	13	540	120	1.49	0m - 1.50m		V
2m	16	540	120	1.52	1.50m - 7.00m		V
3m	15	1680	160	1.52	7.00m - 7.70m		V
4m	15	1680	160	1.55	7.70m - 15.00m		V
5m	14	1680	160	1.56	15.00m - 15.80m		R
6m	17	1680	160	1.57	15.80m - 17.02m		R
7m	19	1680	160	1.64			
8m	15	1680	390	1.80			
9m	18	1680	390	1.91			
10m	17	1680	390	1.92			
11m	17	1680	390	1.98			
12m	20	1680	390	1.91			
13m	21	1680	390	1.96			
14m	20	1680	390	1.95			
15m	22	1680	390	1.96			
16m	99	2500	770	2.00			
17m	99	2500	770	2.09			
18m							
19m							
20m							

Figure 3-9. Three components of acceleration recorded at the soil surface at station KMM007.

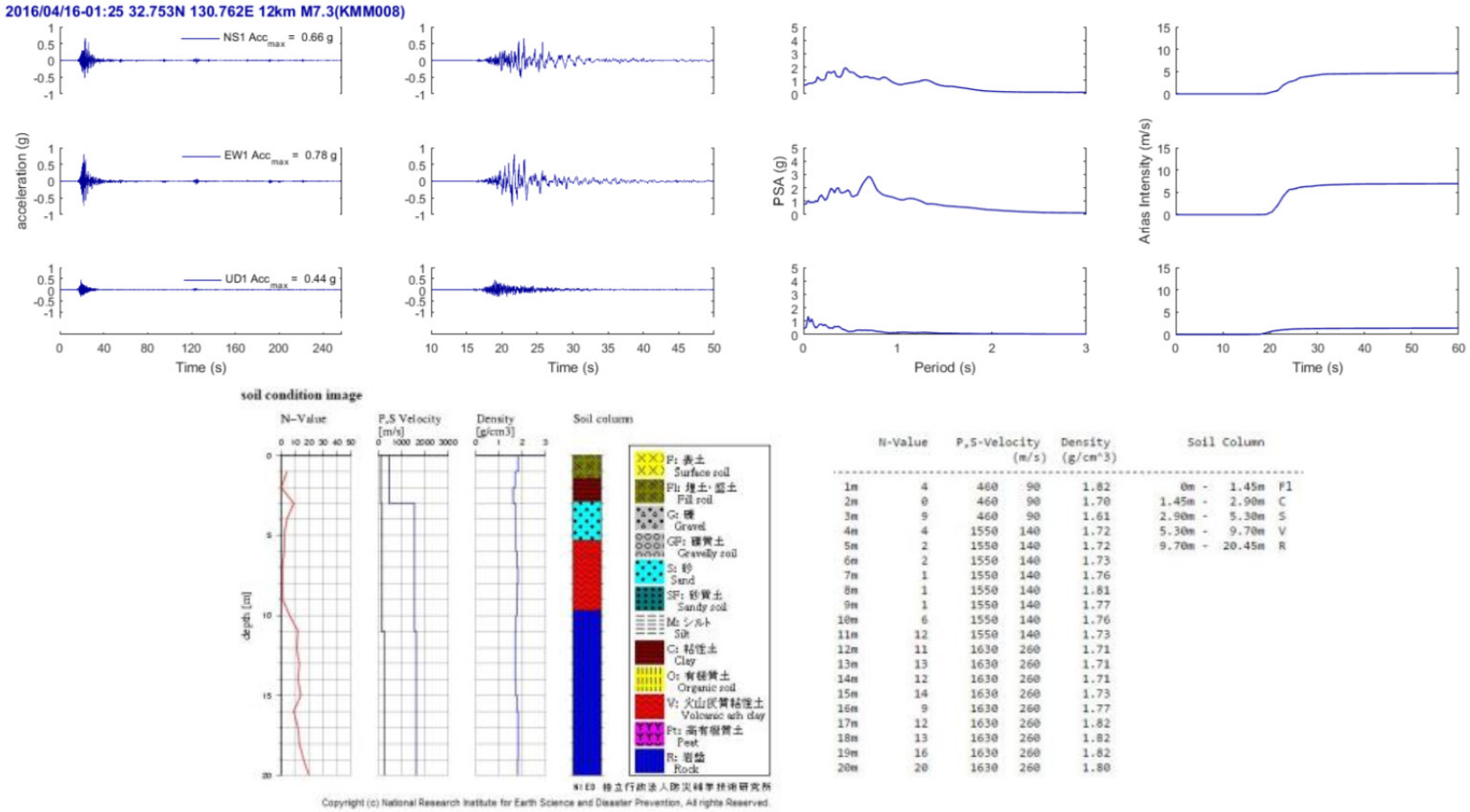

	N-Value	P,S-Velocity (m/s)	Density (g/cm^3)	Soil Column	
1m	4	460	90	1.82	0m - 1.45m Fl
2m	0	460	90	1.70	1.45m - 2.90m C
3m	9	460	90	1.61	2.90m - 5.30m S
4m	4	1550	140	1.72	5.30m - 9.70m V
5m	2	1550	140	1.72	9.70m - 20.45m R
6m	2	1550	140	1.73	
7m	1	1550	140	1.76	
8m	1	1550	140	1.81	
9m	1	1550	140	1.77	
10m	6	1550	140	1.76	
11m	12	1550	140	1.73	
12m	11	1630	260	1.71	
13m	13	1630	260	1.71	
14m	12	1630	260	1.71	
15m	14	1630	260	1.73	
16m	9	1630	260	1.77	
17m	12	1630	260	1.82	
18m	13	1630	260	1.82	
19m	16	1630	260	1.82	
20m	20	1630	260	1.80	

Figure 3-10. Three components of acceleration recorded at the soil surface at station KMM008.

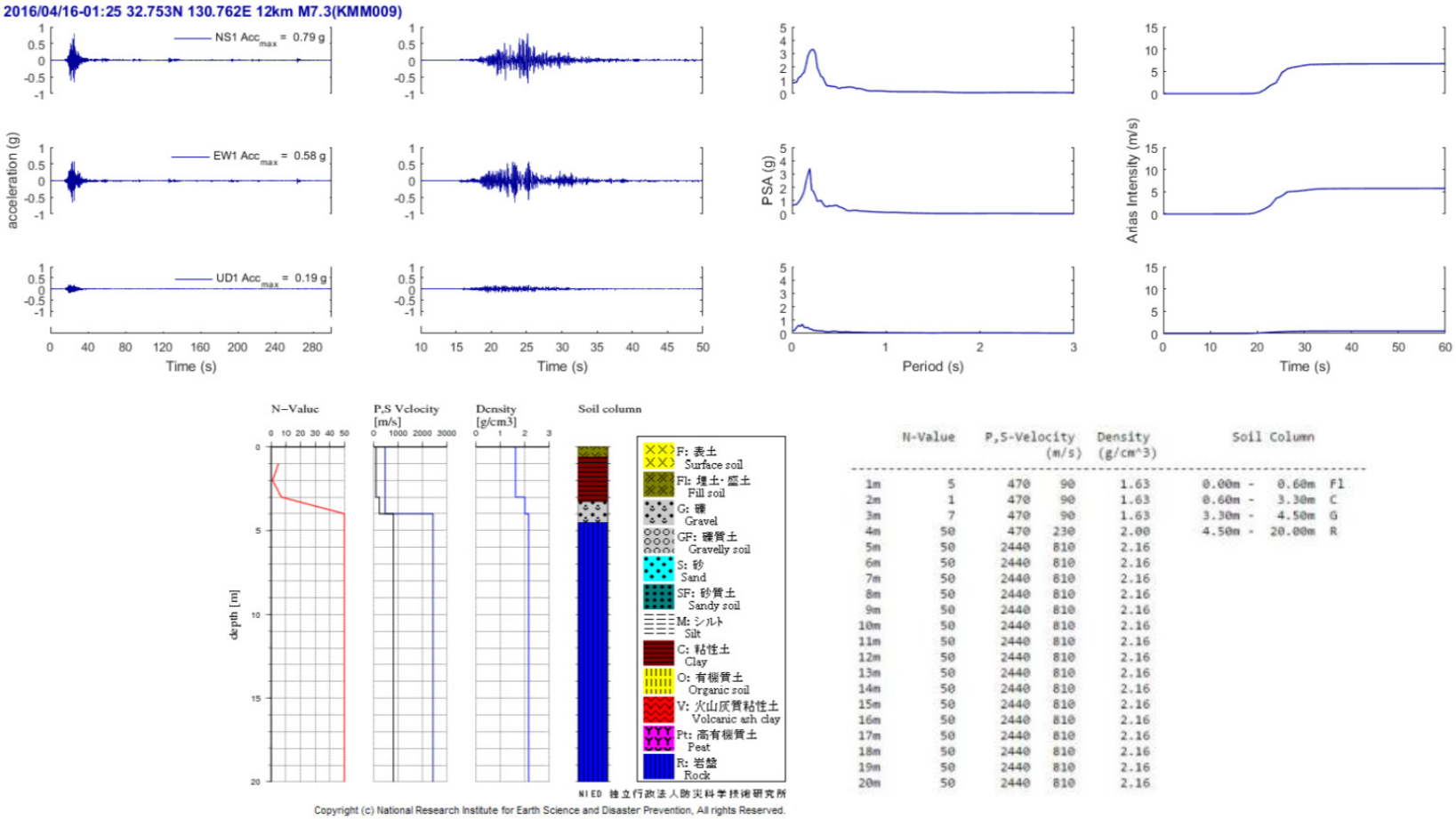

	N-Value	P,S-Velocity (m/s)		Density (g/cm^3)	Soil Column	
1m	5	470	90	1.63	0.00m - 0.60m	Fl
2m	1	470	90	1.63	0.60m - 3.30m	C
3m	7	470	90	1.63	3.30m - 4.50m	G
4m	50	470	230	2.00	4.50m - 20.00m	R
5m	50	2440	810	2.16		
6m	50	2440	810	2.16		
7m	50	2440	810	2.16		
8m	50	2440	810	2.16		
9m	50	2440	810	2.16		
10m	50	2440	810	2.16		
11m	50	2440	810	2.16		
12m	50	2440	810	2.16		
13m	50	2440	810	2.16		
14m	50	2440	810	2.16		
15m	50	2440	810	2.16		
16m	50	2440	810	2.16		
17m	50	2440	810	2.16		
18m	50	2440	810	2.16		
19m	50	2440	810	2.16		
20m	50	2440	810	2.16		

Figure 3-11. Three components of acceleration recorded at the soil surface at station KMM009.

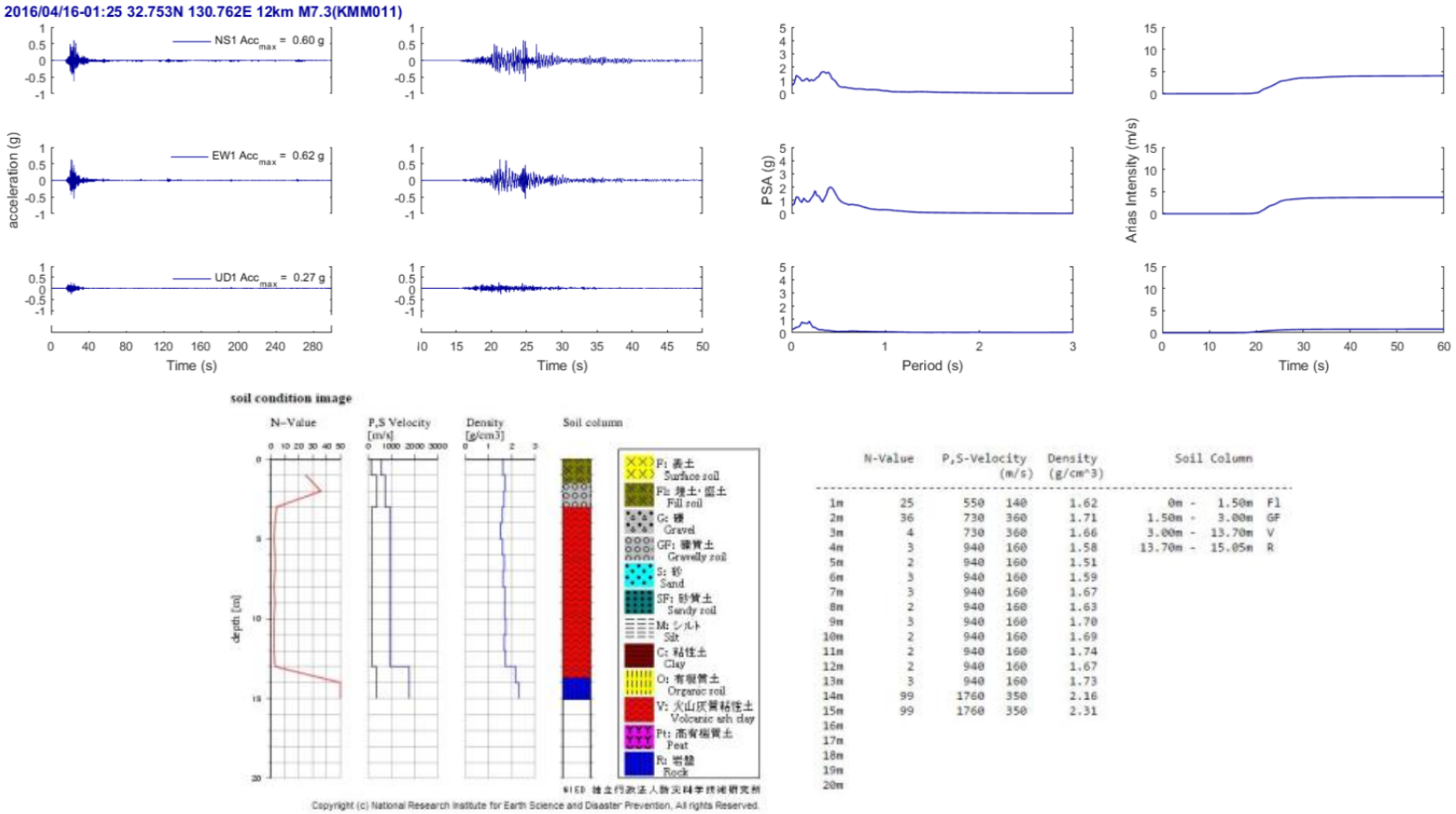

	N-Value	P,S-Velocity (m/s)		Density (g/cm^3)	Soil Column	
1m	25	550	140	1.62	0m - 1.50m	Fl
2m	36	730	360	1.71	1.50m - 3.00m	GF
3m	4	730	360	1.66	3.00m - 13.70m	V
4m	3	940	160	1.58	13.70m - 15.05m	R
5m	2	940	160	1.51		
6m	3	940	160	1.59		
7m	3	940	160	1.67		
8m	2	940	160	1.63		
9m	3	940	160	1.70		
10m	2	940	160	1.69		
11m	2	940	160	1.74		
12m	2	940	160	1.67		
13m	3	940	160	1.73		
14m	99	1760	350	2.16		
15m	99	1760	350	2.31		
16m						
17m						
18m						
19m						
20m						

Figure 3-12. Three components of acceleration recorded at the soil surface at station KMM011.

4.0 Fault Surface Rupture

4.1 Overview

The fault rupture in the foreshocks and mainshock occurred along the Hinagu and Futagawa Faults. The Hinagu Fault is the southernmost fault in this area, just south of Kumamoto, and intersects the Futagawa Fault south of Kumamoto. The Futagawa Fault projects from that intersection point both to the west (the Uto Segment) and to the northeast (the Futagawa Segment) (GSJ, 2016a). Each of these faults were, in general, previously mapped by the Geological Society of Japan prior to these earthquakes. See Figure 4-1 for a depiction of the faults.

Sources vary as to whether the foreshocks ruptured the ground surface, but if they did, it would have been on the Hinagu Fault. In the mainshock, both faults and both segments of the Futagawa Fault appear to have ruptured, although most of the rupture, and the largest surface displacements, were on the Futagawa Segment of the Futagawa Fault. In total, about 28 km of the Futagawa Fault had surface fault rupture and about 6 km of the Hinagu Fault (GSJ, 2016b) .

An overview of the combined surface displacements estimated from satellite data, as provided by the Geospatial Information Authority of Japan (GSI), are reproduced in Figure 4-1, Figure 4-2, and Figure 4-3. Both of these faults are predominately right-lateral strike-slip faults, often with significant vertical movement. Peak surface movements reported are about 2.2-m right-lateral strike slip (GSJ, 2016b) with up to 0.35-m vertical offset (GSJ, 2016b), occurring on the Futagawa Fault. We are not aware of any measurements or reports of potential afterslip on these faults.

The surface trace of the Futagawa Fault extended northeast into the southwestern corner of the Aso Caldera, a region of active volcanism. An approximately 10-km long, sub-linear section of ground movement occurred as a result of the earthquake and is herein called the “depression zone”. Although its origins are not certain at this time, our interpretation is that this “depression zone” is likely a result of near vertical normal faulting on the caldera’s ring fault. Therefore, the depression zone is included in the surface fault rupture section of this report. We are not aware of any previous geological maps that show this area as a fault, active or otherwise, or any maps of any ring faults in the Aso Caldera.

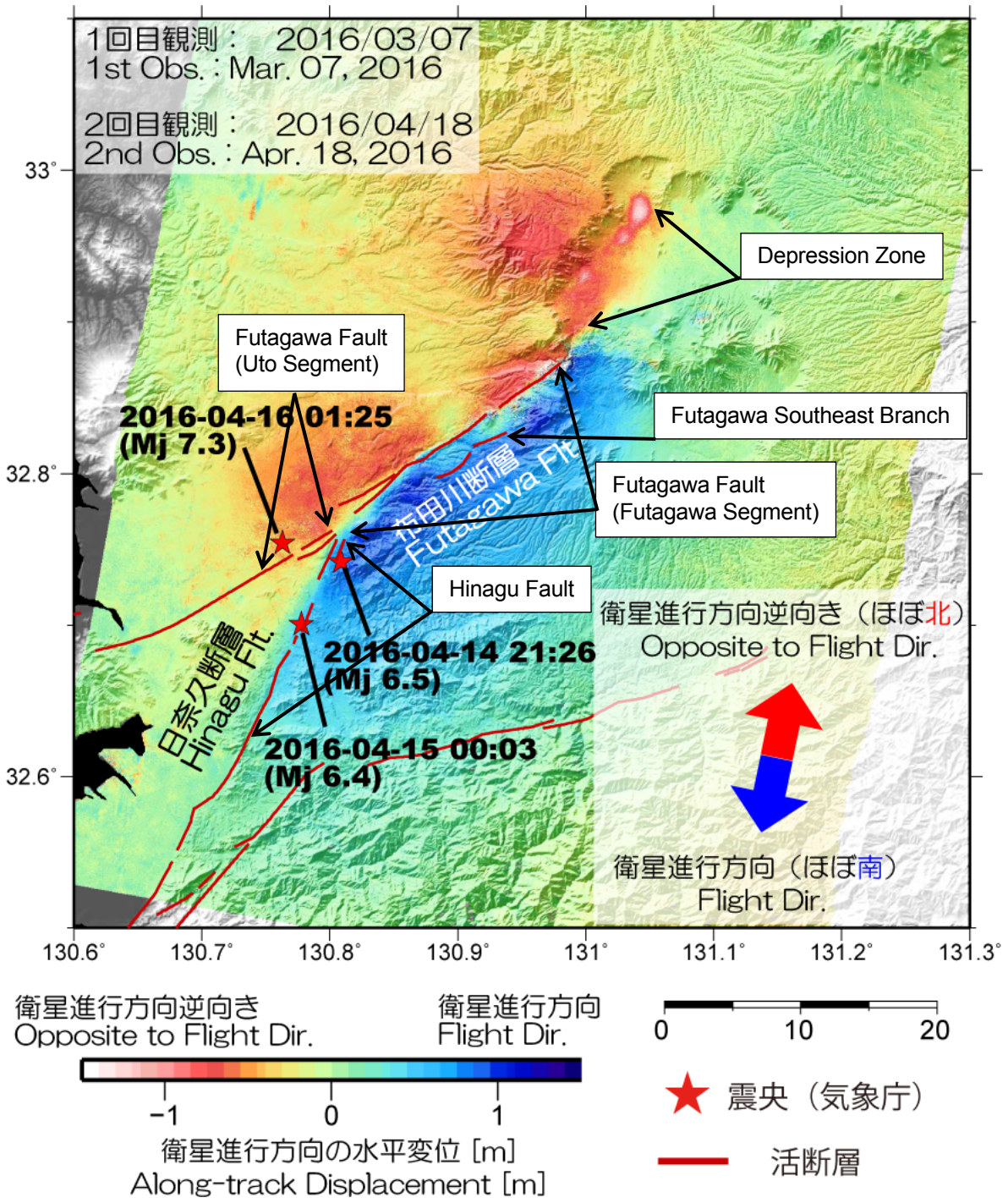

Figure 4-1. Multiple Aperture Interferometry (MAI) processed from ALOS-2 provided by the Geospatial Information Authority of Japan (GSI, 2016). The red lines are previously mapped active fault traces prior to this earthquake sequence.

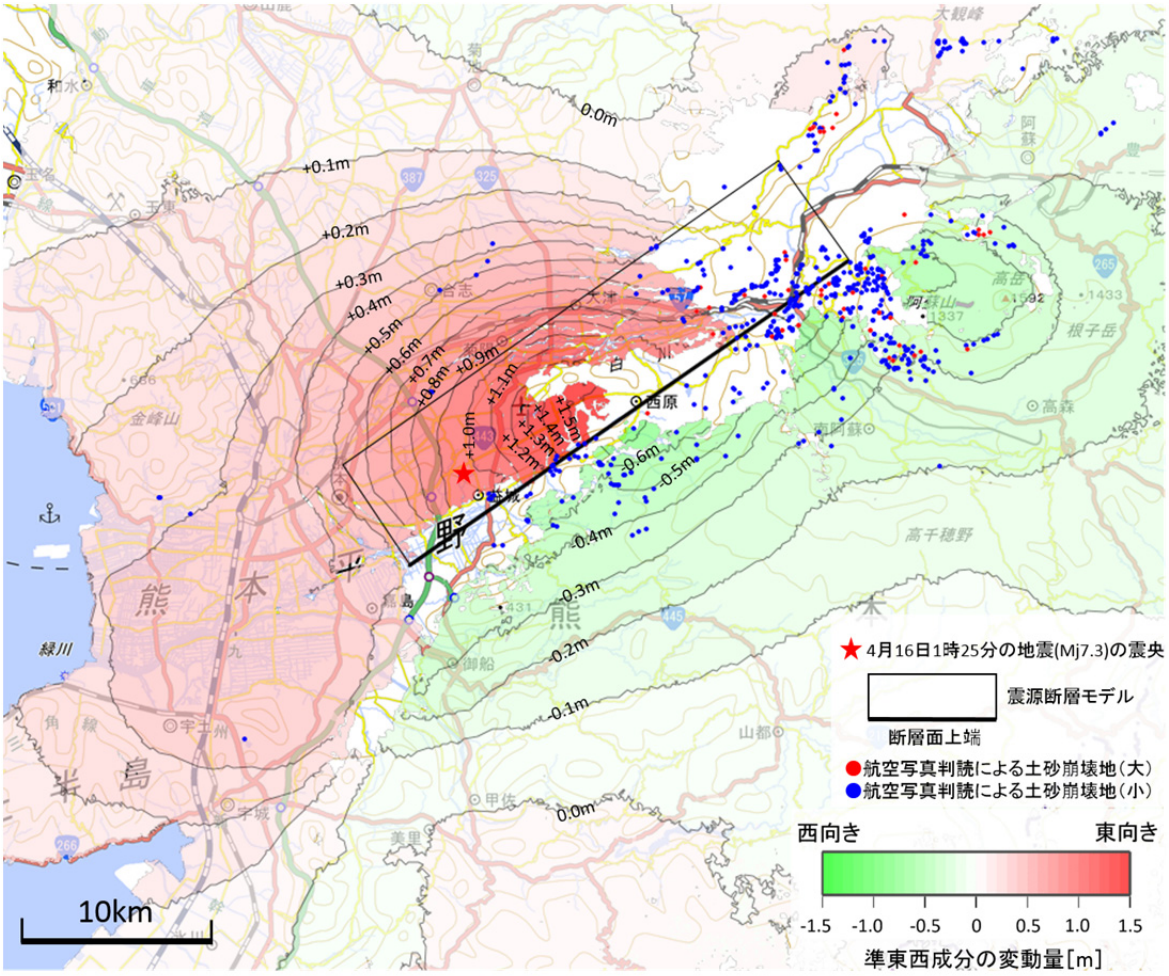

Figure 4-2. Estimated east-west ground movement from ALOS-2 provided by the Geospatial Information Authority of Japan (GSI, 2016). Green (negative) is westward; red (positive) is eastward.

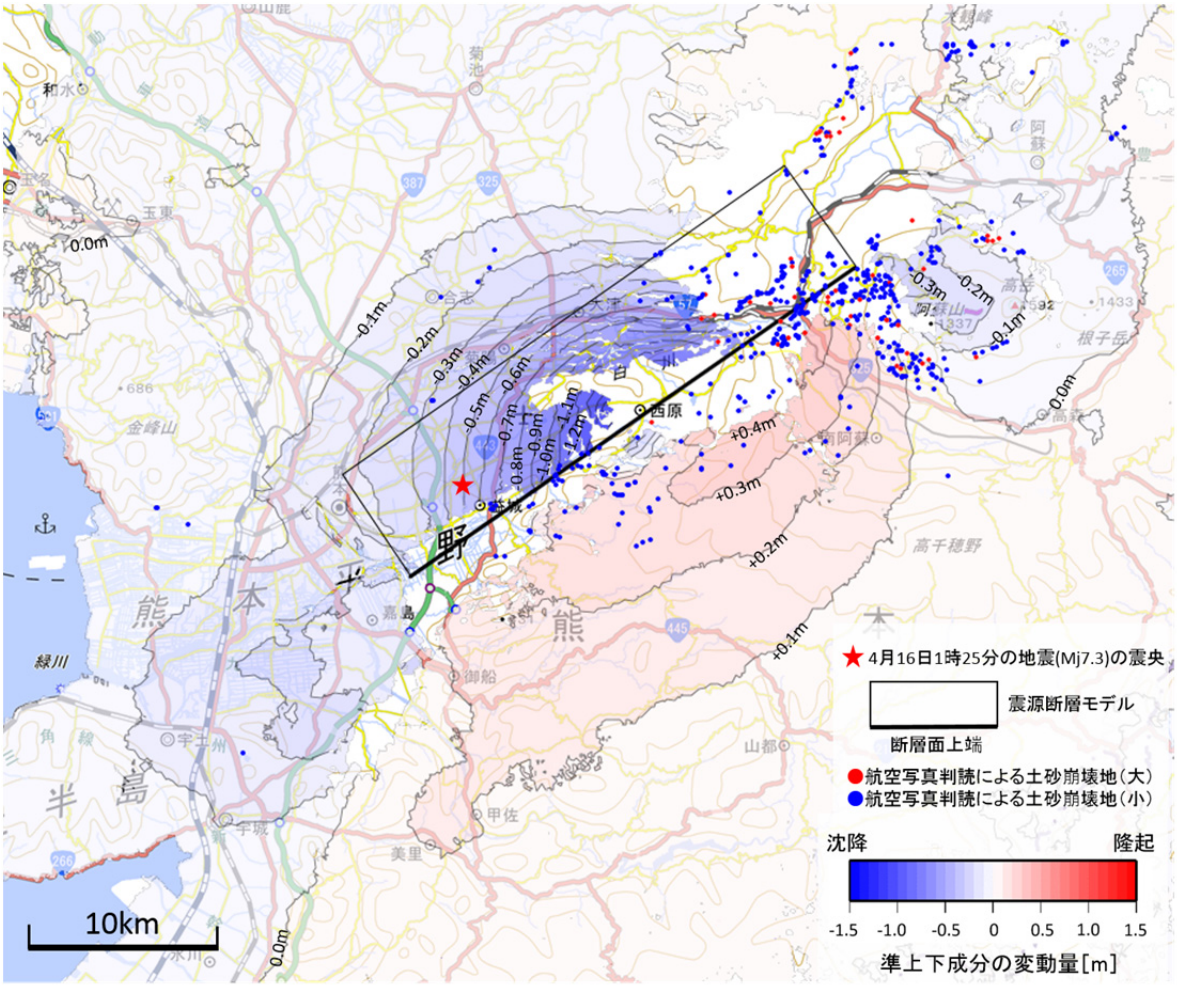

Figure 4-3. Estimated vertical ground movement from ALOS-2 provided by the Geospatial Information Authority of Japan (GSI, 2016). Blue (negative) is downwards; red (positive) is upwards.

4.2 Aerial LIDAR Zone

GEER visited seven (7) sites near the southwestern end of the Futagawa section of the Futagawa Fault. In this area, Asia Air Survey recorded pre- and post-event aerial LIDAR (Figure 4-4), making this area of fault rupture potentially very valuable for follow-on studies given this unique data set. These sites visited by GEER will be described in order from southwest to northeast along the fault rupture (Figure 4-5).

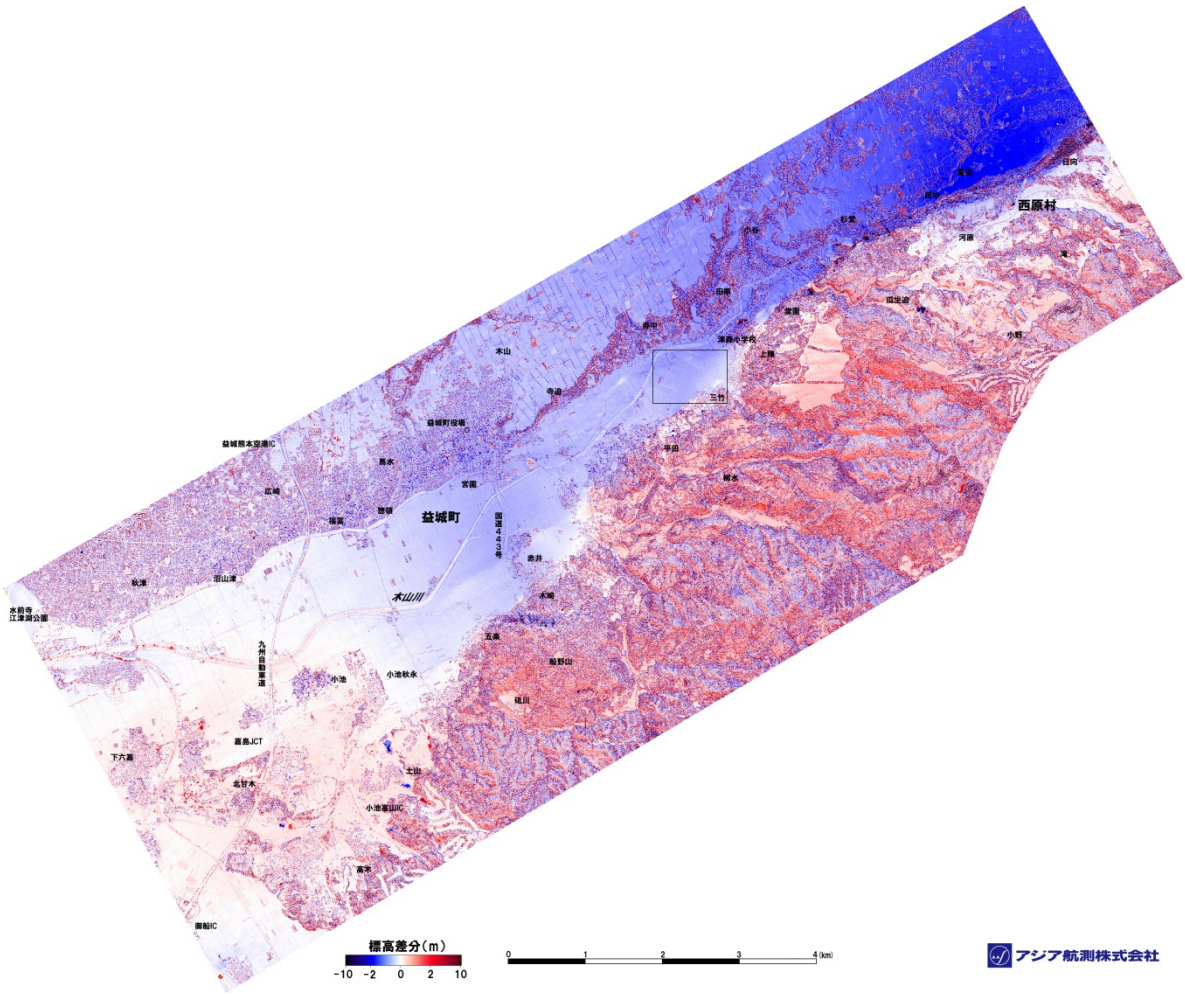

Figure 4-4. Aerial LIDAR recorded ground movement between flights (1) just after the foreshock but before the mainshock, and (2) just after the mainshock from Asia Air Survey (2016).

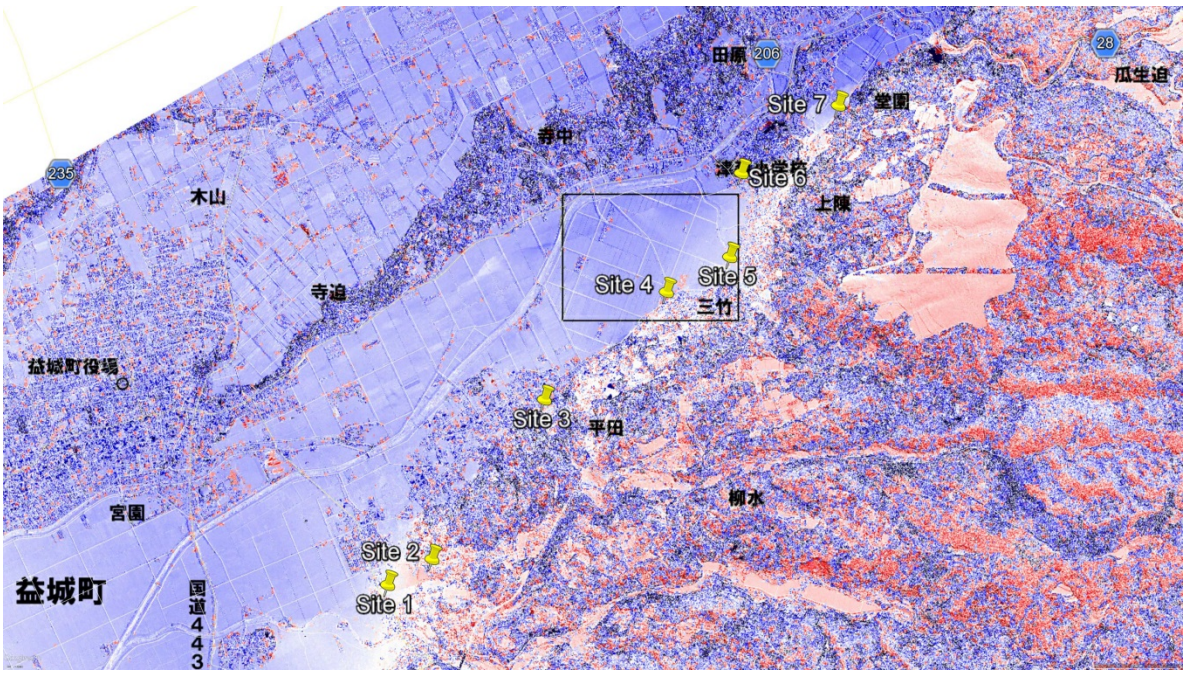

Figure 4-5. Locations of the 7 sites GEER visited in the aerial LIDAR zone, overlain on the Asia Air Survey aerial LIDAR map in Google Earth (Asia Air Survey, 2016).

4.2.1 Site 1

At this site, the Futagawa Fault ruptured through a road, so a sense of the fault deformation was able to be determined. Estimates of the Futagawa Fault offset were based on assuming the road was originally straight through this area. The estimated fault movement, including bending in the ground surface evidenced by bending in the asphalt pavement traffic lines, was about 0.65-m to 0.70-m right-lateral offset over a distance of roughly 7.8 m along the road. Vertical movement here was too small to measure. See Figure 4-6 and Figure 4-7.

Figure 4-6. Roughly 0.65 m to 0.70 m of right-lateral offset along the Futagawa Fault through a road.

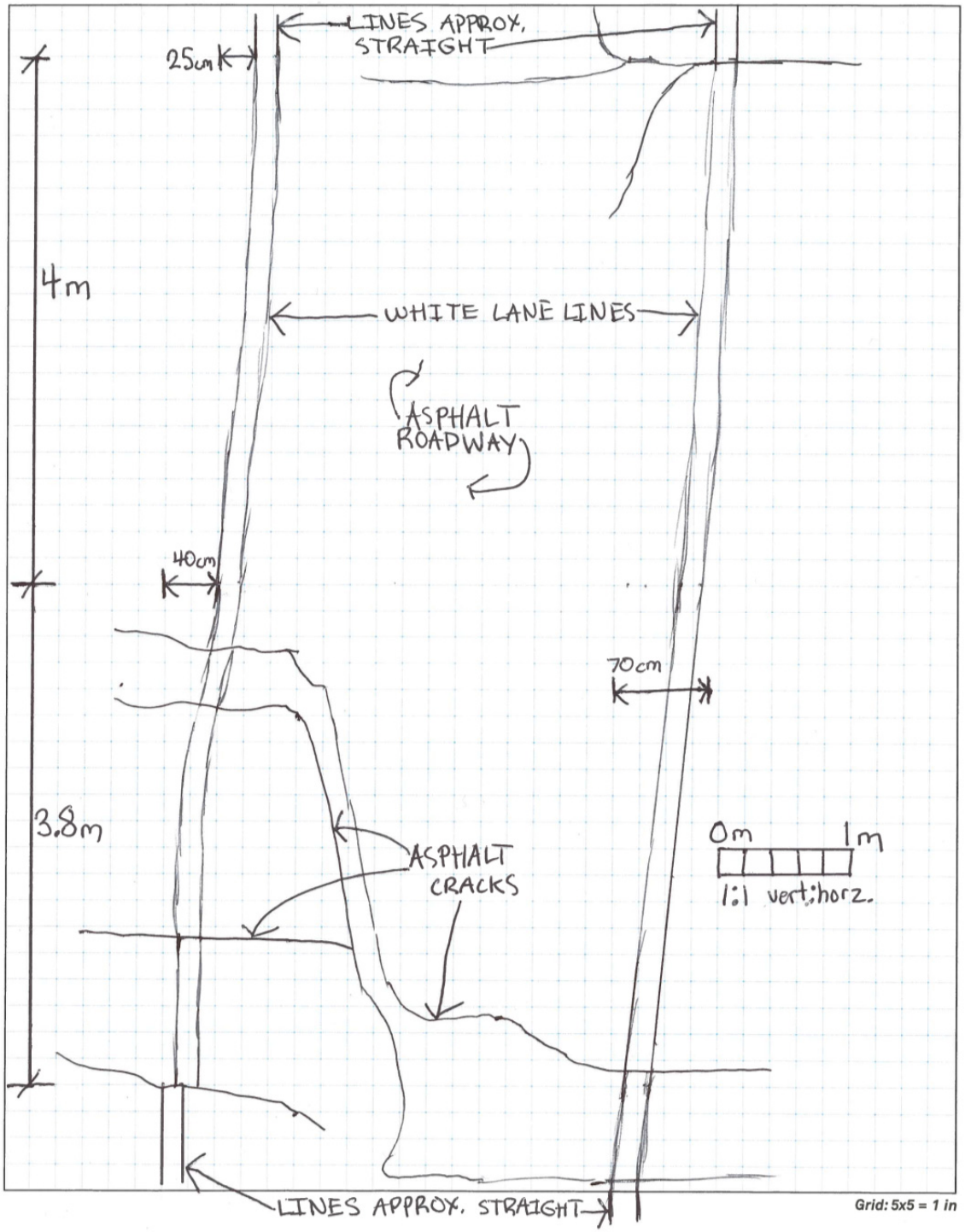

Figure 4-7. Sketch of the estimated deformation distribution and cracking associated with the roughly 0.65 m to 0.70 m of right-lateral offset along the road.

4.2.2 Site 2

At this site, the Futagawa Fault ruptured through a field, a canal, several roads, several retaining walls, and hill. We believe the Futagawa Fault ruptured in at least two strands here. The southern strand appeared to diminish in definition considerably as it transitioned into the hill area. The northern strand may have been more defined in the hill, as the rupture may have been stepping over to the northern strand in this area.

Figure 4-8 shows the northern stand as it propagates through a field, road, and unreinforced concrete retaining walls. At the time of visit, efforts to repair a 200-mm PVC sewer main and concrete manhole underlying the road were underway. The ground rupture tracked directly through the location of the manhole. While no damage to the concrete manhole was observed, misalignment and disengagement of both inlet and outlet pipes was noted (see Figure 7-6).

In the background of Figure 4-8 are two retaining walls damaged by the north strand. A diagonal crack propagated through the taller wall, developing a relative offset of approximately 0.2 m. The shorter wall, shown in Figure 4-9, also fractured with measurements indicating approximately 0.4 m of right-lateral offset.

It was relatively easy to find the southern strand in the fields. Figure 4-10 show the southern strand through fields (background), a canal (foreground) and a fractured unreinforced masonry retaining wall with diagonal crack. It was difficult, however to find the fault rupture as it transitioned into the developed hills in this area. In the field, the fault rupture can be seen moving through the field and into a stone-covered slope, which broke apart at the location of fault rupture.

An unreinforced stone masonry retaining wall along a road, in the hill, near some residential structures, was damaged at the location of the apparent fault rupture through the southern strand. The fault movement was very small or diffuse in this area, so we were not able to definitively measure an offset. A concrete retaining wall below the masonry wall was apparently undamaged, but may have been somewhat curved by the fault. This strand may have gone through the structure below the concrete retaining wall; however, we were not able to examine the structure.

In the road above the masonry wall, we were unable to definitively locate this southern strand of the fault, but some road patches were observed that may have corresponded to some fault movement. Some offsets in a concrete storm drain cover were noted in this upper road.

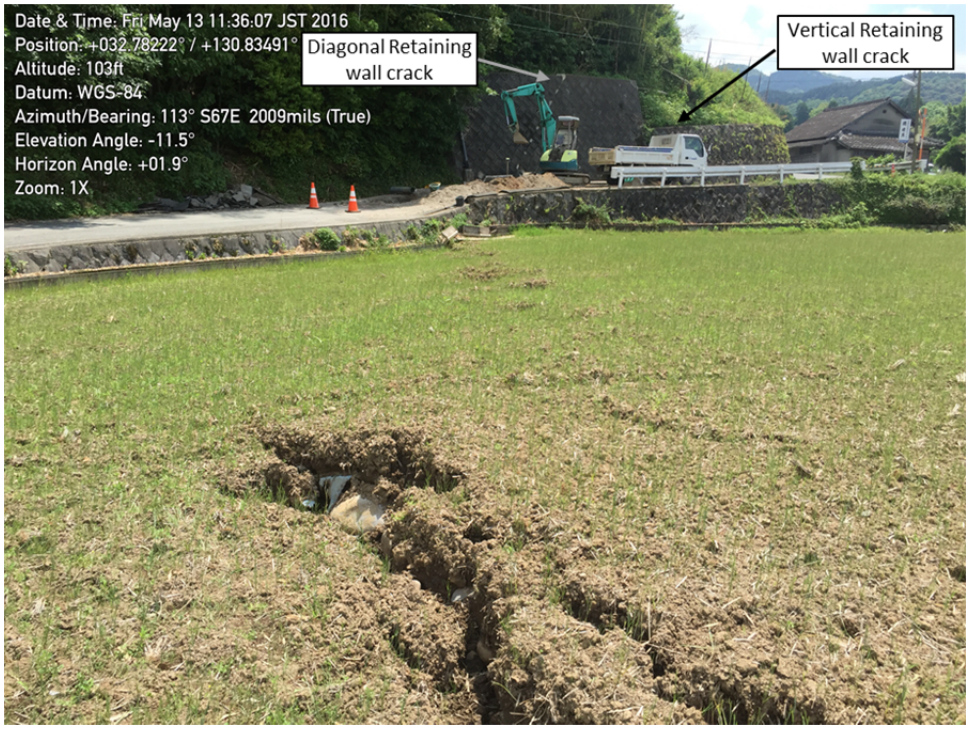

Figure 4-8. Northern strand of the Futagawa surface rupture through a field, road, sewer main, and retaining wall.

Figure 4-9. Roughly 0.4 m of right-lateral offset along the Futagawa Fault through a concrete block retaining wall.

Figure 4-10. Southern strand of Futagawa Fault through fields and unreinforced masonry retaining wall.

4.2.3 Site 3

Two fault strands of the Futagawa Fault were found here. The fault movements appeared to be small and did not appear to go through any significant infrastructure. One strand ruptured through the side of a hill and through a gravel road, and the other strand went through a paved road and through the side yards of several residential structures.

4.2.4 Site 4

The Futagawa Fault ruptured through a road, small canal, and retaining wall with significant movement at this site. The concrete block retaining wall was relatively intact and showed only minor cracking (Figure 4-11). A new temporary water line was installed through this area. Temporary repairs in the area made it difficult to judge fault offsets. In the neighborhood in the hill above the retaining wall significant road repairs were noted, which may have been as a result of fault movement, but the repairs made it not possible to estimate potential fault movement there.

Figure 4-11. Right-lateral offset along the Futagawa Fault through a road and retaining wall, which performed relatively well.

4.2.5 Site 5: Shimojin-Cho River Canal

See Section 9.3.

4.2.6 Site 6

The Futagawa Fault ruptured through a road and several retaining walls here. The right-lateral strike slip movement was estimated to be about 1.2 m on the main strand of the fault (Figure 4-12). Several secondary faults were noted with minor offsets. A concrete block wall on the west side of the road was distorted and bent through the main strand of the fault, but did not break apart or fall over. A part-stone, part-concrete block wall on the eastern side of the road was heavily damaged and collapsed at the location of fault rupture. The structure on the southwest side of the road-fault crossing, less than maybe 1 m from the fault, appeared to be completely undamaged from what we could see on the road, without any cracks in the siding of the structure and without any apparent leaning or distortion of the walls. We were not able to examine in detail any of the homes that passed near or over the fault. The fault must have passed through a very high concrete retaining wall (Figure 4-13); however, we were not able to get close to the wall and were not able to see any damage or cracking or a likely location of where the fault crossed from our vantage point on the road.

In the hill above the high concrete retaining wall, a dense bamboo forest prevented us from accessing the location where the main fault likely ruptured through. In the portion of the hill we were able to reach, there was very significant cracking near the crest of the slope that was likely slope movement as a result of the very steep slope along the northwestern side of the hill. This is also the possible location of where one of the secondary faults crossed into the hill; however, it was not possible to distinguish the large apparent slope movements from any potential secondary fault strand.

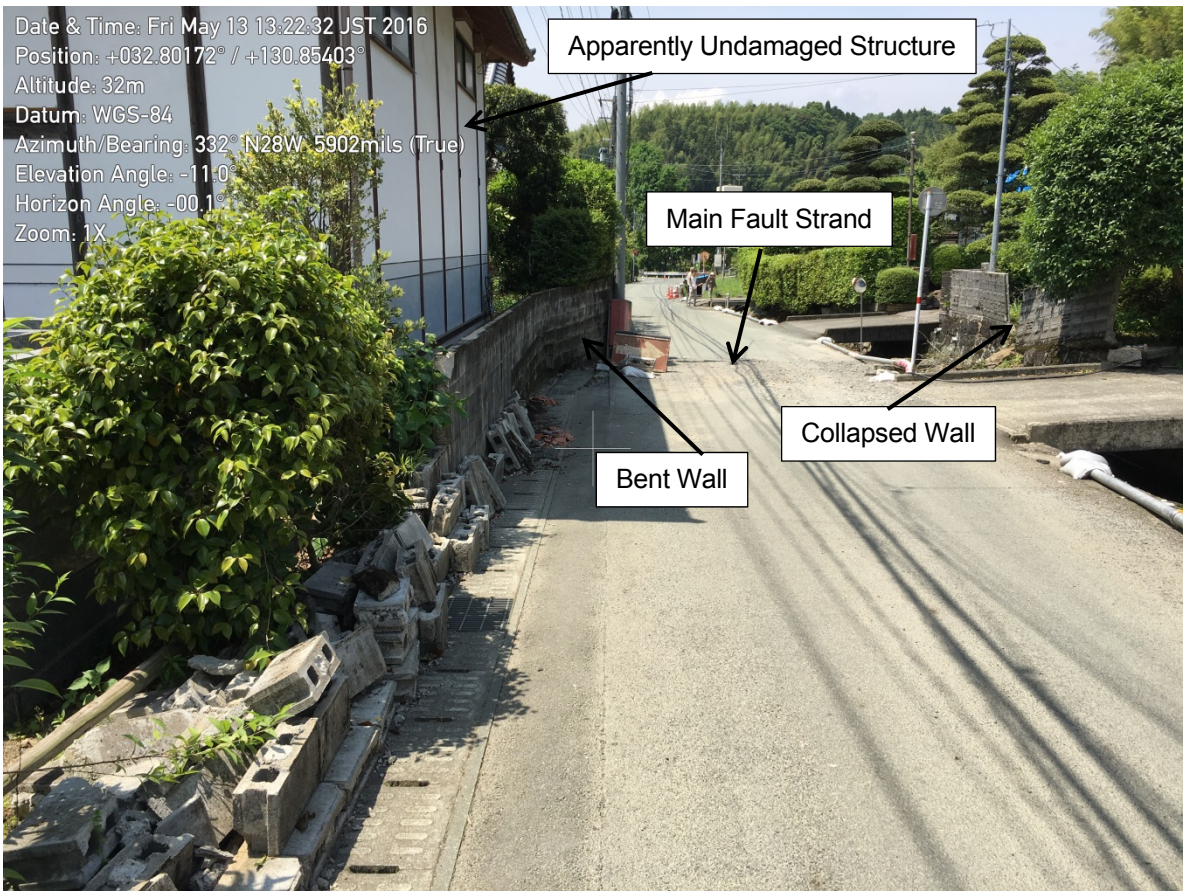

Figure 4-12. Roughly 1.2 m of right-lateral offset along the Futagawa Fault through a road and two walls. The retaining wall on the left was bent but relatively intact, while the wall on the right partially collapsed. The building on the left was immediately astride the fault and suffered no damage visible from the road.

Figure 4-13. Right-lateral offset along the Futagawa Fault likely passed through the large retaining wall behind the residential structures and into the hill behind it; however, we were not able to examine the wall up close and the bamboo jungle behind the wall was too dense to traverse. No visible damage in the retaining wall could be seen from our vantage point.

4.2.7 Site 7

A prominent manifestation of the Futagawa Fault surface rupture was observed approximately 3.5 km south of the Kumamoto Airport (32.80471, 130.85922). Shown previously in Figure 3-3, a distinct offset of approximately 1.8 m can be tracked through the fields. Figure 4-14 shows the surface rupture propagation to the southeast. The rupture occurs through an unreinforced concrete road, across fields of various crops, across another repaired asphalt road, and into the hill at the east. Residential structures, seen in the background of the photo, were highly damaged in this area, as indicated by various levels of structural damage including blue tarped roofs.

Figure 4-14. Roughly 1.8 m of right-lateral offset along the Futagawa Fault through a concrete road and fields.

4.3 Oh-Kirihata Dam

See Section 9.1.

4.4 Aso Caldera Depression Zone

See Section 9.2.

5.0 Landslides

5.1 Introduction

Widespread landsliding was caused by the Kumamoto Earthquakes in the steep volcanic geology of the region. Several hundred landslides are believed to have occurred based on satellite imagery interpretation conducted by the Geospatial Information Authority of Japan (GSI). The GEER reconnaissance team observed numerous landslides while driving through the region. Of the 49 fatalities that occurred as a result of the Kumamoto earthquakes, at least 10 were believed to have been caused by landslides (NZSEE, 2016).

The native slopes in the area are composed of various types of volcanic deposits. These deposits, in general, are very susceptible to weathering and subsequent landsliding. Landslides in these formations are common around the region, and throughout Japan, and have been triggered by both intense rain and seismic events (Wang et al., 2006, Jitousono et al., 2008, Sidle and Chigira, 2004, Yamao et al., 2016). See Appendix A for typical geology of the region.

In the mainshock, a majority of the landsliding closely followed the location of the causative fault. Landslides were predominately in the hills to the southeast of the Futagawa Fault and in the Aso Volcano and Caldera at the northeastern termination of the portion of the Futagawa Fault that rupture in this earthquake, as shown in Figure 5-1. The geospatial organization of the landslides somewhat suggests a possible correlation of landslide concentration to forward directivity and/or fault fling ground motions, given the close proximity of the landsliding to the fault and the high ground motions observed near other areas of steep volcanic deposits that did not seem to exhibit high concentrations of landsliding. However, this observation is only based on a cursory examination of the data.

It is notable that the effect of these landslides was especially disruptive to the transportation systems of the region, including major highways and bridges. Landsliding affected several bridges in the area, including the collapse of one bridge. Many roads and highways were shut down as a result of landslides flowing over roads or as a result of landslides undermining roadways. A transportation tunnel was shut down, likely either a result of landsliding or fault rupture. When GEER visited the region of the earthquake, many major roads were out of service, and based on the degree of damage, it appeared that it may take many months to restore service through some areas. At the time of GEER's visit, one of the few roads that were open to cross into and out of the Aso Caldera was Prefectural Road 23, on the western side of the caldera. Although we were not able to stop along this route, as we drove through it we were able to note extensive engineered systems designed to stabilize the caldera wall slopes. Rock bolts, tiebacks, retaining walls, and rockfall nets and fences were extensive in this area and seemed to have performed well, and may be a case history of good performance for these types of systems, and serve as an example of the importance of this type of lifeline remaining functional after an earthquake.

GEER briefly visited four representative sites of major landslide activity during our reconnaissance. All of these four sites were in the Aso Caldera (see Figure 5-2) and are subsequently described.

平成28年熊本地震・空から見た（航空写真判読による）土砂崩壊地分布図

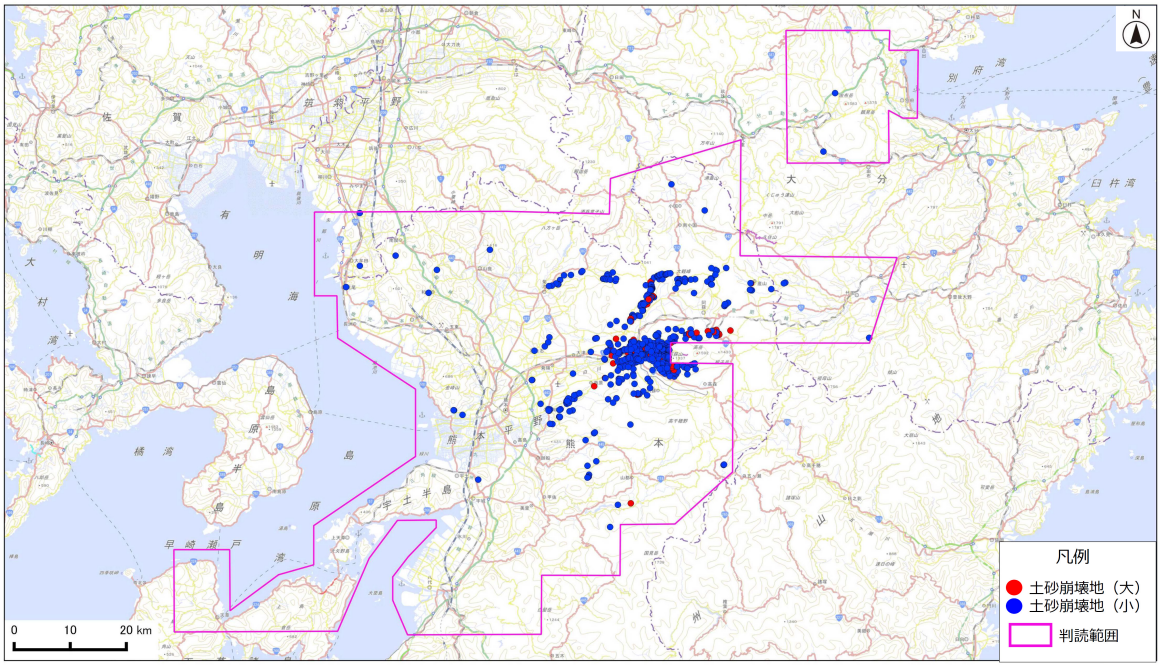

1．この地図は国土地理院が緊急に撮影した航空写真（4月16日、19日及び20日撮影）から、地震により生じた土砂崩壊地の分布を判読したものです。
現地踏査は実施しておらず、実際に崩壊のあった箇所でも把握できていない部分があります。
2．土砂崩壊地は、急傾斜地の崩壊、地すべり、土石流を1つの項目にまとめて表現しています。
3．土砂崩壊地（大）はおおむね1ヘクタール（サッカー場）以上、土砂崩壊地（小）はおおむね0.1ヘクタール（50mプール）～1ヘクタールのものを表しています。
4．土砂崩壊地の中心付近を丸で表しており、土砂崩壊地の形状を表現しているわけではありません。
5．崩壊が連続的に発生しているものを複数箇所として示している場合があります。
6．崩壊の発生を確認して、表記しているものであり、保全対象との関係などから土砂災害ではないものも含まれる場合があります。
7．今後の地震活動、降雨等により、土砂崩壊地の箇所数が増加する可能性があります。
8．正射画像の表示範囲外に土砂崩壊地が表示されることがありますが、当該地域の航空写真は、垂直写真から確認できます。

国土交通省 国土地理院 Geospatial Information Authority of Japan

平成28年4月25日更新

Figure 5-1. Overview of landslides from the Kumamoto Earthquakes produced by the Geospatial Information Authority of Japan (GSI, 2016).

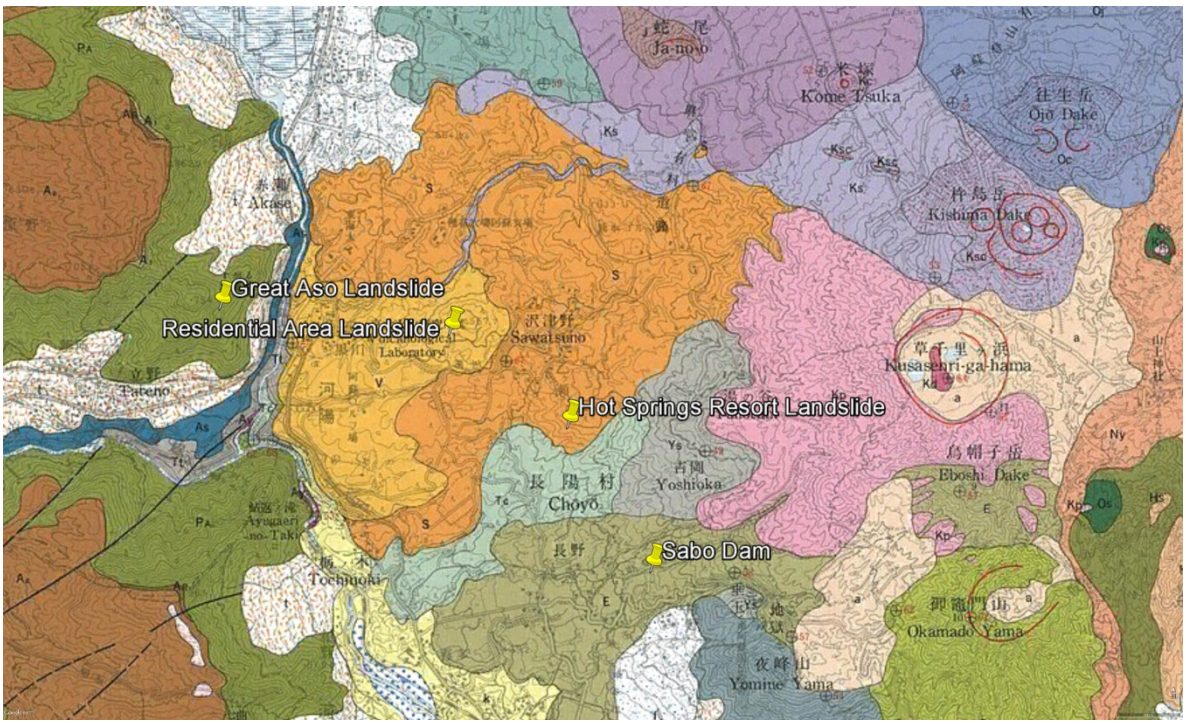

Figure 5-2. Overview of the caldera landslide sites visited by GEER overlain on the GSJ (2016c) geological map (see Appendix B) in Google Earth.

5.2 The Great Aso Landslide

The Great Aso Landslide was likely the largest landslide that occurred in the Kumamoto Earthquakes. The head scarp of the landslide was approximately 350 m higher in elevation than a canyon that ran directly beneath the landslide area. The horizontal distance from the head scarp to the canyon was approximately 700 m. A bridge previously crossed the canyon directly beneath the landslide, but that bridge was destroyed in the earthquake, presumably by this landslide. The remnant of one of the abutments is visible in Figure 5-3. At least one fatality occurred as a result of this landslide (NZSEE, 2016). There was also significant slope failure of the canyon wall slopes throughout this area, independent of the overlying Great Aso Landslide. The Great Aso Landslide source area is mapped as Pyroxene Andesite Lava, lava flow and dike (Pa) in GSJ (2016c).

Extensive UAV video of the landslide and the surrounding area is publically available on the Geospatial Information Authority of Japan website (GSI, 2016), and a digital elevation model of the landslide has been produced by the Japan Asia Group (2016).

Figure 5-3. Front view of the Great Aso Landslide that likely destroyed a bridge, the remnant abutment of which is visible on the left side of the photo. The nearby fault displacement may have also contributed to the bridge collapse.

5.3 Residential Area Landslide

This landslide is shown in Figure 5-4. The landslide runout severely damaged some residential structures (Figure 5-5). Based on Google Earth imagery (Figure 5-6), six structures were destroyed by the landslide. Five people are reported to have died as a result of this landslide (NZSEE, 2016). The residential structures were about 250 m from the head scarp the landslide with a difference in elevation of about 40 m. The landslide flowed in several directions, and the total runout length of the landslide was up to 550 m. The landslide source area is mapped as Volcanological Laboratory Lava, lava flow (V) in GSJ (2016c).

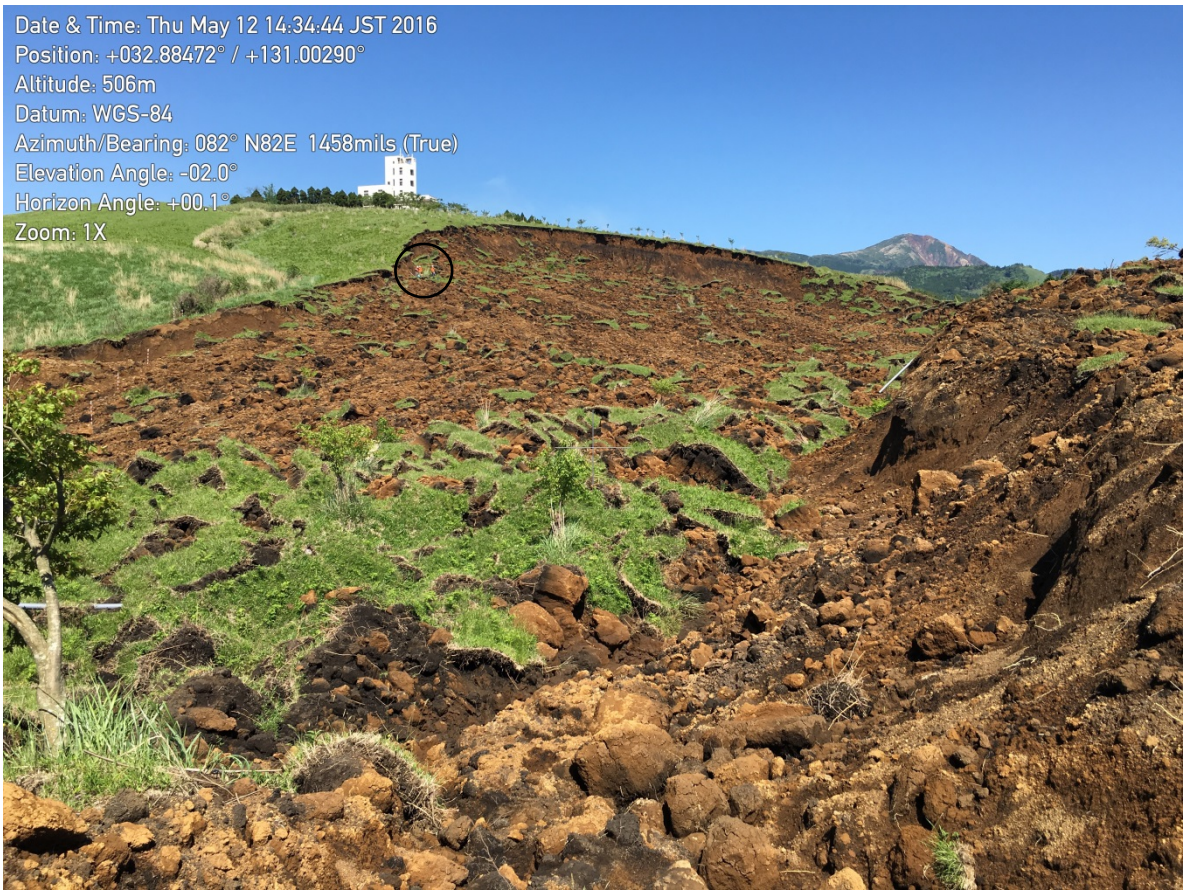

Figure 5-4. The landslide source area, upslope of the residential structures. Note the people in orange on the left side of the slide for scale.

Figure 5-5. Damage to a residential area as a result of the landslide runout. Several structures are missing that would have previously fit within the frame of the photo.

Figure 5-6. Google Earth image of the landslide, with the head scarp at right (at the pin drop) and the residential structures on the left side of the runout.

5.4 Hot Springs Resort Landslide

The runout of this landslide destroyed a hot spring resort and killed two people (Figure 5-7 and Figure 5-8). The resort previously comprised of about nine different buildings, six of which were destroyed by the landslide. The resort was near the tail end of the landslide runout, which was about 250 m from the head scarp (Figure 5-9). The landslide source area is mapped as Sawatsuno Lava, lava flow (S) in GSJ (2016c).

Figure 5-7. A landslide at the former site of a hot springs resort.

Figure 5-8. A closer view of the landslide's crest

Figure 5-9. Google Earth image of the landslide, the hot spring resort was at the tail end of the landslide runout on the left, with the source area on the right.

5.5 Sabo Dam

A “sabo dam” (a Japanese term for a dam meant to stop or abate debris flows; thousands of which have been constructed in Japan; see Mizuyama, 2008) apparently overflowed and partially collapsed as a result of high sediment loading from earthquake-induced mudflows upstream (Figure 5-10 and Figure 5-11). From the downstream vantage point, the area behind the sabo dam appeared to be completely filled with sediment, and thus likely had overtopped. The right side of the dam partially collapsed, and some of the remaining pieces of that portion of the dam could be seen downstream. An examination of the downstream portions of the dam indicated it was made of large concrete blocks. No evidence of steel reinforcement was observed, so we assume the blocks detached as a result of a lack of reinforcement when struck by the sediment flow.

A majority of the sediment we observed downstream of the dam was fine grained; however, numerous boulders, cobbles, gravel, and other sediment was also observed.

Based on an analysis of Google Earth satellite imagery of the area after the earthquake, the source area for these sediment flows appears to have been vast, extending at least 2.5 km upstream of the sabo dam, with width of almost 1 km. Many different flows seem to have occurred, coalescing at various locations before reaching this dam. The flow runout extended approximately 400 m downstream of the sabo dam, just short of a number of structures. However, two small bridges at the end of the runout, that previously crossed the channel emanating from the sabo dam, appear to have been destroyed from the resulting sediment flows. See Figure 5-12.

The Geospatial Information Authority of Japan conducted UAV reconnaissance over the dam and upstream of the dam soon after the mainshock, the video of which is publically available (GSI, 2016). A still image from this video showing the upstream condition of the dam is reproduced in Figure 5-13.

Figure 5-10. Sabo Dam that overflowed and partially collapsed as a result of sediment flows.

Figure 5-11. Close up of the dam. Note the right side of the dam is missing, in contrast to the left side which is intact.

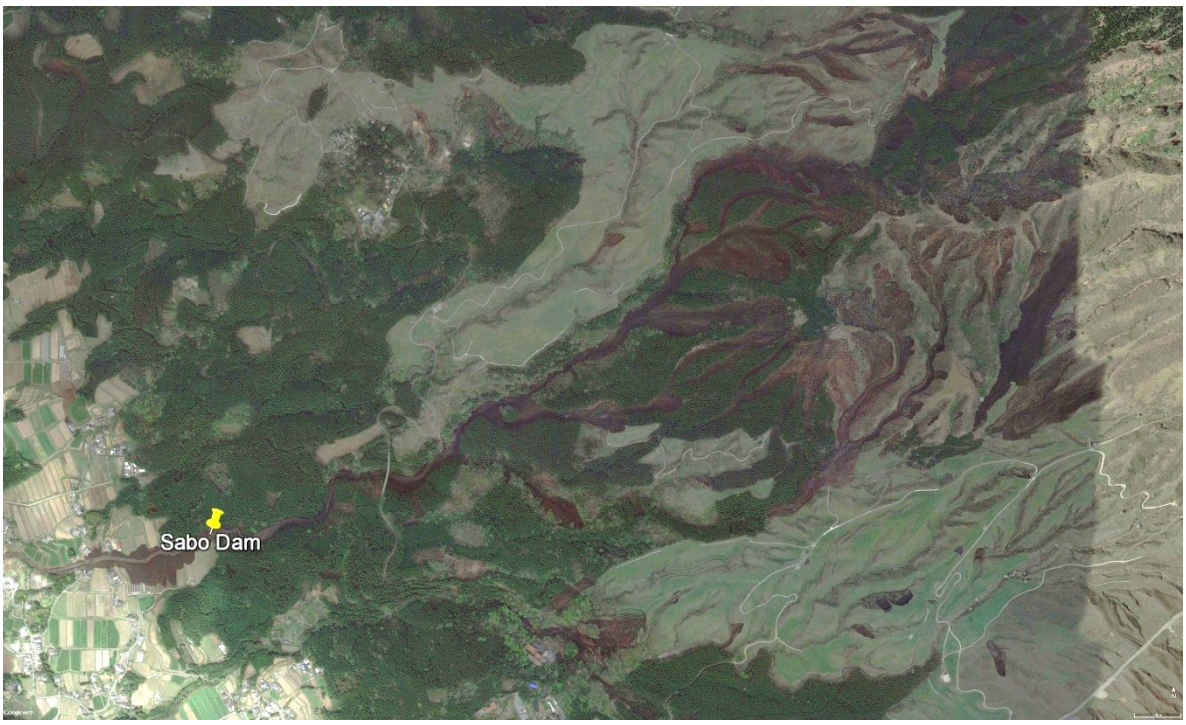

Figure 5-12. Google Earth image of the dam (located at the pin drop), the runout past the dam on the left, and the large ~2.5 km long, ~1 km wide source area to the right.

Figure 5-13. Still image from UAV video footage produced by the Geospatial Information Authority of Japan (GSI, 2016), showing the upstream condition of the dam and the sediment flow, soon after the earthquake.

6.0 Liquefaction and Its Effects

6.1 General Observations

Overall, the GEER team observed less surface manifestation of soil liquefaction following the Kumamoto earthquake sequence than expected from an event with such high intensity shaking. This lack of observed surficial liquefaction evidence was somewhat surprising to the team considering the very large ground motions (e.g., maximum recorded horizontal a_{max} exceeding 1.6g at Mashiki, and several stations recording horizontal accelerations in excess of 0.3g), as noted in Section 3, the relatively high groundwater table in the region, and the abundance of Holocene age alluvium in the region (Hoshizumi et al. 2004).

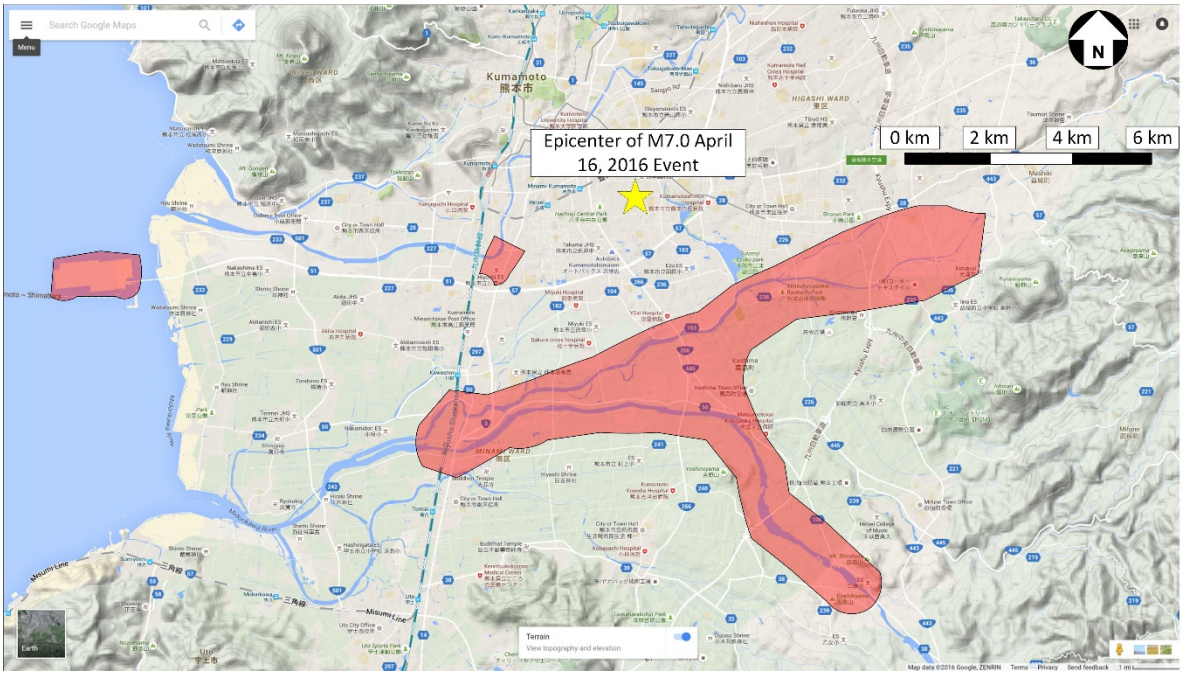

Figure 6-1. Liquefaction vicinity map showing general areas where surface manifestations of soil liquefaction were observed by American and Japanese investigators. Base map courtesy of Google Maps.

Preliminary reconnaissance by Japanese geotechnical investigators (e.g., JGS, 2016) suggested that the most of the surficial liquefaction evidence was found at the southern end of the Kumamoto Prefecture in the Minami Ward and near Kashimi, in the vicinity of the Midorikawa River and its tributaries. Based on our observations, we agree that the majority of the surficial liquefaction evidence was limited to these areas. We also observed significant surficial evidence of liquefaction in an urbanized part of Kumamoto near Kaminogo, adjacent to the southern bank of the Shirakawa River where it bends sharply to the north. Finally, we observed significant surficial evidence of liquefaction on the artificial island west of Kumamoto, near the mouth of the Shirakawa River. These areas are highlighted on the vicinity map presented in Figure 6-1.

We acknowledge that there were likely many more areas within the Kumamoto region that experienced soil liquefaction during the Kumamoto earthquake sequence than those marked in Figure 6-1. However, areas either did not manifest significant surficial evidence of soil liquefaction or were sufficiently limited in their size or were localized such that their detection was difficult for the GEER team.

The general lack of observed surficial liquefaction features throughout the Kumamoto region is currently a point of particular interest to the GEER investigators. For example, publicly available soil borings provided by the Japanese Ministry of Land, Infrastructure, and Transportation; the Kumamoto Prefecture; local municipalities; and private entities (Geonews, 2016; see also Appendix B) show that significant amounts of saturated sand and/or silt layers with relatively low values of SPT resistance (i.e., N<15) are located near the ground surface throughout most of the Kumamoto region. This was also evident at the location of some of the strong motion stations, as noted in Section 3. Most of these sand layers are recorded as being 1-meter thick or more. Available surface geology maps (e.g., Hoshizumi et al. 2004) show that most of the Kumamoto valley area consists of Holocene-age alluvium. Groundwater is usually noted at depths less than 5 meters below the native ground surface, and surface water sources are distributed throughout the Kumamoto region. Further considering the relatively large ground motions that were recorded during the earthquake and the relatively long duration of the strong shaking that is typically associated with a moment magnitude 7.0 event, we do not understand why more infrastructure damage and surface manifestations of soil liquefaction and its effects did not occur. Given the scientific importance associated with this lack of understanding, we strongly recommend further field and geotechnical studies in Kumamoto to address these uncertainties.

6.2 Liquefaction Induced Settlements

6.2.1 Settlements in the Free-Field

Volumetric settlement of soils was observed at a few of the free-field liquefaction sites that were visited by the GEER team. For example, post-earthquake MAI InSAR surveys of the area showed an average settlement of approximately 15 to 20 cm across the artificial island west of Kumamoto. The island is home to park facilities and a large port. Upon arriving at the island, the team observed that post-liquefaction settlement was pervasive across much of the island, with localized settlements up to 60 cm observed at some locations (Figure 6-2 and Figure 6-3). We learned from our Japanese collaborators that the island was surcharged with sand to induce consolidation settlements in the soft native silts. When the surcharge was removed, approximately 3 m of surcharge was permanently retained and built upon. We believe that it was this retained sandy surcharge soil that liquefied during the Kumamoto earthquake sequence. However, an estimated 25 cm of newly-exposed red metal on the pier-supporting piles was visible above the native ground surface, suggesting that the surrounding native silt had also settled in those locations (Figure 6-4). Sand blows up to 1 m in width and its surrounding ejecta were also visible at certain locations (Figure 6-5). These settlements are anticipated to have been caused by sedimentation and reconsolidation primarily.

Further investigation of the GIS soil boring database (Geonews 2016) revealed some interesting findings regarding the artificial island. We observed that certain areas on the island appeared quite impacted and damaged from soil liquefaction. However, other areas of the island were not visibly impacted by liquefaction effects. Figure 6-6 presents a vicinity map of the island and the area that we observed to be significantly affected by liquefaction damage. Note that from Figure 6-6 two borings have been highlighted: Boring 1 and Boring 2. Graphics from these two logs are presented in Figure 6-7. We observe from Boring 1 that significantly more sand is present, and could explain why certain areas of the island seemed more impacted by local soil liquefaction than other. The soil logged in

Boring 2 appears much more fine-grained and plastic. Therefore, we hypothesize that locations on the island that did not experience significant soil liquefaction are likely underlain by soils more representative of Boring 2.

In the Minami Ward and throughout Kashimi, it was common to see settlements of approach fills at bridges, such as shown in Figure 6-8. Nearly all of these settlements were temporarily repaired with a thick asphalt overlay. It was unclear whether the observed settlements at the bridges were due to soil liquefaction, seismic compaction of the approach fill, or some combination of both. However, we are confident that the settlements observed at the bridge shown in Figure 6-8 were due largely to soil liquefaction because of the large lateral spread located adjacent to the bridge. A Google Earth Street View image of the same bridge abutment is shown in Figure 6-9. From comparing these figures, we estimate that approximately 40 cm of settlement occurred at the bridge approach.

Figure 6-2. Free-field liquefaction settlements at a road intersection on the artificial island west of Kumamoto. Settlement of nearly 58 cm were observed at this location.

Figure 6-3. Post-liquefaction settlement of road on the artificial island between 30 cm and 40 cm

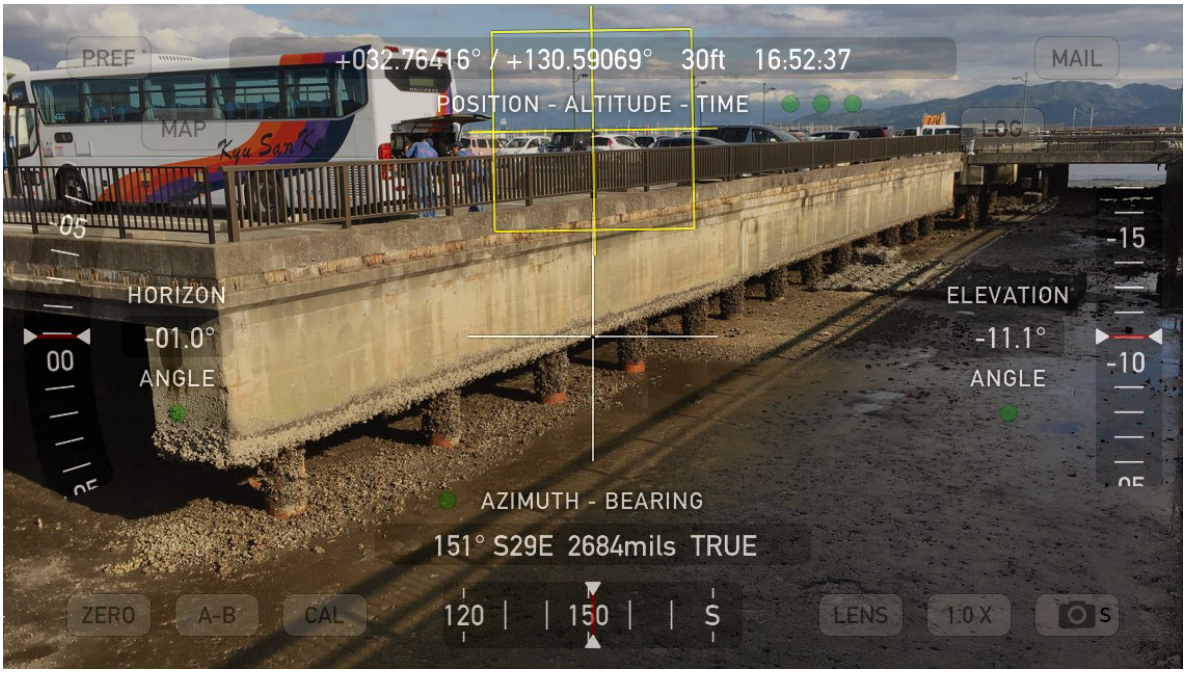

Figure 6-4. Volumetric reconsolidation in native silt apparent from the estimated 25 cm of newly-exposed red steel at the base of the piles supporting the pier.

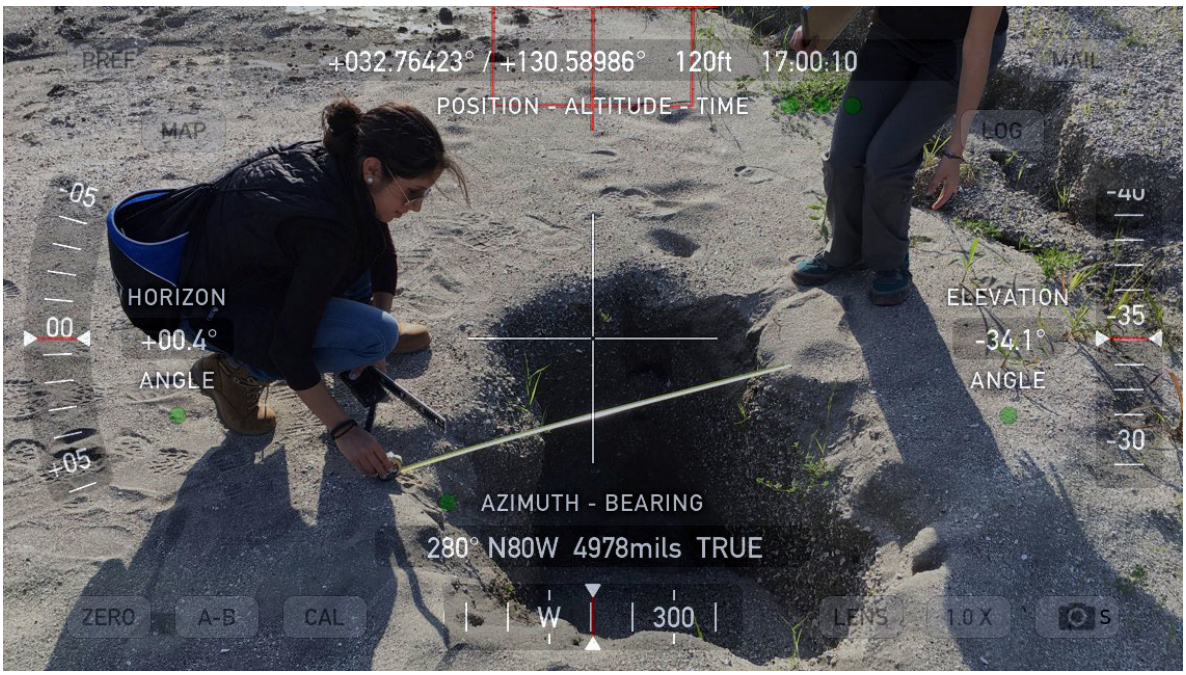

Figure 6-5. Sand blow that is approximately 1 meter in width encountered on the artificial island.

Figure 6-6. Liquefaction and boring vicinity map of the artificial island. The red shaded zone delineates areas where the GEER team observed significant surface evidence of soil liquefaction. Base map from Geonews (2016).

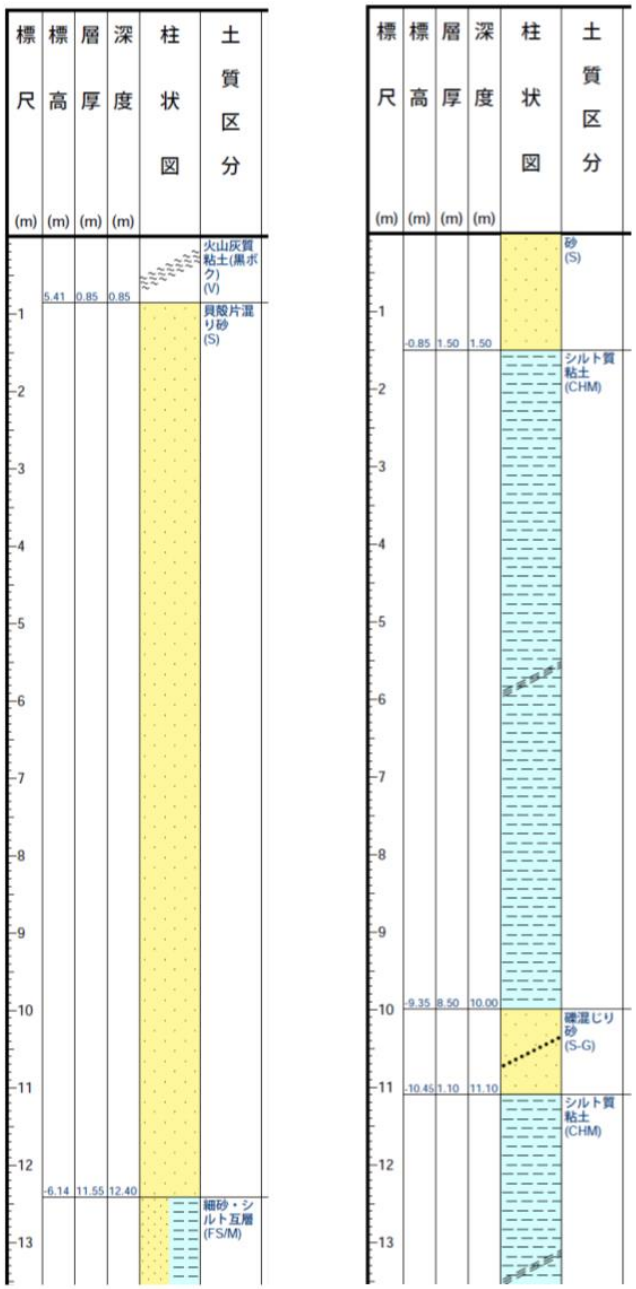

Figure 6-7. Representative borings from the artificial island Geonews (2016). Depths shown are in meters.

Figure 6-8. Liquefaction-induced settlement at bridge approach. Estimated settlements of 36 cm were observed at this site. Location: 32.77322° N 130.78433° E

Figure 6-9. Google Earth Street View image showing the same bridge approach to the Kumamoto earthquake sequence

6.2.2 Settlements beneath Structures

In general, the extent of liquefaction-induced damage to structures was surprisingly limited in Kumamoto and surrounding areas, given the intensity of motions experienced during the foreshocks and the main shock as well as the presence and extent of loose saturated sand layers. The principal significant damage to structures was observed due to soil liquefaction in a concentrated area in Kumamoto south of the Shirakawa River. There are several other places in Minami ward of Kumamoto City, where damage to private houses due to liquefaction occurred. The ground failure indices proposed by Bray and Steward (2000) were used by the GEER team in this neighborhood to identify zones with different degrees of liquefaction-induced damage to structures and identify any potential patterns (Table 6-1). The approximate distribution of damage, as surveyed by the GEER team, is presented in Figure 6-18, showing only a very limited area with extensive damage (settlements greater than 25 cm, tilts exceeding 3 degrees, and lateral movements of greater than 25 cm).

Figures 6-11 through 6-14 show pictures of damage to buildings in this neighborhood due to soil liquefaction. These structures were likely on shallow foundations and generally settled more than the surrounding ground due to shear type deformation under their foundation. No information was available on the type of foundation, ground improvement, or use of liquefaction mitigation strategies in this neighborhood. However, a number of structures were identified with little to no damage while their surrounding ground had experienced substantial settlement with evidence of sand boil. These buildings were likely on pile foundations, which protected them against damage, but the settlement of the surrounding ground and failure of lifelines connected to individual buildings still affected their performance. Obtaining additional information on soil properties as well as foundation type and details

of any mitigation strategy employed in this area will be of great value in evaluating the generally successful performance of most buildings and foundations during these intense series of earthquakes.

Table 6-1. Summary of ground failure indices used to characterize the extent of liquefaction-induced damage to buildings (after Bray and Stewart 2000).

Index	Description	Interpretation
GF0	No Observable Ground Failure	No settlement, tilt, lateral movement, or sediment ejecta
GF1	Minor Ground Failure	Settlement, D < 10 cm; Tilt < 1 degree; no lateral movements
GF2	Moderate Ground Failure	10 cm < D < 25 cm; Tilt of 1-3 degrees; small lateral movements (< 10 cm)
GF3	Significant Ground Failure	D > 25 cm; Tilt of > 3 degrees; Lateral movement > 25 cm

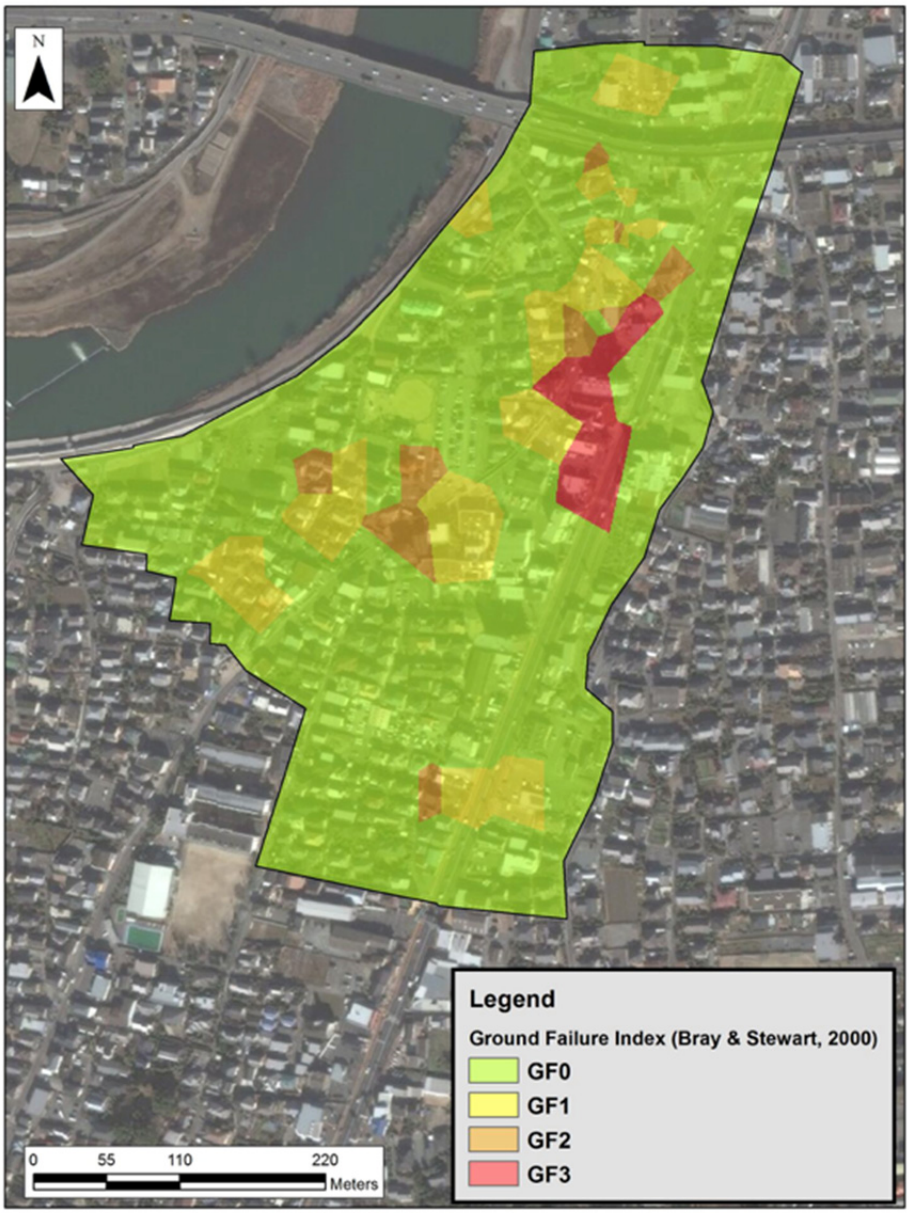

Figure 6-10. Spatial map of liquefaction-induced damage to structures in the south-east corner of the Shirakawa River in Kumamoto following the sequence of foreshocks and aftershocks.

Figure 6-11. Picture of building settlement due to soil liquefaction in the south-east corner of the Shirakawa River (coordinates: 32.770086°N; 130.692403°E). Building settlement with respect to the surrounding ground on the order of 10 cm and 2 degrees tilt.

Figure 6-12. Picture of building with no damage but evidence of sand boil in the south-east corner of the Shirakawa River. Building settlement in the order of 5 cm and tilt 1 to 3 degrees.

Figure 6-13. Picture of building settlement and tilt due to soil liquefaction in the south-east corner of the Shirakawa River. Building settlement with respect to the surrounding ground in the order of 10 cm and tilt of 2 degrees.

6.3 Lateral Spread Displacements

Remarkably, only one significant lateral spread was encountered by the GEER team during the Kumamoto reconnaissance mission. This lateral spread was located in Akisumachi Nuyamazu, adjacent to a bridge along route 232 crossing a tributary of the Midorikawa River at the east of Kumamoto City limits (32.77369° N 130.78384° E). A Google Earth satellite image showing the lateral spread feature, dated April 14, 2016 (U.S. date), is presented in Figure 6-14.

A LIDAR scan was taken at the north side of field exhibiting largest ground cracking (Figure 6-15). This area was boarded by a concrete lined drainage canal to the north, and the river to the south. Based on observations, including limited damage to the drainage canal at the north, the team believe the majority of movement was south toward the river. In the residential area north of the small canal, several extension features were observed in sidewalk blocks and around buildings, indicating slight movement of this area toward the river.

West of the LIDAR scan extension cracks propagated through a one-story concrete block structure resulting in greater than 0.5 m of relative wall displacement. Evidence of surface cracking was observed in the field to the west of this structure, generally oriented parallel to the river. Large road patches were also observed to the west along the river frontage road, likely repairs of lateral spreading. The extent of observable ground cracking to the west was within 100 m of the LIDAR scan position.

Approximately 4 locations with a small amount of possible ejecta were noted. Shown in Figure 6-16, the possible ejecta material was a tan, lean clay (CL), with low plasticity, approximately 50% fines, and 50% fine to medium sand. A very small amount of this material was noted inside of one of the lateral spreading cracks. It is likely heavy rainfall following the events removed further visual evidence.

Along the river in the opposite direction of the scan area (east of the LIDAR station) is a pipeline bridge adjacent to a vehicle bridge. Each bridge is supported a 1/3 points by concrete piers and abutments at either end. The vehicle bridge structure had relatively minor damage and was operational at the time of visit. The bridge span was offset laterally at joints along the bridge (8 cm of right-lateral offset at 1/3 point to the south and 6 cm at the 2/3 point). Figure 6-8 and Figure 6-9 (shown previously) show the soil settlement relative to the pipe and roadway bridge abutments. Settlements on the order of 40 to 60 cm were measured around the abutments. Large patches of new pavement were present at each abutment, likely to compensate for liquefaction-induced settlement in the approach fill adjacent to the bridge.

The 800-mm steel pipeline carries emergency water supply from reservoir tanks located in the agricultural field to the south (32.77072, 130.78779) over the river to populated residential districts. It supplies a population of about 57,000 people. The pipeline experienced damage resulting in leakage during both the foreshock (April 14th) and mainshock (April 16th). Spalding of concrete was apparent around the bolts anchoring the pipeline saddles to each of the four concrete supports. The pipe is equipped with slip joints to account for thermal expansion and contraction near both the north and south abutments. These types of joints typically have a range of about ±50 mm. During the April 14th event, leakage occurred at the slip joint close to the south abutment (Figure 7-3). Observations suggest leakage occurred due to over insertion of the joint, indicating that there was potentially small lateral spreading movement of the pipeline bridge during the foreshock.

This pipeline also experienced damage during the April 16th event. Local water officials said there were 6 leaks along a 1 km of pipeline, including damage and leakage at the south abutment of the pipeline bridge beneath the river frontage road.

Figure 6-14. Lateral spread feature identified adjacent to a bridge.

Figure 6-15. Section of lateral spread relative to location of LIDAR setup and pipeline bridge (32.77369° N 130.78384° E).

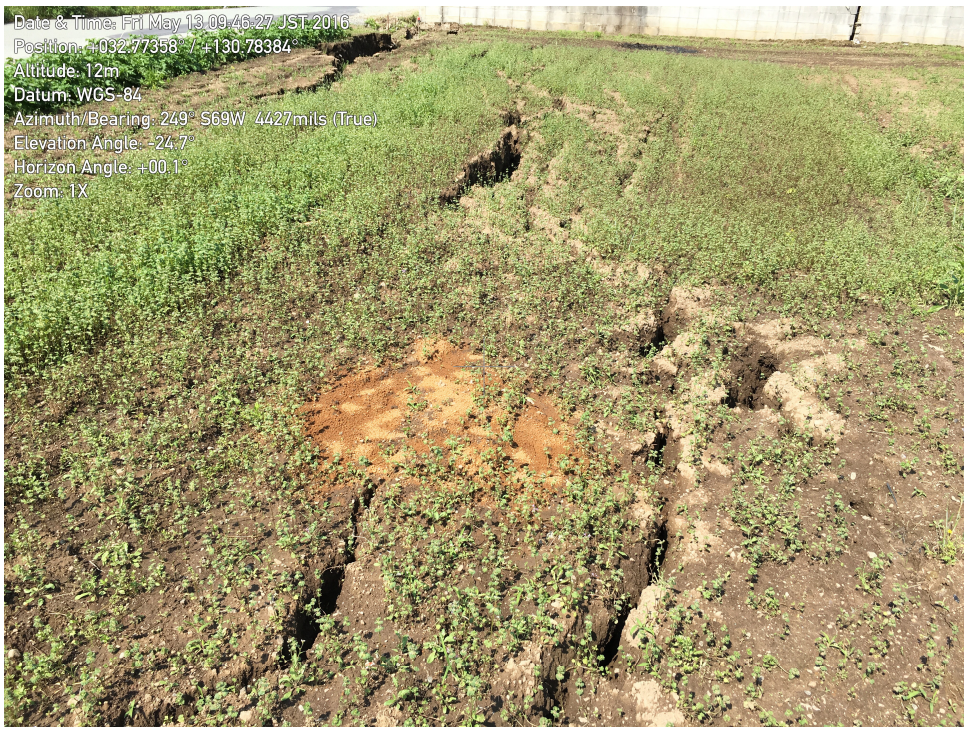

Figure 6-16. Ground cracking from lateral spread and observed ejecta.

One of the current mysteries and future research topics of interest from this event is why more lateral spread displacements did not occur from the Kumamoto earthquake sequence. Members of the GEER team collectively investigated over a dozen bridges located throughout Kumamoto and the surrounding areas, and no significant surficial evidence of lateral spread was observed. Bridge abutments showed no sign of rotations, even at the Route 232 bridge described above. Little to no damage from soil ground deformations were observed in the wingwalls adjacent to and beneath bridges other than at the Route 232 bridge discussed above. With the abundance of river channels, man-made canals, and natural ground slopes encountered throughout the region, one would intuitively think that liquefaction and lateral spread displacement would have occurred throughout Kumamoto. Our best hypothesis is that there are more plastic fines in the native sands than are indicated on the publicly-available Japanese boring logs (Geonews 2016). None of the Japanese boring logs appeared to report the results from laboratory tests measuring actual fines contents in the soil, suggesting that the soil types reported in the Japanese logs were assigned only from visual classifications performed by field personnel. From the Japanese boring logs, the predominant fine-grained soil type that was logged in the area appears to be fat clay (CH), which could definitely impede the triggering of liquefaction in sandy soils and/or prevent horizontal ground deformations. It appears that several zero-displacement lateral spread case histories could be developed from this event. Such case histories are generally lacking from current lateral spread databases, and are considered very valuable. The challenge in developing such case histories would be identifying sites where liquefaction likely triggered in the soil but no lateral spread displacements occurred.

6.3.1 LIDAR Analysis

One of the remarkable features of the Kumamoto earthquakes is the combination of extremely high ground motion and the dearth of liquefaction and lateral spread features. The geologic environment is probably the leading cause for why this was the case. Highly plastic fines associated with the weathering of volcanic material and highly angular volcanic soil evident in sand boils likely floors most of the Valley of Kumamoto City and Mashiki town.

One of the rare lateral displacement locations is on the southeastern margin of Kumamoto City at Akisumachi Nuyamazu, adjacent to Route 232 crossing a tributary of the Midorikawa River (32.77369° N 130.78384° E). LIDAR was captured at this lateral spread (Figure 6-17). This site does not rise to the level of a significant case history, whereas the lack of significant lateral spread along the banks of the Midorigawa (Green River) and Shirogawa (White River) Valleys does. At Akisumachi Nuyamazu, only the portion between the roads was accessible and visible to LIDAR data collection. The zone between the road and the river was completely obscured by vegetation but likely contained continuation of lateral spread deformations. In the zone between the two roads, the average extension of the ground toward the river is estimated from aggregating displacements of objects, structures, and fissures to be 0.71 m, and the vertical displacement down to the river is estimated to be 0.25 m. These represent a minimum possible displacement, knowing that deformation occurred in the vegetated portion of the embankment.

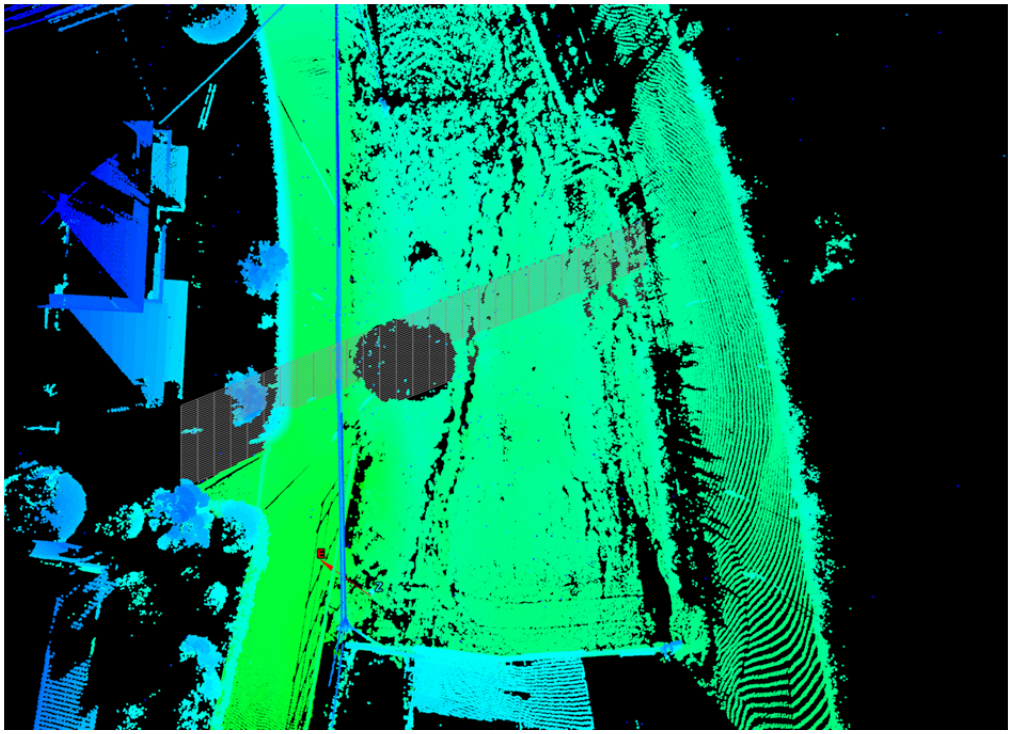

Figure 6-17. LIDAR data through the lateral spread zone (32.77369° N 130.78384° E).

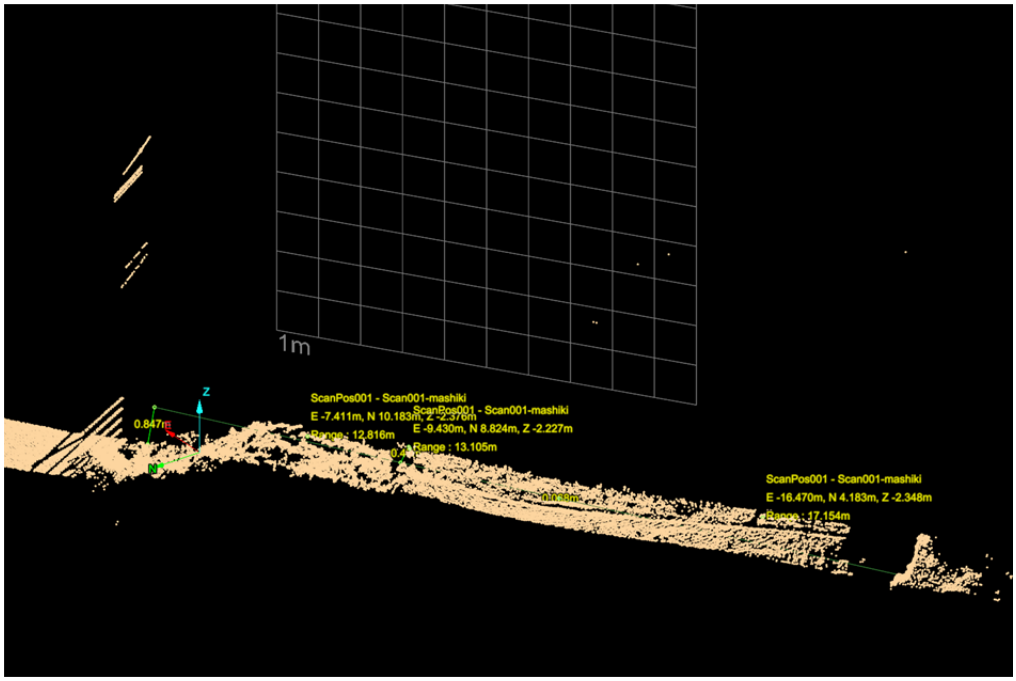

Figure 6-18. Example of lateral and vertical displacement calculation through a narrow to meter section of the lateral spread. Measurements were made continuously through the entire mass at 2 m intervals (32.77369° N 130.78384° E).

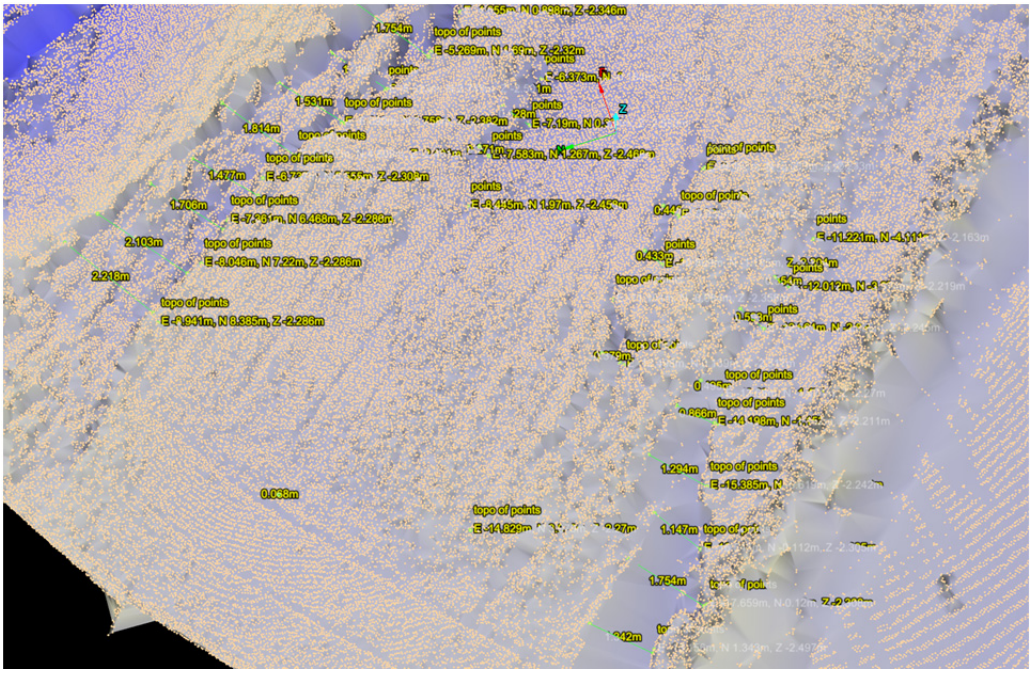

Figure 6-19. Measurements of lateral spread elevations, and fissure locations at Mashiki town (32.77369° N 130.78384° E).

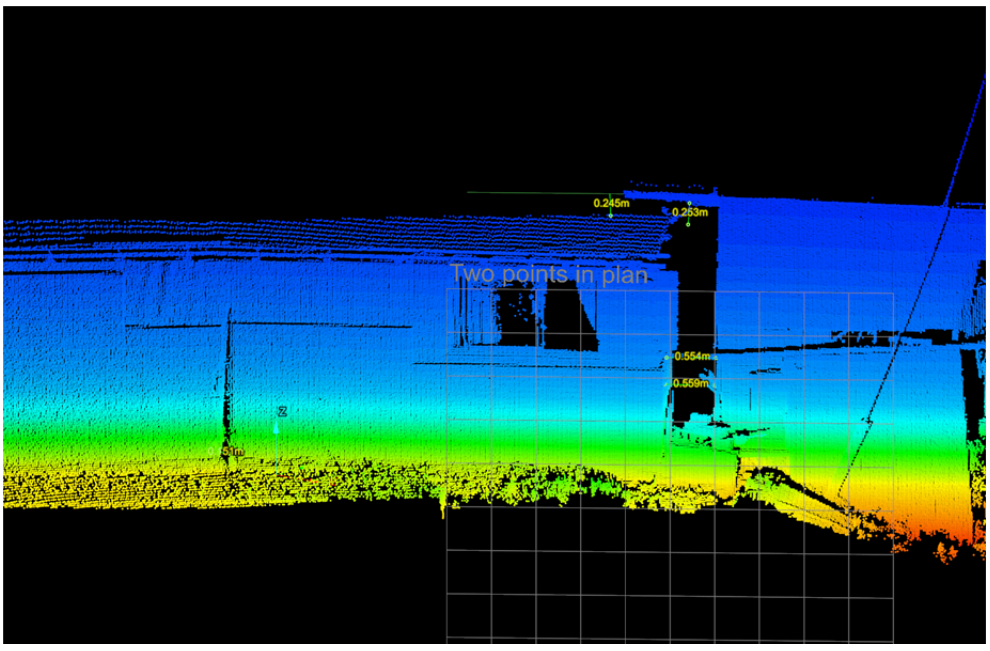

Figure 6-20. LIDAR deformation measurements through damage structures pulled apart bilateral spreading (32.77369° N 130.78384° E).

7.0 Performance of Lifelines

Seismically induced damage to lifeline systems occurred in many areas within the Kumamoto region. Landslides and surface rupture caused significant damage to transportation systems, especially roads and bridges. Widespread interruption to the water, gas, and electric power supply affected thousands of people. Heavy rainfall during the two days following the earthquake sequence hindered lifeline recovery and repair efforts.

Information in this section was obtained from briefings by the Japan Water Works Association (JWWA) Director of Engineer Department & General Institute Yasunori Kimura on May 9th 2016 and Kumamoto City Waterworks and Sewage Bureau (KWSB) Director of Water Technologies Administration Hirofumi Nakashima on May 12th 2016 (Figure 7-1) as well as Kyushu Electric Power Co. (http://www.kyuden.co.jp), Saibu Gas Co. (https://www.saibugas.co.jp/disaster/index.htm#kinkyu), and local media sources. Colleagues at the Kubota Corporation provided valuable information and guidance before, during, and after the reconnaissance mission.

Figure 7-1. Meeting of GEER team members (Drs. Brad Wham and Shideh Dashti) with the Kumamoto City Waterworks and Sewage Bureau Director and Satoshi Suenaga of Kubota Corp. on May 12th, 2016.

7.1 Water Supply

The Kumamoto Region includes 14 municipalities, which share an abundant source of groundwater. A series of four volcanic eruptions of Mount Aso occurring 270,000 to 90,000 years ago resulted in deep pyroclastic flow deposits more than 100 meters thick. Presently these naturally porous deposits serve as deep underground aquifers, from which the region extracts its water supply.

Kumamoto City supplies its 670,000 citizens with clean drinking water from underground aquifers. It is the only city in Japan with greater than 500,000 residences to source water solely from natural groundwater, earning it the title “The home of the richest groundwater in Japan” (Nagata, 2015). It is the largest district in the affected area serving 320,000 customers.

Under typical operating conditions, very little treatment of groundwater is necessary due to natural purification. KWSB informed us that only mild chlorination is typically used as treatment. For shallow wells, some minor UV and flocculation systems are necessary, and a few wells require manganese and iron treatment. For most deep wells, no treatment is necessary. To ensure water quality, taps are checked daily while groundwater is tested every three months and published in an annual water quality report. In general, use of natural groundwater in the area is believed to have improved the pace of water supply recovery in Kumamoto, compared to a scenario where water treatment plants or dams need to be repaired.

As of 2013, Kumamoto City water facilities consist of 3,366 km of pipeline, 19 transmission facilities, 67 distribution facilities, and 96 operational well points. Distributed across the city are a series above and below ground storage tanks for use as disaster recovery water reservoirs. Figure 7-2 presents an overview of water supply pipelines including conduit (raw water), transmission, and distribution mains. The region is supplied by 4,469 km of pipelines, 75% of which are within Kumamoto City. To address vulnerability of water supply, almost all newly installed water pipelines in Kumamoto City have been earthquake resistant ductile iron pipe over the past 10 years.

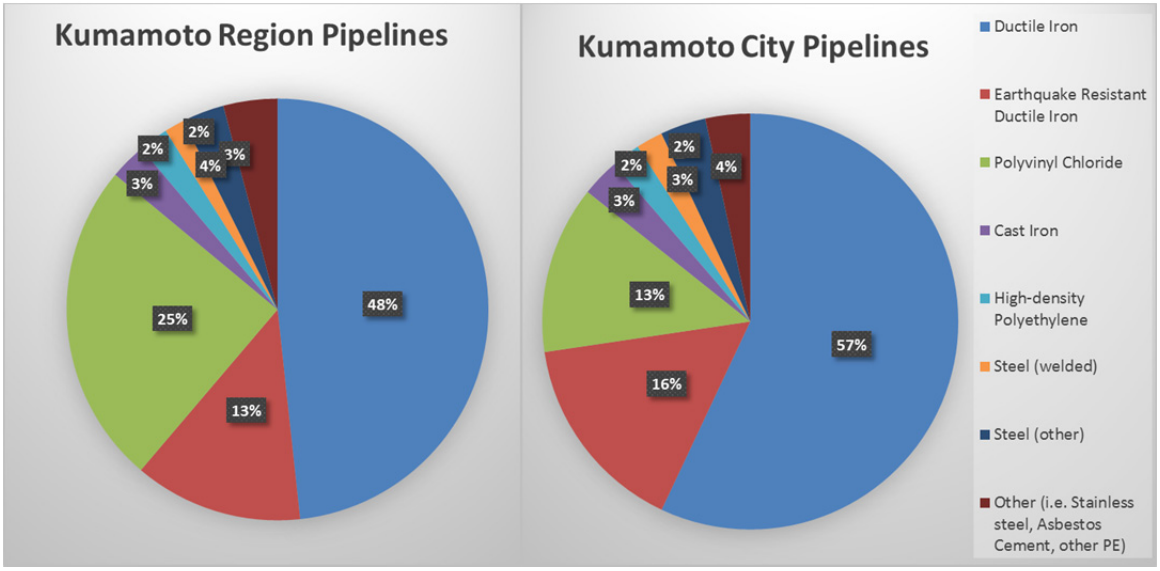

Figure 7-2. Distribution of water supply pipelines (untreated, transmission, and distribution mains) in Kumamoto Region and City (data from JWWA, 2014).

7.1.1 Emergency Water Supply Management

Japan’s national water supply is managed by the Japan Water Works Association (JWWA), established in 1932 to support and regulate local utilities. The association includes seven regional branches, 46 prefectural branches, and about 1400 members from utilities across the country. During emergencies, local municipalities will contact prefecture branches to request support. For significant

events, such as earthquakes recording 5 or higher on the JMA scale, prefecture branches may contact the national JWWA office located in Tokyo, to coordinate national support.

Following the April 16 event, Kumamoto Waterworks and Sewage Bureau (KWSB) requested support from the Kyushu Prefecture Branch, who coordinated nation support through JWWA. Potable water was provided by 88 water trucks, typically ranging in volume from 2 to 4 cubic meters.

Surrounding prefectures also assembled teams for dispatch to damaged areas to assist in damage surveys and repairs. Teams consisted of private and public contractors and engineers, typically JWWA members, equipped with repair materials and tools. As of a May 9th visit to the JWWA headquarters, two waves of teams provided support to damaged areas in Kumamoto. Initial support included 39 teams from 6 prefecture branches. After April 28, a second wave, including 20 teams from all 7 prefecture branches, was sent to continue repair efforts.

Immediately following a natural disaster, it is difficult to identify the level of damage to underground facilities such as water distribution pipelines. Local and dispatched repair teams first focus on leak detection and damage assessment. Repairs to large transmission lines and distribution facilities are preformed first, followed by restoration of branch pipelines and service lines.

7.1.2 Water Supply Damage

The April 14th M_W 6.2 earthquake caused 69 of 96 wells in Kumamoto to stop pumping due to water quality turbidity. The relative proximity of the earthquake focus to the aquifer led to suspended particles in the water and reduction in water quality. About 85,000 households were suspended water supply. Lateral spreading resulted in leakage of an 800-mm diameter transmission main crossing a river (Figure 7-3), which is discussed in greater detail in Section 6.3.

During the April 16th M_W 7.0 event, all 96 supply wells were stopped due to water quality concerns (turbidity). Water service to all 326,000 households in Kumamoto City and over 400,000 customers throughout the region was suspended to avoid depleting limited emergency reservoir supply though damaged pipes. It took 1.5 days for particulates to settle and groundwater to return to acceptable quality levels. During this time, the water bureau worked closely with fire and emergency service providers to ensure adequate supply for life safety and emergency needs. It was fortunate that fire was not a significant issue due largely to the time of day the earthquakes occurred. The City considers this relatively rapid recovery of the water supply to be a success and that other facilities requiring multifaceted treatment procedures may have taken longer to recover.

Leakage occurred in significant pipelines including a 900-mm conduit and a 1350-mm distribution mains as well as multiple ruptures of the previously repaired 800-mm transmission main. Damage to larger transmission pipelines affected the speed of restoration. Repairs and circumventing damaged mains reduced the number of customers without water to 90,000 by April 19, and to about 30,000 by April 22. As of May 12 meeting, 165 pipe repairs were required in Kumamoto City, with the majority occurring at the east side of the city near Mashiki, where significant ground motions were concentrated. Of the 578 km of Earthquake Resistant Ductile Iron Pipe (ERDIP), there were no reported breaks or repairs. There were no reported incidents of ERDIP or other earthquake resistant pipeline crossing manifestations of surface fault rupture.

On a typical day, Kumamoto City consumes about 220,000 m^3 of water. The demand on the system following the April 16 event was 270,000 to 280,000 m^3, a 30% increase in pumping by volume. Leaking of damaged pipelines is considered the primary cause of supply increase. As of our meeting

with KCWSB on May 16, the demand remained 10% higher than typical operating volume, indicating the need to continue pipeline repairs.

Figure 7-3. Leakage of 800 mm diameter bridge pipeline (courtesy of Kumamoto City Water and Sewer Bureau) (32.77326, 130.78428).

Figure 7-4. Repair of a 1350 mm transmission main with leakage from 600 mm flange cap (courtesy of Kubota Corp) (32.76382, 130.75117).

7.2 Sewer System

Although not visited by the GEER team during this reconnaissance mission, there were reports of damage to wastewater treatment plants. Gravity sewer pipelines suffered untold damage from ground settlement and differential movement. For example, Figure 7-5 shows an example of differential movement between a sewer manhole and surrounding ground. Buoyancy effects from liquefaction of pipeline backfill caused sewer mains to rise, resulting in significant damage to roads and a number of reported automobile accidents.

During our visit, efforts to check pipeline damage and pitch at manholes with cameras were ongoing. Repair efforts were also ongoing. An example is shown in Figure 7-6 where surface rupture occurred through a road and underlying sewer main (same site as in Section 4.2.2). In this case there was no evidence of differential vertical movement; however, lateral offset caused disengagement of the 200-mm PVC main at both sides of the concrete manhole structure. Because an operational sewer is not immediately vital to the population, repairs are expected to continue over an extended time period relative to other lifeline systems.

Figure 7-5. Differential movement between sewer manhole and ground surface likely caused by liquefied pipeline backfill (photo courtesy of JSCE).

Figure 7-6. Ongoing repairs of a sewer main where surface rupture caused differential movement and disengagement of a 200-mm PVC main at both the north and south sides of a concrete manhole structure. (32.78212, 130.83507).

7.3 Electric Power

Electricity is provided to the island by the Kyushu Electric Power Co. (KEP). Much of the following information was gathered from periodic updates and reports provided on the company's website (http://www.kyuden.co.jp/) informing customers of system performance and ongoing efforts to restore power. The island generates its power from a combination of oil and gas fired thermal plants, coal, two nuclear power plants and some smaller hydroelectric, wind, and solar plants. The majority of power in the Kumamoto region is supplied by networks of 220 and 500 kilovolt transmission lines (Swan, 2016).

Figure 7-7 shows the number of households without power over time following the foreshocks and main shock. Some damage occurred during the April 14 event with a total of 16,700 customers experiencing power loss. The power company mobilized 2,400 persons to repair damaged transmissions lines. Repair to high voltage distribution systems was completed on April 15.

Approximately 476,000 customers were without power following the April 16 event. Distribution lines and generation facilities suffered damage. Figure 7-7 shows the power recovery during the five days following the main shock. Supplemental power supply and support was provided by surrounding power companies during recovery.

Restoration of power to the majority of the region was relatively rapid due to the locations of power generation and substations outside of the most severe shaking. Landslides in the Aso area caused damage to a 66-kV transmission tower foundation (Tower No. 7 shown in Figure 7-8), threatening collapse. Construction of temporary towers caused delays in supply restoration to the Aso area. Transmission towers within Kumamoto City liquefaction zone demonstrated no observable tilting or foundation settlement (Figure 7-9).

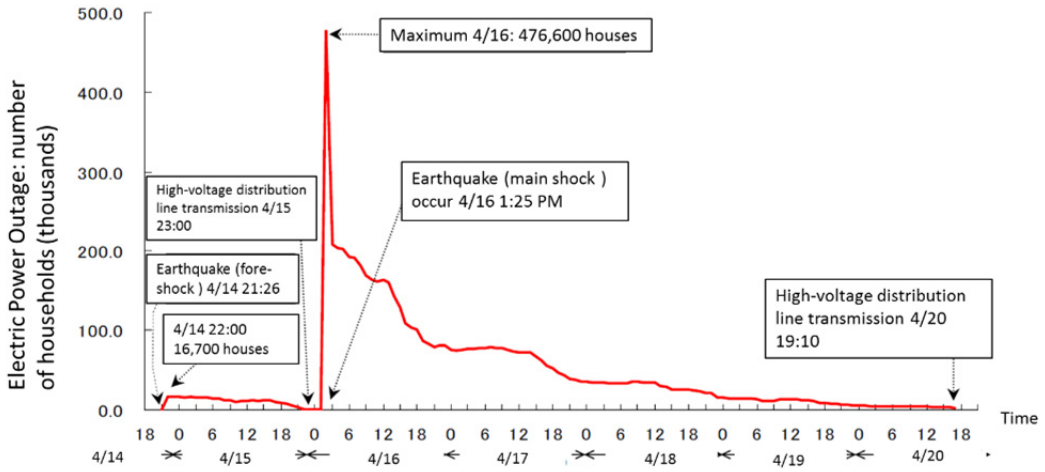

Figure 7-7. Customers without electric power over time following Kumamoto Earthquakes (Kyushu Electric Power).

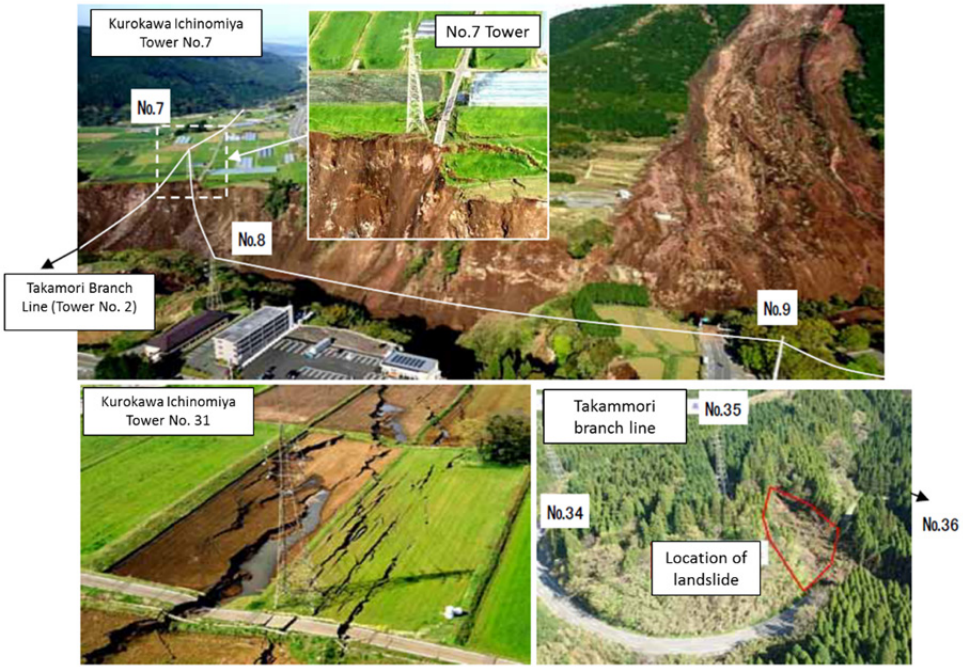

Figure 7-8. Earthquake-induced damage near the 66-kV transmission towers (courtesy of Kyushu Electric Power Co.) (No. 7 Tower: 32.879237, 130.985245) (No. 31 Tower: 32.928217, 130.999955).

Figure 7-9. Transmission tower in a heavily liquefied zone with no observed tilting or foundation settlement. (32.768987, 130.691186).

Two nuclear power stations on the island were subjected to moderate levels of seismic intensity. Neither station was located within Kumamoto Prefecture. The Sendai Nuclear Power station is located in Kagoshima Prefecture, 116-km southwest of the April 16 epicenter, and the Genkai Nuclear Power Station is located 118-km northwest of the epicenter in Saga Prefecture. While the Genkai Station was shut down, Sendai was one of three stations country-wide that has been reinstated following the 2011 Tohoku earthquake and tsunami. Table 7-1 shows the recorded levels of shaking at the two facilities, below the level of triggering emergency action.

Table 7-1. Seismic intensity levels recorded at nuclear power facilities[1].

・Sendai Nuclear Power Station

	Date and Time	JMA Seismic Intensity (Satsumasendai City, Kagoshima pref.)		Sendai Nuclear Power Station (Kyushu Electric Seismic Intensity)		
				Lowest floor of auxiliary building (on base rock)	Upper floor of auxiliary building (1st floor)	Ground surface
①	16 April 2016 01:25 JST	4	Seismic Intensity	3	3	3
			Maximum Acceleration (gal)	8.6	12.6	30.3

・Genkai Nuclear Power Station

	Date and Time	JMA Seismic Intensity (Karatsu City, Saga pref.)		Genkai Nuclear Power Station (Kyushu Electric Seismic Intensity)		
				Lowest floor of auxiliary building (on base rock)	Upper floor of auxiliary building (1st basement floor)	Ground surface
①	16 April 2016 01:25 JST	4	Seismic Intensity	3	3	3
			Maximum Acceleration (gal)	20.3	30.1	23.5

7.4 Natural Gas

Natural gas distribution in the region is provided by Saibu Gas Co. System coverage is limited to Kumamoto City and its suburbs. Individual liquefied petroleum gas tanks are used in rural areas, accounting for a large percentage of households subjected to the most severe damage.

There was no reported damage to gas distribution facilities or high pressure pipelines. Supply from middle pressure B and low-pressure service pipelines was suspended. Widespread suspension of gas service is typical in earthquake-affected areas to avoid ignition of potentially leaking lines. All lines are pressure checked prior to continuation of service, requiring significant effort from the utility company.

[1] http://www.kyuden.co.jp/var/rev0/0053/1900/jV9B8ep7.pdf

Safety checks for the gas conduit were performed in descending order of pressure delivery, beginning with medium-pressure lines followed by low-pressure service lines. Service was resumed for some priority facilities supplied directly from medium-pressure distribution. Priority was given to critical facilities such as hospitals, disaster recovery sites, schools, and homes for the elderly.

Figure 7-10 shows the number of households without gas service following the earthquakes. As a result of the April 14 event, gas supply was suspended to 4,600 customers of Kumamoto Chuo-ku in the southern part of the Kumamoto district. Rapidly mobilized representatives of Saibu Gas Co. reduced the number of suspended services to 1,123 units by the next day as well as taking measures to address 96 of 106 reported leaks. Further repairs were hindered the following day by the April 16 event, which lead to the shutdown of gas supply to 105,000 households in the Kumamoto district.

Low-pressure gas supply was suspended to 105,000 units for a period of three days to prevent a secondary disaster. Some 4,100 units were removed from the target recovery number due to vacancy, collapse, or excessive damage. Service to the 100,884 recovery targets was completed on April 30, ten days after service line re-establishment began. The number of technicians working to restore gas service from Saibu and Japan Gas Association increased from 2,300 to a peak of 4,600 from April 18 to April 25.

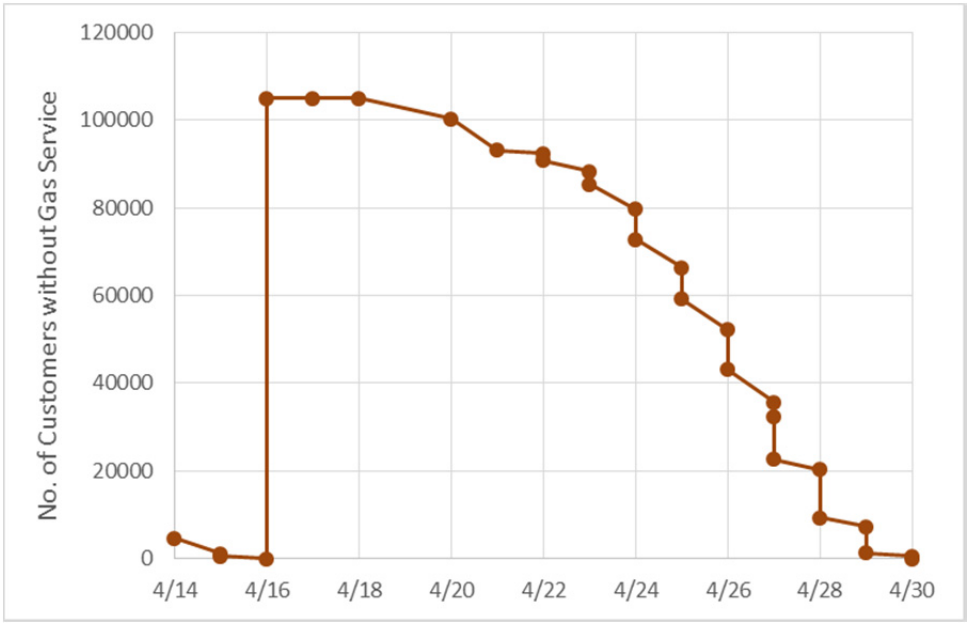

Figure 7-10. Customers without gas service following Kumamoto earthquakes (Saibu Gas Co.).

7.5 Telecommunications

Disruption of telecommunication during a disaster can cause significant distress to victims and relief efforts alike. This was the case during the 2011 Tohoku Earthquake, when access to the internet was limited due to damaged telecommunication facilities and excessive demand. In an effort to improve communication, three major cellular service providers – NTT Docomo Inc., KDDI Corp., and SoftBank Corp.- activated emergency public Wi-Fi hotspots in Kumamoto following the April 14 event, providing temporary access to any phone within range (Murai, 2016). While significant interruption of services

or facility damage was not reported as a result of the earthquake sequence, foresight and collaboration among service providers is making strides toward a more resilient, connected post-disaster society.

7.6 Transportation Networks

Significant damage to roads and highway bridges caused traffic difficulties for days following the earthquakes. Many roadways were damaged from rock and landslides, hindering support efforts in stricken communities. Misalignment of bridge abutments from severe shaking was observed along with excessive settlement around bridge abutments leading to differential vertical offsets.

Rail service was interrupted due to derailment of the Kyushu Shinkan-sen (bullet train) near the Kumamoto station during the April 14 foreshock. Others reported that the Kumamoto Airport suffered minor damage, and flights began to resume gradually three days after the earthquakes (Epstein et al. 2016). Kumamoto Port, constructed on an artificial island, experience severe liquefaction settlement (see Section 6.2.1).

8.0 Remote Sensing Methods

8.1 Light Detection and Ranging (LiDAR)

The terrestrial LIDAR technique (3D laser scanning) consists of sending and receiving laser pulses to build a point file of three-dimensional coordinates of the scanned surface. The time of travel for a single pulse reflection is measured along a known trajectory such that the distance from the laser, and consequently the position of a point of interest, is computed. Using this methodology, data collection occurs at rates of thousands of points per second generating a “point cloud” of three-dimensional coordinates.

The reconnaissance used a Riegl z420i laser scanner as a tripod mounted survey instrument. Multiple scans are collected during each survey area to fill in shadow zones of locations not directly in the line of sight of the laser and to expand the range and data density of the point cloud. Laser data are collected at rates of 8,000-12,000 points per second, scanning 360 degrees in the horizontal direction and plus and minus 40 degrees from the horizontal in the vertical direction. Georeferenced coordinates of the scan locations can be determined by locating the instrument over known survey benchmarks, or collecting GPS data at the time of the reconnaissance via an antenna mounted directly atop the laser, or by post processing the position of known targets in the field.

Data points in scans are collected at a low point density (<1.0 million points each) to assist in registration, and then at to high point density (20-60 million points each, per scan) to maximize the detail of the topographic observations. Point data from each set of scans are processed through a series of filters to remove non-ground surface and transient laser returns from the point cloud data. Points reflected from vegetation, power lines, and other non-ground features were either filtered by algorithm or manually cropped from the point cloud. Next, an isolated point filter algorithm is used to remove single point instances occurring above or below the land surface. These isolated points are usually a result of reflections from moisture in the atmosphere, or reflections off standing water.

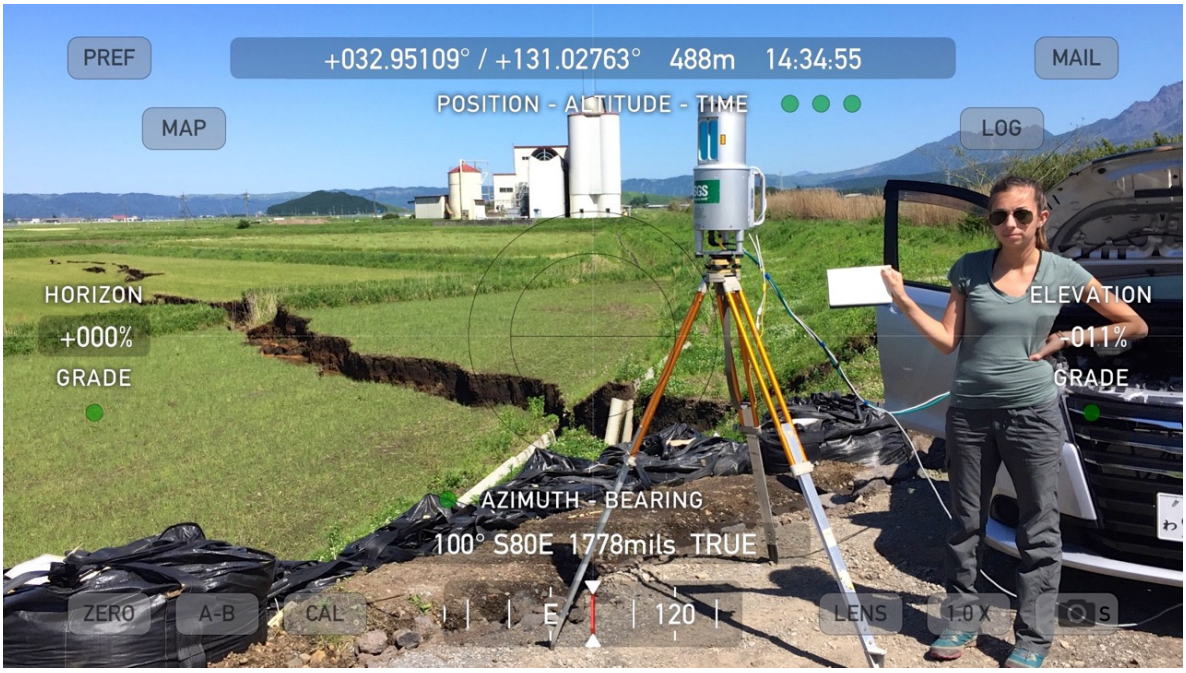

Figure 8-1. Field acquisition of LIDAR data using Riegl Ri-Scan software at the Futagawa fault graben located in Aso Caldera (Site RK7, 32.95109N, 131.02763E, 488m elevation).

A topographic filter algorithm selects the lowest point in a user defined cell of horizontal square dimensions of 2-10 centimeters in the point clouds to remove vegetation from the point clouds. Where the LIDAR point cloud partially penetrates through vegetation and reflects from the ground, this filter eliminates most vegetation data points. An effective alternative way to de-vegetate LIDAR data is to apply a surface proximity algorithm. This surface proximity algorithm first constructs a crude lowest point surface triangular regular network (perhaps at 1-m spacing). Then the dense point cloud is filtered such that only points close to the surface are preserved (perhaps at the 5- to 10-cm level). In some scans, the vast majority of the point data collected represent vegetation and not the ground surface (densely-vegetated ground). In this case, the topographic filter algorithm selects the lowest vegetation point that is topographically higher than the bare ground surface. This is a major source of error in estimating the topography of a bare-earth model.

In order to generate topographic surfaces of ground failure areas, a 2-10 cm minimum separation filter was applied to construct a roughly uniform data set. We used a common reference system (WGS84), and a common vertical datum (NGVD 1988) for LIDAR geo-referencing.

The best fit translation/rotation registration process uses a surface registration algorithm to align the overlapping data within a pair of scans. A final product of LIDAR data processing, that can be used to make contours or detect change, are three-dimensional Triangular Irregular Network (TIN) surface models that represent a topographic surface of each area.

LIDAR data collection occurred in the Kumamoto and Aso crater regions of Kyushu Prefecture.

- Site RK13, Oh-Kirihata Dam
    - 32.84156 N, 130.93227E
    - Oblique surface fault rupture through earth dam and reservoir
- Site RK7, depression zone, Aso Caldera.
    - 32.95109N, 131.02763E, 488-m elevation
    - Normal fault surface rupture, graben in deep soil.
- Site RK9: lateral spread, Mashiki Town
    - 32.77378 N., 130.7838 E.
    - Liquefaction-induced lateral spread
- Site RK11: surface fault rupture through a river levee
    - 32.79742 N., 130.85334 E.
    - Fault rupture and dislocation of agricultural field, levee, and adjacent roads.

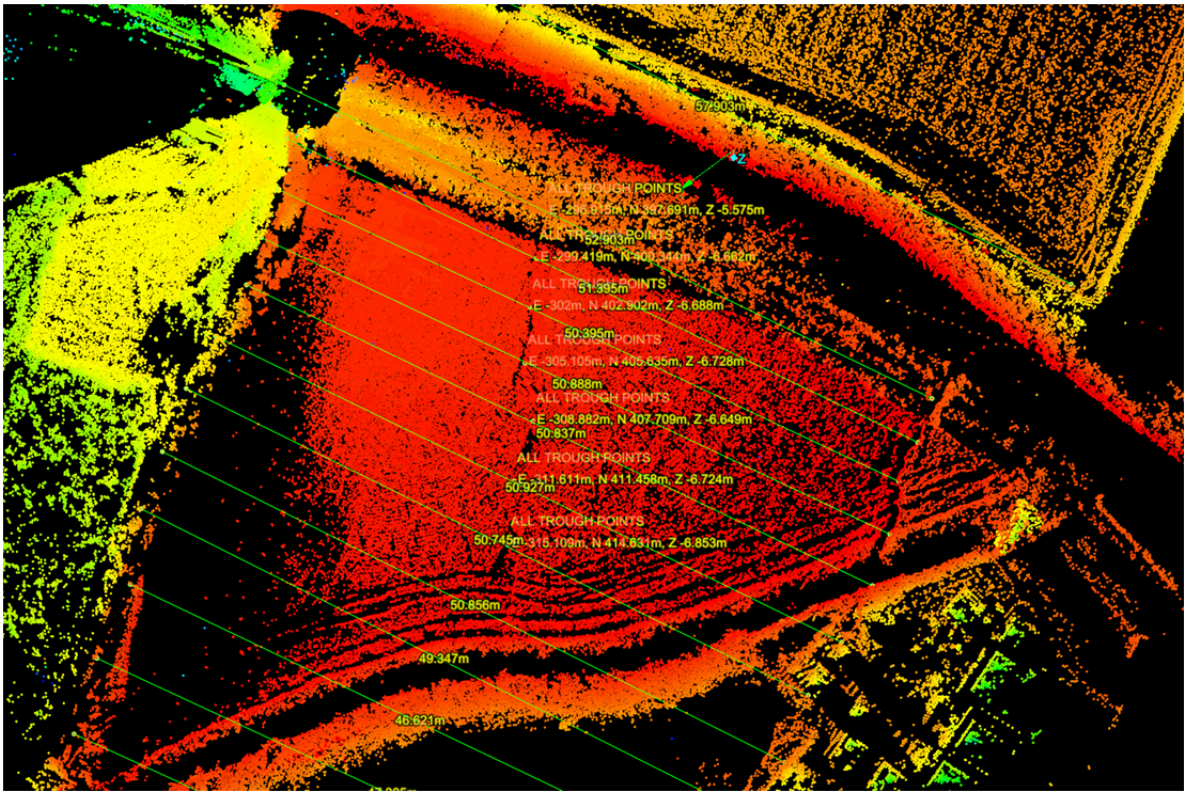

Figure 8-2. Measurements of fault graben offset and width using point-, line-, and area-query tools on LIDAR point cloud data at Aso Caldera (Site RK7, 32.95109N, 131.02763E)

8.2 Unmanned Aerial Vehicle (UAV)

An unmanned aerial vehicle (UAV) was used to capture low-altitude aerial imagery from select sites of interest during the Kumamoto reconnaissance. The UAV used to collect the data for this mission was a small, custom made quadcopter that has been configured for collecting low-level aerial images. The airframe is a Discovery Pro model manufactured by Team Blacksheep (Figure 8-3), with dimensions of approximately 18" x 18" x 4" and a total weight of 3.8 lbs. This small aircraft footprint made it ideal for transport to various sights of interest and flying near damaged structures without the risk of causing significant damage or harm in the event of a malfunction.

The UAV was equipped with a fully autonomous 3D Robotics Pixhawk autopilot that is capable of flying an entire mission with little or no operator input. However, the autopilot could not be deployed on this mission due to Japanese commercial UAV restrictions. The operator was able to monitor the UAV from the ground using a wireless telemetry link connected to a laptop computer. This telemetry link showed the real-time GPS location of the UAV as well as critical flight instruments such as heading, velocity, and artificial horizon. Along with the telemetry link, the operator maintained a separate radio control link at all times. The operator was also equipped with a wireless video down link so the damage visible from the air could be monitored from the ground using first-person view (FPV) goggles in real-time. In the rare event of a loss of communications, the UAV would autonomously return to its starting location and land.

The sensor used to gather the aerial images for this mission was a GoPro Hero 4 Silver Edition. This camera was selected because of its lightweight, small size, and relatively high video resolution. The camera was mounted on a two axis, stabilized gimbal on the UAV that allowed for minimal motion blur cause by the attitude changes of the aircraft. The camera was also able to be tilted on its elevation axis by the operator on the ground. The image the GoPro camera was viewing could also be viewed in real-time by both the operator and geotechnical experts so the UAV could be guided manually to localized earthquake damage. The ultra-wide angle lens of the camera was manually removed and replaced with a 5.4-mm flat lens manufactured by Rage Cams. The flat lens was used to reduce distortion in the 3D models that would subsequently be developed from the captured video images.

Flights were performed over approximately 4 km of the depression zone, over the failed Oh-Kirihata dam, and over the Route 28 bridge and landslide adjacent to the Oh-Kirihata dam. The flights over the depression zone consisted of six reaches and 11 total flights, each one covering an area of approximately 0.7 km^2. All six reaches were flown over a period of approximately 6 hours. Four total flights were performed over the dam and three flights over the bridge and landslide. These seven flights were performed over a period of approximately 2 hours. The altitude of the UAV generally ranged from 10 meters to 60 meters above the ground surface, resulting in image resolutions of approximately 207 pixels per $meter^2$ or greater. No ground control points were surveyed for any of the flights to simplify field operations, but approximately 5 to 10 objects were measured on the ground for each flown reach. These measured objects were subsequently used for scaling of the completed point cloud and textured models.

Three-dimensional point cloud and textured models were developed from the aerial images captured with the GoPro Hero 4 video camera. Structure from Motion (SfM) computer vision technology was used to develop the 3D models. All SfM image processing was performed using the commercial 3D visualization software *PhotoScan 1.1.5*. The customized computer workstation used to operate *PhotoScan* uses two Intel® Xeon i7 E5-2680 v2 CPUs @ 2.80 GHz, with 256 GB of DDR RAM and two nVidia® GeFORCE GTX 780 Ti graphics cards. With this set of workstation specifications, processing times to develop 3D point clouds and meshed surface models were generally less than 12

hours for each site. Finalized dense point clouds were exported from *Photoscan* as .PLY files and were scaled, edited, and analyzed in point cloud manipulation software *CloudCompare 2.6.1* and *I-Site Studio 5.1*.

Figure 8-4 through Figure 8-6 present some screenshots of the 3D point clouds that were developed from the UAV-based video imagery.

Figure 8-3. Discover Pro UAV manufactured by Team Blacksheep. The sensor shown is a GoPro Hero 4 Silver Edition.

Figure 8-4. Screenshot of the 3D point cloud model near the bridge impacted by the depression zone (32.95131° N 131.02774° E).

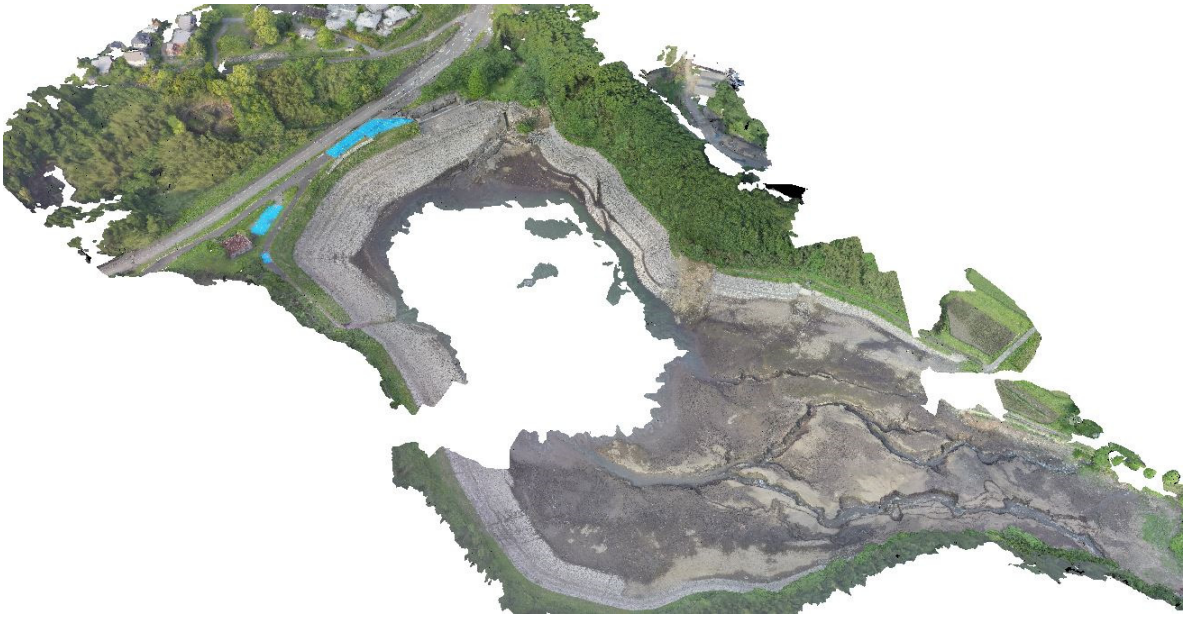

Figure 8-5. Screenshot of the Oh-Kirihata dam 3D textured model developed from UAV-based video imagery (32.83958° N 130.93026° E).

Figure 8-6. Screenshot of the Route 28 bridge and landslide 3D point cloud model developed from UAV-based video imagery (32.84236° N 130.92888° E).

8.3 Geotagged Datasets

During the 3-day reconnaissance, vehicles were used to traverse the roads of the epicentral region. Each vehicle was equipped with smartphones, digital cameras, maps, computers for recording site logs, and GPS units for recording track logs and site locations. The reconnaissance team merged the GPS data, site logs, and digital photos into a common database. Following the reconnaissance, a Google Earth KML file was generated to display the observations on dynamic digital maps. The authors recommend downloading and opening the Google Earth map file for this earthquake to navigate through the report observation sites as they are described in the text.

The primary tools of the reconnaissance effort were smartphone (iPhones and Android devices that are essentially hand held computers, phones, cameras, GPS units, are dictation devices. These devices integrate all the basic functions that were previously done on multiple pieces of equipment. Text messaging proved to be the preferred means of during the reconnaissance. Phones required external power to operate all day during the reconnaissance, provided by car adapters and an external power battery charged before the reconnaissance.

For the reconnaissance, all recorded information, photographs, and data observations were located with latitude and longitude coordinates. GPS track logs passively monitored the locations of travel of each reconnaissance team vehicle during the field day. All observations were recorded and reported as ellipsoid heights in the World Geodetic System of 1984 (WGS84).

9.0 Significant Case Histories and Lessons Learned

9.1 Oh-Kirihata Dam

9.1.1 Field Observations

An approximately 0.5 km long by 0.25 km wide water reservoir was ruptured by the main strand of the Futagawa Fault. The fault crossed the reservoir in two places, along the western flank of the reservoir, where the fault first crossed, and through the intersection of the spillway and the spillway outlet channel, on the northern side of the reservoir (Figure 9-1). Detailed data was captured of this site using terrestrial LIDAR and UAV flights to develop a 3D model of the site.

At the time of our investigation, the reservoir was almost completely drained; however, our understanding from our Japanese colleagues was that it was full or nearly full at the time of the earthquake. The dam was apparently drained immediately after the earthquake and the downstream residents evacuated because a potential dam breach was feared due to outflowing water observed. However, the outflowing water was later traced to a nearby pipeline failure(s).

The reservoir consisted of an uncontrolled spillway located in the right abutment of the dam, with a spillway outflow channel capable of moving water downstream. The embankment dam to the left of the spillway was roughly 100 m wide. Large natural hills extended well up from the full reservoir water level around most of the reservoir. A bench runs along the entire circumference of the reservoir just above the full reservoir water level. The slopes below this bench were typically 23° to 26° in inclination and were covered with riprap and a concrete grid. The bottom of the reservoir was mostly filled with a clayey sediment. A highway crossed over the embankment dam and over the spillway outflow channel. The dam had no emergency spillway. A low-level outflow is present according to our Japanese colleagues; however, we are not able to see it as it is likely under the remaining reservoir water. A gatehouse was present on the northwestern side of the reservoir with multiple outlets available to the dam operators to lower the reservoir water level starting from just below the bench elevation to near the elevation of the reservoir water level at the time of investigation.

Around nearly the entire reservoir bench, slope movements of 0.2 to 0.5 m (measured based on the length of the horizontal offsets in cracks observed on the bench, not necessarily representative of the total magnitude of slope movement if upslope movement occurred too or of the vertical component of slope movement, see Figure 9-2). No slope movement in the upper natural slopes was obvious from the bench; however, we did not hike into the overlying slopes to examine them. At the northwestern corner of the reservoir, at the nearby bridge, a large landslide occurred in the same formation (Figure 9-3). Complete slope failures of the reservoir bench and underlying slope occurred at two locations: just to the east of the spillway and on the eastern flank of the reservoir (Figure 9-4). The reservoir's gatehouse was significantly back tilted, and the reservoir bench in front of the gatehouse was significantly tilted toward the reservoir (Figure 9-5). The movements at and around the gatehouse were much greater than was typical for the reservoir benches elsewhere.

The native rock on the western and northern sides of the reservoir is mapped as Late Pleistocene, Omine Volcano, pyroxene dacite lava and pyroclastic rocks (A0) in GSJ (2016c). The eastern side of the reservoir was mapped as Late Pleistocene, volcanic fan deposits, gravel, sand, and mud (vf).

Clayey sediment was found at the bottom of the reservoir and was highly eroded (several meters vertical) where rapidly flowing streams of water from upstream of the reservoir continued to flow into the reservoir.

The initial fault crossing of the Futagawa Fault (based on our understanding of the rupture sequence) was through the western side of the reservoir, through the reservoir side slope (Figure 9-6). Significant ground disturbance and tree collapse was observed in the natural slope above the reservoir bench. The bench itself was highly distorted at the fault crossing (Figure 9-7). The reservoir side slope below the bench was relatively intact, except that the riprap was disturbed (i.e., "dilated") as a result of shearing and the concrete gridwork was offset and damaged (Figure 9-8). A primary fault break was located here based on dilation of the riprap; however, many other possible secondary strands were noted. It was very difficult to measure fault offsets, or the number of secondary faults, because of large slope movements (discussed above) were coincident with the fault movement here. Many of the offsets in the concrete grid were left lateral and therefore likely slope related. A set of stairs leading from the reservoir bench down to the bottom of the reservoir was located at the approximate location of the fault crossing. The stairs were about 70 to 80 cm higher than the reservoir bench, indicating the bench here may have moved downwards significantly as a result of slope movement, possibly exacerbated by the fault movement. It is estimated, however, that the right lateral strike slip movement of the Futagawa Fault here was at least 50 cm, if not more with secondary faults and ground strain added. LIDAR data may be best to estimate the total movement. No significant vertical fault offset was noted; however, LIDAR data may provide a better estimate.

The location at which the Futagawa Fault exited the reservoir was approximately between the spillway and the spillway outlet channel (Figure 9-9). Disturbance caused by the fault could be noted in the slopes below the spillway, similar to the initial fault crossing into the reservoir discussed above. We examined the inside of the spillway and spillway outlet channel and measured the offsets likely caused by the fault movement (Figure 9-10, Figure 9-11, Figure 9-12, Figure 9-13, Figure 9-14, and Figure 9-15). See Figure 9-16 for a sketch of the offsets measured inside the spillway and outlet channel for details.

The fault movement apparently caused failure of one of the spillway training walls, which caused a significant amount of soil to fall into the spillway (Figure 9-17). A secondary rupture apparently went through the right side of the spillway based on offsets recorded there (Figure 9-18). In the roadway above the spillway, the fault movement caused significant shearing of the road (Figure 9-19). Fault movement was at least 50 cm of right lateral strike slip in this area, potentially with some minor vertical movement; although a significant amount of deformation could have been distributed off of the main fault break in bending or in secondary faults, so the total offset would be best estimated with LIDAR. An unreinforced concrete block retaining wall on the opposite side of the road partially collapsed as a result of fault rupture (Figure 9-20). The retaining wall was about 50 cm in thickness. Above the road, the fault ruptured through a hill that the wall was retaining. Three apparent offsets were noted in a road that went up the side of this hill, as shown in Figure 9-21, based on guardrail distortion and pavement disturbance.

Overlying the spillway outlet channel were two bridges that crossed overhead. One bridge was nearer the reservoir and was overlain by pavement for traffic local to the reservoir. The second bridge, further from the reservoir, was for highway traffic. Large differential vertical movements were noted at the interface between the first bridge and the adjacent ground (Figure 9-22). We assume the differential settlement was a result of material loss caused by movement and/or damage to the abutment retaining walls, similar but less severe than the failure of the left spillway training wall. A much smaller differential settlement was noted on the highway between the bridge and adjacent ground.

9.1.2 LIDAR Analysis

Many aspects of the damage observed in the record above are preserved for measurement in the LIDAR and UAV data. Where the fault rupture passes through the spillway zone and road, the width of the displacement zone is clearly defined in the surface displacements. Below the perimeter of the reservoir, the width of the fault rupture zone can be observed in the disruption and roughening of the rock fill of the embankment facing. Where the fault rupture passes beneath the embankment face, rock fill compressed and individual blocks popped up above the surrounding facing.

An overview of the reservoir LIDAR data can be seen in Figure 9-23, and an example of the roughening of the embankment facing can be seen in Figure 9-24. In Figure 9-23, the width of the Futagawa Fault rupture lays between the polygons. It can be seen the fault enters the reservoir from the southwest slope, crosses a corner of the reservoir, and exits through the dam embankment and spillway. The width of the zone of the fault rupture widens as it crosses the dam, spillway, road, and the hot springs resort on north side of the road. At the southwest, where the fault enters the dam, the width of the fault zone is approximately 9 m. On the northeastern side of the dam where the embankment and spillway are located, the width of the fault rupture zone is 25 m (Figure 9-23).

Within the reservoir, the evidence for surface rupture is the disruption of the embankment rock facing (Figure 9-24). In the LIDAR imagery, this roughness of the reservoir slope facing, as a result of the faulting, is clearly visible in topography. It is possible that the estimated width of the fault zone based on the disruption of the reservoir wall facing is greater than the true width of the zone. However, in the vicinity of the spillway and roadway to the north, direct measurement of the fault rupture zone was similar to the width of the disrupted facing.

Other aspects of the damage to the dam include the failure of concrete spillway as the rupture passed through it. In Figure 9-23, the western spillway wall broke 2 to 3.5 m below the wall top and is leaning into the spillway cavity at 74°. Other gaps and openings in the spillway walls was 1.1 m on the eastern end of the spillway and on the western end was 2.1 m, exposing soil backfill. Had the reservoir water overtopped the spillway, the soil behind the damaged concrete would have easily been eroded and a progressive and potentially catastrophic down-cutting of the spillway would have been possible.

9.1.3 UAV Analysis

UAV imagery captured from the dam resulted in the development of a SfM 3D computer vision point cloud and textured models. Because these models were developed from relatively low-resolution video images rather than high-resolution DSLR digital photographs, the median accuracy of the point cloud models is likely about 10 cm based on previous experience and studies with similar images. Therefore, the LIDAR dataset provides much more accurate data for the measurement of deformations and objects of interest. However, the UAV-based SfM models are excellent for qualitative assessment and study of the dam site because it automatically assigns color to every point in the point cloud model. An overview screenshot of the dam was shown in previously in Figure 8-5. A screenshot of the 3D dense point cloud of the damaged dam is presented in Figure 9-26. A screenshot of the 3D point cloud of the erosion that developed when the dam was drained is presented in Figure 9-27.

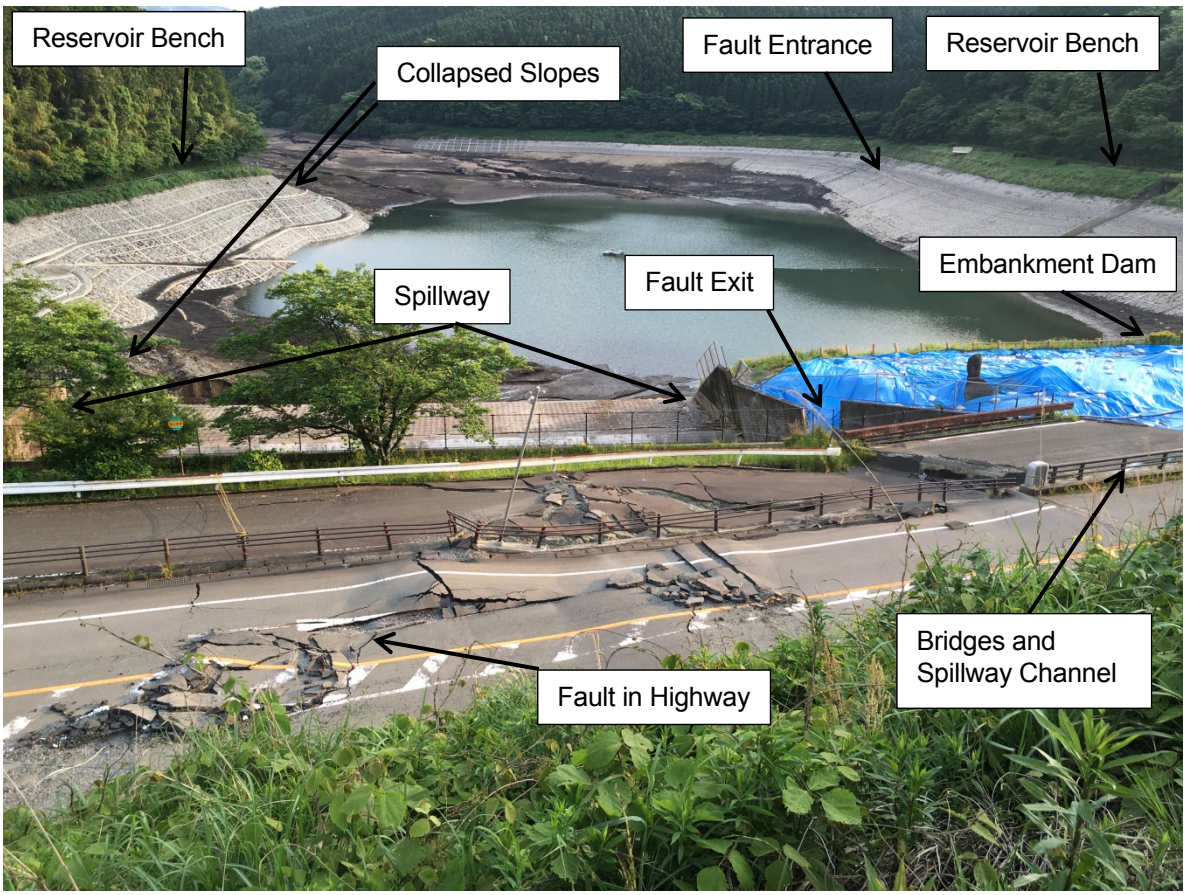

Figure 9-1. Overview of the dam site (32.84167°, 130.93202°).

Figure 9-2. Slope displacements typical of nearly the entire bench running the circumference of the dam.

Figure 9-3. A major landslide of the hill adjacent to the reservoir.

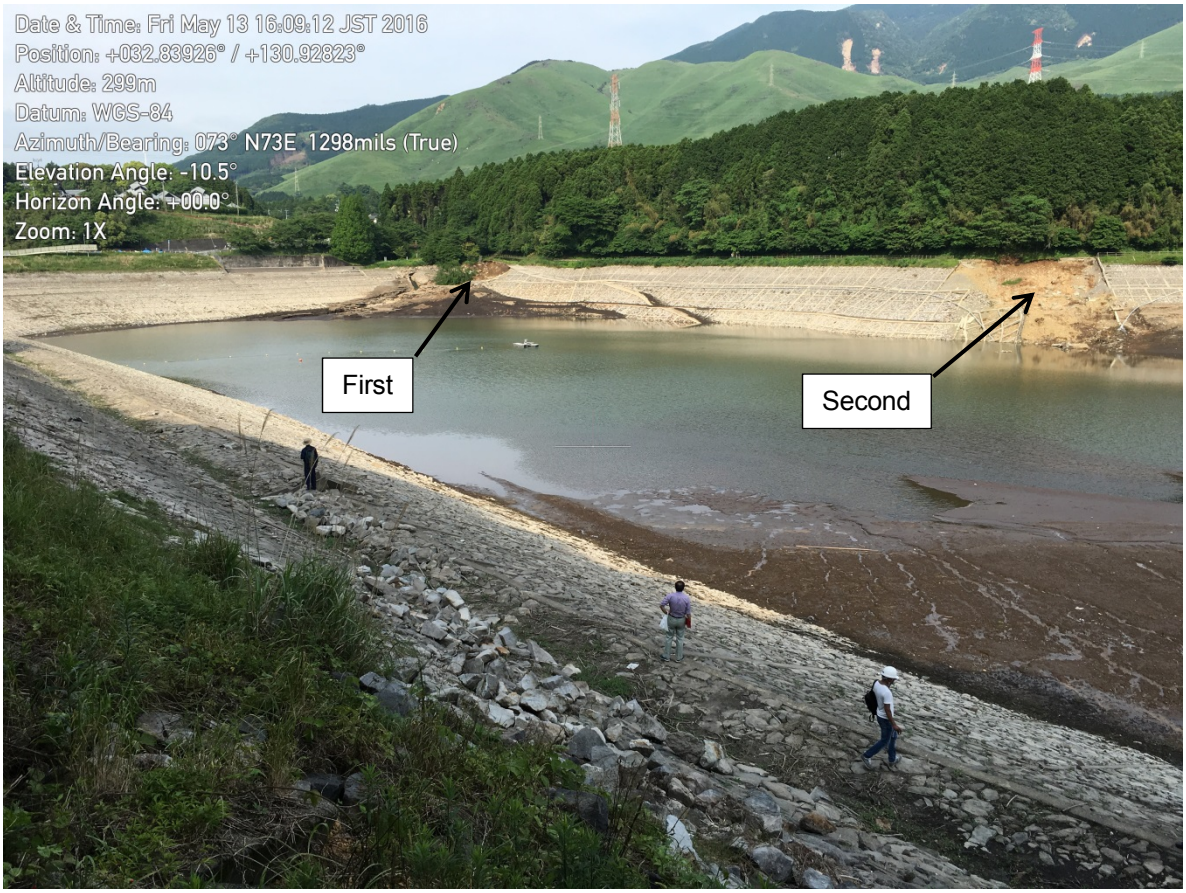

Figure 9-4. The two collapsed side slopes of the reservoir.

Figure 9-5. Significant back tilting of the gatehouse and forward tilting of the reservoir bench in front of the gatehouse.

Figure 9-6. The location of the main fault strands entrance into the reservoir, visible by the “dilation” of the riprap side slope armoring.

Figure 9-7. The reservoir bench at the location of the fault entrance into the reservoir. Note the vertical offset of this staircase, possibly resulting from the combination of fault movement and slope movement here.

Figure 9-8. Deformation caused largely by the fault at the location of the fault entrance into the reservoir, as seen by the riprap dilation and bending of the concrete gridwork.

Figure 9-9. Overview of the condition of the spillway.

Figure 9-10. Damage and offsets at the location of fault rupture, between the spillway and the spillway outlet channel.

Figure 9-11. Detail of the main fault offset, through the intersection of the spillway and spillway outlet channel.

Figure 9-12. A smaller offset at a joint in the spillway outlet channel due to the movement and rotation of the spillway.

Figure 9-13. Another offset at a joint in the spillway outlet channel due to the movement and rotation of the spillway. Note the change in horizontal separation from top to bottom.

Figure 9-14. Another offset at a joint in the spillway outlet channel due to the movement and rotation of the spillway.

Figure 9-15. Overview of the offsets and rotations in the spillway outlet channel joints, facing back towards the spillway.

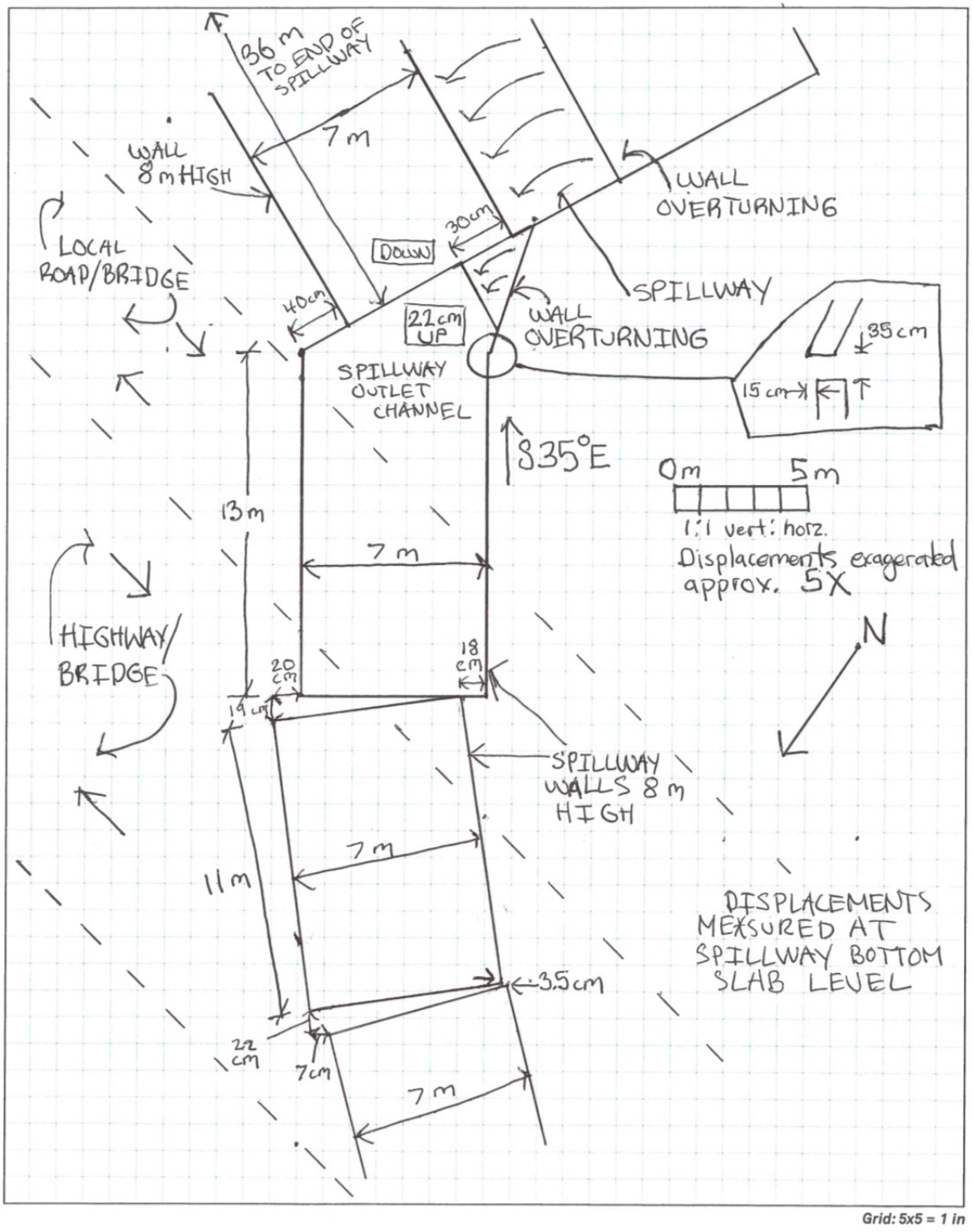

Figure 9-16. A sketch of the offsets measured inside the spillway and spillway outflow channel.

Figure 9-17. A close up of the left spillway training wall.

Figure 9-18. Side view of the spillway, with an apparent secondary rupture in the foreground running through the right side of the spillway.

Figure 9-19. Fault rupture through the highway above the dam spillway.

Figure 9-20. Partial collapse of an unreinforced concrete block retaining wall at the location of fault rupture, above the spillway.

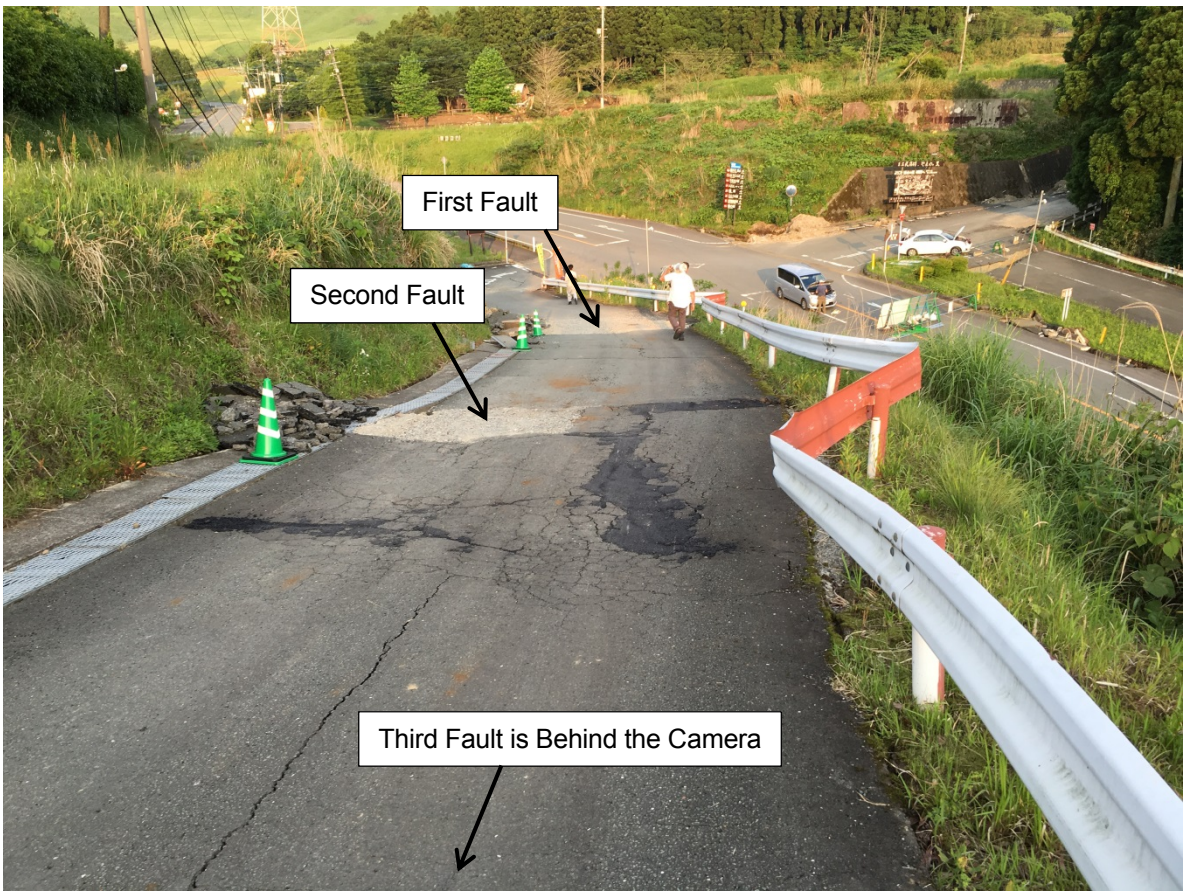

Figure 9-21. Fault ruptures in the hill above the highway and above the spillway. Note the compressions in the guardrail and road patches.

Figure 9-22. Differential settlement at one of the bridges crossing the spillway outlet channel, possibly caused by movement of the spillway walls in response to fault displacement.

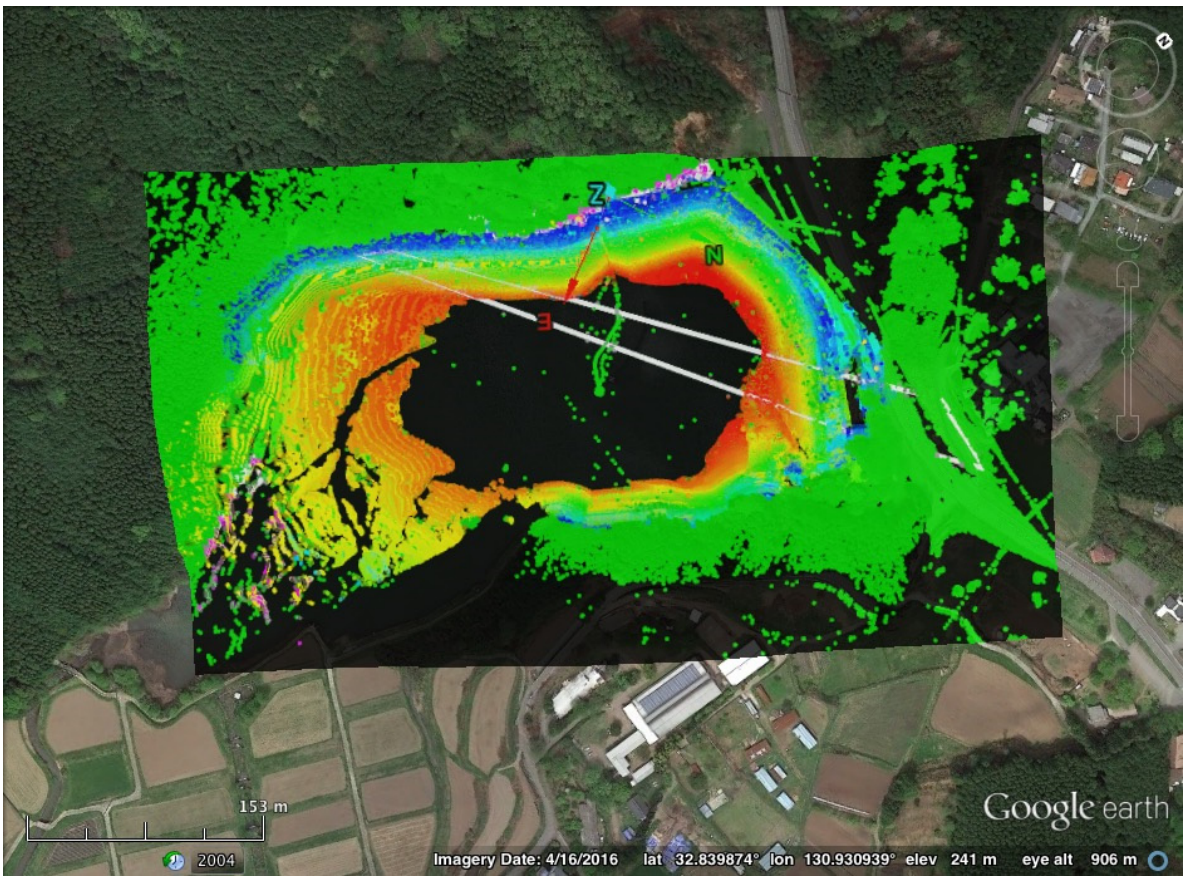

Figure 9-23. Lidar data set for the Oh-Kirihata Dam. Coverage focused on the dam embankment, spillway, and the rupture zone passing beneath the reservoir wall rock facing (32.84123, 130.93158).

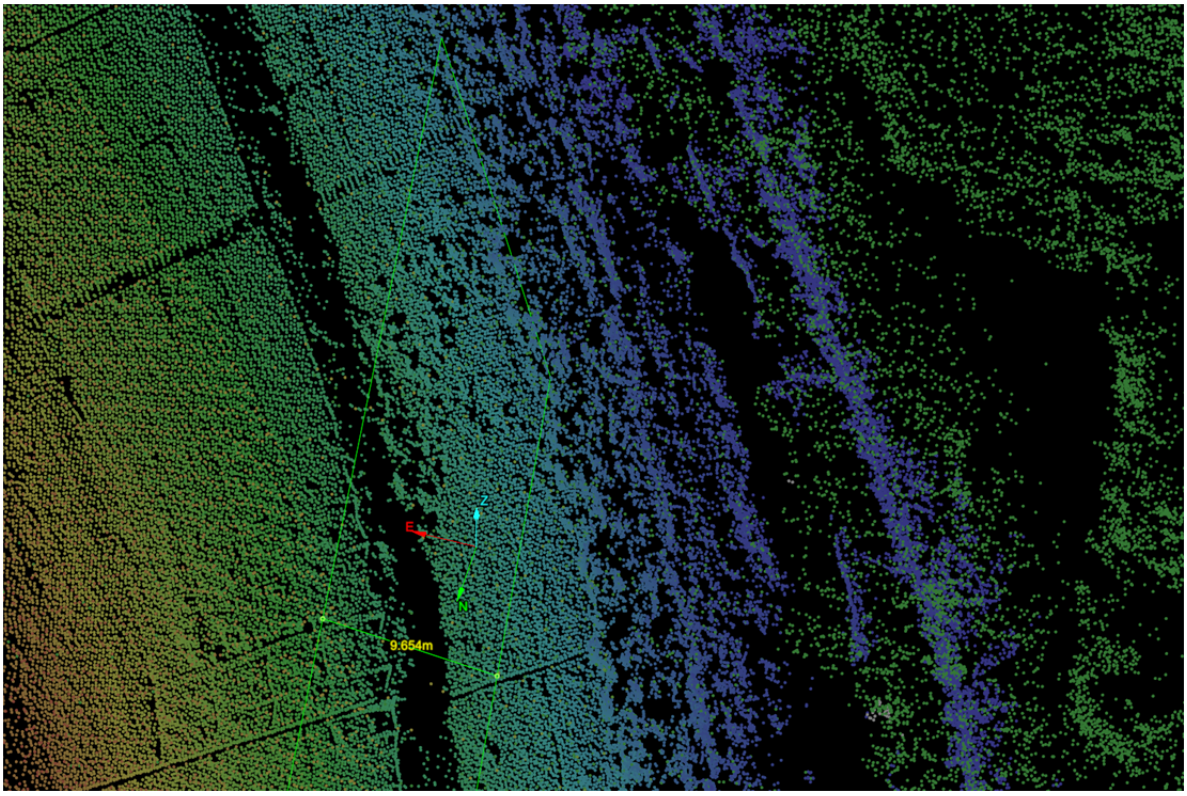

Figure 9-24. Evidence of fault rupture beneath the reservoir wall rock facing: disruption of the rock blanket, here visible in the roughened topography of the wall (32.84123, 130.93158).

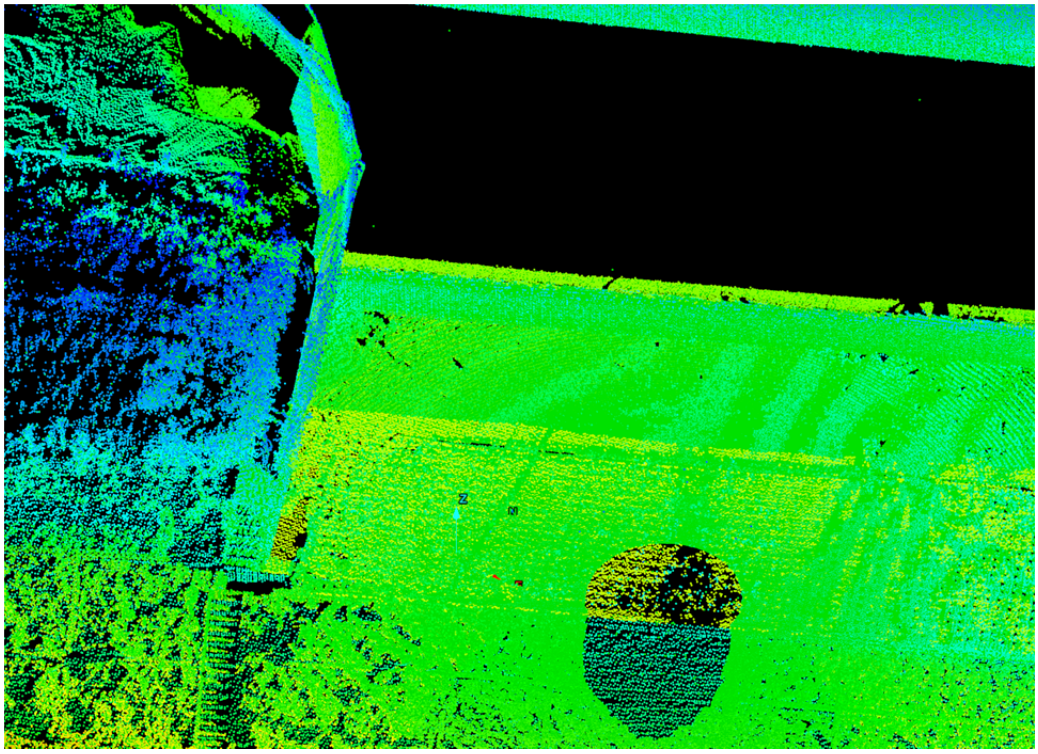

Figure 9-25. Detail of damage to the spillway along the western side of the structure (32.84123, 130.93158).

Figure 9-26. Screenshot of the 3D dense point cloud of the dam developed from UAV-based imagery (32.84123, 130.93158).

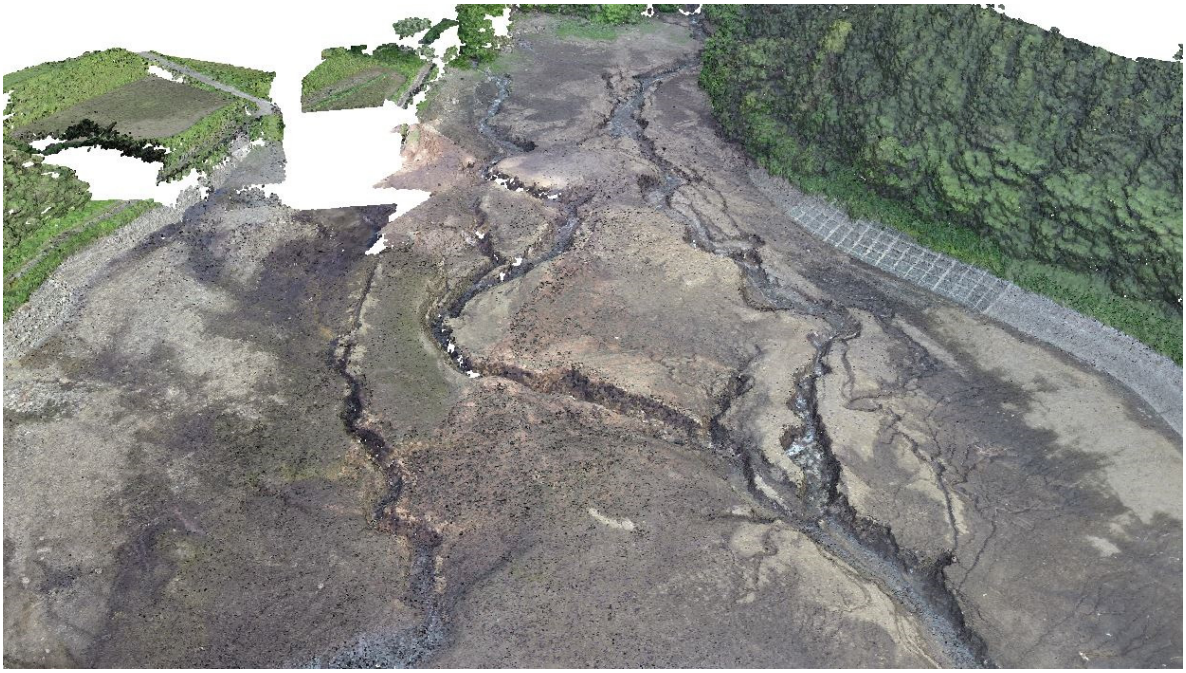

Figure 9-27. Screenshot of the 3D dense point cloud of the erosion zone in the dam; developed from UAV-based imagery (32.84123, 130.93158).

9.2 Aso Caldera Depression Zone

9.2.1 Field Observations

The Futagawa Fault surface fault rupture extended northeast into the southwestern corner of the Aso Caldera, a region of active volcanism. An approximately 10-km-long section of ground movement, herein call the “depression zone”, occurred coseismically (according to the observation of a resident who witnessed the earthquake), roughly projecting out from the point at which the Futagawa Fault ruptured into the caldera, up and to the northwestern end of the caldera. This depression zone was typically a 30-m to 110-m wide trough of depression with near vertical offsets on each side of the trough with vertical movement often 0.5 m to 2.5 m and minor strike-slip movement on the order of tens of cm. See Figure 9-28 for a typical free-field expression of the “depression zone”.

At a location where the depression zone crossed roughly orthogonal to a road (Figure 9-29), a detailed profile across the depression zone was made, noting cracks in the asphalt, concrete storm drain covers, tilting in utility poles, and other features possibly caused by the depression zone ground movement. See Figure 9-30 and Table 9-1 for the measurements made during the investigation. As noted in this profile, the south edge of the depression zone formed a small popup block, where there were two main edges of the depression zone on the south side that bounded a small block of soil that popped up relative to the surrounding area. The typical affect the depression zone had on infrastructure in this area is shown in Figure 9-31 and Figure 9-32.

At one location, a bridge crossed the depression zone, with one abutment outside of the depression zone, and one abutment inside the depression zone. The bridge was relatively undamaged (Figure 9-33). This bridge is of particular interest and should be investigated more closely with any additional studies involving the depression zone. The west abutment of the bridge appears to lie squarely within the zone of depression. This is evident by soil settlement of approximately 38 cm around the bridge (Figure 9-34), but little to no visible settlement of the bridge itself. A slight downward slope towards the western abutment of approximately 1 degree was measured, suggesting that a small settlement may have occurred in the foundation of the abutment, but certainly less than the soil surrounding it.

In the northern-most reach of the depression zone, in the northwestern corner of the caldera, the depression zone consisted of three separate, smaller depression zones, which entered a large hillside (Figure 9-35). The magnitude of vertical depression in this area was not as significant as in other areas. The hill that these strands crossed into is mapped as Hornblende dacite pyroclastic rock, tuff breccia (Dp) in GSJ (2016c).

9.2.2 LIDAR Analysis

LIDAR data was collected along a zone 1-km long and 500-m wide extending from a small agricultural bridge at 32.951048°, 131.027590° and Route 175 at 32.955849°, 131.037093°. The zone is bounded by graben-forming faults along the north and south and can be seen in Figure 9-36.

The LIDAR data was registered and measurements were made on the width and depth of the zone. The width of the depression zone in this data set ranged from 36 m to 106 m. At the west end of the depression zone, the average width is 65 m, and at the eastern end, the average width is 50 m (Figure 9-25).

The depression depth varies across the length of the graben and from the south side to the north side. On the south side of the graben, the average depth of the step of the bounding fissure varied from west-to-east from 1.25 m to 0.5 m. The maximum vertical offset of the graben fissure on the south side was 2.39 m (Figure 9-37).

On the north side of the graben, the overall step was similar in magnitude and mirrored (step-up to the north) to those on the south side (step-down to the north). Consistently, the step up to the north was on average 0.6 m throughout the graben zone captured in the LIDAR. The maximum step-up was 1.74 m.

9.2.3 UAV Analysis

UAV aerial video imagery was collected along a nearly linear stretch of the depression zone that extended approximately 4 km (from 32.95093° N 131.02748° E to 32.97965° N 131.05195° E). Flights were performed by visually identifying ground cracks visible from the air, and following them to the northeast until they disappeared into the crater wall. This series of UAV flights was performed in six total segments. SfM models developed from each of these segments were stitched together to create a single 3D point cloud of the entire 4-km reach that was flown. As was mentioned previously, the point cloud accuracy of these models is likely no lower than about 10 cm based on previous studies and experience with these types of video images. A screenshot of the bridge located within the depression zone was presented in Figure 8-4. A screenshot of the 3D point cloud model of the entire 4-km reach of the depression zone that was flown by the UAV is presented in Figure 9-39. Example ground surface profiles across the depression zone are provided in Figure 9-40.

A Nikon D7100 DSLR camera was also manually used to capture approximately 50 images of the homes and road impacted by the depression zone (32.95663° N 131.03670° E). These images were also processed by SfM computer vision and a 3D point cloud model of the scene was developed. Based on comparisons with measurements manually performed at the site, this model has a dimensional mean accuracy of approximately 2 cm. Screenshots of the 3D textured model of the damaged homes and road are presented in Figure 9-41 and Figure 9-42.

9.2.4 Interpretation

Although many theories have been proposed by various investigators of this earthquake (e.g., Konagai et al., 2016, GSI, 2016), and is not usually referred to as fault rupture in other reconnaissance reports, our interpretation is that this depression zone is likely caused by near vertical normal faulting on the caldera's ring fault, with the second, antithetic fault (and hence the zone of depression) created as a result of the deep, soft soil profile in the caldera or as a result of underlying interaction with a ring dike (a sub-circular dike of igneous rock created along a ring fault) or other deeper geological structure.

Ring faults typically encircle the caldera of a volcano, allowing the caldera to collapse relative to the caldera walls as magma is released (e.g., Fichtner and Tkalcic, 2010, Goldman et al, 2015, Geyer and Marti, 2014). There is debate about whether ring faults tend to dip towards or away from the caldera; however, they are typically expected to be near vertical faults, potentially with some strike-slip component (see Figure 9-43). The type of ground movement observed in this earthquake is strikingly similar to the layout of the fault structure of the California Long Valley Caldera, where the strike-slip Hilton Creek Fault enters the caldera near, but not entirely coincident, with the caldera's ring fault (e.g., Chen et al., 2014).

Secondary, antithetic faults that form graben structures in soil can be created through deep soil profiles when the primary normal fault curves progressively steeper as the fault propagates from bedrock to the ground surface (Bray et al., 1994; see Figure 9-44). If this was the case, this would imply that the bedrock movement was normal faulting at a shallower angle (e.g., 60° dip) and only curved to near vertical at the ground surface. Borings conducted by others prior to the earthquake in the caldera indicate deep lake deposits, with very soft clay, reaching a void ratio of up to 5 to 7, and ranging in thickness between about 20 m to 70 m (e.g., Appendix B). Based on the boring logs

presented in Appendix B, no distinct geological changes were noted across the width of the depression zone (e.g., shallow rock on one side and deep soil on the other). Soil was found to significant depths on each side of the depression zone, including soft lake deposits on both sides. The soil conditions did vary significantly from boring location to boring location but did not appear to systemically change across the depression zone. An argument supporting the soil-caused formation of the secondary fault and graben structure is the lack of a well-defined depression zone in areas not floored with thick soil deposits.

Based on the data collect, the north side of the depression zone is likely the primary fault, while the south side is likely the secondary, antithetic fault. This interpretation is based on a small popup block of soil that occurred on the south edge of the depression (Figure 9-30), which is usually associated with the secondary fault side. There were more cracks and general disturbance on the south side of the depression zone, which would be more typical of the secondary fault side (the hanging wall of the primary fault), and limited disturbance north of the depression zone, which would be more typical of the footwall side of the primary fault (Figure 9-30). If the primary fault was on the north side of the depression zone, that would imply the causative fault was an inward dipping normal fault (dipping inwards towards the center of the caldera), which is what many literature sources suggests is common for ring faults.

At the bridge that crossed the depression zone, the question of interest is, “if the depression zone is a fault-related feature causing settlement of the entire soil column extending to the ground surface, wouldn’t the piles founded in that same soil column also have settled by the same amount?” Further studies are required to understand how the soil around the bridge foundations settled, but not the bridge itself. These observations lend credence to the theory that the depression zone was caused by a sediment-related phenomenon like consolidation or compaction of sediment and not fault-related. However, it is also possible that the bridge piles crossed the fault at depth, causing the piles to keep the entire structure on a single side of the fault and thus limiting damage and distortion of the bridge (e.g., Oettle and Bray, 2013).

Figure 9-28. The zone of depression viewed in several rice fields.

Figure 9-29. Road along which the detailed profile of cracks and offsets was measured.

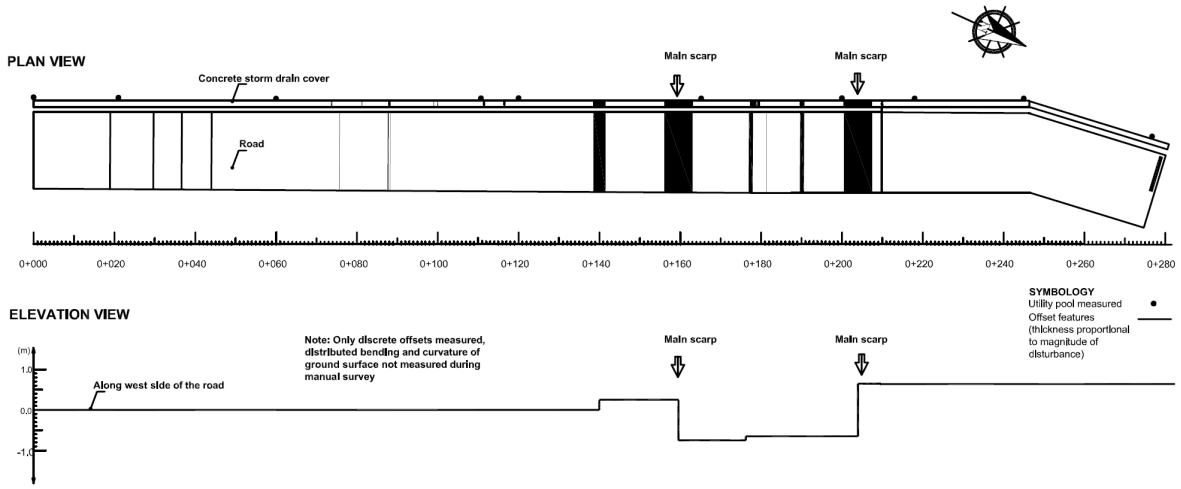

Figure 9-30. Profile of observed cracks and offsets along a road that crossed the depression zone, as measured by GEER.

Table 9-1. Observations of cracks and offsets along a road that crossed the depression zone.

Station	Horizontal Movements	Vertical Movements	Comments
0+000.00 (Lat: 32.95499 Long: 131.03763)	-	-	Initial point arbitrarily established southeast of the depression zone. No damage was noted southeast of this location.
0+019.19	1-2 mm extension crack in asphalt pavement	-	-
0+021.00	-	-	1° utility pole tilt toward 290° from north
0+029.60	New extension cracks in asphalt pavement	-	Utility crossing
0+036.70	2 mm extension crack in asphalt pavement	-	-
0+044.10	1-2 mm extension crack in asphalt pavement	-	-
0+060.00	-	-	1/2° utility pole tilt toward 60° from north
0+073.70	30 mm extension gap in concrete storm drain cover	-	-
0+075.20	4 mm extension crack in asphalt pavement	-	-
0+081.30	15 mm extension gap in concrete storm drain cover	-	
0+087.80	5 mm and 25 mm extension cracks in asphalt pavement	10 mm north-side down in concrete storm drain cover	-
0+098.70	10 mm extension gap in concrete storm drain cover	-	-
0+099.20	15 mm extension gap in concrete storm drain cover	-	-
0+110.70	-	-	1.5° utility pole tilt toward 20° from north
0+111.50	10 mm extension gap in concrete storm drain cover	-	-
0+116.50	8 mm extension gap in concrete storm drain cover	-	-
0+120.00	-	-	1° utility pole tilt toward 20° from north
0+140 (bounding edge of pop up block)	Left/Right-lateral offset not noted, 120 mm extension gap in concrete storm drain cover	200 mm to 300 mm north-side up	Pavement repaired
0+161 (main scarp forming the southeast side of depression zone)	**Minor left-lateral movement (10 mm to 20 mm), extension/compression not measured due to repairs and extent of disturbance**	**900 mm to 1100 mm north-side down**	**Pavement repaired**
0+165.20	-	-	2° utility pole tilt toward 100° from north
0+179	7 mm, 25 mm, 30 mm, and 60 mm extension gaps in concrete storm drain covers	100 mm north-side up	Pavement repaired
0+181.40	5 mm extension crack in asphalt pavement	-	-

0+190	130 mm extension gap in concrete storm drain cover	-	Pavement repaired
0+204 (main scarp forming the northwest side of depression zone)	**15 mm to 20 mm left-lateral offset, extension/compression not measured due to repairs and extent of disturbance**	**1200 mm to 1400 mm north-side up**	**Pavement repaired**
0+209.50	25 mm extension crack in asphalt pavement	10 mm north-side down	-
0+218.70	-	-	1/2° utility pole tilt toward 160° from north
0+246.11	-	-	1° utility pole tilt toward 165° from north
0+277.00	-	-	1° utility pole tile toward 60° from north.
0+279	Uncertain due to repairs	-	Pavement repaired on west side of road only. No new damage was observed northwest of this location.

Figure 9-31. One edge of the zone of depression caused a large grade change immediately adjacent to a residential structure.

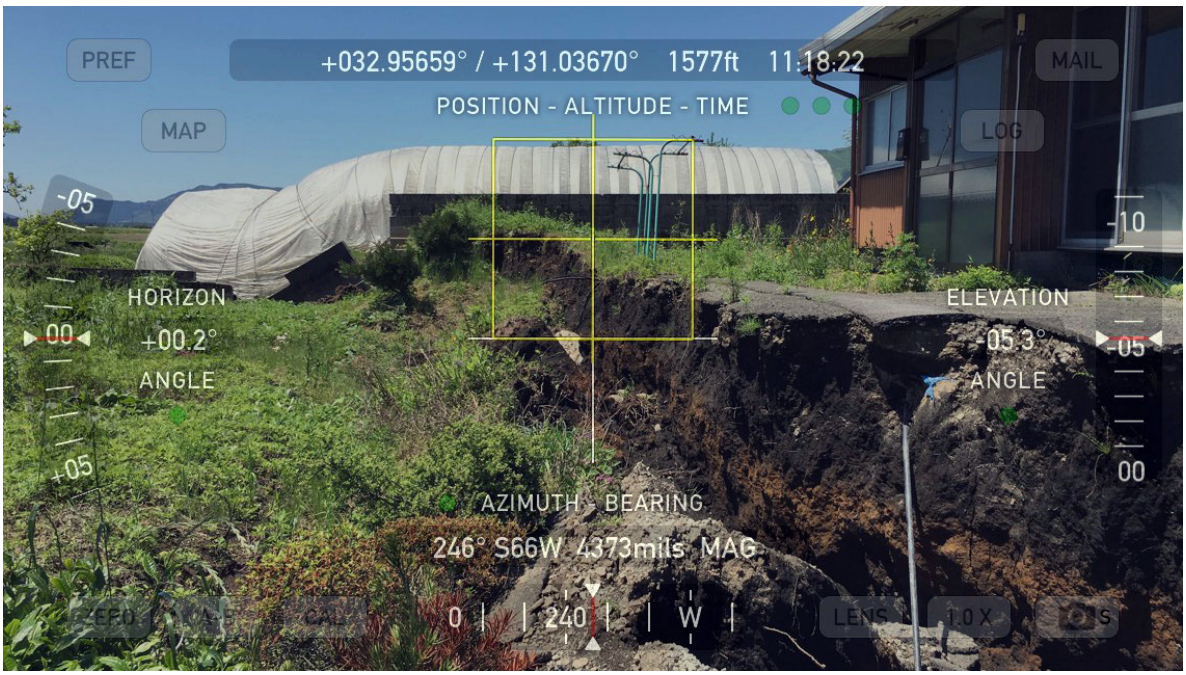

Figure 9-32. One edge of the zone of depression crosses next to a residential structure and beneath a greenhouse structure.

Figure 9-33. A bridge that spanned an edge of the depression zone (close to 32.9511°, 131.0275°).

Figure 9-34. No foundation settlement at the west bridge abutment located in the depression zone.

Figure 9-35. The depression zone crosses into a hill.

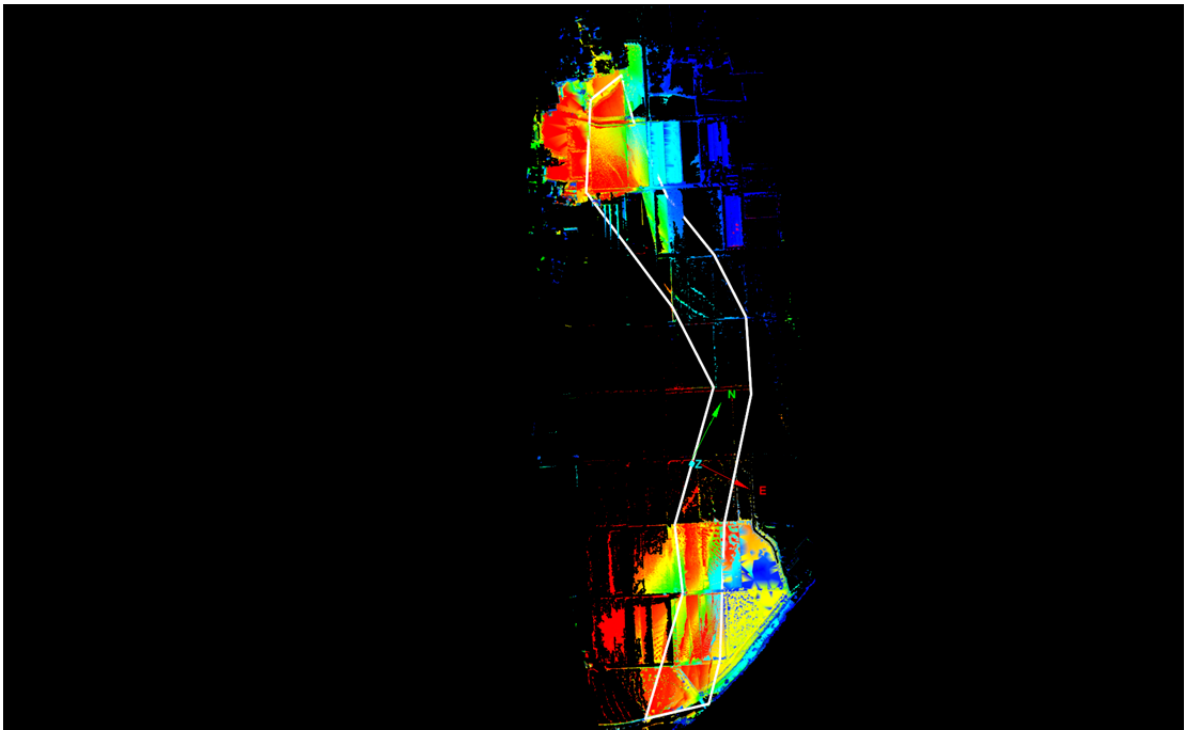

Figure 9-36. LIDAR data set from the Aso San depression zone. The white polygon defines the width of the fault zone captured with LIDAR (approximately 32.9511, 131.0275).

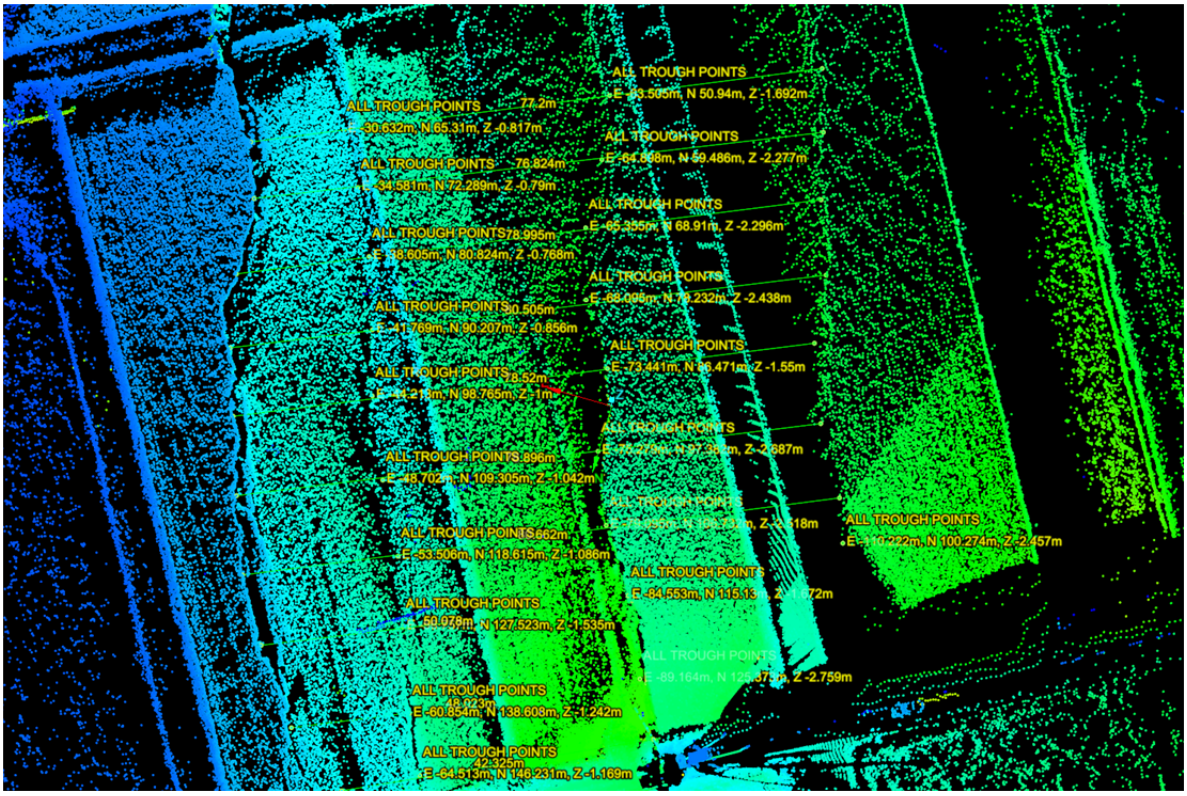

Figure 9-37. Measurements of varying graben width were performed at 10 m steps orthogonal to the axis of the graben. In this figure, the depression fissures on the west end of the LIDAR capture are clearly visible, as well as intermediate fissures that typically had vertical displacements less than 10 cm (approximately 32.9511, 131.0275).

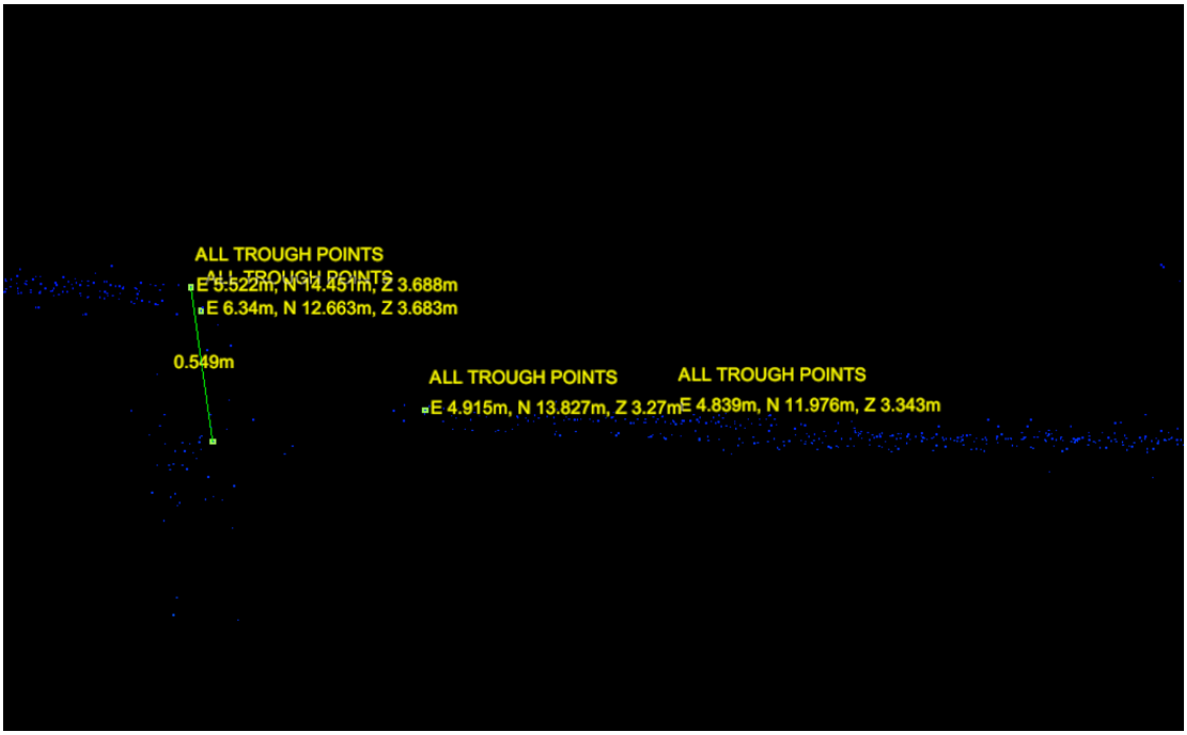

Figure 9-38. Example of fissure step-down measurement along the north side of the graben. Point query was used to determine the vertical elevation offset (approximately 32.9511, 131.0275).

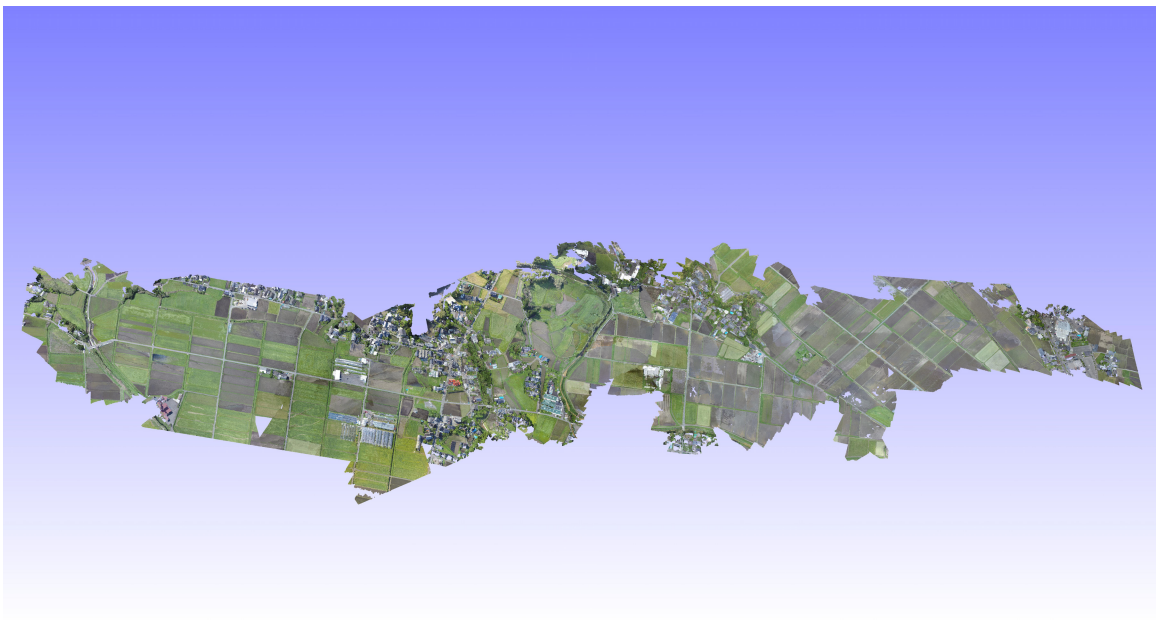

Figure 9-39. Screenshot of the stitched 3D point cloud model of the 4km reach of the (32.9511°, 131.0275) .

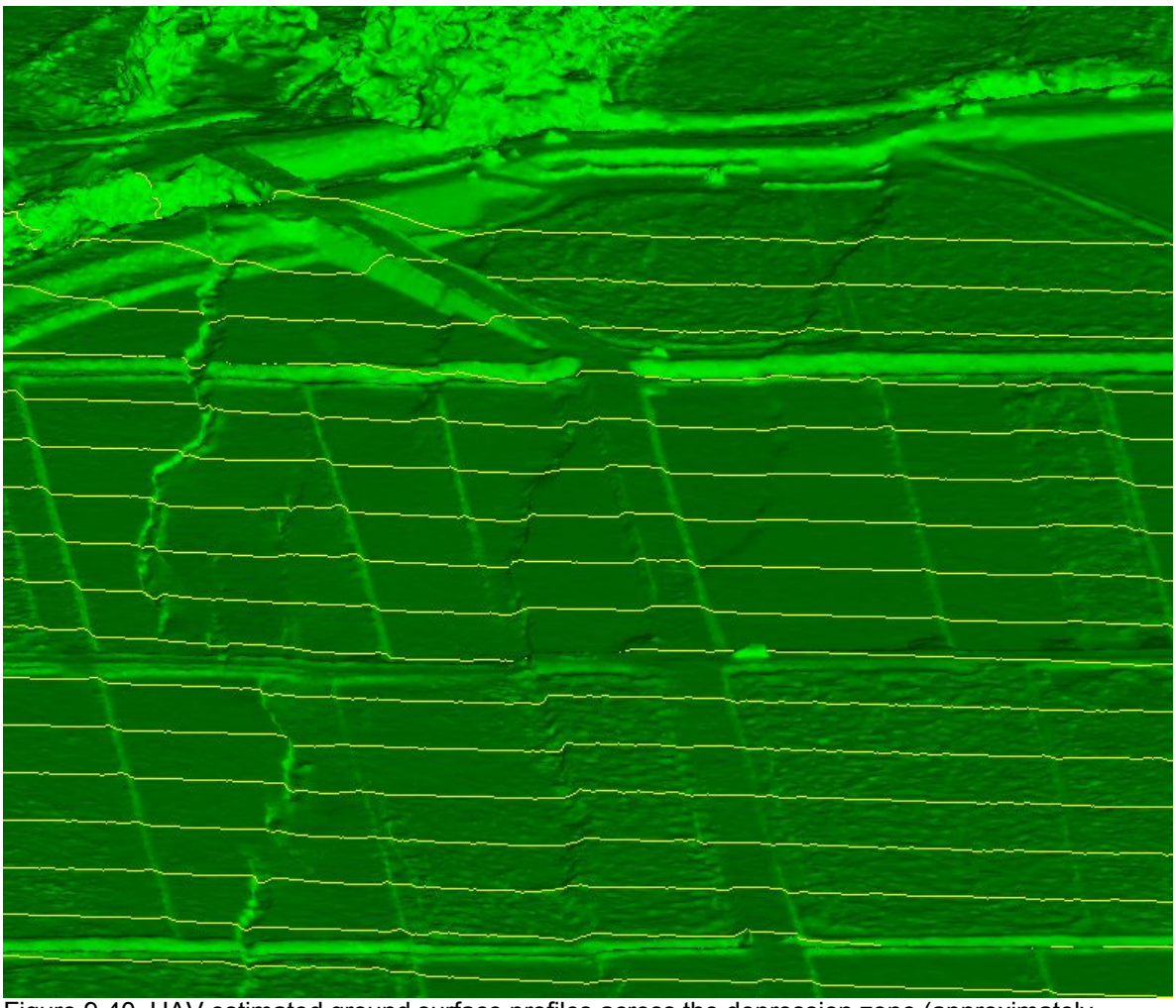

Figure 9-40. UAV estimated ground surface profiles across the depression zone (approximately 32.9511°, 131.0275).

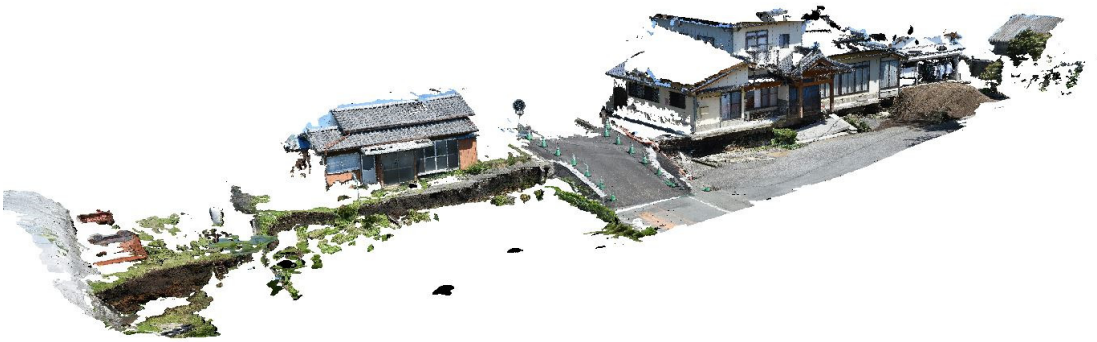

Figure 9-41. Screenshot of the 3D textured model of homes and road damaged by the depression zone (32.95663° N 131.03670° E). The model was developed from approximately 50 digital photographs captured with a Nikon D7100 DSLR camera.

Figure 9-42. Screenshot of a 3D textured model of a house damaged by the depression zone. The model was developed from approximately 50 digital photographs captured with a Nikon D7100 DSLR camera (32.95663° N 131.03670° E).

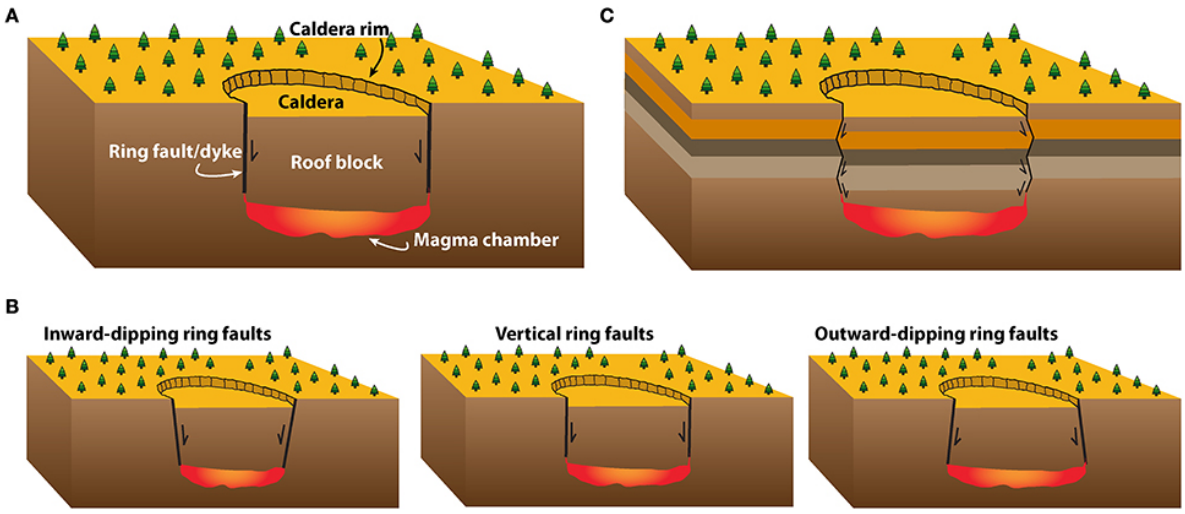

Figure 9-43. Various potential ring fault configurations (from Geyer and Marti, 2014).

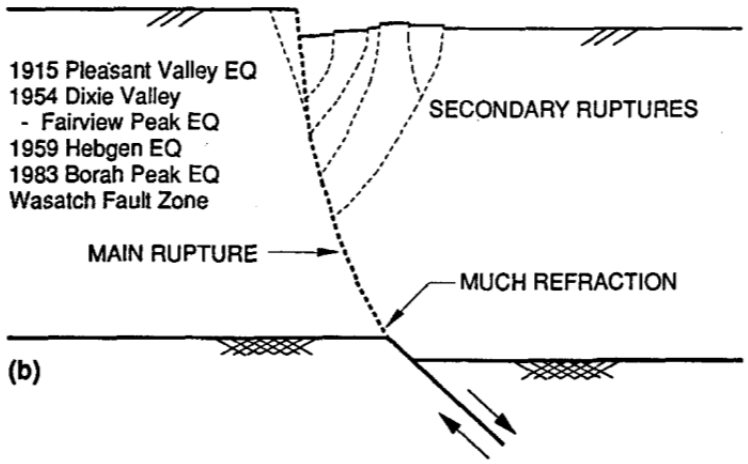

Figure 9-44. Possible mechanism of the depression zone formation, showing steepening of a normal fault through soil causing the formation of secondary, antithetic faults and a drop-down graben structure (from Bray et al., 1994).

9.3 Shimojin-Cho River Canal

9.3.1 Field Observations

In the zone where aerial LIDAR was recorded pre- and post-mainshock, one site was of particular importance for its potential use as a case history for fault rupture through levees and other embankments. At this site, two separate, conjugate strands of the Futagawa Fault converged and ruptured through a canal. Terrestrial LIDAR data was recorded here to capture the ground deformations across the canal as a result of surface fault rupture from the two fault strands (Figure 9-45). UAV video of this area, taken soon after the earthquake before repairs were done to the canal, is publically available from the Geospatial Information Authority of Japan (GSI, 2016).

The typical northeastern trending strand of the Futagawa Fault that ruptured through the canal had a typical right-lateral strike slip movement. The second, conjugate strand was left-lateral strike slip fault. This second strand appeared to be a link between a northern strand of the Futagawa Fault that was about 0.6 km north of the canal site and the strand of the Futagawa that ruptured through here. This link strand trended roughly northwest from the canal site (Figure 9-46). Both of the faults that ruptured through the levee here had significant vertical movement, causing the earth block bounded by the two fault strands (to the southwest of the canal) to popup. The southern Futagawa strand and the link formed at roughly a 50 to 60° angle, which is expected for a pair of conjugate strike-slip faults.

Globally, this set of conjugate faults occurred in an area just north of the Hinagu and Futagawa Fault intersection, in an area where the Futagawa Fault is changing strike to the east, and near where the two northern/southern strands of the Futagawa eventually converge into a single strand. Therefore, it is globally an area of complex tectonics.

The left-lateral strike slip fault had a measured movement of about 30 cm left lateral and 10 cm vertical, as measured where it crossed a concrete road. Measuring the right-lateral strike slip fault movement was difficult due to repair work done on the canal (Figure 9-47), so the LIDAR data is recommended for offset estimation. Several small offsets in the canal wall, likely caused by secondary faults, were observed away from the two primary strands at this location. Red stakes placed by others appear to mark the cracked locations of the canal walls.

Based on the GSI UAV video that shows the opposite side of the canal (Figure 9-45), which GEER did not visit, the left-lateral fault strand does not appear to extend to the other side of the canal. The continuation of the southern Futagawa strand on this side of the canal occurs as two subparallel strands which quickly converge again.

In the developed area just to the northeast of the canal, the fault appears to have ruptured between, or partially through, two structures below the road, but we could not investigate the structures in detail. The road repairs made it difficult to measure fault offsets here. The fault appeared to have gone through a stone retaining wall above this road; however, the wall does not appear to have been significantly damaged beyond small separations between individual stones (Figure 9-48).

9.3.2 LIDAR Analysis

Terrestrial LIDAR captured the main-strand right lateral fault rupture deformations through the stream levee, the left-lateral displacement to the north, and the general characteristics of the surface rupture passing through the adjacent field (Figure 9-49). The levee break occurs at a complex zone of fault interaction where two strands of the Futagawa Fault meet. It is expected that this zone will have complex structural fault splays as a result of stress interactions between these two strands. The main strand offsets were measured by placing target reflectors on the west sides of the offset of the west

side of the stream through the concrete levee, and to measure road offset on the east side of the stream.

The right-lateral horizontal offset was 66.5 cm and the vertical offset was 15 cm up to the north. Note that this offset is counter to the 'down-to-the-north' trend of much of the strike slip portion of the Futagawa Fault, nor the normal offset in the Aso San region. This offset may represent a pop-up block of soil. This offset of the levee is closely matched with the offsets observed in the surrounding agricultural field (57 cm horizontal offset and 28 cm vertical offset). Across the stream on the east bank, the horizontal offset is on average 1.0 m with a vertical offset of 13 cm. The offset zone of the northern left-lateral fault splay had a horizontal offset of 29 cm and a vertical step down-to-the-north of 13 cm. Width of the fault rupture zone was 3.9 m to 4.2 m near the river crossing.

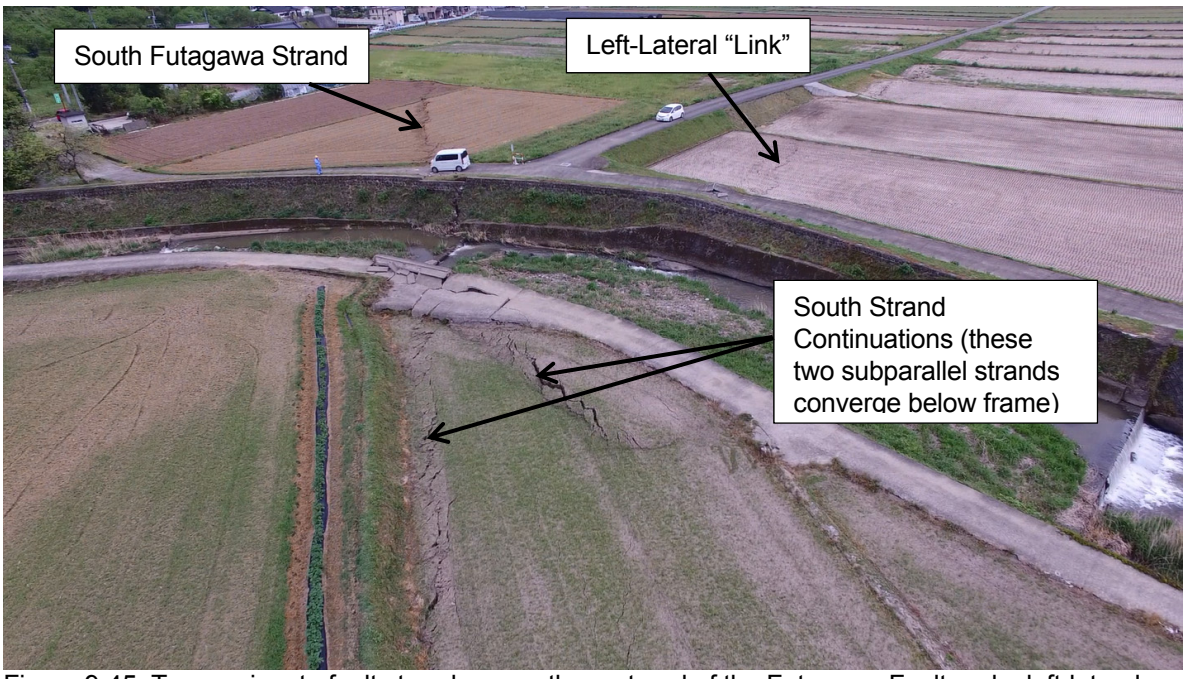

Figure 9-45. Two conjugate fault strands, a southern strand of the Futagawa Fault and a left-lateral link between a more northern strand of the Futagawa Faults (not shown, about 0.6 km north) and this southern strand, rupture through a canal. The link fault does not appear to continue to the other side of the canal (in the bottom of the photo). The south Futagawa strand in the bottom of the photo occurs as two subparallel strands that converge below the frame. This image is a still from UAV video provided by the Geospatial Information Authority of Japan (GSI, 2016).

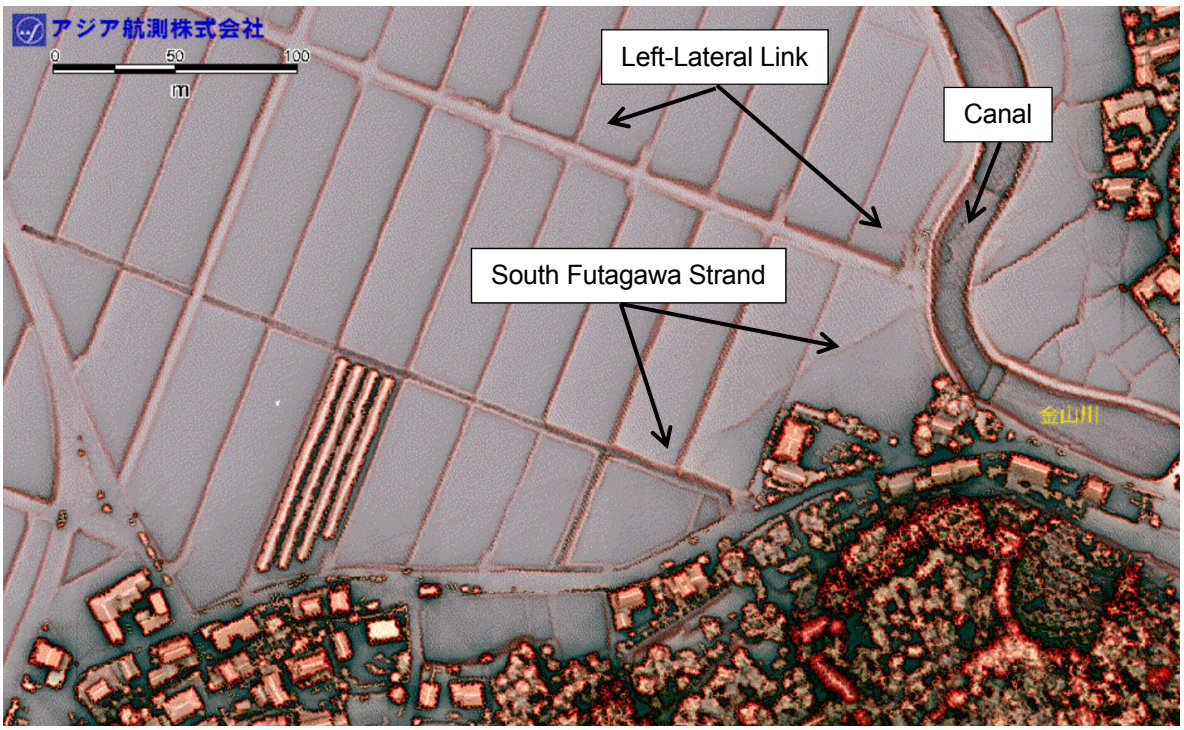

Figure 9-46. Aerial LIDAR of the canal area, showing differential movement from just before and just after the mainshock, from Asia Air Survey (2016).

Figure 9-47. Terrestrial LIDAR setup at the fault crossing of the canal. Vertical movement of the fault strands and the associated popup block can be seen in the photo. Repair work is evident at the location of the main southern strand fault crossing.

Figure 9-48. Fault rupture through a road and a retaining wall on the Futagawa Fault. No significant damage observed in the stone block retaining wall.

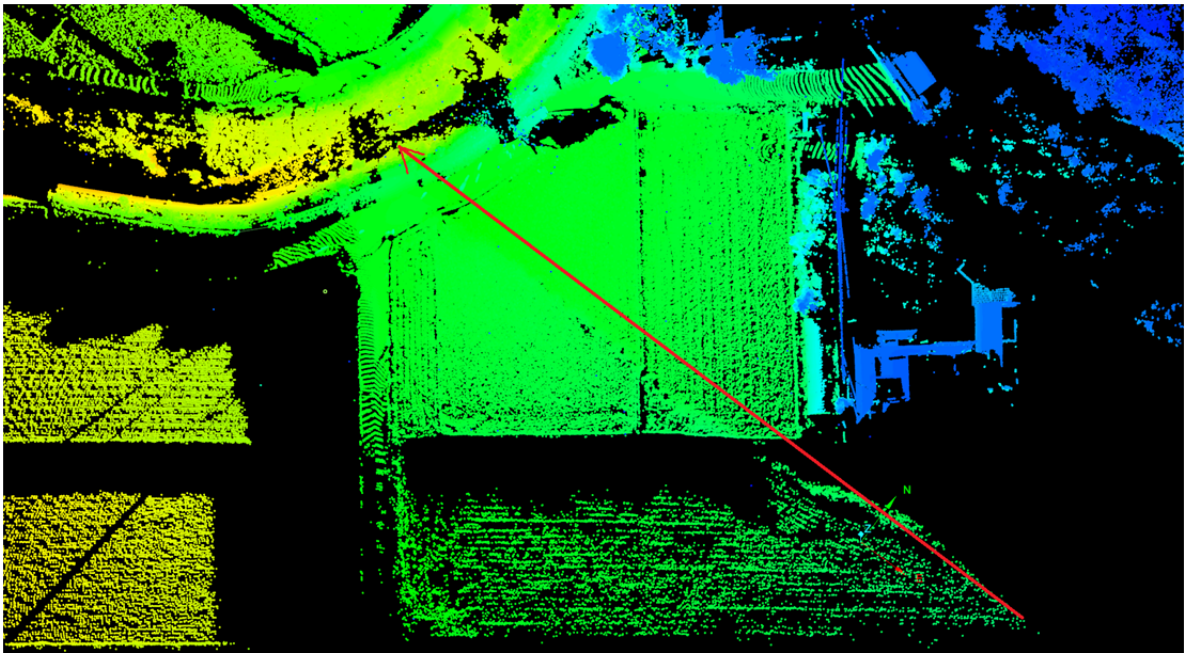

Figure 9-49. Projection of the main strand of the Futagawa fault from the southwest (lower right) to the northeast (upper left). The levee break occurs in the upper left portion of the image at the arrow tip (approximately 32.79731, 130.85361).

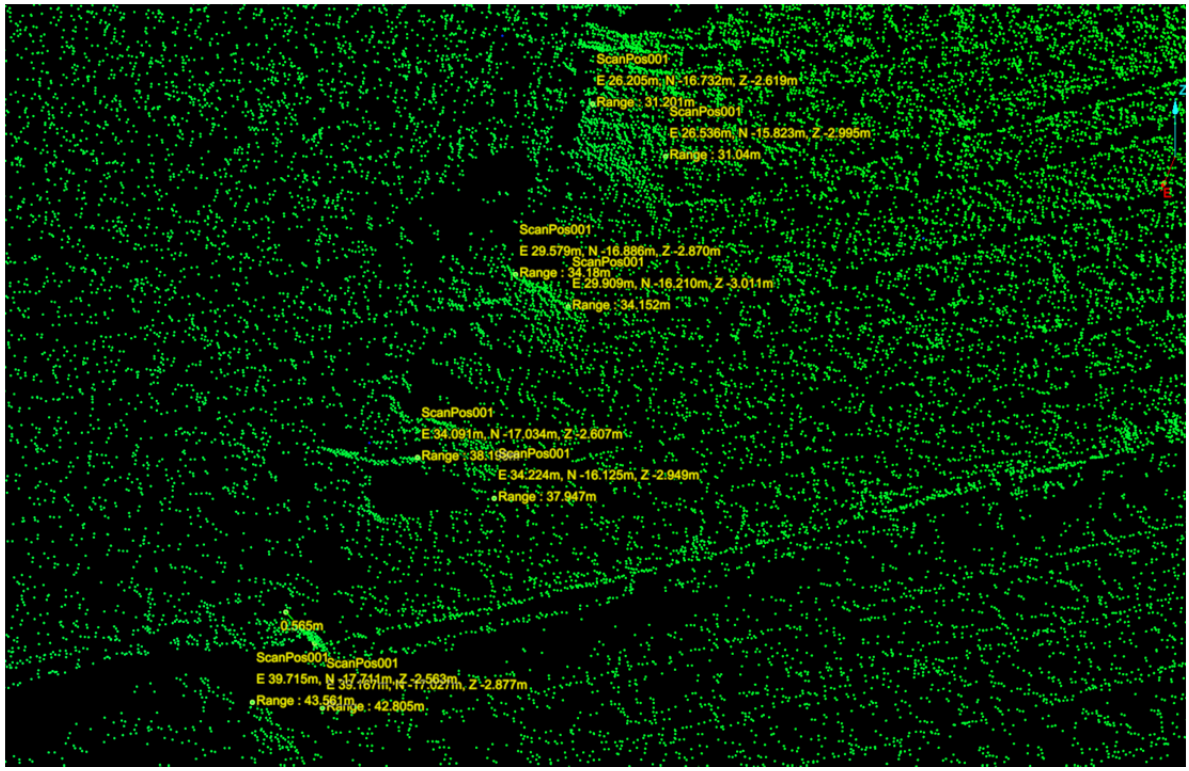

Figure 9-50. Example of measurement of horizontal offset (note offset in the plowed field) and vertical step of the Futagawa fault crossing an agricultural field (approximately 32.79731, 130.85361).

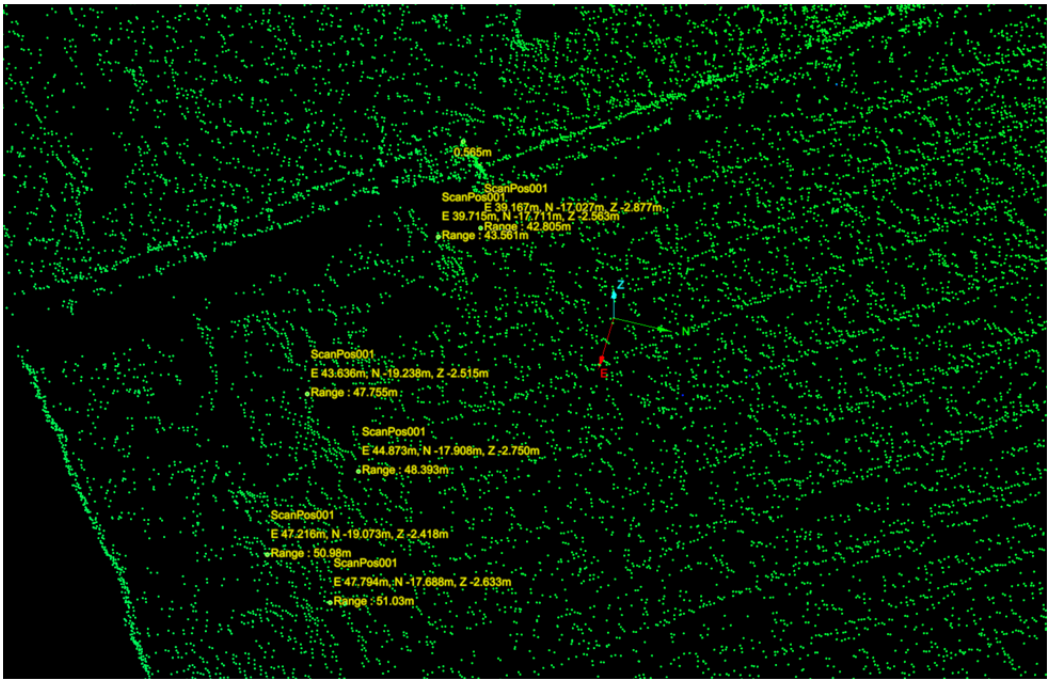

Figure 9-51. Example of measurement of horizontal offset (note offset in the plowed field) and vertical step of the Futagawa fault crossing an agricultural field (approximately 32.79731, 130.85361)

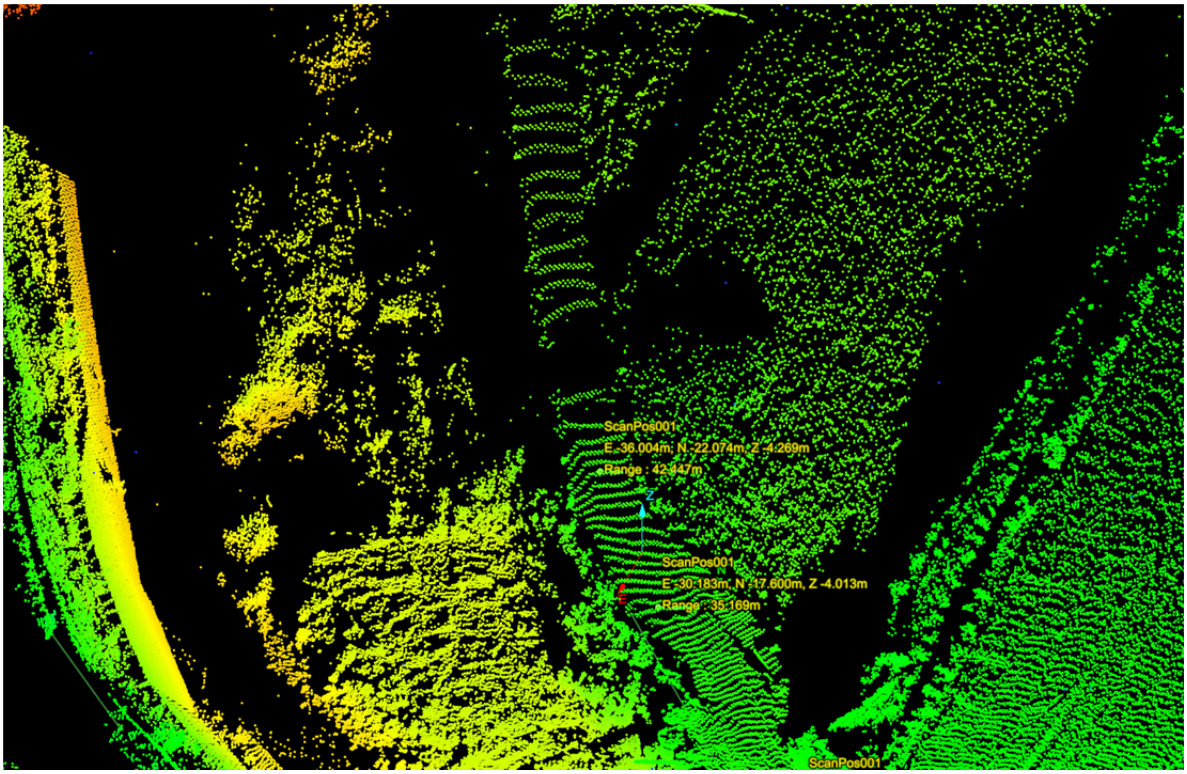

Figure 9-52. Road offset on the east side of the levee offset of the Futagawa fault (approximately 32.79731, 130.85361).

9.4 Zero-Displacement Lateral Spread

As mentioned earlier in the report, the GEER team was quite surprised at the lack of evidence of lateral spread during the Kumamoto earthquake sequence. Of particular interest to the engineering community would be a location where liquefaction is believed to have triggered, but no horizontal deformations occurred. These types of case histories have been referred to as zero-displacement lateral spread (Youd et al. 2009), and are generally lacking from most of the current empirical lateral spread databases.

We believe that a zero-displacement lateral spread may have occurred at the large highway bridge on Route 501 crossing the southern tributary of the Midorikawa River near Minamihashirikami (32.69389° N 130.64776° E). The bridge is shown in both Figure 9-53 and Figure 9-54. Investigation beneath the northern abutment of this bridge revealed very minor ground cracks and some small sand boils comprised of fine, dark sand as presented in Figure 9-55. No evidence of lateral spread was visible in the free-field around the bridge, but the existence of sand boils and minor cracking near the northern abutment suggests that at least one soil layer liquefied during the Kumamoto earthquake sequence. This bridge is located approximately 12 kilometers to the southwest of the epicenter of the main shock.

Japanese collaborators provided the GEER team with embankment designs for the Route 501 bridge site and generalized soil profiles that were used for the foundation design of the bridge. The generalized soil profiles show a 4-meter thick non-liquefiable soil cap consisting of soft silt underlain by a 4.5-meter thick sand layer with field SPT resistance of 8 blow counts per foot. Similarly, the generalized soil profile of the southern abutment of the bridge showed a 5.0-meter thick non-liquefiable layer consisting of soft silt, underlain by 2.5 meters of very loose sand with field SPT resistance of 1 blow count per foot. Investigation of the Japanese GIS boring database in the vicinity of the bridge (Geonews 2016) generally supports the generalized soil profiles, and suggests that thick (i.e., > 2 meters) layers of loose sandy material are common along the river bank adjacent to the bridge. All of this existing information and known topography of the site suggest that significant lateral spread displacements should have occurred in the vicinity of the bridge due to the loose sand layer underlying the non-liquefiable crust. However, no fines contents were indicated either on the publicly available soil borings or on the generalized soil profiles. We suspect that the fines content in the suspect sandy layers are quite high and likely limited the horizontal displacements due to its undrained shear strength. Only additional subsurface investigation at this site will be able to shed more light on this potentially important lateral spread displacement case history.

We also find it very interesting to better understand what contributed to the lateral spread displacement at the Route 232 bridge, as described in Section 6.3. We believe that it could be valuable to the engineering community to explore the differences between the Route 501 and the Route 232 bridge sites to understand what contributed to the stability of the former and the instability of the latter. We also believe that many more zero-displacement lateral spread case histories likely occurred during the Kumamoto earthquake sequence. The significant challenge associated with documenting these case histories will be identifying sites where we believe liquefaction triggered in the soil, but lateral displacements did not occur. With the help and collaboration of our Japanese colleagues, we may be able to identify more potential zero-displacement lateral spread case histories in the near future.

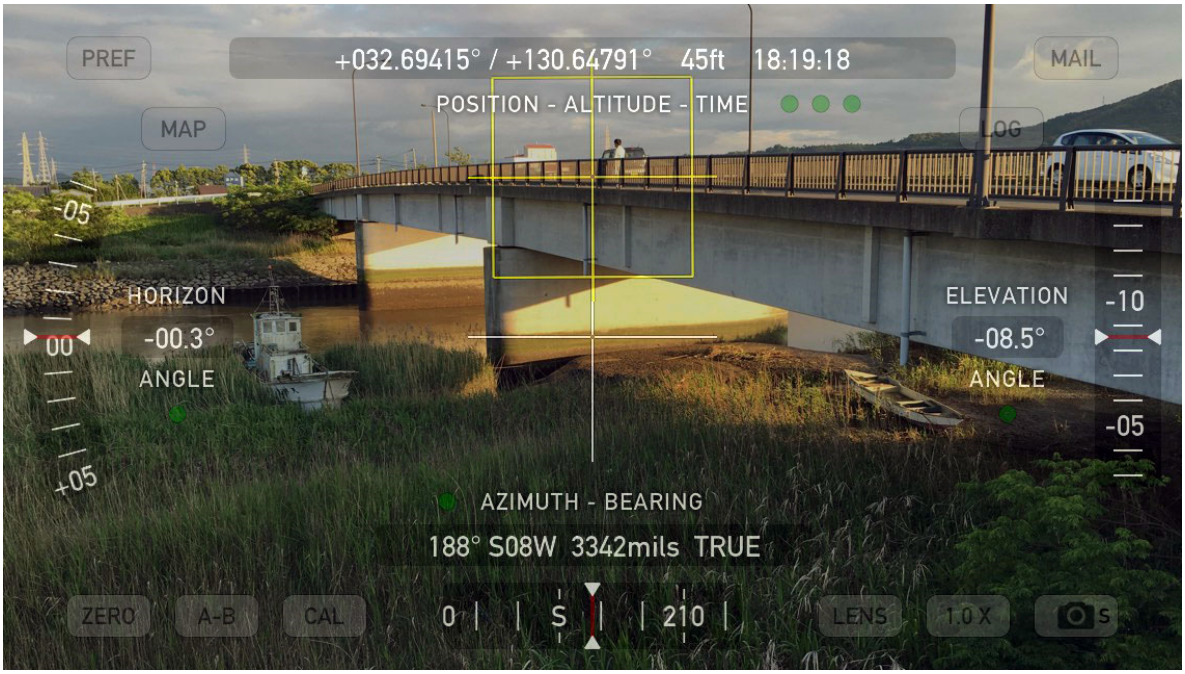

Figure 9-54. View of the Route 501 bridge looking to the south.

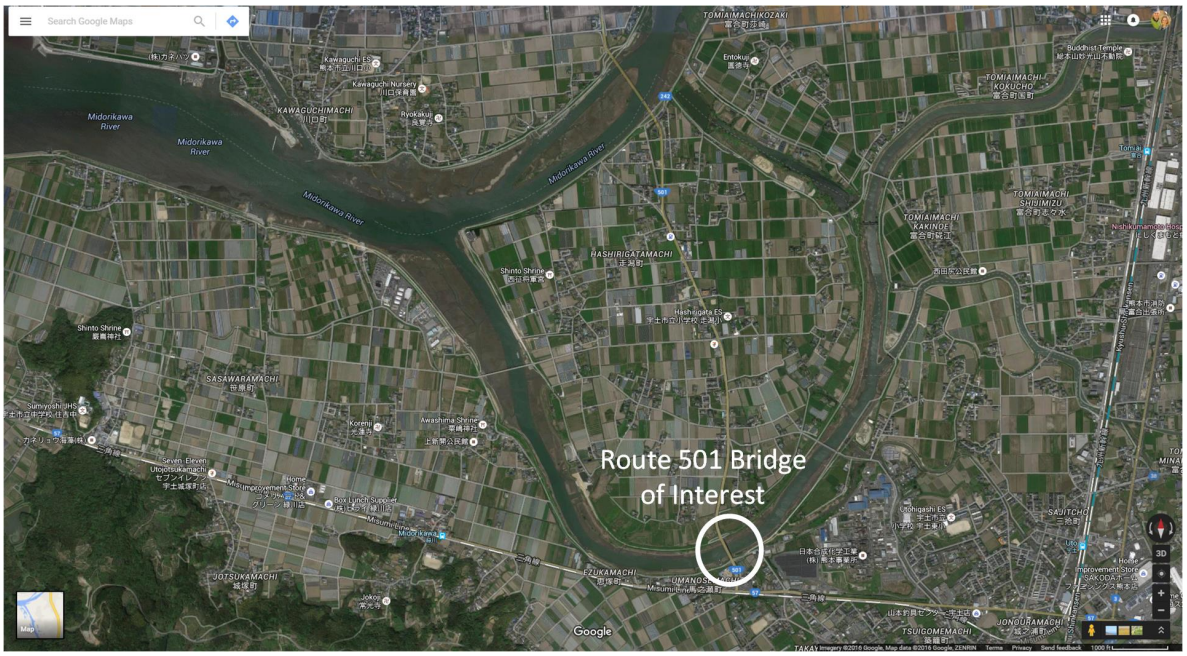

Figure 9-53. Overview map of Route 501 bridge, where we believe a zero-displacement lateral spread may have occurred.

Figure 9-55. Evidence of liquefaction beneath the northern abutment of the Route 501 bridge. No evidence of significant lateral spread was observed by the research team.

10.0 Conclusions

The 2016 Kumamoto earthquakes are a series of events that resulted in substantial damage to infrastructure, buildings, cultural heritage of Kumamoto Castle, roads and highways, slopes, and river embankments due to earthquake-induced landsliding and debris flows. Surface fault rupture produced offset and damage to roads, buildings, river levees, and an agricultural dam. Surprisingly, given the extremely intense earthquake motions, liquefaction occurred only in a few districts of Kumamoto City and in the port areas indicating that the volcanic soils were less susceptible to liquefying than expected given the intensity of earthquake shaking, a significant finding from this event.

Significant Case Histories: The primary objective of the GEER reconnaissance effort is the identification of important case histories that will likely be targets for future investigations that help develop methodologies to mitigate damage in future earthquakes. Important case histories identified by the participants from this earthquake included:

Surface Rupture: Oh-Kirihata Dam

An approximately 0.5-km long by 0.25-km wide water reservoir was ruptured by the main strand of the Futagawa Fault. The fault crossed the reservoir in two places, along the western flank of the reservoir, where the fault first crossed, and through the intersection of the spillway and the spillway outlet channel, on the northern side of the reservoir (Figure 9-1). Around nearly the entire reservoir bench, slope movements of 0.2 m to 0.5 m occurred. Complete slope failures of the reservoir bench and underlying slope occurred at two locations: just to the east of the spillway and on the eastern flank of the reservoir. The reservoir's gatehouse was significantly back tilted, rendering it inoperable.

The bench itself was highly distorted at the fault crossing, and the reservoir side slope below the bench was relatively intact, except that the riprap was disturbed (i.e., "dilated") as a result of shearing. The location at which the Futagawa Fault exited the reservoir was approximately between the spillway and the spillway outlet channel. Disturbance caused by the fault could be noted in the slopes below the spillway, again due to dilated riprap. The fault movement apparently caused failure of one of the spillway training walls. A secondary rupture apparently went through the right side of the spillway based on offsets recorded there.

Surface Rupture: Aso Caldera Depression Zone

The Futagawa surface fault rupture extended northeast into the southwestern corner of the Aso Caldera, a region of active volcanism. An approximately 10-km-long section of graben-structure ground movement, herein call the "depression zone", occurred coseismically, roughly projecting out from the point at which the Futagawa Fault ruptured into the caldera, up and to the northwestern end of the caldera. This depression zone ranged from 36-m to 106-m wide through the zone captured with LIDAR with near vertical offsets as large as 2.5 m at each end of the depression zone. Our interpretation is that this depression zone is likely caused by nearly vertical normal faulting on the caldera's ring fault, with a secondary fault (and hence the zone of depression) created as a result of the deep, soft soil profile in the caldera or as a result of underlying interaction with a ring dike or other deeper geological structure. Borings conducted by others prior to the earthquake in the caldera

indicate deep lake deposits, with very soft clay, reaching a void ratio of 5 to 7, and ranging in thickness between about 20 m to 70 m.

Surface Rupture: Shimojin-Cho River Canal

One site of importance as a case history was the Futagawa Fault rupture through a river levee and embankment at Shimojin District. At this site, two separate strands of the Futagawa Fault converged and ruptured through a canal. The northeastern trending strand of the Futagawa Fault that ruptured through the canal had the typical right-lateral strike-slip movement of this earthquake. The second strand was a left-lateral strike slip fault. This second strand appeared to be a link between a northern strand of the Futagawa Fault that was about 0.6 km north of the canal site and the strand of the Futagawa that ruptured through here.

Zero-Displacement Lateral Spread

Of particular interest to the engineering community would be a location where liquefaction is believed to have triggered, but no horizontal deformations occurred. These types of case histories have been referred to as zero-displacement lateral spread (Youd et al. 2009), and are generally lacking from most of the current empirical lateral spread databases.

We believe that a zero-displacement lateral spread may have occurred at the large highway bridge on Route 501 crossing the southern tributary of the Midorikawa River near Minamihashirikami (32.69389° N 130.64776° E). No evidence of lateral spread was visible in the free-field around the bridge, but the existence of sand boils and minor cracking near the northern abutment suggests that at least one soil layer liquefied during the Kumamoto earthquake sequence. This bridge is located approximately 12 kilometers to the southwest of the epicenter of the main shock.

Paucity of Liquefaction and Lateral Spread Features

Ground motions from both the April 14 event on the Hinagu fault and the April 16 7.0 event on the Futagawa fault exceeded 1g in Mashiki town and central Kumamoto. One important observation was the surprising lack of widespread and pervasive liquefaction and lateral spread failure of the ground given the intensity of these motions. Soil borings indicate that much of the alluvial plane is underlain by volcanic sand deposits. Why these did not liquefy in abundance is worthy of further investigation to understand what aspect of the soil structure has resisted liquefaction susceptibility and consequences in terms of excessive deformation. The regional source material for alluvium is the volcanic debris shed from Aso san caldera. It may be that a combination of grain angularity of the volcanic rock and shards, and the prevalence of highly plastic weathered clay from volcanic ash in the void space of the sands has produced a low-susceptibility soil for liquefaction. Soil borings inside Aso san indicate deep accumulations of high void ratio (Smectite) clays. Erosion of these materials and re-deposition in the Kumamoto plane may lead to depositions of dirty sands with a high plasticity fines fraction. A campaign of soil sampling with reliable SPT/CPT data where liquefaction was not observed would be warranted to better understand why the geo-spatial extent of liquefaction was limited.

11.0 References

Asia Air Survey (2016). “2016 Kumamoto Earthquake (English)”. http://www.ajiko.co.jp/article/detail/ID5725UVGCD/ Accessed on 05/28/2016.

Bray, J.D., Seed, R.B., Cluff, L.S., Seed, H.B., (1994). “Earthquake Fault Rupture Propagation through Soil.” *Journal of Geotechnical Engineering, ASCE.*

Chen, R., Branum, D.M., Willis, C.J., and Hill, D.P. (2014). “Scenario Earthquake Hazards for the Long Valley Caldera-Mono Lake Area, East-Central California, *US Geological Survey Open-File Report 2014-1045.*

Epstein, Woody; Takanao Nishimoto, Koji Okumura, Sam Swan, Peter Yanev, (2016). “The Kumamoto Earthquake Investigation: A Preliminary Report,” http://www.eqclearinghouse.org/2016-04-15-kumamoto/files/2016/04/The-Kumamoto-Earthquake-Investigation_-A-Preliminary-Report.pdf Accessed on 05/28/16.

Fichtner, A., and Tkalcic, H. (2010). “Insights into the Kinematics of a Volcanic Caldera Drop: Probabilistic Finite-Source Inversion of the 1996 Bardarbunga, Iceland, Earthquake.” *Earth and Planetary Science Letters.*

Geonews, (2016). 2016 Kumamoto earthquake reconstruction assistance boring log emergency public site (平成28年（2016年）熊本地震 復興支援 ボーリング柱状図 緊急公開サイト). http://geonews.zenchiren.or.jp/api/2016KumamotoEQ/index.html. Created on 04/16/2016. Last updated on 05/23/2016. Accessed on 05/27/2016.

Geyer, A., and Marti, J. (2014). “A short review of our current understanding of the development of ring faults during collapse caldera formation.” *Frontiers in Earth Science.*

Goldman, R.T., Albright, J.A., and Grosfils, E.B. (2015). “Ring Fault and Caldera Formation: Insights Provided by Three-Dimensional Elastic Finite Element Models.” *46th Lunar and Planetary Science Conference.*

Goto, H. (2016). 2016 Kumamoto Earthquake. Report submitted to DPRI, Kyoto University, Japan.

GSI (2016). “平成２８年熊本地震に関する情報”. Geospatial Information Authority of Japan, http://www.gsi.go.jp/BOUSAI/H27-kumamoto-earthquake-index.html Accessed on 05/28/2016.

GSJ (2016a). “Report 3 (April 22, 2015): Emergency Survey Report”. Geological Survey of Japan, AIST, http://g-ever.org/updates/?p=334 Accessed on 05/28/2016.

GSJ (2016b). “「第四報」 緊急現地調査報告 [2016年5月13日]
2016年熊本地震に伴って出現した地表地震断層”. Geological Survey of Japan, AIST, https://www.gsj.jp/hazards/earthquake/kumamoto2016/kumamoto20160513-1.html Accessed on 05/28/2016.

GSJ (2016c). “GEOLOGICAL MAP OF ASO VOLCANO 1:50,000.” Geological Survey of Japan, AIST.

GSJ (2016d). “Seamless Geologic Map of Japan”. Geological Survey of Japan, AIST, https://gbank.gsj.jp/seamless/seamless2015/2d/index.html?lang=en Accessed on 06/01/2016.

Hoshizumi, H., Ozaki, M., Miyazaki, K., Matsuura, H., Toshimitsu, S., Uto, K., Uchiumi, S., Komazawa, M., Hiroshima, T., and Sudo, S. (2004). *Geological Map of Japan 1:200,000, Kumamoto.* Geological Survey of Japan, AIST.

IRIS (2016) Web link: https://www.iris.edu/hq/files/programs/education_and_outreach/retm/tm_160415_japan/160415_japan.pdf

Ishizaka et al. (1975). “The Quaternary Research [Tokyo], vol. 34: https://www.jstage.jst.go.jp/article/jaqua1957/34/5/34_5_335/_pdf

Japan Asia Group (2016). “災害調査活動への取り組み”. http://www.kkc.co.jp/service/bousai/csr/disaster/201604_kumamoto/index.html Accessed on 05/28/2016.

Japan Water Works Association, (2014). “Water Statistics: FY2013.” Report No. 96.

Japanese Geotechnical Society, (2016). “Disaster report of the 2016 Kumamoto earthquake” [preliminary report] (地盤工学会 平成28年熊本地震 災害報告[速報版])”, https://www.jiban.or.jp/images/somufile/H28kumamoto_%20jishinsaigai_sokuho20160418-3.pdf (retrieved: 05/26/2016).

Jitousono, T., Shimokawa, E. and Teramoto, Y. (2008). “Debris Flow Induced by Deep-Seated Landslides at Minamata City, Kumamoto Prefecture, Japan in 2003.” *International Journal of Erosion Control Engineering.*

Konagai, K., Kiyota, T., Shiga, M., Tomita, H., Okuda, H., and Kajihara, K. (2016). “Ground fissures that appeared in Aso Caldera Basin in the 2016 Kumamoto Earthquake, Japan.” *JSCE Journal of Disaster FactSheets, FS2016-E-0003.*

Kyushu Electric Power Co. News & Announcements. http://www.kyuden.co.jp/notice_160416.html. Accessed 05/29/2016.

Mizuyama, T. (2008). “Structural Countermeasures for Debris Flow Disasters.” *International Journal of Erosion Control Engineering.*

Murai, Shusuke. (2016) “Connectivity, news and social media become crucial lifelines in quake-hit areas.” Japan Times http://www.japantimes.co.jp/news/2016/04/15/national/connectivity-news-and-social-media-become-crucial-lifelines-in-quake-hit-areas/#.V09yx5ErJhE. Accessed 05/21/2016.

Nagata, Tsutomu, (2015). “Introduction of Kumamoto City, Home of the Richest Groundwater in Japan: To our Asian Neighbors.” Water Conservation Section, Kumamoto City. http://www.wepa-db.net/pdf/0810forum/paper25.pdf Accessed on 05/26/16

NZSEE (2016). “Learning from Earthquakes Mission: Kumamoto Earthquake 2016, Japan.” In-Country Report No 2 of 14th May 2016, *New Zealand Society for Earthquake Engineering Inc.*

Oettle, N.K., and Bray, J.D. (2013). “Geotechnical Mitigation Strategies for Earthquake Surface Fault Rupture.” *Journal of Geotechnical and Geoenvironmental Engineering, ASCE.*

Sidle, R.C., and Chigira, M. (2004). “Landslides and Debris Flows Strike Kyushu, Japan.” *EOS*, Transactions, American Geophysical Union.

Swan, Sam. (2016). An Overview of the Kumamoto Earthquake Sequence. Acceptable Risk LLC. http://www.eqclearinghouse.org/2016-04-15-kumamoto/files/2016/04/The-Kumamoto-Earthquake-Investigation_-A-Preliminary-Report.pdf Accessed on 05/28/16.

Wang, C., Esaki, T., Xie, Mowen, and Qiu, C. (2006). “Landslide and Debris-Flow Hazard Analysis and Prediction using GIS in Minamata–Hougawachi Area, Japan.” *Environmental Geology.*

Yamao, M., Sidle, R.C., Gomi, T., and Imaizumi, F. (2016). “Characteristics of Landslides in Unwelded Pyroclastic Flow Deposits Southern Kyushu, Japan.” *Natural Hazards and Earth Systems Sciences.*

Appendix A

Geologic Maps of the Kumamoto Region, Kyushu

Hideo HOSHIZUMI, Masanori OZAKI, Kazuhiro MIYAZAKI, Hirohisa MATSUURA, Seiichi TOSHIMITSU, Kozo UTO, Shigeru UCHIUMI, Masao KOMAZAWA, Toshio HIROSHIMA and Sadahisa SUDO (2004) NI-52-11 20 万分の1地質図幅「熊本」 GEOLOGICAL MAP OF JAPAN 1:200,000, KUMAMOTO, Geological Survey of Japan, AIST. [next page].

and

GEOLOGICAL MAP OF ASO VOLCANO 1:50,000, Geological Survey of Japan, AIST. [second page].

地質図編集：星住英夫・尾崎正紀・宮崎一博・松浦浩久・
利光誠一・宇都浩三・内海　茂，　平成10 -12, 15年
重力編集：駒澤正夫・広島俊男，　平成15年
鉱床分布編集：須藤定久，　平成15年

熊　本　　KUMAMOTO

Compiled by Hideo Hoshizumi, Masanori Ozaki, Kazuhiro Miyazaki, Hirohisa Matsuura,
Seiichi Toshimitsu, Kozo Uto and Shigeru Uchiumi for geology in 1998-2000, 2003
by Masao Komazawa and Toshio Hiroshima for gravity in 2003
by Sadahisa Sudo for mineral deposits in 2003

GEOLOGICAL MAP OF JAPAN 1:200,000,
KUMAMOTO

1:200,000　　等高線間隔は100m

5　0　5　10　15　20km

GEOLOGICAL SURVEY OF JAPAN, AIST　©　2004
AIST03-G06040

		埋立地及び干拓地 Reclaimed land	r	
完新世 Holocene	H	沖積層 Alluvium	a	礫，砂及び泥 Gravel, sand and mud
後期更新世 Late Pleistocene	Q3	低位段丘堆積物 Lower terrace deposits	tl	礫，砂及び泥 Gravel, sand and mud
	Q3	中位段丘堆積物 Middle terrace deposits	tm	礫，砂及び泥 Gravel, sand and mud
	Q3	高位段丘堆積物 Higher terrace deposits	th	礫，砂及び泥 Gravel, sand and mud
	Q	火山麓扇状地堆積物 Volcanic fan deposits	vf	礫，砂及び泥 Gravel, sand and mud
完新世 Holocene	Q	雲仙火山 Unzen volcano　新期雲仙火山 Younger Unzen volcano 1991-95年土石流堆積物 Lahar deposits (1991-95A.D.)	U_{4d}	角閃石デイサイト火山灰，火山礫及び火山角礫 Hornblende dacite ash, lapilli and block
	Q3	1991-95年火砕流堆積物 Pyroclastic flow deposits (1991-95A.D.)	U_{4p}	角閃石デイサイト火山灰，火山礫及び火山角礫 Hornblende dacite ash, lapilli and block
	Q3	1991-95年溶岩ドーム Lava dome (1991-95A.D.)	U_4	角閃石デイサイト溶岩 Hornblende dacite lava
	Q	火山麓扇状地堆積物 Volcanic fan deposits	U_{3d}	角閃石デイサイト-安山岩火山灰，火山礫及び火山角礫 Hornblende dacite to andesite ash, lapilli and block
後期更新世 Late Pleistocene	Q3	火砕流及び岩屑なだれ堆積物 Pyroclastic flow and debris avalanche deposits	U_{3p}	角閃石デイサイト-安山岩火山灰，火山礫及び火山角礫 Hornblende dacite to andesite ash, lapilli and block
	Q3	溶岩 Lava	U_3	角閃石デイサイト-安山岩溶岩 Hornblende dacite to andesite lava
中期更新世 Middle Pleistocene	Q2	古期雲仙火山 Older Unzen volcano　後期 Late Stage 火砕流及び火山麓扇状地堆積物 Pyroclastic flow and volcanic fan deposits	U_{2p}	角閃石デイサイト-安山岩火山灰，火山礫及び火山角礫 Hornblende dacite to andesite ash, lapilli and block
	Q2	溶岩 Lava	U_2	角閃石デイサイト-安山岩溶岩 Hornblende dacite to andesite lava
	Q2	前期 Early Stage 火砕流及び火山麓扇状地稚積物 Pyroclastic flow and volcanic fan deposits	U_{1p}	角閃石デイサイト火山灰，火山礫及び火山角礫（軽石を含む） Hornblende dacite to ash, lapilli and block with pumice
	Q2	溶岩 Lava	U_1	角閃石デイサイト溶岩 Hornblende dacite lava
後期更新世 Late Pleistocene	Q3	久木野層 Kugino Formation	Kg	砂，泥及び礫，軽石を伴う Sand, mud and gravel with pumice
	Q3	阿蘇火山 Aso volcano 中央火口丘群 Central cones	Acf	デイサイト-流紋岩溶岩及び火砕岩 Dacite to rhyolite lava and pyroclastic rocks
	Q3		Acb	玄武岩-安山岩溶岩及び火砕岩 Basalt to andesite lava and pyroclastic rocks
	Q3	阿蘇-4火砕流椎積物 Aso-4 Pyroclastic Flow Deposits	A_4	角閃石デイサイト溶結凝灰岩，及び非溶結のガラス火山灰及び軽石 Hornblende dacite welded tuff and non-welded deposit of vitric ash and pumice
	Q3	大峰火山 Omine volcano	Ao	輝石デイサイト溶岩及び火砕岩 Pyroxene dacite lava and pyroclastic rocks
	Q3	阿蘇-3火砕流椎積物 Aso-3 Pyroclastic Flow Deposits	A_3	角閃石安山岩-デイサイト溶結凝灰岩，及び非溶結のガラス火山灰，スコリア及び軽石 Hornblende andesite to dacite welded tuff and non-welded deposit of vitric ash, scoria and pumice
中期更新世 Middle Pleistocene	Q2	赤井火山 Akai volcano	Aa	輝石デイサイト溶岩及び火砕岩 Pyroxene dacite lava and pyroclastic rocks
	Q2	阿蘇-1及び阿蘇-2火砕流椎積物 Aso-1 and Aso-2 Pyroclastic Flow Deposits	A_{21}	角閃石デイサイト-安山岩溶結凝灰岩，及び非溶結のガラス火山灰，スコリア及び軽石 Hornblende dacite to andesite welded tuff and non-welded deposit of vitric ash, scoria and pumice
	Q2	長洲層 Nagasu Formation	Ng	砂，泥及び礫，軽石を伴う Sand, mud and gravel with pumice
	Q2	大野流紋岩及び相当層 Ōno Rhyolite and its equivalent	Or	角閃石流紋岩-デイサイト溶岩 Hornblende rhyolite to dacite lava
	Q2	先阿蘇火山岩類及び塔ノ坂安山岩 Pre-Aso Volcanic Rocks and Tōnosaka Andesite	Kr	安山岩溶岩及び火砕岩 Andesite lava and pyroclastic rocks
	Q2	諏訪池玄武岩及び相当層 Suwanoike Basalt and its equivalent	Vs	玄武岩溶岩及び火砕岩 Basalt lava and pyroclastic rocks
	Q2	芳野層及び口之津層群北有馬層 Yoshino Formation and Kuchinotsu Group Kitaarima Formation	Yo	シルト，砂及び礫 Silt, sand and gravel
	Q2	金峰火山 Kimbō volcano 新期噴出物（一ノ岳火山岩） Late Stage Products (Ichinodake Volcanic Rock)	K_3	安山岩溶岩及び火砕岩 Andesite lava and pyroclastic rocks
	Q2	中期噴出物（ニノ岳及び三ノ岳火山岩類） Middle Stage Products (Ninodake and Sannodake Volcanic Rocks)	K_2	安山岩溶岩及び火砕岩 Andesite lava and pyroclastic rocks
	Q	土石流堆積物（一部火砕流堆積物を伴う） Lahar deposits with pyroclastic flow deposits	Kf	礫，砂，泥及び火砕岩 Gravel, sand, mud and pyroclastic rocks
前期更新世 Early Pleistocene	Q1	古期噴出物（古金峰，松尾火山岩類及び石神山火山岩類） Early Stage Products (Ko-kimbō, Matsuo and Ishigamiyama Volcanic Rocks)	K_1	玄武岩溶岩及び火砕岩 Basalt lava and pyroclastic rocks
中期更新世 Middle Pleistocene	Q2	多良岳火山 Taradake volcano 新期安山岩 Late Stage Andesite	T_4	安山岩-デイサイト溶岩及び火砕岩 Andesite to dacite lava and pyroclastic rocks
	Q2	新期玄武岩 Late Stage Basalt	T_3	玄武岩-安山岩溶岩及び火砕岩 Basalt to andesite lava and pyroclastic rocks
前期更新世 Early Pleistocene	Q1	古期安山岩 Early Stage Andesite	T_2	安山岩-デイサイト溶岩及び火砕岩 Andesite to dacite lava and pyroclastic rocks
	Q1	古期玄武岩及び郡川火山岩類 Early Stage Basalt and Kōrigawa Volcanic Rocks	T_1	玄武岩-安山岩溶岩及び火砕岩 Basalt to andesite lava and pyroclastic rocks
	Q1	今市火砕流堆積物 Imaichi Pyroclastic Flow Deposits	I	輝石デイサイト溶結凝灰岩 Pyroxene dacite welded tuff
	Q1	耶馬溪火砕流堆積物 Yabakei Pyroclastic Flow Deposits	Yb	角閃石デイサイト溶結凝灰岩，一部非溶結のガラス火山灰及び軽石 Hornblende dacite welded tuff, partly non-welded deposit of vitric ash and pumice
	Q1	山甲川流紋岩及び五馬市デイサイト Yamakōgawa Rhyolite and Itsumaichi Dacite	Yr	流紋岩-デイサイト溶岩及び火砕岩 Rhyolite to dacite lava and pyroclastic rocks
	Q1	口之津層群西正寺層及び加津佐層 Kuchinotsu Group Saishōji and Kazusa Formations	Kc	シルト，砂及び礫 Silt, sand and gravel
	Q	有喜火山岩類，南串山火山岩類，上滴水安山岩及び大岳火山岩類 Uki Volcanic Rocks, Minamikushiyama Volcanic Rocks, Kamitarumizu Andesite and Ōtake Volcanic Rocks	Ukv	火山砕屑岩，礫，砂及び泥 Volcaniclastic rocks, gravel, sand and mud
	Q1		Uk	安山岩溶岩及び火砕岩 Andesite lava and pyroclastic rocks
新第三紀 Neogene　後期鮮新世 Late Pliocene	N3	日岳玄武岩 Hidake Basalt	Hb	玄武岩溶岩及び火砕岩 Basalt lava and pyroclastic rocks
	N3	武雄流紋岩，中間流紋岩及び相当層 Takeo Rhyolite, Nakama Rhyolite and their equivalent	Rt	流紋岩溶岩，貫入岩を伴う Rhyolite lava with intrusive rocks
	N3	吉ノ本安山岩，渡神岳火山岩類及び相当層 Yoshinomoto Andesite, Togamidake Volcanic Rocks and their equivalent	Ys	安山岩-デイサイト溶岩及び火砕岩 Andesite to dacite lava and pyroclastic rocks
	N3	釈迦岳火山岩類及び相当層 Shakadake Volcanic Rocks and their equivalent	Sh	安山岩溶岩及び火砕岩 Andesite lava and pyroclastic rocks
前期鮮新世 Early Pliocene	N3	久留米層及び黒木層 Kurume and Kuroki Formations	K	泥岩，砂岩及び礫岩（褐炭及び火山灰層の薄層を挟む） Mudstone, sandstone and conglomerate with thin beds of lignite and ash
	N3	井備ノ尾岳安山岩 Ibinoodake Andesite	Ib	安山岩溶岩及び火砕岩 Andesite lava and pyroclastic rocks
	N3	上虎口玄武岩及び相当層 Kamikoku Basalt and its equivalent	Bk	玄武岩溶岩 Basalt lava
	N3	中津江ひん岩 Nakatsue Porphyrite	Np	輝石ひん岩 Pyroxene porphyrite
	N3	鯛生層群及び前津江累層 Taio Group and Maetsue Formation	Ta	安山岩溶岩及び火砕岩（デイサイト火砕岩，礫岩，砂岩及びシルト岩を伴う） Andesite lava and pyroclastic rocks with dacite pyroclastic rocks, conglomerate, sandstone and siltstone
鮮新世 Pliocene	N3	先多良岳安山岩類 Pre-Taradake Andesites	Tp	安山岩溶岩及び火砕岩 Andesite lava and pyroclastic rocks
後期中新世 Late Miocene	N2	北松浦玄武岩類及び相当層 Kitamatuura Basalts and their equivalent	Mb	玄武岩溶岩及び火砕岩 Basalt lava and pyroclastic rocks
	N2		Ma	安山岩-デイサイト溶岩及び火砕岩 Andesite to dacite lava and pyroclastic rocks
中新世 Miocene	N1-2	杵島地域の変質安山岩 Altered andesite of Kishima district	an	変質安山岩 Altered andesite
古第三紀 Paleogene　前期漸新世 Early Oligocene	PG4	杵島層群（杵島層を除く） Kishima Group, except Kishima Formation	P_5	砂岩，砂岩泥岩互層，泥岩及びデイサイト凝灰岩 Sandstone, interbedded mudstone and sandstone, mudstone and dacite tuff
	PG3	杵島層及びその相当層 Kishima Formation and its equivalent	P_4	砂岩及び泥岩（礫岩及び石炭の薄層を挟む） Sandstone and mudstone with thin beds of conglomerate and coal
	PG3	相知層群及びその相当層 Ōchi Group and its equivalent	P_3	砂岩，泥岩，礫岩及び石炭（凝灰岩の薄層を挟む） Sandstone, mudstone, conglomerate and coal with thin beds of tuff
後期始新世 Late Eocene	PG3	万田層群及びその相当層 Manda Group and its equivalent	P_2	砂岩泥岩互層，砂岩及び泥岩（石炭の薄層を挟む） Interbedded mudstone and sandstone, sandstone and mudstone with thin beds of coal
	PG2	大牟田層群及び諫早層群 Ōmuta and Isahaya Groups	P_{1b}	砂岩泥岩互層，砂岩，泥岩，礫岩及び石炭（凝灰岩の薄層を挟む） Interbedded mudstone and sandstone, sandstone, mudstone, conglomerate and coal with thin beds of tuff
	PG2	銀水層及び鉾ノ甲層 Ginsui and Hokonokō Formations	P_{1a}	礫岩，砂岩及び泥岩（まれに石炭の薄層を挟む） Conglomerate, sandstone and mudstone, rarely with thin bed of coal
後期白亜紀 Late Cretaceous　コニアシアン－サントニアン Coniacian－Santonian	K2	姫浦層群 Himenoura Group	Hm	礫岩（赤色頁岩を伴う），砂岩及びシルト岩 Conglomerate, sandstone, siltstone and red shale
セノマニアン－チュロニアン Cenomanian－Turonian	K2	御船層群 Mifune Group 上部 Upper Formation	Mf_3	赤色泥岩，砂岩及び酸性凝灰岩 Red mudstone, sandstone and acid tuff
	K2	下部 Lower Formation	Mf_2	砂岩及び砂岩泥岩互層 Sandstone and alternating beds of sandstone and mudstone
	K2	基底部 Basal Formation	Mf_1	礫岩（砂岩及び泥岩の薄層を挟む） Conglomerate with thin beds of sandstone and mudstone

第四紀 Quaternary

印刷校訂：　中島和敏
この地質図の作成に当たっては、国土地理院長の承認を得て、同院発行の20万分の１地勢図を使用しました。（承認番号　平15総使、第73号）

赤色の経緯度数値は世界測地系による．
Latitude and longitude values in red color are referred to the International Terrestrial Reference Frame (ITRF)

緑川地図印刷株式会社　印刷（11色刷）

文献引用例

星住英夫・尾崎正紀・宮崎一博・松浦浩久・利光誠一・宇都浩三・内海　茂・駒澤正夫・広島俊男・須藤定久（2004）
20万分の１地質図幅「熊本」，産業技術総合研究所　地質調査総合センター

BIBLIOGRAPHIC REFERENCE

Hoshizumi, H., Ozaki, M., Miyazaki, K., Matsuura, H., Toshimitsu, S., Uto, K., Uchiumi, S., Komazawa, M., Hiroshima, T. and Sudo, S. (2004)
Geological Map of Japan 1:200,000, Kumamoto. Geological Survey of Japan, AIST

前期白亜紀後期－後期白亜紀前期 Late Early Cretaceous to early Late Cretaceous	K1-2	佐賀花崗岩 Saga Granite	Sag	細-中粒ざくろ石含有白雲母黒雲母花崗岩（ペグマタイトを伴う） Fine- to medium-grained garnet-bearing muscovite-biotite granite with pegmatite
	K1-2	筒ヶ岳花崗岩(Tsu)及び鷹取花崗岩(Tat) Tsutsugatake Granite and Takatori Granite	Tsu・Tat	細-中粒白雲母黒雲母花崗岩（ペグマタイトを伴う） Fine- to medium-grained muscovite-biotite granite with pegmatite
	K1-2	菊池花崗岩(Ki)及び鯛生花崗岩(Tai) Kikuchi Granite and Taio Granite	Ki・Tai	中-粗粒黒雲母花崗岩（部分的に白雲母または角閃石を含む）及び黒雲母花崗閃緑岩 Medium- to coarse-grained biotite granite (partly muscovite or hornblende-bearing) and biotite granodiorite
	K1-2	玉名花崗閃緑岩(Tam)及び相知花崗閃緑岩(Och) Tamana Granodiorite and Ōchi Granodiorite	Tam・Och	粗粒角閃石黒雲母花崗閃緑岩 Coarse-grained hornblende-biotite granodiorite
	K1-2	深江花崗岩 Fukae Granite	Fuk	細粒黒雲母花崗岩，角閃石黒雲母花崗閃緑岩-石英閃緑岩（アプライト及びペグマタイトを伴う） Fine-grained biotite granite, hornblende-biotite granodiorite to quartz diorite with aplite and pegmatite
	K1-2	仏坊花崗閃緑岩 Butsubō Granodiorite	Bu	細粒斑状角閃石黒雲母花崗閃緑岩（球状閃緑岩を伴う） Fine-grained porphyritic hornblende-biotite granodiorite with orbicular diorite
	K1-2	城山トーナル岩 Jōyama Tonalite	Jo	中粒黒雲母角閃石トーナル岩 Medium-grained biotite-hornblende tonalite
	K1-2	北多久斑れい岩類 Kitataku Gabbroic Rocks	KGb	粗粒かんらん石紫蘇輝石斑れい岩，紫蘇輝石角閃石斑れい岩，角閃石斑れい岩，石英閃緑岩及びコートランド岩 Coarse-grained olivine-hypersthene gabbro, hypersthene-hornblende gabbro, hornblende gabbro, quartz diorite and cortlandite
白亜紀 Cretaceous	m8	白亜紀高温低圧型変成岩類（肥後変成岩類：原岩の一部は三畳紀-ジュラ紀低温高圧型変成岩類である間の谷変成岩類，その他の部分の原岩は時代未詳） Cretaceous low P/T metamorphic rocks (Higo Metamorphic Rocks; a part of protoliths is the Triassic-Jurassic high P/T Manotani Metamorphic Rocks, and age of the other parts of the protoliths is unknown) 黒雲母帯 Biotite zone	b	白雲母黒雲母片岩，緑泥石白雲母黒雲母片岩及び緑簾石アクチノ閃石緑泥石片岩 Muscovite-biotite schist, chlorite-muscovite-biotite schist and epidote-actinolite-chlorite schist
		珪線石帯 Sillimanite zone	s	珪線石黒雲母片岩，珪線石黒雲母片麻岩，角閃石片岩及び結晶質石灰岩 Sillimanite-biotite schist, sillimanite-biotite gneiss, hornblende schist and crystalline limestone
		ざくろ石-菫青石帯 Garnet-cordierite zone	gc	ざくろ石菫青石黒雲母片麻岩，黒雲母片麻岩，ミグマタイト，角閃岩及び結晶質石灰岩 Garnet-cordierite-biotite gneiss, biotite gneiss, migmatite, amphibolite and crystalline limestone
			Hp	変成泥岩及び変成砂岩 Metamudstone and metasandstone
			Hl	結晶質石灰岩 Crystalline limestone
			Hv	変成苦鉄質火山岩及び火山砕屑岩 Metamorphosed mafic volcanic and volcaniclastic rocks
			Hu	変成超苦鉄質岩 Metamorphosed ultramafic rocks
三畳紀－ジュラ紀 Triassic-Jurassic	m5	三畳紀-ジュラ紀低温高圧型変成岩類（周防変成岩類：筑後・木の葉・間の谷変成岩類） Triassic-Jurassic high P/T metamorphic rocks (Suō Metamorphic Rocks : Chikugo, Konoha and Manotani Metamorphic Rocks)	Cp	泥質片岩（珪質片岩を伴う）及び砂質片岩 Pelitic schist (with siliceous schist) and psammitic schist
			Cb	苦鉄質片岩 Mafic schist
			Cl	結晶質石灰岩 Crystalline limestone
後期ペルム紀 Late Permian	P	水越層 Mizukoshi Formation	Mz	礫岩，砂岩，粘板岩質頁岩及び石灰岩 Conglomerate, sandstone and slate with limestone lense
石炭紀－ペルム紀 Carboniferous-Permian	m3	石炭紀-ペルム紀低温高圧型変成岩類（三郡-蓮華変成岩類：脊振山地南部の"三郡変成岩類"・木山変成岩類） Carboniferous-Permian high P/T metamorphic rocks (Sangun-Renge Metamorphic Rocks : "Sangun" Metamorphic Rocks in southern margin of Sefuri Mountains and Kiyama Metamorphic Rocks)	Sp	泥質片岩（珪質片岩を伴う）及び砂質片岩 Pelitic schist (with siliceous schist) and psammitic schist
			Sb	苦鉄質片岩 Mafic schist
			Su	蛇紋岩 Serpentinite
先ペルム紀 Pre-Permian	Pz	山鹿変斑れい岩（石炭紀-ペルム紀もしくは三畳紀-ジュラ紀の低温高圧型変成作用を被る） Yamaga Metagabbro (suffered high P/T metamorphism in Carboniferous-Permian or Triassic-Jurassic time)	mg	変斑れい岩及び角閃岩 Metagabbro and amphibolite
時代未詳 unknown age	U		u	蛇紋岩 Serpentinite

＊100万分の1日本地質図第3版（地質調査所，1992）の時代区分及び岩体区分記号
Notation for time-Stratigraphic division and rock type in the Geological Map of Japan 1 : 1,000,000, 3rd Edition (Geological Survey of Japan, 1992)

- 断層（破線部は推定） Fault (broken where inferred)
- 活断層（破線部は推定） Active fault (broken where inferred)
- 海底活断層（破線部は推定） Submarine active fault (broken where inferred)
- 背斜 Anticline
- 向斜 Syncline
- アンチフォーム Antiform
- シンフォーム Synform
- 等重力線（1980年正規重力式に基づくブーゲー異常）仮定密度2.3g／cm³，５ミリガル間隔 Gravity contour [Bouguer anomalies based on the Normal Gravity Formular (1980)] Assumed density 2.3g/cm³, contour interval 5 milligals
- H　高重力異常域 Area of higher gravity
- L　低重力異常域 Area of lower gravity
- 火口線及びカルデラ縁 Vent and caldera rims
- 崩壊地形 Rims of slope failure
- 温泉 Hot spring
- 鉱泉 Mineral spring
- X　稼行鉱山 Working mine
- X　休廃止鉱山 Closed mine
- 稼行採石場 Working quarry

Au	金 gold	Mn	マンガン manganese	ka	カオリン kaolin
Ag	銀 silver	Cr	クロム chromium	ls	石灰石 limestone
Cu	銅 copper	fd	長石 feldspar	c	石炭 coal

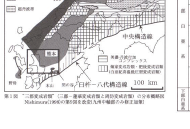

第１図　"三郡変成岩類"（三郡－蓮華変成岩類と周防変成岩類）の分布概略図
Nishimura(1998)の第9図を改変(九州中軸部のみ修正加筆)

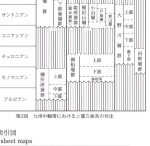

第2図　九州中軸帯における上部白亜系の対比

5万分の１地質図幅索引図
Index to 1:50,000 geological sheet maps

唐　津 Karatsu NI-52-16-4 (1956)	浜　崎 Hamasaki NI-52-10-16 (未刊行，unpublished)	脊振山 Sefuri San NI-52-10-12 (未刊行，unpublished)	甘　木 Amagi NI-52-10-8 (未刊行，unpublished)	吉　井 Yoshii NI-52-10-4 (未刊行，unpublished)	耶馬溪 Yabakei NI-52-4-16 (未刊行，unpublished)
伊万里 Imari NI-52-17-2 (1958)	武　雄 Takeo NI-52-11-13 (未刊行，unpublished)	佐　賀 Saga NI-52-11-9 (未刊行，unpublished)	久留米 Kurume NI-52-11-5 (未刊行，unpublished)	日　田 Hita NI-52-11-1 (未刊行，unpublished)	森 Mori NI-52-5-13 (未刊行，unpublished)
早　岐 Haiki NI-52-17-3 (1966)	鹿　島 Kashima NI-52-11-14 (未刊行，unpublished)	大牟田 Ōmuta NI-52-11-10 (未刊行，unpublished)	山　鹿 Yamaga NI-52-11-6 (未刊行，unpublished)	八方ヶ岳 Yahō-ga-Take NI-52-11-2 (未刊行，unpublished)	宮　原 Miyanoharu NI-52-5-14 (1997)
大　村 Ōmura NI-52-17-3 (1966)	諫　早 Isahaya NI-52-11-15 (未刊行，unpublished)	荒　尾 Arao NI-52-11-11 (未刊行，unpublished)	玉　名 Tamana NI-52-11-7 (未刊行，unpublished)	菊　池 Kikuchi NI-52-11-3 (未刊行，unpublished)	阿蘇山 Aso San NI-52-5-15 (未刊行，unpublished)
長　崎 Nagasaki NI-52-17-4 (未刊行，unpublished)	肥前小浜 Hizen-Obama NI-52-11-15 (未刊行，unpublished)	島　原 Shimabara NI-52-11-12 (未刊行，unpublished)	熊　本 Kumamoto NI-52-11-8 (未刊行，unpublished)	御　船 Mifune NI-52-11-4 (未刊行，unpublished)	高　森 Takamori NI-52-5-16 (未刊行，unpublished)
肥前高島付野母崎 Hizen-Takashima Incl. Nomozaki NI-52-18-1 (1962)	口之津 Kuchinotsu NI-52-11-13 (未刊行，unpublished)	三　角 Misumi NI-52-12-9 (未刊行，unpublished)	八　代 Yatsushiro NI-52-12-5 (未刊行，unpublished)	砥　用 Tomochi NI-52-12-1 (未刊行，unpublished)	鞍　岡 Kuraoka NI-52-16-4 (1958)

7万5千分の1 小城 1;75,000 Ogi
7万5千分の1 豆田 1;75,000 Mameda
20万分の1 熊本 1;200,000 Kumamoto
7万5千分の1 大牟田 1;75,000 Ōmuta
7万5千分の1 山鹿 1;75,000 Yamaga
7万5千分の1 口之津 1;75,000 Kuchinotsu
7万5千分の1 島原 1;75,000 Shimabara

20万分の１地質図幅索引図
Index to 1:200,000 geological sheet maps

唐津（第2版） Karatsu (2nd Edition) NI-52-16 (1997)	福　岡 Fukuoka NI-52-10 (1993)	中　津 Nakatsu NI-52-4 (未刊行，unpublished)
長崎（第2版） Nagasaki (2nd Edition) NI-52-17 (1989)	熊　本 Kumamoto NI-52-11 (2004)	大　分 Ōita NI-52-5 (1956)
野母崎 Nomozaki NI-52-18 (1997)	八　代 Yatsushiro NI-52-12 (未刊行，unpublished)	延　岡 Nobeoka NI-52-6 (1981)

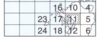

熊　本
KUMAMOTO
1:200,000
NI－52－11

Miller, J., Banno, S., Hashimoto, M. and Iwasaki, M. (1963) K-Ar ages of micas from the Sonogi and Kiyama, metamorphic terrains in Kyushu, Japan. Japan. Jour. Geol. Geogr., vol.34, p.197-203.
三浦哲彦・飯盛喜代春・坂井　晃 (1987)　佐賀平野の地盤沈下と地下水の塩水化について．地質と調査，no.1, p.28-34.
三浦哲彦・赤峰剛徳・下山正一 (1996)　有明粘土層の堆積環境とその鋭敏性について．土木学会論文集，no.541, p.119-131.
宮地六美・松本徰夫 (1992)　多良岳火山区における火山岩類のフィッション・トラック年代．松本徰夫教授記念論文集，p.187-191.
宮地六美・酒井治孝 (1991)　北西部九州，第三紀層中火砕岩類のフィッション・トラック年代．地質学雑誌，vol.97, p.671-674.
水野篤行 (1962a)　西日本地域における古第三系および下部新第三系古生物年代学的研究(第1報，西彼杵半島周辺の古第三系の層序と貝類化石群について)．地質学雑誌，vol.68, p.640-648.
水野篤行 (1962b)　西日本地域における古第三系および下部新第三系古生物年代学的研究(第2報，西彼杵半島周辺の古第三系の対比と古生物年代学的区分について)．地質学雑誌，vol.68, p.687-693.
水野篤行 (1963)　西日本地域における古第三系および下部新第三系古生物年代学的研究(第3報，貝類化石群の層位的・地理的分布)．地質学雑誌，vol.69, p.38-50.
水野篤行 (1995)　西日本地域の漸新統-下部中新統の軟体動物群生層序(演旨)．日本地質学会第102年学術大会講演要旨，p.136.
森山善蔵・日高　稔 (1979)　5万分の1土地分類基本調査「日田」，表層地質図及び各論．大分県，p.34-40.
村上　篁・黒田和男 (1971)　土地分類基本調査「諫早」5万分の1表層地質図及び表層地質図各論．経済企画庁，21p.
村田茂雄・森永陽一郎 (1957)　諫早古第三系．九州鉱山誌，vol.25, p.41-52.
永川勝久・小畑正明・板谷徹丸 (1997)　肥後変成帯のK-Ar年代．地質学雑誌，vol.103, p.943-952.
長尾　功 (1926)　九州古第三紀層々序(其六，七，八)．地学雑，vol.38, p.596-603, 663-671, 706-712.
長尾　功 (1927)　九州古第三紀層の層序(其十五，十六)．地学雑，vol.39, p.501-512, 592-604.
長岡信治・松岡数充・武藤鉄司・原口　強・近藤　寛 (1993)　雲仙岳西方橘湾の海底活断層．雲仙火山災害の調査研究(第2報)，平成4年度教育特別研究費(特別分)研究成果，長崎大学，p. 28-43.
長岡信治・横山祐典・中田正夫・前田保夫・奥野淳一・白井克己 (1997)　有明海南東岸玉名平野の地形発達史と完新世海面変化．地理学評論，Ser. A, vol.70, p.287-306.
中原功一朗・長谷義隆・松田博貴・秋元和実・塚脇真二・尾田太良 (2002)　有明海底柱状試料(AR98-A～CおよびAR98-E)の珪藻化石群集の変化に基づく過去1万年間の水域環境変遷．熊本大学理学部紀要(地球科学)，vol.17, p.35-46.
Nishimura, Y. (1998)　Geotectonic subdivision and areal extent of the Sangun Belt, Inner Zone of Southwest Japan. J. Metamorph. Geol., vol.16, p.129-140.
西村祐二郎・柴田　賢 (1989) "三郡変成岩"の変斑れい岩質岩の産状とK-Ar年代．地質学論集，no.33, 343-357.
野間泰二 (1965)　5万分の1土地分類基本調査「佐賀」，表層地質図及び説明書．経済企画庁，31p.
Obata, M., Yoshimura, Y., Nagakawa, K., Odawara, S. and Osanai, Y. (1994) Crustal anatexis and melt migrations in the Higo metamorphic terrane, west-central Kyushu, Kumamoto, Japan. Lithos, vol.32, p.135-147.
小形昌徳 (1989)　九州北西部，多良岳地域の火山地質．地質学雑誌，vol.98, p.755-768.
小形昌徳・高岡宣雄 (1991)　多良岳地域の火山岩類のK-Ar年代．火山，vol.36, p.187-191.
Okada, H. (1960) Sandstone of the Cretaceous Mifune Group, Kyushu, Japan. Mem. Fac. Sci., Kyushu Univ., Ser. D (Geol.), vol.10, p.1-40.
Okada, H. (1992) Calcareous nannofossils and biostratigraphy of the Paleogene sequences of the northern Kyusyu, Japan. Jour. Geol. Soc. Japan, vol.98, p.509-528.
岡本和明・原　郁夫・鈴木盛久 (1989)　九州，甲佐地域間の谷-肥後変成岩の地質構造(予報)．地質学論集，no.33, p.187-198.
小野晃司・渡辺一徳 (1983)　阿蘇カルデラ．月刊地球，vol.5, p.73-83.
小野晃司・渡辺一徳 (1985)　阿蘇火山地質図．火山地質図4，地質調査所．
小野晃司・松本徰夫・宮久三千年・寺岡易司・神戸信和 (1977) 竹田地域の地質．地域地質研究報告(5万分の1図幅)，地質調査所，145p.
小山内康人・浜本拓志・亀井淳志・大和田正明・加々美寛雄 (1996)　九州肥後変成帯の高温変成作用と地殻進化．テクトニクスと変成作用(原　郁夫先生退官記念論文集)，創文，p.113-123.
Osanai, Y., Hamamoto, T., Maishima, O. and Kagami, H. (1998) Sapphirine-bearing granulites and related high-temperature metamorphic rocks from the Higo metamorphic terrane, west-central Kyushu, Japan. J. Metamorph. Geol., vol.16, p.53-66.
大島恒彦 (1960)　佐賀県多久市相浦附近の球状閃緑岩．佐賀大学教育学部論文集，no.9, p.171-186.
大島恒彦 (1961)　佐賀県多久市・北多久斑糲岩類．佐賀大学教育学部論文集，no.10, p.87-100.
大島恒彦 (1964)　背振山地南部変成岩帯に関する予察的研究．佐賀大学教育学部論文集，12, p.59-69.
大島恒彦 (1973)　5万分の1土地分類基本調査「武雄」，表層地質図及び各論．佐賀県，p.30-36.
大島恒彦 (1976)　5万分の1土地分類基本調査「鹿島」，表層地質図及び各論．佐賀県，p.19-23.
大島恒彦 (1984)　佐賀平野の軟弱地盤．月刊地球，vol.6, p.687-691.
大塚裕之 (1966)　口之津層群の層序および堆積物-口之津層群の地史学的研究(I)．地質学雑誌，vol.72, p.371-384.
大塚裕之・古川博恭 (1988)　九州・琉球地方の下部及び中部更新統の層序．地質学論集，no.30, p.155-168.
大塚裕之・外間喜春・田中利明・後村信幸・竹之内貴裕・上野宏共 (1995)　島原半島南部の地質の再検討．鹿児島大学理学部紀要(地学・生物学)，no.28, p.181-241.
大塚専一 (1899, 1900)　20万分の1地質図幅「佐賀」及び同説明書．地質調査所，103p.
大築洋之助 (1917)　唐津炭田地形及び地質図並説明書．地質調査所．
佐賀県 (1954)　佐賀県炭田地質図(5万分の1)及び佐賀県の地質と地下資源．141p.
阪口和則・西村暉希 (1999)　大村市南部三浦半島の地質．長崎県地学会誌，no.63, p.1-14.
阪口和則・西村暉希・堀口承明 (1989)　諫早市西諫早付近の第四系-とくに古貝津湖層と火山灰層の分布-．長崎県地学会誌，no.49, p.1-18.
榊　昌宏・山本博達 (1967)　熊本県山鹿地域の変斑れい岩．柴田秀賢教授退官記念論文集，p.175-179.
坂島俊彦・早坂康隆・広瀬丈洋 (1998)　九州における三郡-中国帯の延長-木の葉変成岩の帰属-．九州のテクトニクスワーキンググループ研究連絡誌，no.2, p.21-26.
Sakashima T., Terada, K., Takeshita, T. and Sano, Y. (2003) Large-scale displacement along the Median Tectonic Line, Japan: evidence from SHRINP zircon U-Pb dating of granites and gneisses from the South Kitakami and paleo-Ryoke belts. J. Asian Earth Sci., vol.21, p.1019-1039.
笹田政克 (1987)　豊肥地域の先第三紀基盤岩類．地調月報，vol.38, p.385-422.
佐藤光男・井上　保 (1968)　熊本県上益城郡矢部町西方の"間の谷変成帯"について．福岡教育大学紀要，第3分冊，no.18, p.155-161.
佐藤聡美・松田博貴 (2003)　有明海緑川河口付近の堆積過程．熊本大学理学部紀要(地球科学)，vol.17, p.1-13.
沢井長雄・松村法行・板谷徹丸 (1998)　九州北中部，星野金鉱床地域の火山岩と金鉱床のK-Ar年代．地質学雑誌，vol. 104, p. 377-386.
澤村昌俊・田中豊俊・千足恭平・鹿田昭男 (1983)　久留米層最下部層中の凝灰岩に含まれるジルコンのフィッション・トラック年代．地質学雑誌，vol.89, p.129-131.
柴田　賢・西村祐二郎 (1989)　三郡結晶片岩の同位体年代．地質学論集，no.33, p.311-315.
下山正一 (2001)　筑紫平野と有明海．町田・太田・河名・森脇・長岡編，日本の地形7-九州・南西諸島-．東京大学出版会，p.86-92.
下山正一・溝田智俊 (1997)　佐賀平野・上場台地・唐津平野の地形発達と第四系．日本地質学会第104年学術大会見学旅行案内書，p.45-68.
下山正一・松本直久・湯村弘志・竹村恵二・岩尾雄四郎・三浦哲彦・陶野郁雄 (1994)　有明海北岸低地の第四系．九州大学理学部研究報告(地球惑星)，vol.18, p.103-129.
下山正一・小杉正人・松岡数充・片岡久子・佐藤直弘・遠藤邦彦・野井英明・竹村恵二・市原季彦・三浦哲彦・陶野郁雄 (1996)　有明海奥部低地の古環境統合解析．関東平野，no.4, p.53-76.
下山正一・木下裕子・宮原百々・田中ゆか里・市原季彦・竹村恵二 (1999)　旧汀線高度からみた九州の後期更新世地殻変動様式．地質学雑誌，vol.105, p.311-331.
新エネルギー・産業技術総合開発機構 (1990a)　平成元年度全国地熱資源総合調査(第3次)広域熱水流動系調査　鶴見岳地域，火山岩分布・年代調査報告書要旨，164p.
新エネルギー・産業技術総合開発機構 (1990b)　有明海地域物理探査再解析報告書．石炭資源開発基礎調査(平成元年度)，17p.
新エネルギー・産業技術総合開発機構 (1991)　有明海地域海上試錐2有7号調査報告書．石炭資源開発基礎調査(平成2年度)，21p.
新エネルギー・産業技術総合開発機構 (1995)　阿蘇山西部地域(第3次)．地熱開発促進調査データ処理報告書，no.38, p.1144-1145.
新エネルギー総合開発機構 (1983a)　有明海地域57有1号海上試錐調査報告書．石炭資源開発基礎調査(昭和57年度)，15p.
新エネルギー総合開発機構 (1983b)　有明海地域58有2号海上試錐調査報告書．石炭資源開発基礎調査(昭和58年度)，21p.
新エネルギー総合開発機構 (1984)　有明海地域物理探査報告書．石炭資源開発基礎調査(昭和58年度)，22p.
新エネルギー総合開発機構 (1985)　有明海地域59有3号海上試錐調査報告書．石炭資源開発基礎調査(昭和59年度)，16p.
新エネルギー総合開発機構 (1986a)　有明海地域試錐工事60有4号調査報告書．石炭資源開発基礎調査(昭和60年度)，15p.
新エネルギー総合開発機構 (1986b)　有明海地域物理探査報告書．石炭資源開発基礎調査(昭和60年度)，14p.
新エネルギー総合開発機構 (1987a)　有明海地域海上試錐61有5号調査報告書．石炭資源開発基礎調査(昭和61年度)，18p.
新エネルギー総合開発機構 (1987b)　有明海地域物理探査再解析報告書．石炭資源開発基礎調査(昭和61年度)，15p.
新エネルギー総合開発機構 (1988)　有明海地域海上試錐62有6号調査報告書．石炭資源開発基礎調査(昭和62年度)，18p.
首藤次男 (1993)　内弧における造盆運動と広域テクトニクス-北部九州の第三紀堆積盆を例として-．地学雑誌，vol.102, p.849-867.
杉谷　隆 (1983)　有明海北岸平野における最終間氷期以後の地形発達史，その定量的研究．地理学評論，vol.56, p.403-419.
鈴木弘道 (1976)　国際重力基準網1971と日本重力基準網1975．測地学会誌，vol.22, p.112-129.
鈴木和博・足立　守・高木秀雄・小山内康人 (1998)　肥後変成岩のCHIMEモナザイト年代．日本地質学会第105年学術大会講演要旨，p.214.
Takai, M., Miyachi, M. and Hirano, I. (1984) Paleomagnetism and fission-track ages of Kimbo volcano, Southwest Japan. Rock Magnet. Paleogeophys., vol.11, p.21-25.
玉生志郎・上村不二雄・笹田政克・角　清愛 (1982)　豊肥地熱地域地質図．特殊地質図21-1．地質調査所．
Tamura, M. (1976) Cenomanian bivalves from the Mifune Group, Japan. Part 1. Mem. Fac. Educ., Kumamoto Univ., no.25, Nat. Sci., p. 45-59, 3 pls.
Tamura, M. (1977) Cenomanian bivalves from the Mifune Group, Japan. Part 2. Mem. Fac. Educ., Kumamoto Univ., no.26, Nat. Sci., p.107-144, 13 pls.
Tamura, M. (1979) Cenomanian bivalves from the Mifune Group, Japan. Part 3. Mem. Fac. Educ. Kumamoto Univ., no.28, Nat. Sci., p.59-74.
田村　実 (1990)　御船層群の不整合について．熊本大学教育学部紀要，no.39, p.17-20.
田村　実・田代正之 (1966)　熊本市南方の上部白亜系．熊本大学教育学部紀要，no.14, p.24-33.
Tamura, M. and Tashiro, M. (1967) Cretaceous trigoniids from the Mifune Group. Mem. Fac. Educ., Kumamoto Univ., no.15, Nat. Sci., p.13-23.
田村　実・渡辺一徳 (1982)　5万分の1土地分類基本調査「菊池」，表層地質図及び各論．熊本県，p.22-26.
Tamura, M., Tashiro, M. and Motojima, T. (1968) The correlation of the Mifune Group with the upper formation of the Goshonoura Group, with description of some important pelecypods from the strata. Mem. Fac. Educ., Kumamoto Univ., no.16, Nat. Sci., p. 28-43.
Tamura, M., Matsumura, M. and Matsumoto, T. (1974) On the age of Mifune Group, central Kyushu, Japan, with a description of ammonite from the group. Mem. Fac. Educ., Kumamoto Univ., no.23, Nat. Sci., p.47-57.
田村　実・渡辺一徳・谷村洋征 (1983)　5万分の1土地分類基本調査「御船」，表層地質図及び各論．熊本県，p.25-34.
田村　実・岡崎美彦・池上直樹 (1991)　御船層群上部よりの肉食・草食恐竜化石群の産出について．熊本大学教育学部紀要，no.40, p.31-45.
Tashiro, M. (1976) Bivalve faunas of the Cretaceous Himenoura Group in Kyushu. Spec. Pap. Palaeont. Soc. Japan, no.19, p.1-120.
富田宰臣・石橋　毅・原　眞澄 (1992)　九州中部大牟田市地域の三池炭田古第三紀層と産出化石．九州大学理学部研究報告(地球惑星科学)，vol.17, p.25-43.
土志田潔・宇都浩三・内海　茂 (2002)　熊本金峰山のK-Ar年代．日本火山学会講演予稿集，2002, no.2, p.179.
Tsuji, S. (1967) Petrology of the Higo Metamorphic Complex in the Kosa-Hamamati Area, Kumamoto Prefecture, Kyushu. Japan. Jour. Geol. Geogr., vol.38, p.13-25.
塚脇真二・松田博貴・長谷義隆・秋元和実・中原功一朗・浅野いずみ・小沢広和・岡村　真・古田徳仁・堂満華子・尾田太良・滝川　清 (2002)　海底柱状試料に基づく有明海中央部における過去1万年間の環境変遷史．熊本大学理学部紀要(地球科学)，vol.17, p.1-33.
内海　茂・宇都浩三・星住英夫 (2004)　20万分の1熊本地域の火山岩類のK-Ar年代．地質調査研究報告，(印刷中)
植田良夫・大貫　仁 (1968)　本邦変成岩のK-Ar dating(Ｉ)-九州八代片麻岩類，木山並びに彼杵変成岩-．岩鉱，vol.60, p.159-166.
Ui, T. (1971)　Genesis of magma and structure of magma chamber of several pyroclastic flows in Japan. J. Fac. Sci. Univ. Tokyo, Ser. II, vol.18, p.53-127.
浦田英夫 (1957)　福岡県八女郡黒木町附近の新第三系について．九州大学教養部地学研究報告，no.4, p.33-43.
浦田英夫 (1958)　福岡県久留米市南方の新第三系について．九州大学教養部地学研究報告，no.5, p.25-37.
浦田英夫 (1985)　福岡県久留米-黒木地域新第三系再論．九州大学教養部地学研究報告，no.24, p.13-30.
浦田英夫・千足恭平・小原浄之介・鹿田昭男・唐木田芳文・沢村昌俊・田中豊俊 (1982)　5万分の1土地分類基本調査「久留米」，表層地質図及び各論．福岡県，p.31-36.
宇都浩三・須藤　茂 (1985)　豊肥地熱地域の火山岩のK-Ar年代．地調報告，no.264, p.67-83.
渡辺一徳 (1972)　阿蘇カルデラ西部の地質．熊本大学教育学部紀要，vol.21, p.75-85.
渡辺一徳 (1982)　阿蘇火砕流堆積物と大江層との層序関係．熊本大学教育学部紀要，自然科学，no.31, p.25-32.
渡辺一徳 (1998)　第三節 地質各論．新熊本市史編纂委員会編，新熊本市史，通史編 第1巻 自然・原始・古代，p.78-108.
渡辺一徳・藤本雅太郎 (1993)　5万分の1土地分類基本調査「山鹿・荒尾・大牟田・久留米」，表層地質図及び各論．熊本県，p.17-25.
渡辺一徳・藤本雅太郎 (1994)　5万分の1土地分類基本調査「八方ヶ岳」，表層地質図及び各論．熊本県，p.14-21.
渡辺一徳・藤本雅太郎 (1995)　5万分の1土地分類基本調査「日田・森・宮原」，表層地質図及び各論．熊本県，p.16-26.
渡辺一徳・星住英夫 (1995)　雲仙火山地質図，火山地質図8，地質調査所．
渡辺一徳・益田悦郎 (1983)　いわゆる中位段丘堆積物としての小串層及び大江層について．熊本大学教育学部紀要，自然科学，no.32, p.29-37.
渡辺公一郎 (1989)　熊本県大矢野島～宇土半島に分布する鮮新世火山岩類のフィッション・トラック年代．九州大学工学部彙報，vol.62, p.561-566.
渡辺公一郎・林　正雄・藤井　誠・木戸道男 (1987)　九州中部，津江山地における後期新生代火山岩類のフィッション・トラック年代．地団研専報，no. 33, p. 137-147.
山口　勝・富田宰臣・野井英明 (1987a)　5万分の1土地分類基本調査「大牟田・山鹿・荒尾」，表層地質図及び各論．福岡県，p.27-35.
山口　勝・中田節也・西山忠男・野井英明 (1987b)　5万分の1土地分類基本調査「日田・八方ヶ岳」，表層地質図及び各論．福岡県，p.29-34.
山本博達 (1955)　筑後変成岩・玉名花崗閃緑岩接触部におけるジルコンの行動．福岡学芸大学紀要，第2部，no.5, p.59-67.
Yamamoto, H. (1962) Plutonic and metamorphic rocks along the Usuki-Yatsushiro tectonic line in the western part of central Kyushu. Bull. Fukuoka Gakugei Univ., Pt, III, no.12, p.93-173.
山本博達 (1964)　熊本市東方木山地域の変成岩．九州大学理学部研究報告，vol.7, p.33-38.
山下傳吉 (1895, 1896)　20万分の1地質図幅「熊本」及び同説明書．地質調査所，97p.
山崎謙一・井口　隆 (1989)　三池炭田の地質層序．日本地質学会第96年学術大会講演要旨，p.176.
山崎達雄 (1953)　唐津炭田層序．地質学雑誌，vol.59, p.403-419.
山崎達雄 (1959)　唐津炭田の地質構造と貫入火成岩類．九州大学生産科学研究所報告，no.26, p.33-53.
山崎達雄・松本徰夫・蔵田正俊 (1965)　諫早炭田の地質(附．九州北西部諸炭田との関係)．九州大学生産科学研究所報告，no.40, p.8-27.
Yamazaki, T., Matsumoto, Y. and Tomita, T. (1959) Contribution to the sedimentary petrology of the so-called "Honeishi", north Kyushu. Rep. Res. Inst. Sci. Ind., Kyushu Univ., no.25, p.39-46.
柳　哮 (1967)　筑後変成岩について(講演要旨)．地質学雑誌，vol.73, p.113.
柳　哮 (1969)　筑後変成岩の岩石学的研究．九州大学理学部研究報告(地質学)，vol.9, p.89-98.
柳田寿一 (1958)　上部二畳系水越層．地質学雑誌，vol.64, no.752, p.222-230.
Yanagida, J. (1963) Brachiopods from the Upper Permian Mizukoshi Formation, central Kyushu. Mem. Fac. Sci., Kyushu Univ., Ser. D (Geol.), vol.14, p.69-78.
矢野健二・豊原富士夫・武田昌尚・土肥直之 (1991)　九州西部，三郡変成岩上に衝上している変斑れい岩．日本地質学会第98年学術大会講演要旨，p.336.
横瀬久芳・梁島達也・菊池　航・杉山直史・篠原　章・竹内　徹・長尾敬介・小玉一人 (1999)　別府-島原地溝帯西部域の過去5百万年間における間欠的火山活動．岩鉱，vol.94, p.338-348.
Yokoyama, Y., Nakada, M., Maeda, Y., Nagaoka, S., Okuno, J., Matsumoto, E., Sato, H. and Matsushima, Y. (1996) Holocene sea-level change and hydro-isostasy along the west coast of Kyushu, Japan. Paleogeogr. Paleo-climat. Paleoecol., vol.123, p.29-47.

阿蘇火山地質図
GEOLOGICAL MAP OF ASO VOLCANO
1：50,000

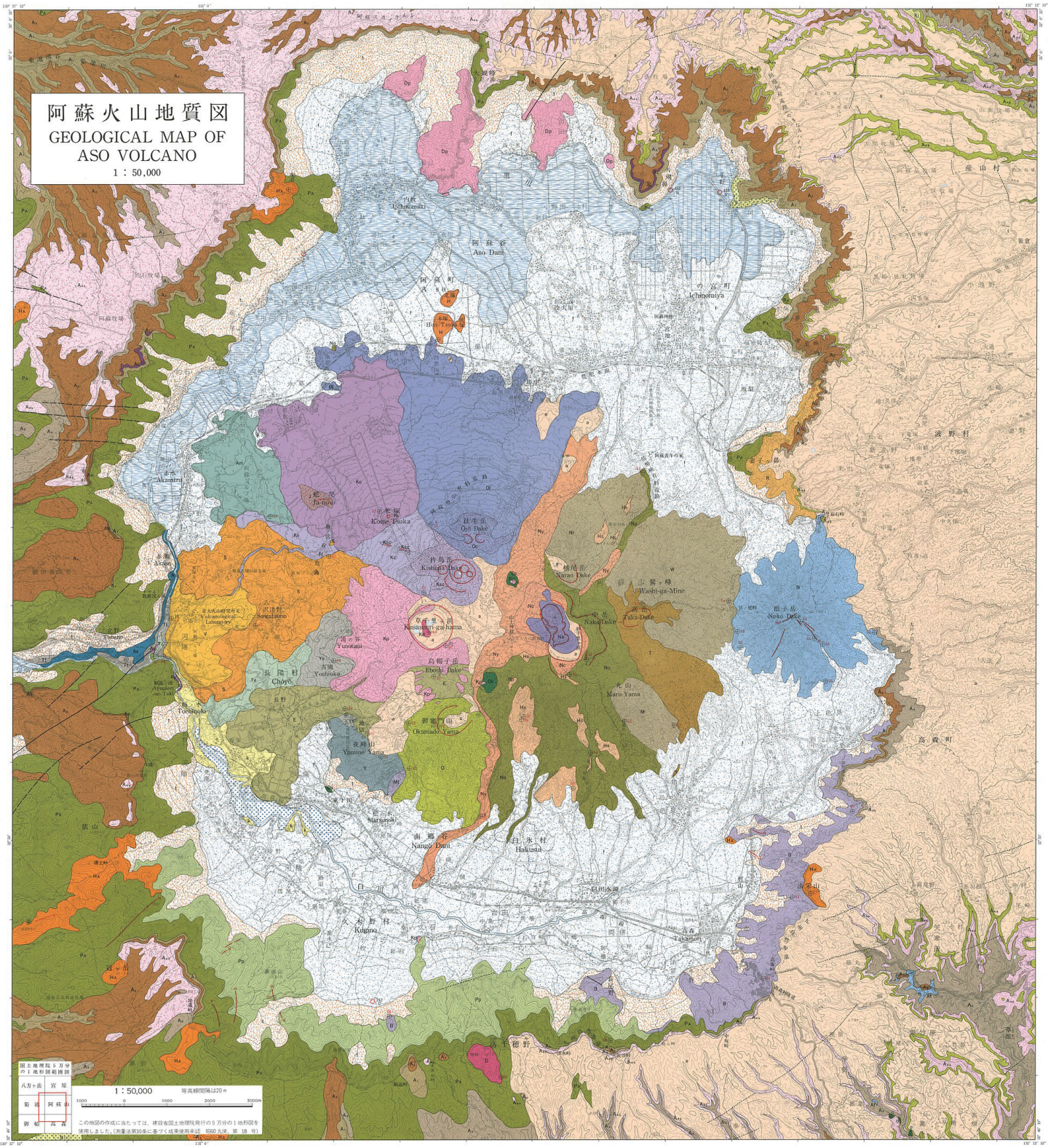

国土地理院5万分の1地形図範囲図

八方ヶ岳	宮原	
菊池	阿蘇山	
御船	高森	

1：50,000　等高線間隔は20m

1000　0　1000　2000　3000m

この地図の作成に当たっては、建設省国土地理院発行の5万分の1地形図を使用しました。(測量法第30条に基づく成果使用承認　昭60九測、第 16 号)

新生代　第四紀
Cenozoic　Quaternary
更新世最後期～完新世
Latest Pleistocene to Holocene

阿蘇火山　Aso Volcano
後カルデラ火山及び堆積物
Post-caldera volcanoes and deposits

降下火山灰 Air-fall ash
a 火山灰 Volcanic ash

カルデラ埋積層 Caldera-fill deposit
c 泥、砂及び礫 Mud, sand and gravel

崖錐 Talon
t 礫、砂及びシルト Gravel, sand and silt

河岸段丘堆積物 River terrace deposit
砂及び礫 Sand and gravel

扇状地堆積物 Fan deposit
f 砂、礫及びシルト Sand, gravel and silt

中岳火山 Nakadake Volcano
最新期火砕丘 Youngest pyroclastic cone
Ns 成層した火山灰及び火山岩塊 (一部溶岩state) Layered volcanic ash and block, partly welded
新期山体(溶岩流／堆積岩丘) Young volcanic edifice (Lava flow/tuff cone)
Ny 溶岩流／堆積岩 (Ao) Lava flow/tuff
古期山体 Old volcanic edifice
No 火砕岩、溶岩流及び岩脈 (Ao,B) Pyroclastic rock, lava flow and dike

米塚火山(溶岩流／スコリア丘) Komezuka Volcano (Lava flow, scoria cone)
Ko Kc 溶岩流／スコリア (B) Lava flow/scoria

往生岳火山(溶岩流／スコリア丘) Ojodake Volcano (Lava flow, scoria cone)
Oj Oc 溶岩流／スコリア (B) Lava flow/scoria

杵島岳火山(溶岩流／スコリア丘) Kishimadake Volcano (Lava flow, scoria cone)
Ks Ksc 溶岩流／スコリア (B) Lava flow/scoria

高岳火山 Takadake Volcano
T 火砕岩及び溶岩流 (Ao,B) Pyroclastic rock and lava flow

赤水溶岩 Akamizu Lava
Am 溶岩流 (Ao) Lava flow

姥ノ尾スコリア丘 Jano-o Scoria Cone
J スコリア (B) Scoria

草千里ヶ浜火山 Kusasenrigahama Volcano
中央火口丘 Central cone
主軽石丘 Main pumice cone
Kp 軽石、一部は強く溶結 (D) Pumice, in part densely welded

烏帽子岳火山 Eboshidake Volcano
E 溶岩流及び火砕岩 (A) Lava flow and pyroclastic rock

夜峰山火山 Yomineyama Volcano
Y 火砕岩(大部分溶結) (Ao) Pyroclastic rock(mostly welded)

杉ノ水火山 Matsunoki Volcano
Mt 火砕岩及び溶岩流 (B) Pyroclastic rock and lava flow

新竈門山火山 Okamadoyama Volcano
O 溶岩流及び火砕岩 (A) Lava flow and pyroclastic rock

丸山火山 Maruyama Volcano
M 火砕岩及び溶岩流 (B,Ao) Pyroclastic rock and lava flow

楢尾岳火山 Naraodake Volcano
Nr 火砕岩及び溶岩流 (Ao,B) Pyroclastic rock and lava flow

鷲ヶ峰火山 Washigamine Volcano
W 火砕岩及び溶岩流 (Ao,B) Pyroclastic rock and lava flow

古期小火山体 Older small volcanoes
Os 溶岩流 (A,Ahp) Lava flow

赤瀬溶岩 Akase Lava
As 溶岩流 (Ao) Lava flow

武津野溶岩 Suwatsuno Lava
S 溶岩流 (D) Lava flow

火山研究所溶岩 Volcanological Laboratory Lava
V 溶岩流 (Rpb) Lava flow

吉図溶岩 Yoshioka Lava
Ys 溶岩流 (B,Ao) Lava flow

白水火山 Hakusui Volcano
Hs 溶岩流、降下軽石を伴う (D,A) Lava flow, with air-fall pumice

本塚火山 Hontsuka Volcano
H 溶岩流、一部は水中溶岩 (Dh) Lava flow, partly subaqueous

久木野層 Kugino Formation
k シルト、砂及び火山灰 Silt, sand and volcanic ash

立野溶岩 Tateno Lava
Tt 溶岩流 (D) Lava flow

栃ノ木溶岩 Tochinoki Lava
Tc 溶岩流、溶結火砕岩を伴う (A) Lava flow, with welded pyroclastic rock

鮎返ノ滝溶岩 Ayugaerinotaki Lava
Ay 溶岩流 (B) Lava flow

九重火山 Kujū Volcano
Kj 非溶結のガラス火山灰・軽石 (Dh) Non-welded deposit of vitric ash and pumice

阪田火砕流 Handa Pyroclastic Flow

阿蘇火山 Aso Volcano　先カルデラ噴出物 Products of pre-caldera stage
As 溶結凝灰岩 (Dh) Welded tuff
As-4B 火砕流 Aso-4B Pyroclastic Flow
As-4A 火砕流 Aso-4A Pyroclastic Flow
As-3 火砕流 Aso-3 Pyroclastic Flow
As-3/2 降下火砕物 Aso-3/2 Air-fall Pyroclastics
As-2A, B 火砕流 Aso-2A, B Pyroclastic Flow
As-2R 溶結火砕岩 Aso-2R Welded Pyroclastics
As-2/1 溶岩 Aso-2/1 Lava
As-1 火砕流 Aso-1 Pyroclastic Flow
As-4 非溶結のガラス火山灰・軽石 (Dh) Non-welded deposit of vitric ash and pumice
同上、異質岩塊に富む (Dh) Ditto, rich in accidental block
ガラス火山灰、軽石またはスコリア (A,D) 及び溶結凝灰岩 Vitric ash, pumice or scoria and welded tuff
As' 溶結凝灰岩 (Dh) Welded tuff
As 成層した火山灰・軽石 (D) Layered volcanic ash and pumice
溶結凝灰岩、一部は非溶結のスコリア (A,D) Welded tuff, in part non-welded deposit of scoria
強溶結火砕岩、一部は二次流動 (A) Densely welded pyroclastic rock, in part secondary-flowed
As 溶岩流 (Ao,A) Lava flow
溶結凝灰岩 (D) Welded tuff

第三紀－第四紀
Tertiary to Quaternary
後期鮮新世－更新世火山岩類
Late Pliocene-Pleistocene volcanic rocks

根子岳火山 Nekodake Volcano
N Hz 溶岩流、火砕岩及び岩脈 (Ao,B,Ahp,Ah) Lava flow, pyroclastic rock and dike
黒雲母流紋岩 Biotite rhyolite
R 溶岩流 (Rhb) Lava flow
角閃石デイサイト溶岩 Hornblende dacite lava
D 溶岩流 (Dh) Lava flow
角閃石安山岩溶岩 Hornblende andesite lava
Ha 溶岩流、小貫入岩体及び岩脈 (Ah) Lava flow, small intrusive body and dike
輝石安山岩溶岩 Pyroxene andesite lava
Pa 溶岩流及び岩脈 (A,Ao,Ahp) Lava flow and dike
輝石安山岩火砕岩 Pyroxene andesite pyroclastic rock
Pp 火山角礫岩及び凝灰角礫岩 (A,Ahp) Volcanic breccia and tuff breccia
角閃石デイサイト火砕岩 Hornblende dacite pyroclastic rock
Dp 凝灰角礫岩 (Dh) Tuff breccia
玄武岩火砕岩 Basalt pyroclastic rock
B 火山角礫岩及び凝灰集塊岩、溶岩流を伴う (B) Volcanic breccia and agglomerate with lava flow
礫層 Gravel bed
礫及び砂 Gravel and sand

中生代 Mesozoic　白亜紀 Cretaceous
大野川層群 Ōnogawa Group
G 砂岩及び泥岩 Sandstone and mudstone

温泉 Hot spring
噴気孔 Fumarole
噴火口 Crater
伏在溶岩前縁 Concealed lava front
断層 Fault
リニアメント Lineament
化学分析試料採取地点 Sample locality for chemical analysis
黒数字は裏面第2表の分析番号に同じ、赤数字は全岩化学分析値のSiO2重量% Black figure refers sample number in Table 2 of the backside. Red figures mean SiO_2 wt % of bulk rock chemical analysis.
基盤に達した試錐 Drill-hole site, reached to the basement rocks
数字は地表からの基盤までの深さ(m) G：花崗岩 C：白亜紀堆積岩 Figures mean the depth of the basement top from the land surface in meters. G：granite C：Cretaceous sedimentary rocks
(B) 普通輝石かんらん石玄武岩 Augite-olivine basalt
(Ao) (±紫蘇輝石)普通輝石かんらん石 安山岩 (± Hypersthene) augite ≥ olivine andesite
(A) (±かんらん石)紫蘇輝石≥普通輝石 安山岩 (± Olivine) hypersthene ≥ augite andesite
(Ahp) (±角閃石)紫蘇輝石≥普通輝石 安山岩 (± Hornblende) hypersthene ≥ augite andesite
(Ah) (±輝石)角閃石安山岩 (± Pyroxene) hornblende andesite
(D) 普通輝石紫蘇輝石デイサイト Augite-hypersthene dacite
(Dh) 輝石角閃石デイサイト Pyroxene-hornblende dacite
(Rpb) 輝石黒雲母流紋岩 Pyroxene-biotite rhyolite
(Rhb) 角閃石黒雲母流紋岩 Hornblende-biotite rhyolite

Appendix B

Select Boring Logs of Interest

Originating source for each boring log provided on the boring log. Coordinates for each boring are provided on the individual logs by the original source. The database of local boring logs reviewed by GEER to locate these boring logs was found at:
http://www.web-gis.jp/2016KumamotoEQ/KumamotoLatLon_v11.html

Artificial Island Boring Logs
(Representative Selection)

ボーリング柱状図

調　査　名

事業・工事名

ボーリングNO.

シートNO.

ボーリング名	NO. 1	調査位置	熊本市沖新町					北　緯	32° 45′ 50.0974″
発注機関				調査期間	～			東　経	130° 35′ 18.5893″
調査業者名		主任技師		現場代理人		コア鑑定者		ボーリング責任者	
孔口標高	6.26 m	角度	180° 上 90° 下 0°	方向	北 0° 西 270° 東 90° 南 180°	地盤勾配	鉛直 90° 水平 0°	使用機種	
総掘進長	48.50 m								

試錐機	東邦油圧式_D-0	ハンマー落下用具	コーンプーリー法
エンジン	ﾔﾝﾏｰ_NS90C	ポンプ	V-3

標尺 (m)	標高 (m)	層厚 (m)	深度 (m)	柱状図	土質区分	色調	相対密度	相対稠度	記事
	5.41	0.85	0.85		火山灰質粘土(黒ボク)(V)	暗褐灰		軟	中塑性若干小礫を混じえる。・
1～12	-6.14	11.55	12.40		貝殻片混り砂(S)	淡灰～淡褐灰	緩い		貝殻片を多く含む細～中粒砂主体。
13～14	-8.04	1.90	14.30		細砂・シルト互層(FS/M)	暗灰	中ぐらい		均等細粒砂と高塑性な粘土質シルトとの不規則な細互層。
15					粘土質シルト～シルト質粘土(M)	青灰～暗青灰～暗灰		極軟	高含水で高塑性撹乱により流動化し易い高鋭敏均一海成細粒土。又貝殻細片、有機物を若干含む。下部では貝殻細片少なくなり、有機物の含有多くなる。

地層岩体区分	孔内水位(m)／測定月日

標準貫入試験

深度 (m)	10cmごとの打撃回数 0－10	10－20	20－30	打撃回数／貫入量 (cm)	N値
1.15～1.45	2	4	3	9／30	9
2.15～2.45	4	3	4	11／30	11
3.15～3.45	3	3	3	9／30	9
4.15～4.45	5	5	5	15／30	15
5.15～5.46	1／8	2／11	2／12	5／31	5
6.15～6.45	5	4	4	13／30	13
7.15～7.45	3	4	4	11／30	11
8.15～8.45	5	5	5	15／30	15
9.15～9.45	7	7	8	22／30	22
10.15～10.45	4	4	4	12／30	12
11.15～11.45	3	3	3	9／30	9
12.15～12.45	2	3	4	9／30	9
13.15～13.45	6	7	8	21／30	21
14.15～14.47	1／11	1	1／11	3／32	3

原位置試験 深度 (m)	試験名および結果

試料採取 深度 (m)	試料番号	採取方法
15.00	1-1	

室内試験	掘進月日

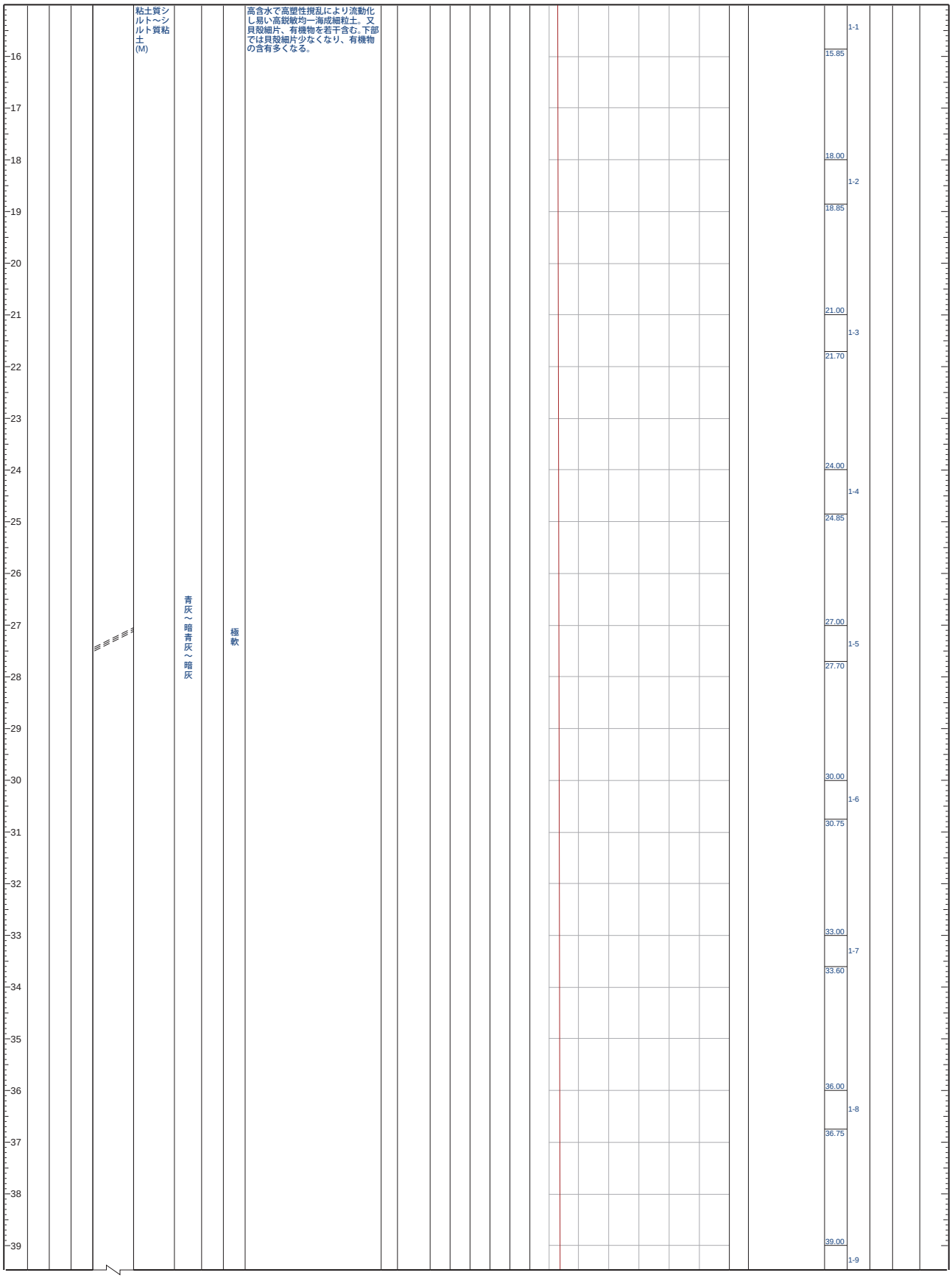
粘土質シルト～シルト質粘土
(M)
青灰～暗青灰～暗灰
極軟
高含水で高塑性撹乱により流動化し易い高鋭敏均一海成細粒土。又貝殻細片、有機物を若干含む。下部では貝殻細片少なくなり、有機物の含有多くなる。
15.85
18.00
18.85
21.00
21.70
24.00
24.85
27.00
27.70
30.00
30.75
33.00
33.60
36.00
36.75
39.00
1-1
1-2
1-3
1-4
1-5
1-6
1-7
1-8
1-9

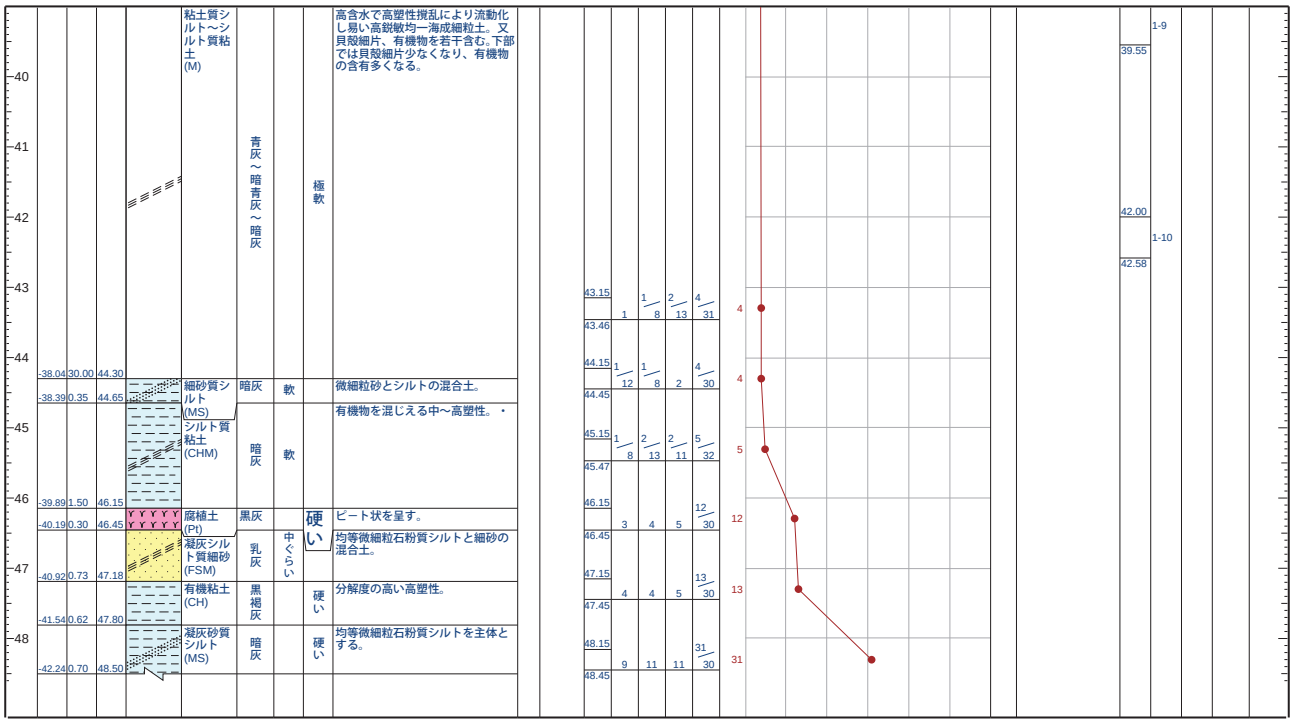
粘土質シルト～シルト質粘土 (M)
青灰～暗青灰～暗灰
極軟
高含水で高塑性撹乱により流動化し易い高鋭敏均一海成細粒土。又貝殻細片、有機物を若干含む。下部では貝殻細片少なくなり、有機物の含有多くなる。
-38.04
30.00
44.30
-38.39
0.35
44.65
細砂質シルト (MS)
暗灰
軟
微細粒砂とシルトの混合土。
シルト質粘土 (CHM)
暗灰
軟
有機物を混じえる中～高塑性。・
-39.89
1.50
46.15
-40.19
0.30
46.45
腐植土 (Pt)
黒灰
硬い
ピート状を呈する。
凝灰シルト質細砂 (FSM)
乳灰
中くらい
均等微細粒石粉質シルトと細砂の混合土。
-40.92
0.73
47.18
-41.54
0.62
47.80
有機粘土 (CH)
黒褐灰
硬い
分解度の高い高塑性。
凝灰砂質シルト (MS)
暗灰
硬い
均等微細粒石粉質シルトを主体とする。
-42.24
0.70
48.50
40
41
42
43
44
45
46
47
48
43.15
43.46
44.15
44.45
45.15
45.47
46.15
46.45
47.15
47.45
48.15
48.45
1-9
39.55
42.00
1-10
42.58

ボーリング柱状図

調　査　名

事業・工事名

ボーリングNO.

シートNO.

ボーリング名	本堤 沈下計	調査位置	熊本県熊本市新港地内 E護岸(No.24+5)			北　緯	32° 45′ 54″
発注機関				調査期間	1996-09-20 ～ 1996-09-25	東　経	130° 35′ 28.69″
調査業者名		主任技師		現場代理人		コア鑑定者		ボーリング責任者	
孔口標高	0.65 m	角度	上 180° 90° 下 0° 0°	方向	北 0° 東 90° 南 180° 西 270°	地盤勾配	鉛直 90° 水平 0°	使用機種	試錐機	YSO－1	ハンマー落下用具	コーンプーリー法
総掘進長	49 m								エンジン	NS-90	ポンプ	SP-40

標尺 (m)	標高 (m)	層厚 (m)	深度 (m)	柱状図	土質区分	色調	相対密度	相対稠度	記事	地層岩体区分	孔内水位 (m) ／ 測定月日	標準貫入試験 深度 (m)	10cmごとの打撃回数 0－10	10－20	20－30	打撃回数／貫入量 (cm)	N値 0 10 20 30 40 50	原位置試験 深度 (m)	試験名および結果	試料採取 深度 (m)	試料番号	採取方法	室内試験	掘進月日
0					砂 (S)	暗灰	緩い		サンドマット															
	-0.85	1.50	1.50																					
					シルト質粘土 (CHM)				極軟弱粘性土状シルト，粘土分を主体に、貝殻片，腐植物を混入															
						暗灰		非常に軟らかい																
	-9.35	8.50	10.00																					
					礫混じり砂 (S-G)	暗灰	緩い		細～中砂状薄い粘性土との互層状															
	-10.45	1.10	11.10																					
					シルト質粘土 (CHM)				極軟弱粘性土状シルト，粘土分を主体に、貝殻片，腐植物を混入															
						暗灰		非常に軟らかい																
15																								

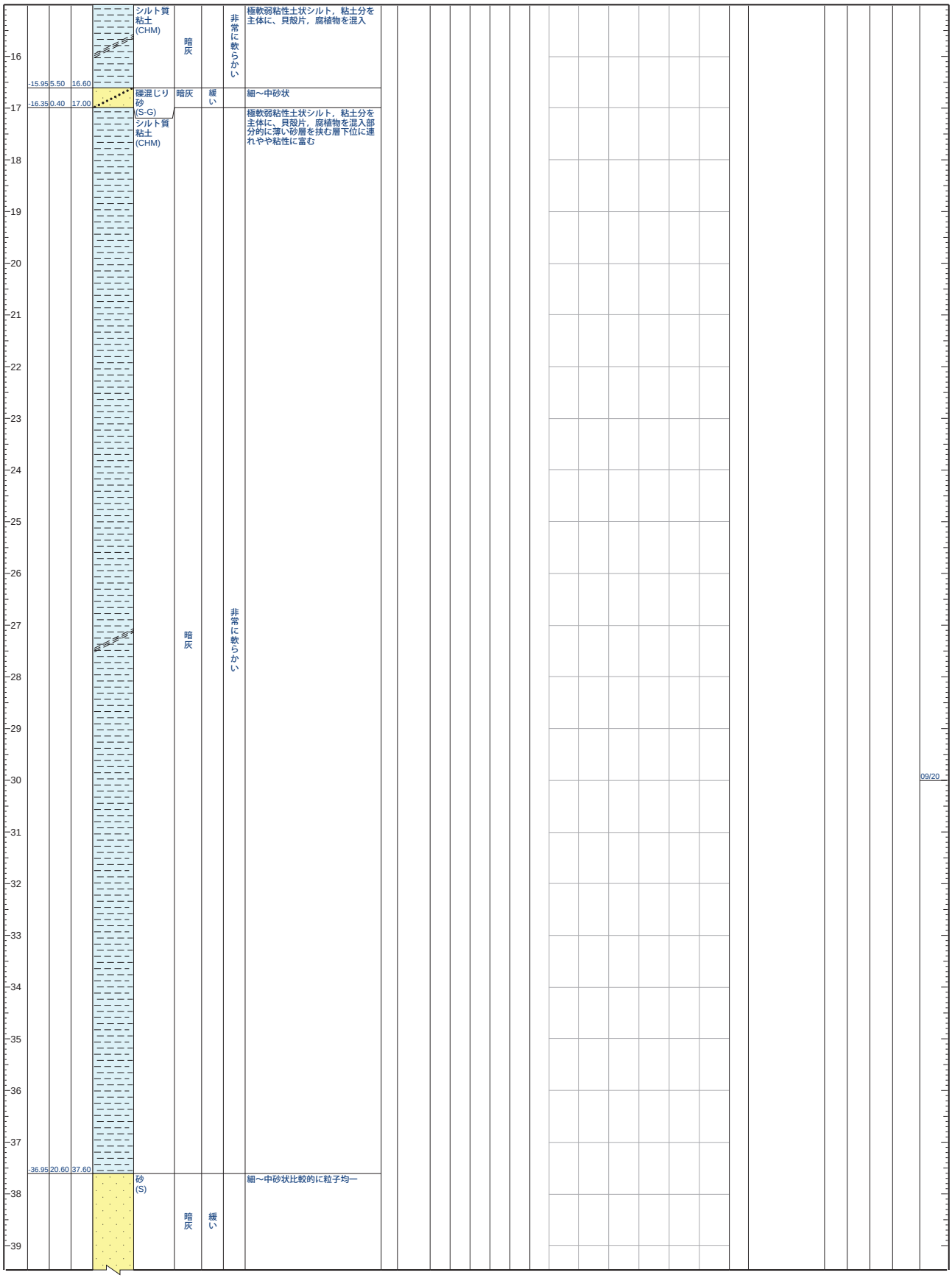
-15.95
5.50
16.60
シルト質粘土 (CHM)
暗灰
非常に軟らかい
極軟弱粘性土状シルト，粘土分を主体に、貝殻片，腐植物を混入
-16.35
0.40
17.00
礫混じり砂 (S-G)
暗灰
緩い
細～中砂状
シルト質粘土 (CHM)
極軟弱粘性土状シルト，粘土分を主体に、貝殻片，腐植物を混入部分的に薄い砂層を挟む層下位に連れやや粘性に富む
暗灰
非常に軟らかい
-36.95
20.60
37.60
砂 (S)
細～中砂状比較的に粒子均一
暗灰
緩い
09/20

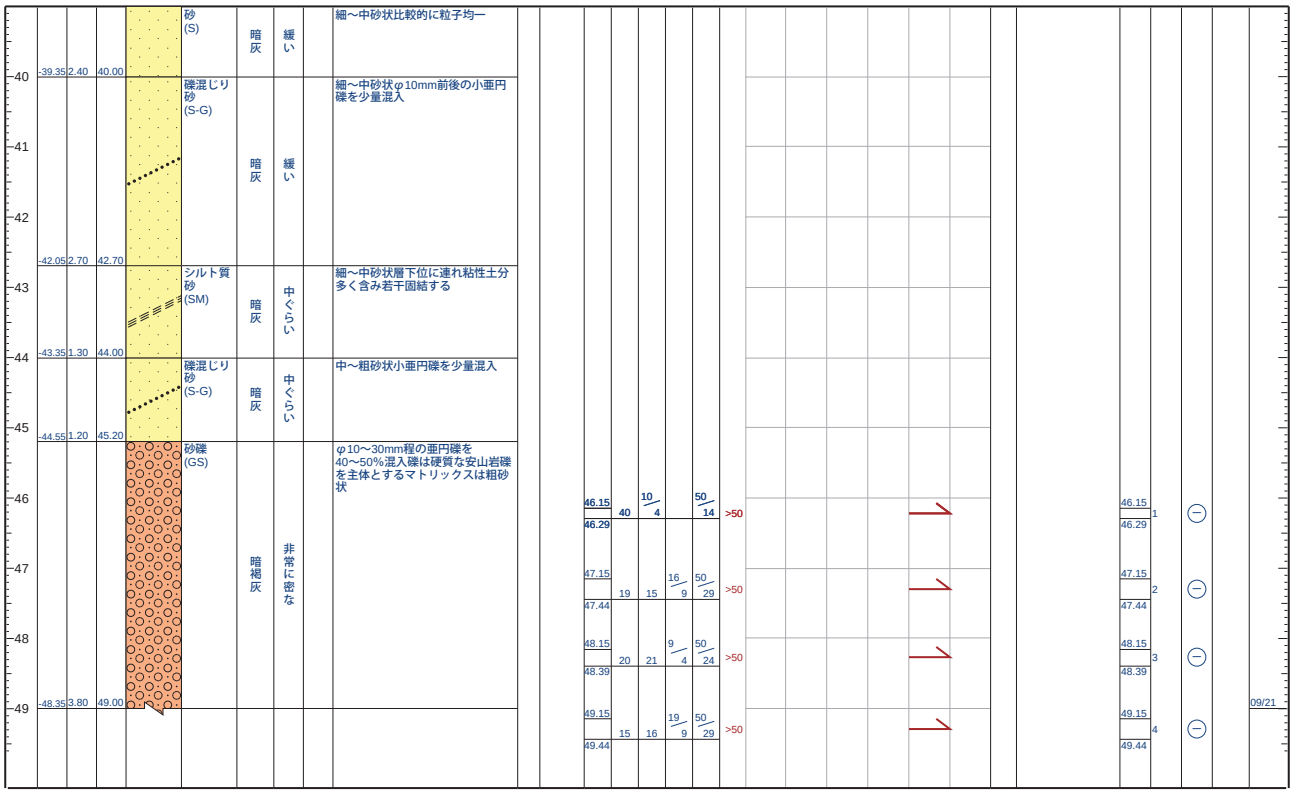
-39.35
2.40
40.00
砂
(S)
暗灰
緩い
細～中砂状比較的に粒子均一
礫混じり砂
(S-G)
暗灰
緩い
細～中砂状φ10mm前後の小亜円礫を少量混入
-42.05
2.70
42.70
シルト質砂
(SM)
暗灰
中ぐらい
細～中砂状層下位に連れ粘性土分多く含み若干固結する
-43.35
1.30
44.00
礫混じり砂
(S-G)
暗灰
中ぐらい
中～粗砂状小亜円礫を少量混入
-44.55
1.20
45.20
砂礫
(GS)
暗褐灰
非常に密な
φ10～30mm程の亜円礫を40～50%混入礫は硬質な安山岩礫を主体とするマトリックスは粗砂状
-48.35
3.80
49.00
40
19
15
20
21
15
16
10/4
16/9
9/4
19/9
50/14
50/29
50/24
50/29
>50
>50
>50
>50
46.15
46.29
47.15
47.44
48.15
48.39
49.15
49.44
1
2
3
4
09/21

土　　性　　図

ボーリング名称 ： 843054010057　　地盤高 ： -1.25m

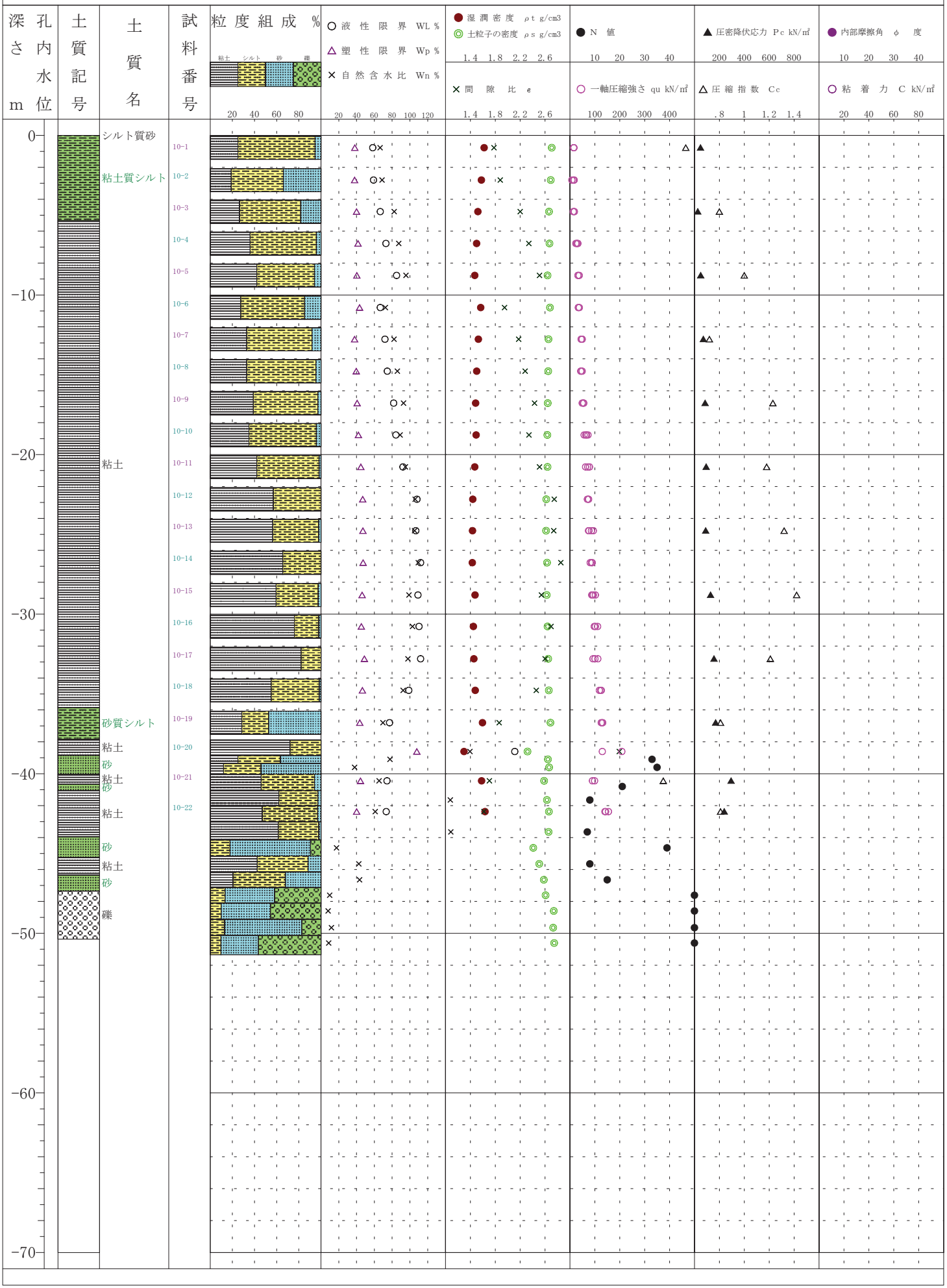

Shirakawa River Building
Liquefaction Area Boring Logs

ボーリング柱状図

調　査　名　新土河原地区外地質調査業務

事業・工事名　新土河原地区外地質調査業務

ボーリングNO.

シートNO.

ボーリング名	右2(右岸8k370付近)	調査位置				北　緯	32° 46' 04.1221"
発注機関	国土交通省 九州地方整備局 熊本河川国道事務所			調査期間	平成17年02月25日 ～ 平成17年03月29日	東　経	130° 41' 29.6750"
調査業者名	株式会社東建ジオテック	主任技師	中薗幸宗	現場代理人	草葉　健	コア鑑定者	桑野代介	ボーリング責任者	鳥田貴照
孔口標高	10.96 m	角度	180°(上) 90° 0°(下)	方向	0°(北) 90°(東) 180°(南) 270°(西)	地盤勾配	角度 水平 0° 26° 90°	使用機種	試錐機	東邦BD-1	ハンマー落下用具	トンビ
総掘進長	25.00 m								エンジン	ヤンマーF-7	ポンプ	東邦BG-3C

標尺 (m)	標高 (m)	層厚 (m)	深度 (m)	柱状図	土質区分	色調	相対密度	相対稠度	記事	地層・岩体区分	孔内水位 (m) / 測定月日	標準貫入試験 深度 (m)	10cmごとの打撃回数 0～10	10～20	20～30	打撃回数／貫入量 (cm)	N値	原位置試験 深度 (m)	試験名および結果	試料採取 深度 (m)	試料番号	採取方法	室内試験	掘進月日
1	7.46	3.50	3.50		シルト質細砂(FSM)砂質土(SF)	暗褐			堤体盛土でローム質の火山灰質細砂を主体とする。 盛土としては比較的均質であるが、所により安山岩礫点在する。。 深度1.0m付近には草根混入。 含水比は少ない～中位。 深度3.2～3.5mにはコンクリート片を混入し、砕けて礫状に採取される。		03/03 5.00 ▽	1.15	3	4	5	12				1.50	S-1		03/02
2												1.45												
3												2.15	4	3	4	11				2.00				
4	5.96	1.50	5.00		砂質シルト(MS)粘性土(C)	暗褐			火山灰質の砂質粘土主体。 径10～20mm亜円礫混入する。 含水量はやや多い。下部に向けさらに多くなる。			2.45	50/2			50/1								
5												3.15												
6												3.17												
7	4.26	1.70	6.70		砂質シルト(MS)粘性土(C)	暗褐			火山灰質の砂質粘土。層相均質であるが、シルト～細砂多く混入する。所により砂質土状を呈する。 含水比は中位～やや多い。			4.15	1/30			1								
8												4.45								4.30	S-1			
9												5.15	1	1	1	3				5.10				
10												5.45								5.50	S-2			
11												6.15	1	2	2	5				6.30				
12	2.36	1.90	8.60		シルト質細砂(FSM)砂質土(SF)	黒			火山灰質の細砂を主体とする。粒径均一。深度6.8m付近には径30～50mmの礫を混入。 シルト分をやや多く混入。含水量やや少なく固結土状。ポロポロと砕けやすい。			6.45	9	12	8	29				7.00				
13												7.15												
14												7.45	6	6	8	20				8.00	S-3			
15												8.15								8.70				
16	1.11	1.25	9.85		礫質土(FG)砂質土(SF)	黒			火山灰質細砂よりなり、粒径均一。粘性土分含有量は少ない。含水量は中位。 深度8.0m付近に粘土層薄層挟在。			8.45	6	6	8	20				9.00				
17												9.15								9.70	S-4			
18												9.45	1	1	2	4				10.50				
19	-0.54	1.65	11.50		砂質粘土(CHS)粘性土(C)	暗青灰			比較的均質であるが、砂分を少量混入する。 含水比は中位で、粘着性が強い。			10.15	1/15			1/15				11.20	S-5			
20												10.45												
21												11.15												
22												11.5												
23												12.15	3	2	2	7				13.00	S-6			
24												12.45												
25												13.15	1	1	1	3								
26												13.45												
27												14.15	1	1	2	4								
28												14.45												
29												15.15	1	1	1	3								
30												15.45												
31	-5.04	5.40	16.90		シルト質細砂(FSM)砂質土(SF)	黒			粒径均一である。 シルト分をやや多く混入する。 含水比は中位～やや多い。 深度16.0m付近よりシルト分が次第に減少し、下位の細砂層に漸移する。			16.15	3	4	5	12								
32												16.45												
33												17.15	8	9	10	27								
34												17.45												
35												18.15	10	13	9	32								
36												18.45												
37												19.15	10	13	14	37								
38												19.45												
39												20.15	13	16	16	45		20.00	透水試験 4.54E-03					
40												20.45						20.50						
41												21.15	10	7	9	26								
42	-11.04	6.35	23.25			暗灰						21.45												
43						黒						22.15	5	2	3	10								
44					粘土質シルト(MC)粘性土(C)	暗灰			均質である。 粘土分をやや多く含有する。 含水量がやや多く非常に軟質である。 下部に向かって粘土分が徐々に多くなる。			22.45													
45												23.15	1/15	1	1	3/35								
46												23.5												
47						暗灰						24.15	2	1	1	4								
48	-14.04	2.75	25.00									24.45												
49												25.15	1/15	1/15		2								
50												25.45												

ボーリング柱状図

調　　査　　名　白川河道部地質調査業務

事業・工事名

ボーリングNO.

シートNO.

ボーリング名		調査位置							北　緯	32° 46' 18.088"	
発注機関	国土交通省 九州地方整備局 熊本河川国道事務所			調査期間	～ 1993-08				東　経	130° 41' 26.79"	
調査業者名	応用地質株式会社	主任技師		現場代理人		コア鑑定者			ボーリング責任者		
孔口標高	6.14 m	角度	180° 上 / 下 90°	方向	0° 北 / 90° 東 / 180° 南 / 270° 西	地盤勾配	角度 90° / 水平 0°	使用機種	試錐機		ハンマー落下用具	
総掘進長	5.00 m								エンジン		ポンプ	

標尺 (m)	標高 (m)	層厚 (m)	深度 (m)	柱状図	土質区分	色調	相対密度	相対稠度	記事	地層・岩体区分	孔内水位 (m) / 測定月日	標準貫入試験 深度 (m)	10cmごとの打撃回数 0～10	10～20	20～30	打撃回数／貫入量 (cm)	N値	原位置試験 深度 (m)	試験名および結果	試料採取 深度 (m)	試料番号	採取方法	室内試験	掘進月日
1	5.14	1.00	1.00		砂利・礫混り砂	褐灰																		
2					砂	暗褐灰																		
3	2.14	3.00	4.00																					
4	1.14	1.00	5.00		砂利・礫混り砂	灰褐																		
5																								

Depression Zone Boring Logs

ボーリング柱状図

調　査　名

事業・工事名

ボーリングNO.

シートNO.

ボーリング名	No.1	調査位置	熊本県阿蘇郡阿蘇町狩尾			北　緯	32° 57′ 8.2000″
発注機関				調査期間	1997-10-03 ～ 1997-12-11	東　経	131° 1′ 32.3000″
調査業者名		主任技師		現場代理人		コア鑑定者		ボーリング責任者	
孔口標高	475.5 m	角度	上 180° 90° 下 0° 0°	方向	北 0° 東 90° 南 180° 西 270°	地盤勾配	鉛直 90° 水平 0°	使用機種	試錐機	YSO-1	ハンマー落下用具	コーンプーリー法
総掘進長	42.50 m								エンジン	NFD-8	ポンプ	SP-40

標尺 (m)	標高 (m)	層厚 (m)	深度 (m)	柱状図	土質区分	色調	相対密度	相対稠度	記事	地層岩体区分	孔内水位 (m) / 測定月日
1	474.05	1.45	1.45		埋土 (Fl)	黒褐			0～0．15m栗石 0．15～1．45m玉石混じりローム		
2					砂質ローム (LmS)	黒褐～暗褐			黒ボク～赤ボク主体礫を若干混入		
3	471.50	2.55	4.00								
4					火山灰質砂 (SV)	淡茶灰～暗灰			4．5～4．7mローム挟む微細砂から細砂状下部やや粒径大		
5											
6											10/24 6.60
7											10/11 7.40
8	467.50	4.00	8.00								
9					礫混じり砂 (S-G)	暗茶灰			φ10～50mmの火山岩、軽石亜円礫混入部分的に砂礫上を呈する．9．15～9．35mは暗灰の砂質シルトを挟む		
10	465.70	1.80	9.80								
	465.50	0.20	10.00		微細砂 (FS)	黒灰			均一		
	465.35	0.15	10.15			黒灰			砂シーム状		
	465.20	0.15	10.30		砂質シルト (MS)	暗灰			均質		
11	464.50	0.70	11.00		シルト質粘土 (CHM)	黒					
	463.95	0.55	11.55		腐植物混じり粘土 (CH)	黒灰					
12	463.20	0.75	12.30		シルト質砂 (SM)	暗灰			砂シーム状		
	462.45	0.75	13.05		シルト質粘土 (CHM)	暗灰			砂シーム状		
13					砂混じり粘土 (CH-S)				部分的に粘土を薄く挟む		
14					細砂 (FS)	黒灰					
15											

標準貫入試験

深度 (m)	10cmごとの打撃回数 0～10	10～20	20～30	打撃回数／貫入量 (cm)	N値
1.15	1	1	1	3/30	3
1.45	14		6		
2.15	1	1		2/36	2
2.51	20	16			
3.15	0	1		1/37	1
3.52	15	22			
4.15	3	3	3	9/30	9
4.45					
5.15	2	3	3	8/30	8
5.45					
6.15	2	3	5	10/30	10
6.45					
7.15	3	3	4	10/30	10
7.45					
8.15	6	6	6	18/30	18
8.45					
9.15	2	5	7	14/30	14
9.45					
10.15	1	1	1	3/30	3
10.45					
11.15	2	2	2	6/30	6
11.45					
12.15	1	2	2	5/30	5
12.45					
13.15	7	20	23/7	50/27	>50
13.42					
14.15	16	23	11/4	50/24	>50
14.39					
15.15	3	7	8	18/30	18

原位置試験 深度 (m)	試験名および結果
11.00	孔内水平載荷試験
11.00	Eb=20kgf/cm^2

試料採取 深度 (m)	試料番号	採取方法
10.50	T1-1	
11.00		

室内試験	掘進月日
	10/11
	10/14

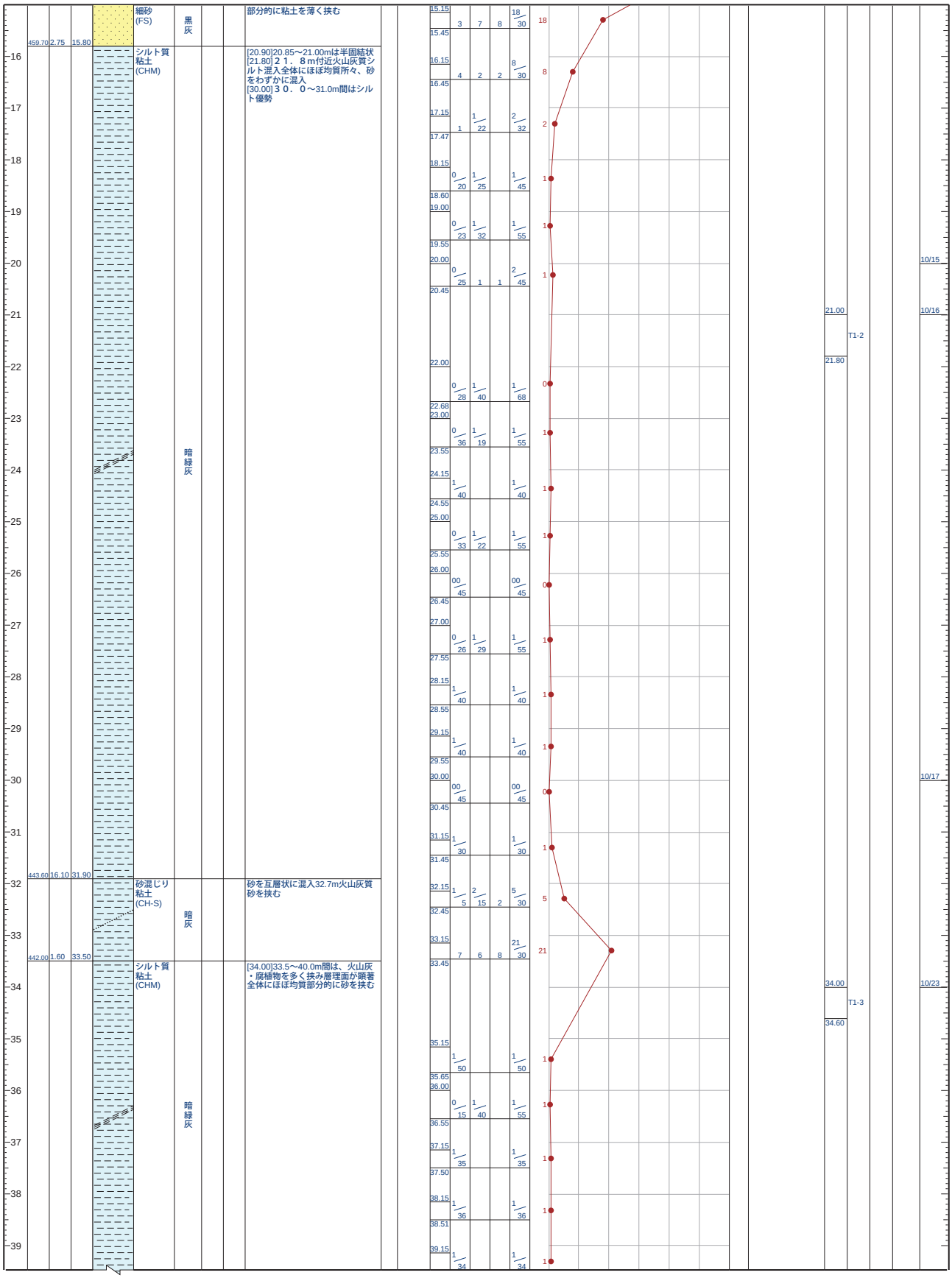
細砂 (FS)
黒灰
部分的に粘土を薄く挟む
459.70 2.75 15.80
シルト質粘土 (CHM)
[20.90]20.85～21.00mは半固結状
[21.80]２１．８m付近火山灰質シルト混入全体にほぼ均質所々、砂をわずかに混入
[30.00]３０．０～31.0m間はシルト優勢
暗緑灰
443.60 16.10 31.90
砂混じり粘土 (CH-S)
砂を互層状に混入32.7m火山灰質砂を挟む
暗灰
442.00 1.60 33.50
シルト質粘土 (CHM)
[34.00]33.5～40.0m間は、火山灰・腐植物を多く挟み層理面が顕著
全体にほぼ均質部分的に砂を挟む
暗緑灰
T1-2
T1-3
10/15
10/16
10/17
10/23

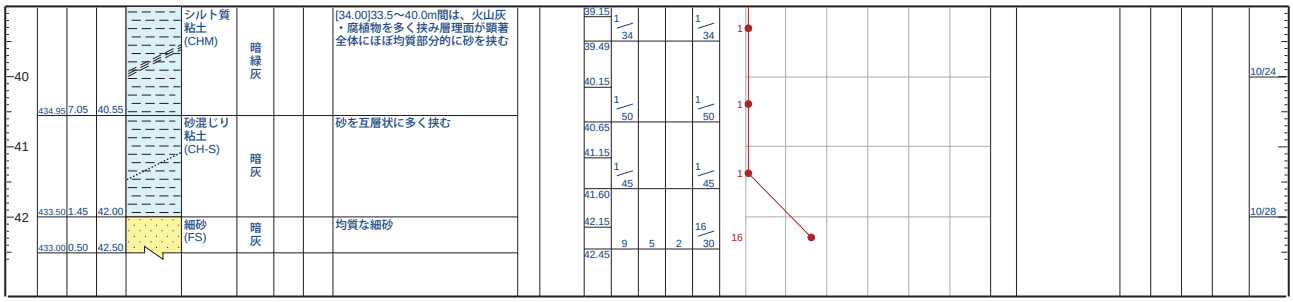
40
41
42
434.95
7.05
40.55
433.50
1.45
42.00
433.00
0.50
42.50
シルト質粘土 (CHM)
暗緑灰
[34.00]33.5～40.0m間は、火山灰・腐植物を多く挟み層理面が顕著全体にほぼ均質部分的に砂を挟む
砂混じり粘土 (CH-S)
暗灰
砂を互層状に多く挟む
細砂 (FS)
暗灰
均質な細砂
39.15
39.49
40.15
40.65
41.15
41.60
42.15
42.45
1/34
1/50
1/45
9
5
2
16/30
1
1
1
16
10/24
10/28

ボーリング柱状図

調　査　名　阿蘇三期地区農地集積加速化基盤整備事業第2号業務委託

事業・工事名　平成20年度　農地集積基盤　第0140-0-202号

ボーリングNO.

シートNO.

ボーリング名	No.1	調査位置	阿蘇市三久保地内			北　緯	32° 57′ 32.6000″
発注機関	阿蘇地域振興局　農林部　農地整備課			調査期間	2009-01-24 ～ 2009-03-16	東　経	131° 01′ 52.2000″
調査業者名	株式会社　三和地質コンサルタント 電話 (096-365-5741)	主任技師	瀬井真輔	現場代理人	段下圭一郎	コア鑑定者	瀬井真輔	ボーリング責任者	段下圭一郎
孔口標高	475.28 m	角度	上 180° 90° 下 0° 0.00°	方向	北 0° 東 90° 南 180° 西 270°	地盤勾配	鉛直 90° 水平 0° 90.00°	使用機種	試錐機	YSO-05型	ハンマー落下用具	トンビ法
総掘進長	12.00 m								エンジン	ヤンマーN9型	ポンプ	YSO-GP40型

標尺 (m)	標高 (m)	層厚 (m)	深度 (m)	柱状図	土質区分	色調	相対密度	相対稠度	記事	地層岩体区分	孔内水位 (m) ／ 測定月日
1	473.98	1.30	1.30		粘土 (CH)	暗茶～黒灰		軟らかい	上部20cm付近までは農耕土。 粘性中位で、含水量は中位～多い。 0.60mより腐植物を多く混入する。		02/11 1.60
2	471.48	2.50	3.80		シルト (M)	灰～暗灰		に軟らかい	全体に土性均一である。 含水量多く、粘性が強い。 腐植物や草根を混入する。 非常に軟らかい。		
4	468.88	2.60	6.40		砂混じりシルト (M-S)	暗灰		軟らかい	全体に細粒砂が混じる粘性土。 含水量多く、粘性が強い。 部分的に砂の混入量が多い箇所が見受けられる。 腐植物や草根が点在する。		
7	464.98	3.90	10.30		砂 (S)	黒灰		中ぐらい	粒径均一な細粒砂が主体である。 含水量多い。 7.70～8.30m間はシルト混じり砂～砂質シルト状となる。 部分的にシルト分をブロック状に混入する。 最下部ではφ5mm内の礫が点在する。		
12	463.28	1.70	12.00		砂 (S)	黒灰			粒径均一な細粒砂が主体である。 含水量中位。 φ5mm内の礫が点在する。		

標準貫入試験

深度 (m)	10cmごとの打撃回数 0～10	10～20	20～30	打撃回数／貫入量 (cm)	N値
1.15	1			1/35	1
1.50	35			35	
2.15	00			00/35	0
2.50	35			35	
3.15	00			00/35	0
3.50	35			35	
4.15	1			1/35	1
4.50	35			35	
5.15	1	1		2/35	2
5.50	20	15		35	
6.15	1	1		2/30	2
6.45	25	5		30	
7.15	6	6	5	17/30	17
7.45	00	1		4/30	4
8.15	15	5	3	30	
8.45	2	4	7	13/30	13
9.15				30	
9.45	1	7	17	25/30	25
10.15				30	
10.45	9	12	13	34/30	34
11.15				30	
11.45	6	9	18	33/30	33
12.00				30	
12.30					

原位置試験

深度 (m)	試験名および結果

試料採取

深度 (m)	試料番号	採取方法
3.00	1-1	
3.80		

室内試験	掘進月日
物理三軸圧密	02/10
	02/12
	02/13

ボーリング柱状図

調　査　名　阿蘇中部地区広域営農団地農道整備事業第9号業務委託

事業・工事名

ボーリングNO.　　シートNO.

ボーリング名	Bor.0	調査位置	阿蘇市的石外地内					北　緯	32° 55′ 00.0000″
発注機関	熊本県 阿蘇地域振興局 農林部 農地整備課			調査期間	2008-12-18 ～ 2008-12-20			東　経	130° 59′ 27.0000″
調査業者名	（株）東亜建設コンサルタント 電話 (096-384-2265)	主任技師	時松　奈緒子	現場代理人	時松　奈緒子	コア鑑定者	時松　奈緒子	ボーリング責任者	段下 圭一郎
孔口標高	464.82 m	角度	上 180° 90° 下 0° 0.00°	方向	北 0° 東 90° 南 180° 西 270°	地盤勾配	鉛直 90° 水平 0° 0.00°	使用機種	
総掘進長	10.00 m								

試錐機	吉田式 YSO-1型	ハンマー落下用具	コンプーリー
エンジン	ヤンマー NFAD-8型	ポンプ	吉田式GP-5

標尺 (m)	標高 (m)	層厚 (m)	深度 (m)	柱状図	土質区分	色調	相対密度	相対稠度	記事	地層岩体区分	孔内水位 (m) ／ 測定月日
1	463.32	1.50	1.50		盛土 (BS)	暗褐 茶褐			0.2mまでは農耕土 基盤整備の造成土 0.2～0.9mはシルト混り砂 0.9m以深は礫混り粘性土 φ2～5mmの礫を混入する		12/18 1.50
2	461.02	2.30	3.80		有機質シルト (MO)	黒灰			腐植物を多く含む 細～中砂の薄層を帯状に挟む 層下部は砂分多い 含水量は中位 【区分：粘性土】		
4	460.72	0.30	4.10		砂 (S)	黒灰			粒径均一な細砂　含水量は中位		
	459.82	0.90	5.00		有機質シルト (MO)	暗褐灰			腐植物を多く含む 粘性，含水量は中位 【区分：粘性土】		
6	457.42	2.40	7.40		砂質シルト (MS)	暗灰			臭気強い 腐植物が点在する 粘性は中位 最上部は粘土分優勢 含水量は中位 【区分：粘性土】		
8	456.82	0.60	8.00		シルト混り砂 (S-M)	暗灰			粒径均一な細砂主体 全体にシルト分を混入 含水量多い 【区分：砂質土】		
9	454.82	2.00	10.00		砂質シルト (MS)	暗灰			粘性やや強い 臭気がやや感じられる 腐植物が点在する 含水量は中位 【区分：粘性土】 含水量多い 10.1m以深は細砂 部分的にφ2cm程の細礫を混入		

標準貫入試験

深度 (m)	10cmごとの打撃回数 0－10	10－20	20－30	打撃回数／貫入量 (cm)
1.15	0	1		1
	20	15		35
1.50				
3.15	0	1		1
		25		35
3.50				
4.15	1			1
	35			35
4.50				
5.15	1			1
	35			35
5.50				
7.15	0	1		1
	15	20		35
7.50				
8.15	1			1
	35			35
8.50				
9.15	1			1
	35			35
9.50				
10.15	7	7	7	21
10.45				30

N 値　0　10　20　30　40　50

原位置試験 深度 (m)	試験名および結果

試料採取 深度 (m)	試料番号	採取方法	室内試験	掘進月日
1.50	TW0-1	A	物理的 圧密 三軸	12/18
2.30				
6.00	TW0-2	A	物理的 圧密 三軸	
6.80				12/19

ボーリング柱状図

調　査　名　阿蘇中部地区広域営農団地農道整備事業第9号業務委託

事業・工事名

ボーリングNO.

シートNO.

ボーリング名	Bor.2	調査位置	阿蘇市的石外地内					北　緯	32° 55′ 33.0000″
発注機関	熊本県 阿蘇地域振興局 農林部 農地整備課			調査期間	2008-10-14 〜 2008-10-28			東　経	130° 59′ 52.0000″
調査業者名	（株）東亜建設コンサルタント 電話 (096-384-2265)	主任技師	時松　奈緒子	現場代理人	時松　奈緒子	コア鑑定者	時松　奈緒子	ボーリング責任者	宮崎 貴明
孔口標高	470.43 m	角度	180° 上 90° 下 0° 0.00°	方向	北 0° 270° 西 90° 東 180° 南	地盤勾配	鉛直 90° 水平 0° 0.00°	使用機種	試錐機 東邦式 D0-C型 / ハンマー落下用具 自動落下
総掘進長	38.00 m								エンジン ヤンマー NFAD-8型 / ポンプ 東邦式 BG-3C型

標高 (m)	層厚 (m)	深度 (m)	土質区分	色調	相対密度	相対稠度	記事
469.63	0.80	0.80	礫混り粘土 (CH-G)	黒褐			φ1〜3cmの礫を混入 盛土　【区分：粘性土】
465.08	4.55	5.35	有機質シルト (MO)	黒褐		非常に軟かい	含水量は非常に多い 【区分：粘性土】 4m貫入試料に腐植物を多く含む コアは指圧で容易に凹む 粘性は弱い 極めて軟質な状態 腐植物片を含むシルト層
464.63	0.45	5.80	火山灰質砂 (SV)	白灰			崩壊性やや有り【区分：砂質土】 含水量非常に多い 粒径均一な火山微細砂
			砂混りシルト (M-S)	黒灰		非常に軟かい	色調が淡灰色に変化する 【区分：粘性土】 含水量は多い 14m付近で腐植物を少量混入する 7,8m貫入試料に腐植物を多量混入 11.5〜12.0m間，15m付近で火山灰を混入 水平層理が見られる 部分的に砂分を混入する 極めて軟質なシルト層 粘性は中位〜やや強い

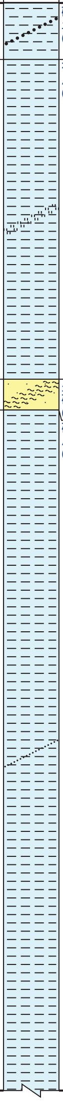

孔内水位 (m) ／ 測定月日

10/27 1.15

10/17 2.00

標準貫入試験

深度 (m)	0-10	10-20	20-30	打撃回数／貫入量 (cm)
1.15–1.49	1	1/12	1/12	3/34
2.00–2.35	0/35			0/35
3.00–3.25	0/25			0/25
4.00–4.45	0/45			0/45
5.15–5.57	1/15	1/15	2/12	4/42
6.00–6.35	0/35			0/35
7.00–7.40	0/40			0/40
8.00–8.25	0/25			0/25
9.00–9.70	0/70			0/70
10.00–10.70	0/70			0/70
11.00–11.40	0/40			0/40
12.00–12.52	0/52			0/52
13.00–13.70	0/70			0/70
14.00–14.50	0/50			0/50
15.00–15.35	0/35			0/35

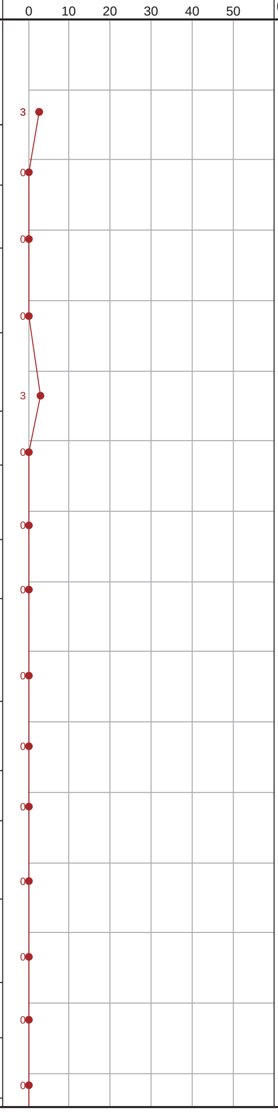

原位置試験　深度 (m)　試験名および結果

試料採取　深度 (m)　試料番号　採取方法

室内試験

掘進月日

10/17

10/18

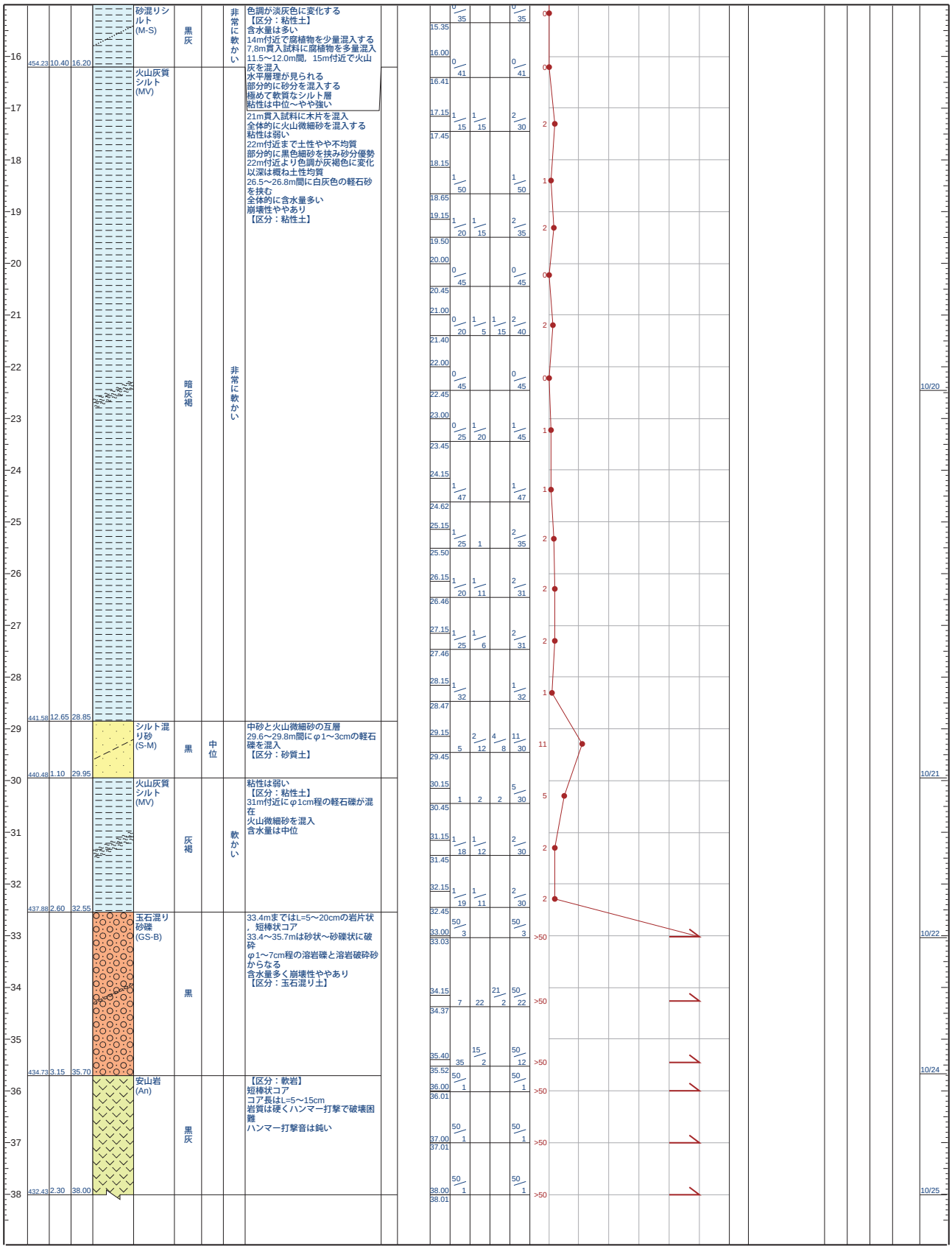
砂混りシルト (M-S)
黒灰
非常に軟かい
色調が淡灰色に変化する
【区分：粘性土】
含水量は多い
14m付近で腐植物を少量混入する
7.8m貫入試料に腐植物を多量混入
11.5～12.0m間，15m付近で火山灰を混入
454.23 10.40 16.20
火山灰質シルト (MV)
暗灰褐
非常に軟かい
水平層理が見られる
部分的に砂分を混入する
極めて軟質なシルト層
粘性は中位～やや強い
21m貫入試料に木片を混入
全体的に火山微細砂を混入する
粘性は弱い
22m付近まで土性やや不均質
部分的に黒色細砂を挟み砂分優勢
22m付近より色調が灰褐色に変化
以深は概ね土性均質
26.5～26.8m間に白灰色の軽石砂を挟む
全体的に含水量多い
崩壊性ややあり
【区分：粘性土】
441.58 12.65 28.85
シルト混り砂 (S-M)
黒
中位
中砂と火山微細砂の互層
29.6～29.8m間にφ1～3cmの軽石礫を混入
【区分：砂質土】
440.48 1.10 29.95
火山灰質シルト (MV)
灰褐
軟かい
粘性は弱い
【区分：粘性土】
31m付近にφ1cm程の軽石礫が混在
火山微細砂を混入
含水量は中位
437.88 2.60 32.55
玉石混り砂礫 (GS-B)
黒
33.4mまではL=5～20cmの岩片状，短棒状コア
33.4～35.7mは砂状～砂礫状に破砕
φ1～7cm程の溶岩礫と溶岩破砕砂からなる
含水量多く崩壊性ややあり
【区分：玉石混り土】
434.73 3.15 35.70
安山岩 (An)
黒灰
【区分：軟岩】
短棒状コア
コア長はL=5～15cm
岩質は硬くハンマー打撃で破壊困難
ハンマー打撃音は鈍い
432.43 2.30 38.00
10/20
10/21
10/22
10/24
10/25

ボーリング柱状図

調　査　名　阿蘇中部地区広域営農団地農道整備事業第9号業務委託

事業・工事名

ボーリングNO.　　シートNO.

ボーリング名	Bor.5	調査位置	阿蘇市的石外地内					北　緯	32° 55′ 50.0000″
発注機関	熊本県 阿蘇地域振興局 農林部 農地整備課			調査期間	2008-10-21 ～ 2008-11-01			東　経	131° 00′ 21.0000″
調査業者名	（株）東亜建設コンサルタント 電話 (096-384-2265)	主任技師	時松　奈緒子	現場代理人	時松　奈緒子	コア鑑定者	時松　奈緒子	ボーリング責任者	芦原　清行
孔口標高	469.58 m	角度	上 180° 90° 下 0° 0.00°	方向	北 0° 東 90° 南 180° 西 270°	地盤勾配	鉛直 90° 水平 0° 0.00°	使用機種	
総掘進長	31.00 m								

試錐機	東邦式 D0-D型	ハンマー落下用具	自動落下
エンジン	ヤンマー NFAD-8型	ポンプ	東邦式 BG-3C型

標尺 (m)	標高 (m)	層厚 (m)	深度 (m)	柱状図	土質区分	色調	相対密度	相対稠度	記事
	465.28	4.30	4.30		礫混り粘性土 (C-G)	暗褐		軟かい～中位	2m付近より軟質な火山礫を混入 礫径はφ5～40mmで混入率は約40% 2.7～3.6m間に軽石を多く含む 3.0～3.5mは軽石の風化土 土性不均質で色調が著しく変化 含水量は少ない 【区分：粘性土】 河川堤防盛土
	463.78	1.50	5.80		砂 (S)	黒	密な		【区分：砂質土】 粒径均一な細砂 非常に締まっている 含水量は多い
	462.58	1.20	7.00		礫混り砂 (S-G)	黒	密な		砂は粒径均一な細砂 礫の混入率は約20% 含水量多い　【区分：砂質土】 礫はφ2～10mmの亜円～亜角礫
					砂 (S)	黒	中位		【区分：砂質土】 粒径均一な微細～細砂 下部になるにつれ微細砂多くなる 層上部は締まった状態 下部になるにつれ徐々に緩くなる 含水量は多い 層下部で含水量非常に多くなる 粘性なし
	455.98	6.60	13.60		砂質シルト (MS)	褐灰		軟かい～中位	火山微細～細砂とシルトからなる 部分的に黒色細砂を互層状に挟む 粘性は弱い～中位 含水量は多い 【区分：砂質土】 全体的にはシルト分優勢

地層岩体区分	孔内水位 (m) ／ 測定月日
	10/22 3.90

標準貫入試験

深度 (m)	10cmごとの打撃回数 0－10	10－20	20－30	打撃回数／貫入量 (cm)
1.15	1	2	3	6／33
1.48				
2.15	1	2	2	5／32
2.47				
3.00	0			0／46
3.46				
4.20	13	15	18	46／30
4.50				
5.15	9	11	15	35／30
5.45				
6.15	9	10	11	30／30
6.45				
7.15	7	8	9	24／30
7.45				
8.15	8	10	14	32／30
8.45				
9.15	6	7	8	21／30
9.45				
10.15	6	6	7	19／30
10.45				
11.15	4	5	6	15／30
11.45				
12.15	4	4	6	14／30
12.45				
13.15	4	4	4	12／30
13.45				
14.15	1	1		3／35
14.50	11	14	1	
15.15	1	1		2／31
	17	14		

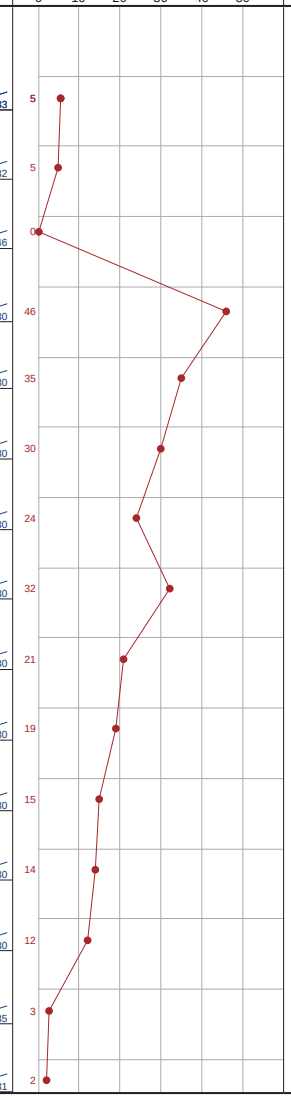

原位置試験

深度 (m)	試験名および結果

試料採取 深度 (m)	試料番号	採取方法	室内試験
5.15	5-1	A	物理的
5.45			
6.15	5-2	A	物理的
6.45			
9.15	5-3	A	物理的
9.45			

掘進月日
10/21
10/22
10/23

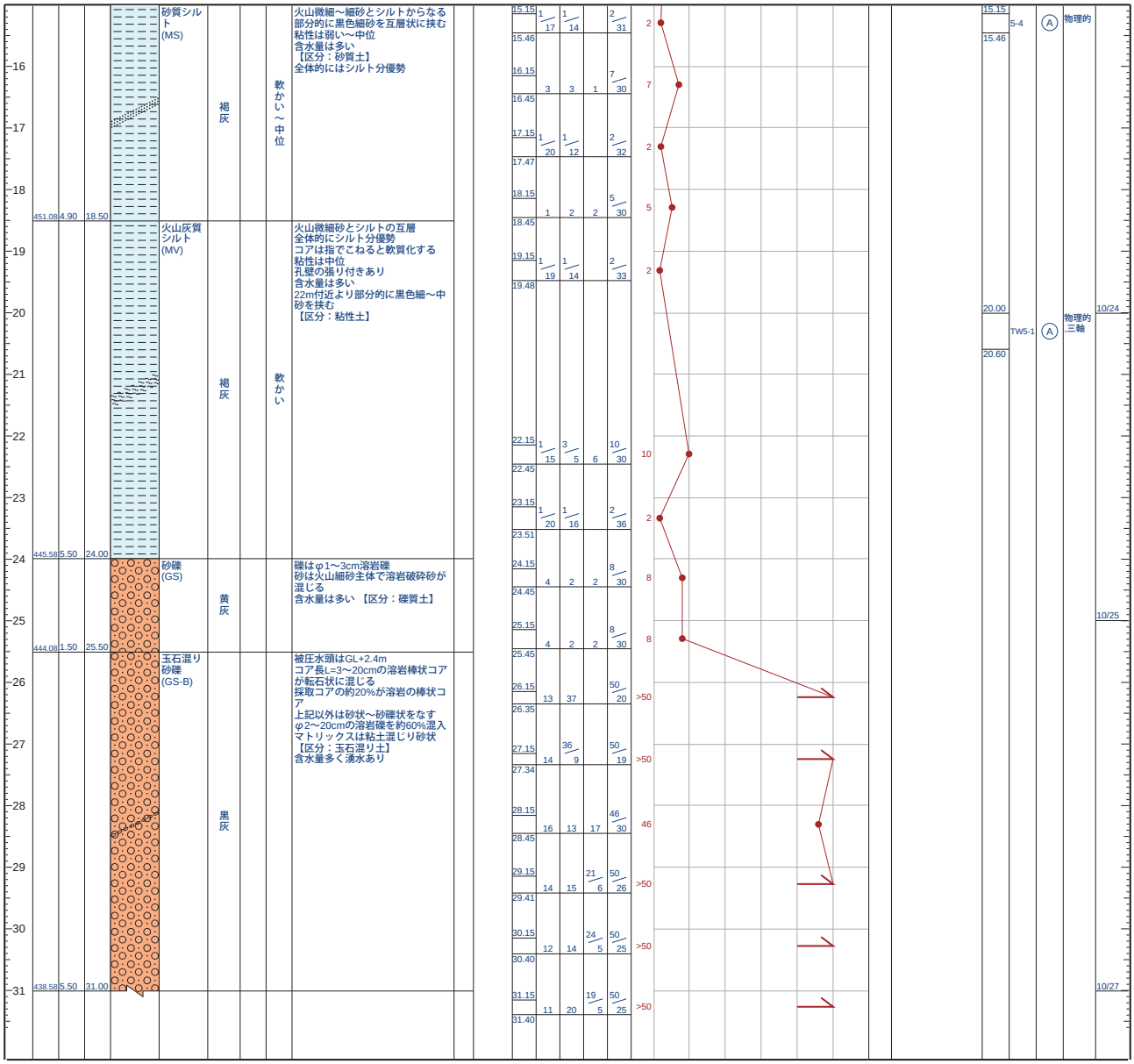
砂質シルト
(MS)
褐灰
軟かい～中位
火山微細～細砂とシルトからなる
部分的に黒色細砂を互層状に挟む
粘性は弱い～中位
含水量は多い
【区分：砂質土】
全体的にはシルト分優勢
451.08
4.90
18.50
火山灰質
シルト
(MV)
褐灰
軟かい
火山微細砂とシルトの互層
全体的にシルト分優勢
コアは指でこねると軟質化する
粘性は中位
孔壁の張り付きあり
含水量は多い
22m付近より部分的に黒色細～中砂を挟む
【区分：粘性土】
445.58
5.50
24.00
砂礫
(GS)
黄灰
礫はφ1～3cm溶岩礫
砂は火山細砂主体で溶岩破砕砂が混じる
含水量は多い 【区分：礫質土】
444.08
1.50
25.50
玉石混り
砂礫
(GS-B)
黒灰
被圧水頭はGL+2.4m
コア長L=3～20cmの溶岩棒状コアが転石状に混じる
採取コアの約20%が溶岩の棒状コア
上記以外は砂状～砂礫状をなす
φ2～20cmの溶岩礫を約60%混入
マトリックスは粘土混じり砂状
【区分：玉石混り土】
含水量多く湧水あり
438.58
5.50
31.00
15.15
15.46
16.15
16.45
17.15
17.47
18.15
18.45
19.15
19.48
22.15
22.45
23.15
23.51
24.15
24.45
25.15
25.45
26.15
26.35
27.15
27.34
28.15
28.45
29.15
29.41
30.15
30.40
31.15
31.40
>50
46
5-4
TW5-1
A
物理的
三軸
20.00
20.60
10/24
10/25
10/27

ボーリング柱状図

調　査　名　笹原橋橋梁改築測量設計業務委託

事業・工事名

ボーリングNO.　　シートNO.

ボーリング名	No.1	調査位置	阿蘇市阿蘇町狩尾地内					北　緯	32° 57′ 23.7600″
発注機関	阿蘇市役所			調査期間	2007-01-20 ～ 2007-01-21			東　経	131° 02′ 17.3400″
調査業者名	双建コンサルタント株式会社 電話 (096-366-0755)	主任技師	齋藤　慎也	現場代理人	齋藤　慎也	コア鑑定者	西浦　譲二	ボーリング責任者	岡田　清隆
孔口標高	476.13 m	角度	上 180° / 下 0°, 90°	方向	北 0°, 東 90°, 南 180°, 西 270°	地盤勾配	鉛直 90°, 水平 0°	使用機種	
総掘進長	12.00 m							試錐機	D0-C型
								エンジン	NFAD8-K型
								ハンマー落下用具	
								ポンプ	BG-3C型

標尺 (m)	標高 (m)	層厚 (m)	深度 (m)	柱状図	土質区分	色調	相対密度	相対稠度	記事	地層岩体区分	孔内水位 (m) / 測定月日
0	475.83	0.30	0.30		表土 (SF)	暗褐			細礫を含む黒ボク質シルト		
1					砂質シルト (MS)	暗褐		非常に軟らかい	黒ボク質の二次火山灰土 粘性中位の軟いシルトからなる 微細砂を15~20%位，下部に従いやや多く混入 3m以深は含水量多く，細礫点在		
2											
3	472.63	3.20	3.50								3.25
4	471.23	1.40	4.90		シルト質砂礫 (GSM)	暗茶褐	緩い		径40mm以下の亜円礫主体 礫間充填物は細砂～中粗砂で ,4mまではシルトの割合が多い 含水量が非常に多い		
5	469.93	1.30	6.20		礫混り砂 (S-G)	黒灰	緩い		細中砂からなり，粗砂及び径10mm以下細礫が多く混じる シルト分を10%前後混入		
6	468.83	1.10	7.30		砂質シルト (MS)	黒灰		軟い	軟質な二次火山灰土 微細砂が20%位混入		
7					砂 (S)	黒灰	中位～密な		微細砂～細砂からなる 粒径非常に均一 上部の1m区間にシルト分が斑状に点在 10m以深は僅かに細礫が混じる 含水量は中位		
8											
9											
10	465.43	3.40	10.70								
11	464.63	0.80	11.50		砂質シルト (MS)	黒灰	軟い		軟弱な二次火山灰 含水量が多く粘性は中位 微細砂が25%位混入		
12	464.13	0.50	12.00		砂 (S)	黒灰	中位		粒子の揃った微細砂～細砂 細礫等の混入物はない		

標準貫入試験

深度 (m)	10cmごとの打撃回数 0|10	10|20	20|30	打撃回数／貫入量 (cm)
1.05	1			1/1
1.43	38/38			38/38
2.15	1/30			1/30
2.45				
3.15	1/36			1/36
3.51				
4.15	2/30	1/30	4/30	7/30
4.45				
5.15	1/30	2/30	3/30	6/30
5.45				
6.15	1/30	2/30	1/30	4/30
6.45				
7.15	2/30	4/30	5/12	11/32
7.47				
8.15	7/30	10/30	13/30	30/30
8.45				
9.15	10/30	10/30	14/30	34/30
9.45				
10.15	1/30	2/15	1/5	4/30
10.45				
11.15	1/19	1/17		2/36
11.51				
12.15	7/30	7/30	7/30	21/30
12.45				

N 値: 0 10 20 30 40 50

原位置試験 深度 (m)	試験名および結果

試料採取 深度 (m)	試料番号	採取方法

室内試験	掘進月日

ボーリング柱状図

調　査　名　平成１２年度　阿蘇大津道路地質調査業務

事業・工事名

ボーリングNO.

シートNO.

ボーリング名		調査位置				北緯	32° 54' 56.049"
発注機関	国土交通省 九州地方整備局 熊本河川国道事務所			調査期間	～ 2001-03	東経	130° 58' 55.183"
調査業者名	株式会社東建ジオテック	主任技師		現場代理人		コア鑑定者		ボーリング責任者	
孔口標高	464.83 m	角度	180°上下 90°	方向	0°北 90°東 180°下南 270°西	地盤勾配	0°	使用機種	試錐機		ハンマー落下用具	
縦掘進長	32.00 m						90°		エンジン		ポンプ	

標尺 (m)	標高 (m)	層厚 (m)	深度 (m)	柱状図	土質区分	色調	相対密度	相対硬度	記事	地層・岩体区分	孔内水位 (m) / 測定月日
1	463.93	0.90	0.90		表土	暗褐					0.70 / 02
2	463.38	0.55	1.55		シルト質砂	暗灰					
	462.8	0.35	1.90		砂質シルト	暗灰					
3					阿蘇質シルト	黒褐					
4	460.83	2.10	4.00								
5					粘土質シルト	暗灰					
6											
7	457.13	3.70	7.70								
8	456.78	0.35	8.05		砂混りシルト	暗灰					
9					シルト	黄緑灰					
10	454.88	1.90	9.95								
11					粘土質シルト	緑灰					
12											
13											
14											
15											
16											
17											
18											
19											
20	446.28	8.60	18.55		礫	暗灰					
21	445.68	0.60	19.15		シルト混り砂	暗灰					
	445.28	0.40	19.55		火山灰質シルト	灰緑灰					
	444.68	0.60	20.15		軟岩						
22					凝灰角礫岩	暗黒					
23											
24											
25											
26	439.93	4.75	24.90		礫	暗黒					
	439.03	0.90	25.80		軟岩						
27					凝灰角礫岩	暗黒					
28											
	438.03	1.00	26.80		礫	暗赤褐					
	437.73	0.30	27.10		軟岩						
29					凝灰角礫岩	暗黒					
30											
31											
32	432.83	5.00	32.00								

標準貫入試験

深度 (m)	10cmごとの打撃回数 0～10	10～20	20～30	打撃回数 / 貫入量 (cm)	N値
2.15				01	1
2.45					
3.65				01	1
3.95					
5				50/5	
7				01/50	1
7.5					
8.15				04	4
8.45					
9.15				05	5
9.45					
10.15				05	5
10.45					
11.15				06	6
11.45					
12.15				06	6
12.45					
13.15				07	7
13.45					
14.15				09	9
14.45					
15.15				11	11
15.45					
16.15				19	19
16.45					
17.15				06	6
17.45					
18.15				08	8
18.45					
19.15				10	10
19.45					
20.15				28	28
20.45					
21.15				50/28	50
21.45					
22.15				26	26
22.45					
23				50/04	50
23.04					
24.15				50/15	50
24.35					
25.15				50/25	50
25.4					
26.15				09	9
26.45					
27				50/15	50
27.25					
27.55					
28.4				34	34
28.7					
29.3				50	50
30					
30.3				50	50
31					
31.3				50	50
32					
32.3				50	50

原位置試験

深度 (m)	試験名および結果
4.60	孔内水平載荷試験 00021.01
7.30	孔内水平載荷試験 00023.36
11.50	孔内水平載荷試験 00067.12

試料採取 深度 (m)	試料番号	採取方法

室内試験

掘進月日

ボーリング柱状図

調　査　名　平成１２年度　阿蘇大津道路地質調査業務

事業・工事名

ボーリングNO.

シートNO.

ボーリング名		調査位置		北緯	32° 54' 49.15"
発注機関	国土交通省 九州地方整備局 熊本河川国道事務所		調査期間 ～ 2001-03	東経	130° 58' 38.804"
調査業者名	株式会社東建ジオテック	主任技師	現場代理人 / コア鑑定者	ボーリング責任者	
孔口標高	465.25 m	角度	上 180° / 下 0°、90°	方向	北 / 東 90° / 南 180° / 西 270°
総掘進長	40.00 m	地盤勾配	水平 0° / 垂直 90°	使用機種	試錐機 / エンジン / ハンマー落下用具 / ポンプ

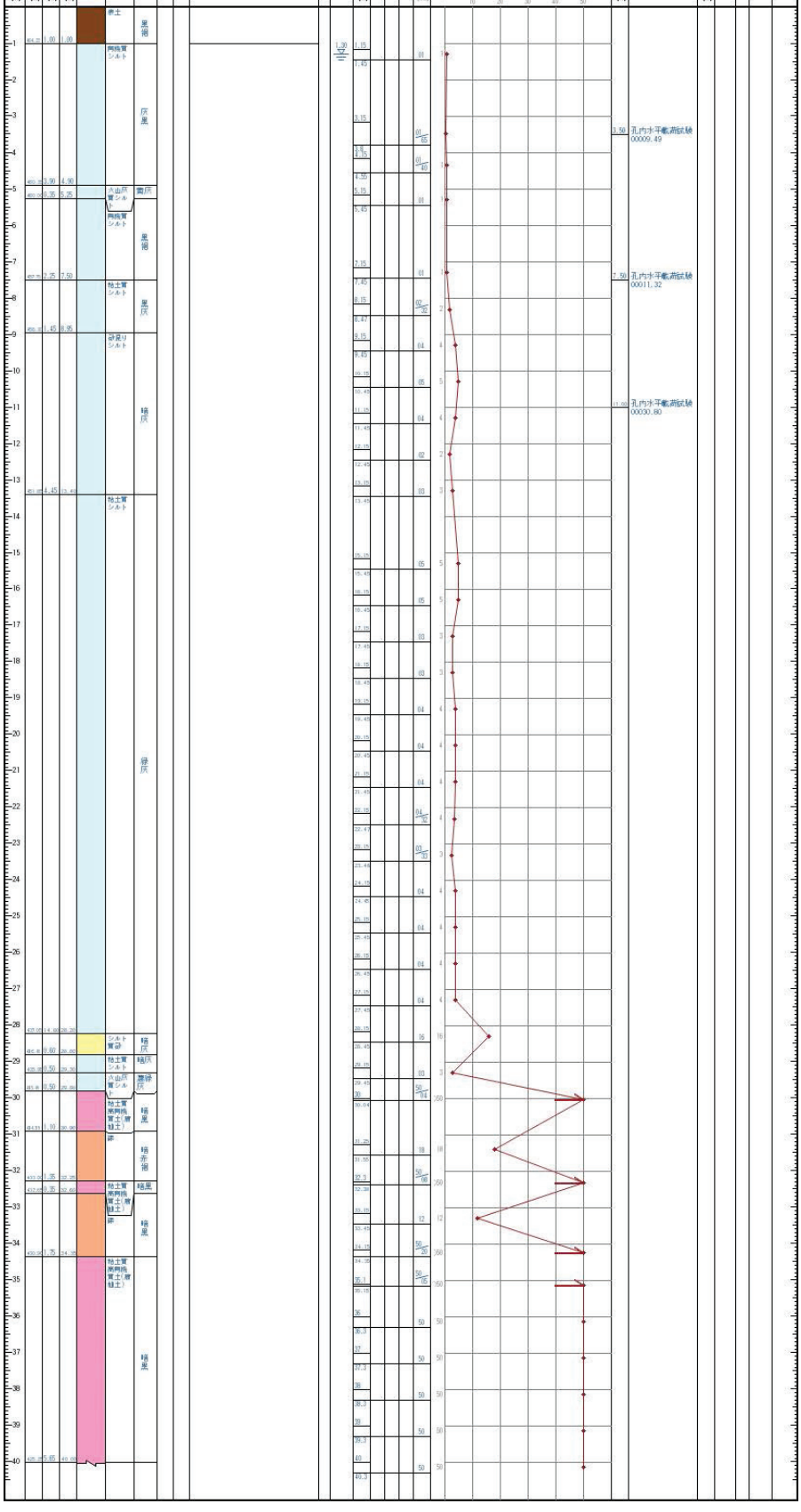

Route 501 Zero-Displacement Lateral Spread Boring Logs

表１１－１（a）　解析結果のまとめ

プレロード部 右岸

区間：No. 197～199

参考としたボーリング地点：Ｈ１－No.２

計画盛土高：５.５ｍ　サーチャージ：２.０ｍ　実盛厚さ：７.５ｍ

盛土材：ρｔ＝１.９t/㎥，Ｃ＝1.0tf/㎡，φ＝３０°

地盤

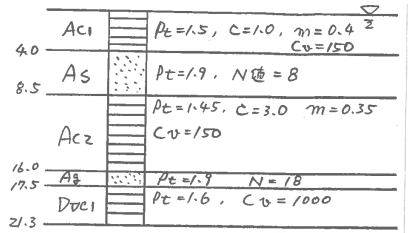

施工期間

◦平成８年10月から平成９年10月までの360日

◦ただし、平成９年６月から平成９年10月までは土工は中止。放置期間としては使える。

沈下量（天端中央）

・弾性沈下（粘土）……　１６cm
・即時沈下（砂）　……　１１cm
・圧密沈下　・Ac1 ……　５５cm
　　・Ac2 ……　５０cm
　　・Dvc1……　１０cm
　　１４２cm

圧密時間（日）

圧密度（%）			残留沈下量10cmに要する日数
80	90	95	
250	600	850	600＜360日　N.G

対策工：サンドドレーン2.5ｍピッチ（四角形配置）
安定を確保するための１日のまき出し厚さ：6.0cm/日

土工工程

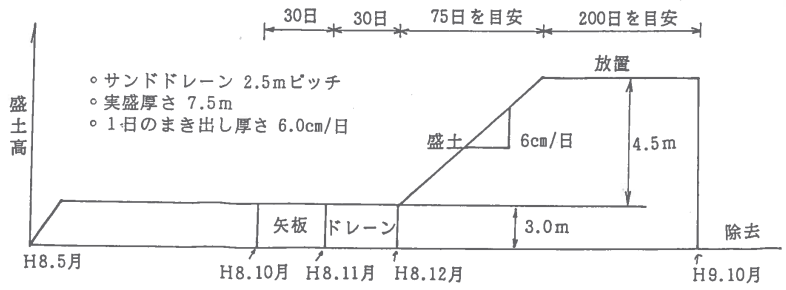

動態観測：変位杭，盛土内水位計，地表面沈下板，層別沈下計が必要。
測定頻度は、施工中は毎日。施工後は１～２週間に１度。

プレロード部 左岸

区間：No. 205～207

参考としたボーリング地点：Ｈ７－No.３

計画盛土高：５.５ｍ　サーチャージ：２.０ｍ　実盛厚さ：７.５ｍ

盛土材：ρｔ＝１.９t/㎥，Ｃ＝1.0tf/㎡，φ＝３０°

地盤

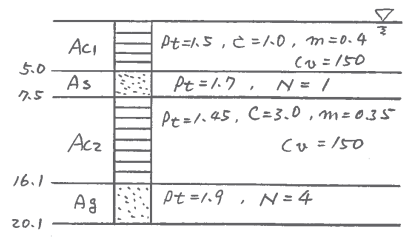

施工期間

◦平成９年１月から平成９年10月までの270日

◦ただし、平成９年６月から平成９年10月までは土工は中止。放置期間としては使える。

沈下量（天端中央）

・弾性沈下（粘土）……　２０cm
・即時沈下（砂）　……　１２cm
・圧密沈下　・Ac1 ……　６５cm
　　・Ac2 ……　５０cm
　　１４７cm

圧密時間（日）

圧密度（%）			残留沈下量10cmに要する日数
80	90	95	
400	750	1150	800＜270日　N.G

対策工：サンドドレーン2.0ｍピッチ（四角形配置）
安定を確保するための１日のまき出し厚さ：7.5cm/日

土工工程

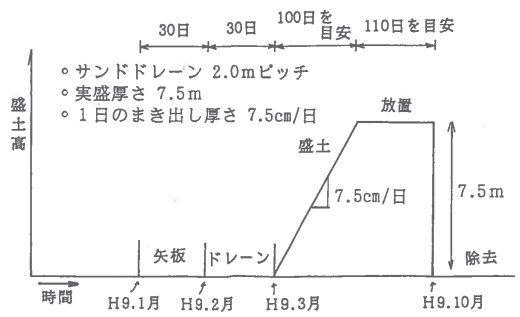

動態観測：変位杭，盛土内水位計，地表面沈下板，層別沈下計が必要。
測定頻度は、施工中は毎日。施工後は１～２週間に１度。

表１１－１（b）　解析結果のまとめ

一般盛土部，右岸，低盛土区間

区間：No.167～194

参考としたボーリング地点：Ｈ１－No.1

検討した盛土高　Ｈ＝１.２m

盛土材：ρｔ＝１.９t/m³，Ｃ＝1.0tf/m²，φ＝３０°

地盤

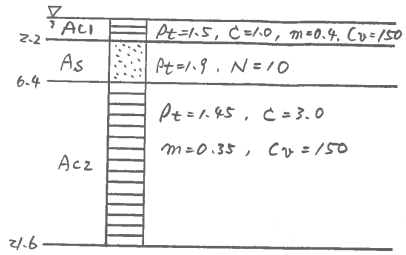

施工期間

堤内側であるため、平成８年５月の施工開始時期より、平成11年１月の舗装開始時期まで、見込める。約1,000日

沈下量（天端中央）

種　類	計画断面	交通荷重考慮
弾性沈下（粘土）	2.0cm	4.0cm
即時沈下（砂）	3.0cm	6.0cm
圧密沈下　Ac1	6.0cm	15.0cm
Ac2	12.0cm	35.0cm
トータル	23.0cm	60.0cm

交通荷重を考慮した最終沈下量に対する圧密時間（日）

圧密度（%）			残留沈下量10cmに要する日数
80	90	95	
∞	∞	∞	∞

対策工：サーチャージ。サーチャージ量は交通荷重分（計画高1.2mに対して、1.8m）計画高＋サーチャージで３mを目安とする。

サーチャージを加えた場合の圧密時間（日）

圧密度（%）			残留沈下量に要する日数	
80	90	95	15cm	10cm
1600	2600	4000	1000	1600

土工工程

- 計画高＋サーチャージで実盛厚さは３mが目安となる。
- 安定性は問題ないので、なるべく早く盛り上げて、舗装間際までサーチャージをかけておく。

動態観測：沈下板の設置。沈下管理だけで良い。測定頻度施工中は毎日。後は１～２週間毎に１度。

一般盛土部，右岸，高盛土区間

区間：No.194～197

参考としたボーリング地点：Ｈ１－No.2

検討した盛土高　Ｈ＝４.５m

盛土材：ρｔ＝１.９t/m³，Ｃ＝1.0tf/m²，φ＝３０°

地盤

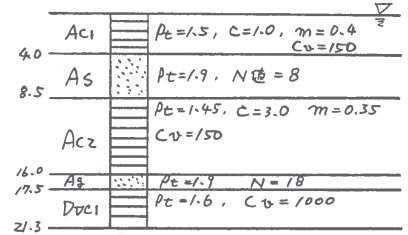

施工期間

- 一段階目の盛土は平成８年５月より。
- 二段階目の盛土は平成８年10月より。
- 二段階目の盛土より、舗装開始時期まで、約800日見込める。

沈下量（天端中央）

- 弾性沈下（粘土）　……　7.0cm
- 即時沈下（砂）　……　9.0cm
- 圧密沈下　・Ac1　……　30.0cm
  - ・Ac2　……　35.0cm
  - ・Dvc1……　5.0cm

トータル　85.0cm

圧密時間（日）

圧密度（%）			残留沈下量10cmに要する日数
80	90	95	
325	650	950	475

実盛厚さ：4.5＋0.85＝5.35m で検討

１日９cmのまき出し厚さで　Fs＞1.1

供用開始時の安全率　Fs＝1.41＞1.25　O.K

土工工程

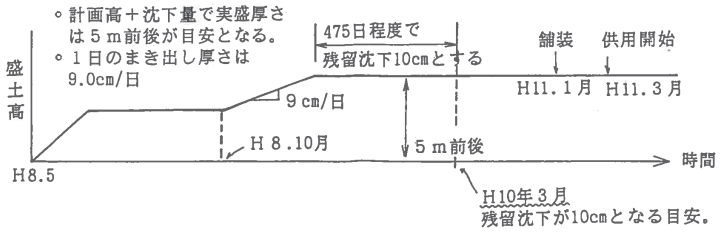

動態観測：沈下板，変位杭の設置。測定頻度は、施工中は毎日。後は１～２週間毎に１度。

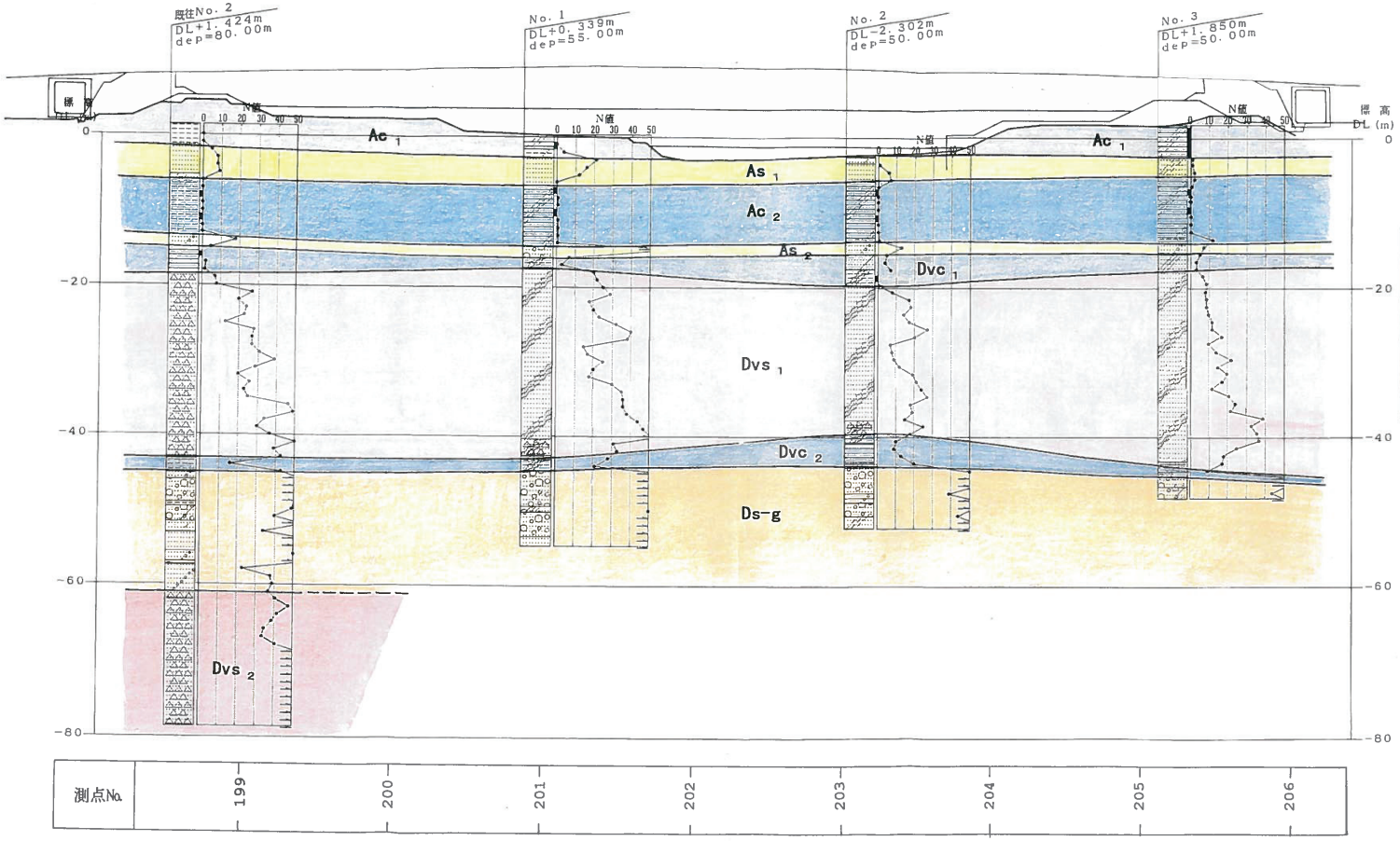

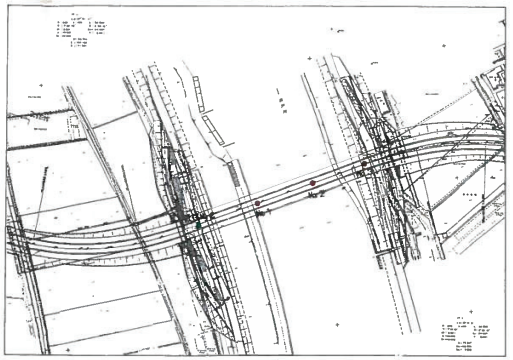

		地層名	記号	N値	記事
新生代	第四紀	沖積粘性土層 1	Ac_1	0～4	・均質な軟弱粘性土 ・層厚 0～1.3m
		沖積砂質土層 1	As_1	0～21	・シルト分を含む細砂主体 ・層厚 2.7～4.5m
		沖積粘性土層 2	Ac_2	0～2	・均質な軟弱粘性土 ・層厚 7.5～8.2m
		沖積砂質土層 2	As_2	5～50	・礫混じり細砂～砂礫状 ・層厚 1.5～1.9m
	更新世	火山灰質粘性土層 1	Dvc_1	1～7	・植良火砕流堆積物．シルト状 ・層厚 1.2～3.6m
		火山灰質砂質土層 1	Dvs_1	7～50	・阿蘇火砕流堆積物．砂～礫状 ・層厚 20.0～26.3m
		火山灰質粘性土層 2	Dvc_2	8～21	・阿蘇火砕流堆積物．粘土状 ・層厚 1.2～3.9m
		洪積砂・礫質土層	$Ds-g$	23～50	・砂～砂礫主層．粘土伏わ ・16.1m以上
		火山灰質砂質土層 2	Dvs_2	31～50	・火砕流堆積物． ・17.7m以上

図２．５　地層断面図(S=1:500)

ボーリング柱状図

調　査　名

事業・工事名

ボーリングNO.

シートNO.

ボーリング名	No.1-b	調査位置	熊本県宇土市馬之瀬町地内			北　緯	32° 41′ 34.2000″
発注機関				調査期間	1996-12-20 ～ 1997-03-24	東　経	130° 38′ 51.6000″
調査業者名		主任技師		現場代理人		コア鑑定者		ボーリング責任者	
孔口標高	1.9 m	角度	上 180° 90° 下 0° 0°	方向	北 0° 東 90° 南 180° 西 270°	地盤勾配	鉛直 90° 水平 0°	使用機種	試錐機	YSO-05	ハンマー落下用具	
総掘進長	4.00 m								エンジン	NFD-8	ポンプ	GP-5

標尺 (m)	標高 (m)	層厚 (m)	深度 (m)	柱状図	土質区分	色調	相対密度	相対稠度	記事	地層岩体区分	孔内水位 (m) ／ 測定月日	標準貫入試験 深度 (m)	10cmごとの打撃回数 0－10	10－20	20－30	打撃回数／貫入量 (cm)	N値 0 10 20 30 40 50	原位置試験 深度 (m)	試験名および結果	試料採取 深度 (m)	試料番号	採取方法	室内試験	掘進月日
1	-2.10	4.00	4.00		砂混じり粘土 (CH-S)	暗茶灰			希に玉石を含む											1.50	Tb-1			
2																				2.30				
3																				3.00	Tb-2			
4																				4.00	Tb-3			02/14

ボーリング柱状図

調　査　名　大牟田熊本宇土線道路改良地質調査

事業・工事名

ボーリングNO.

シートNO.

ボーリング名	NO.2	調査位置	熊本県宇土市走潟町			北　緯	32° 41′ 39.1000″
発注機関				調査期間	～	東　経	130° 38′ 51.3000″
調査業者名		主任技師		現場代理人		コア鑑定者		ボーリング責任者	
孔口標高		角度	180° 上 90° 下 0°	方向	北 0° 西 270° 90° 東 180° 南	地盤勾配	鉛直 90° 水平 0°	使用機種	試錐機		ハンマー落下用具	
総掘進長	80.00 m								エンジン		ポンプ	

標尺 (m)	標高 (m)	層厚 (m)	深度 (m)	柱状図	土質区分	色調	相対密度	相対稠度	記事	地層岩体区分	孔内水位 (m) ／ 測定月日
		2.80	2.80		シルト (M)	暗青褐灰		極軟	高含水・高塑性。有機物混じえる。		
		3.90	6.70		小礫混じり砂 (S-G)	暗青灰		極軟	φ5～20m/m礫を10%程度含む細粒砂主体。		
		7.87	14.57		粘土質シルト (MC)				高含水・高塑性。貝殻細片混じえる。撹乱により流動化し易い。		
					礫混じり中砂 (MS-G)	暗灰～暗褐灰	中くらい		上部で13cm大の安山岩礫を挟む。φ2cm以下の礫10%。		

標準貫入試験

深度 (m)	10cmごとの打撃回数 0－10	10－20	20－30	打撃回数／貫入量 (cm)
1.00	00			00/62
1.62	62			
2.00	00			00/69
2.69	69			
3.15	1	1	3	5/31
3.46	9	9	13	
4.15	2	3	3	8/30
4.45	2	3	3	8/30
5.15	2	3	3	8/30
5.45	3	3	3	9/30
6.15	3	3	3	
6.45	00			00/80
7.00	80			
7.80	00			00/80
8.00	80			
8.80	00			00/80
10.00	80			
10.80	00			00/80
11.00	80			
11.80	00			00/80
13.00	80			
13.80	00			00/80
14.00	80			
14.57	00			00/57
15.15	57			
	9	6	3	18/30

N 値: 0 10 20 30 40 50

原位置試験 深度 (m)	試験名および結果

試料採取 深度 (m)	試料番号	採取方法
9.00		
9.75		
12.00		
12.80		

室内試験	掘進月日

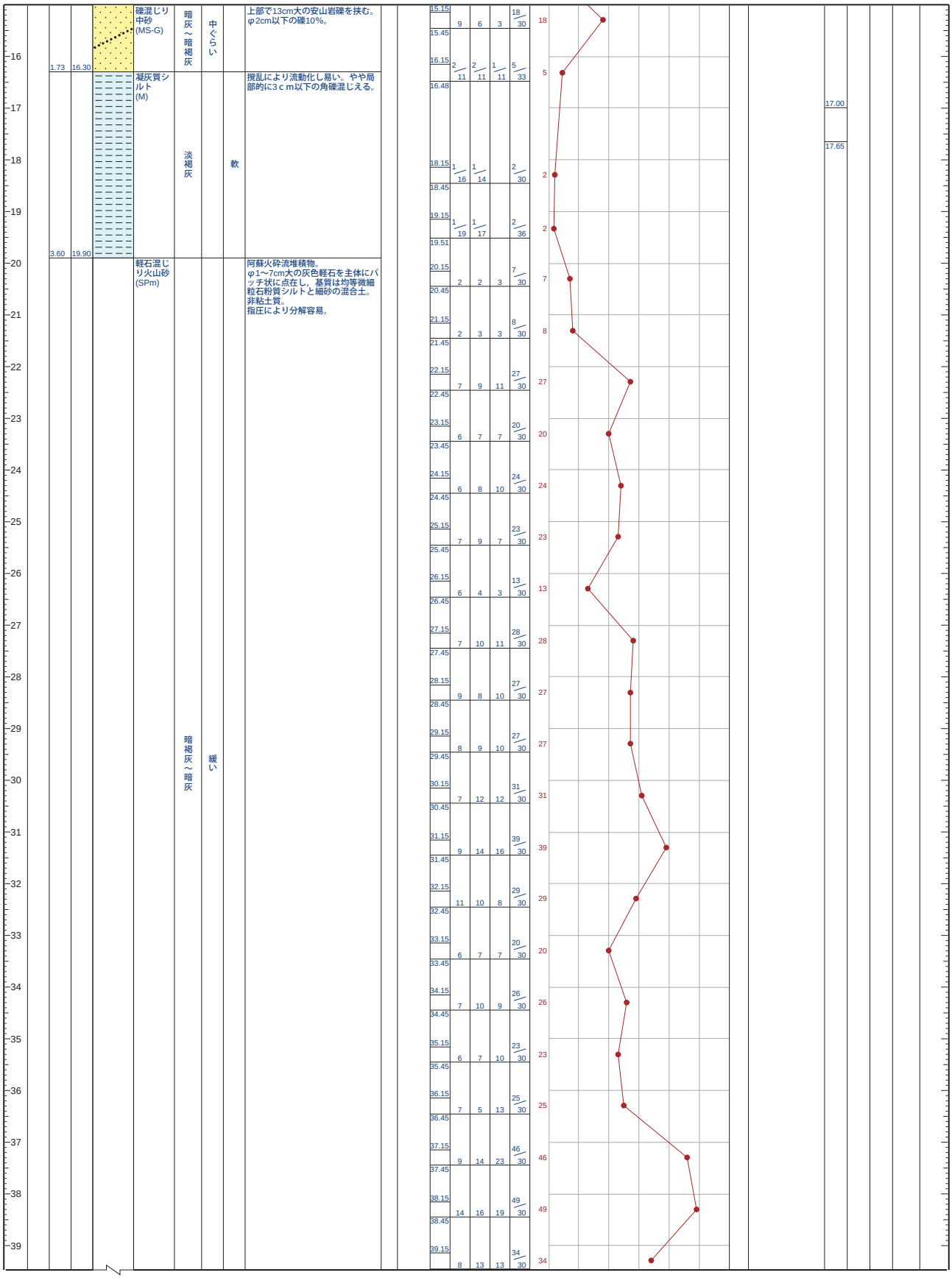
礫混じり中砂 (MS-G)
暗灰～暗褐灰
中ぐらい
上部で13cm大の安山岩礫を挟む。
φ2cm以下の礫10%。
1.73
16.30
凝灰質シルト (M)
淡褐灰
軟
撹乱により流動化し易い。やや局部的に3ｃｍ以下の角礫混じえる。
3.60
19.90
軽石混じり火山砂 (SPm)
暗褐灰～暗灰
緩い
阿蘇火砕流堆積物。
φ1~7cm大の灰色軽石を主体にパッチ状に点在し，基質は均等微細粒石粉質シルトと細砂の混合土。
非粘土質。
指圧により分解容易。
17.00
17.65

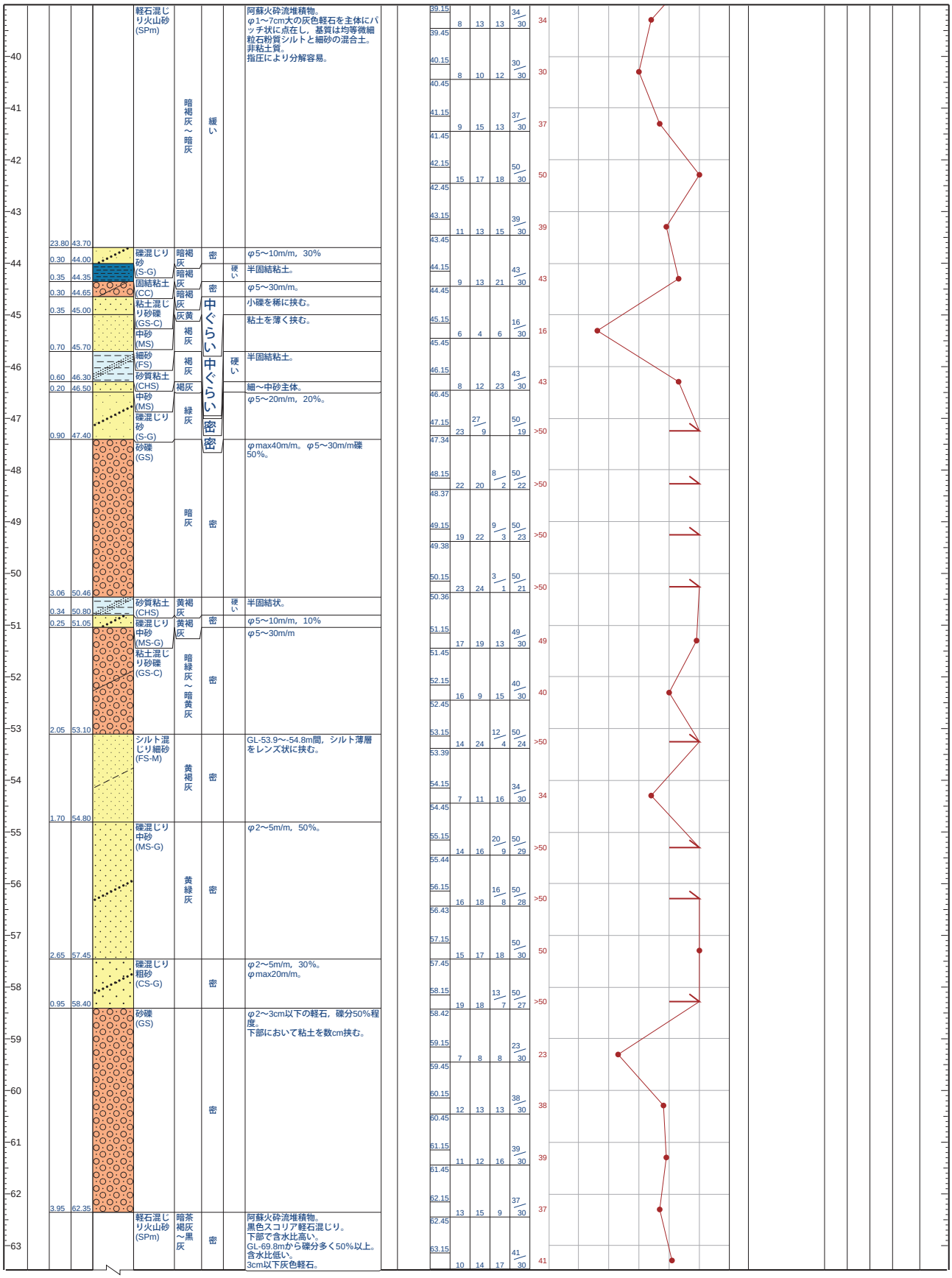
軽石混じり火山砂 (SPm)
暗褐灰～暗灰
緩い
阿蘇火砕流堆積物。
φ1～7cm大の灰色軽石を主体にパッチ状に点在し，基質は均等微細粒石粉質シルトと細砂の混合土。
非粘土質。
指圧により分解容易。
23.80 43.70
礫混じり砂 (S-G)
暗褐灰
密
φ5～10m/m，30%
0.30 44.00
固結粘土 (CC)
暗褐灰
硬い
半固結粘土。
0.35 44.35
粘土混じり砂礫 (GS-C)
暗褐灰
密
φ5～30m/m。
0.30 44.65
中砂 (MS)
暗褐灰
中ぐらい
小礫を稀に挟む。
0.35 45.00
細砂 (FS)
黄褐灰
粘土を薄く挟む。
0.70 45.70
砂質粘土 (CHS)
褐灰
硬い
半固結粘土。
0.60 46.30
中砂 (MS)
褐灰
細～中砂主体。
0.20 46.50
礫混じり砂 (S-G)
緑灰
中ぐらい
φ5～20m/m，20%。
0.90 47.40
砂礫 (GS)
暗灰
密
φmax40m/m。φ5～30m/m礫50%。
3.06 50.46
砂質粘土 (CHS)
黄褐灰
硬い
半固結状。
0.34 50.80
礫混じり中砂 (MS-G)
黄褐灰
密
φ5～10m/m，10%
0.25 51.05
粘土混じり砂礫 (GS-C)
暗緑灰～暗黄灰
密
φ5～30m/m
2.05 53.10
シルト混じり細砂 (FS-M)
黄褐灰
密
GL-53.9～-54.8m間，シルト薄層をレンズ状に挟む。
1.70 54.80
礫混じり中砂 (MS-G)
黄緑灰
密
φ2～5m/m，50%。
2.65 57.45
礫混じり粗砂 (CS-G)
密
φ2～5m/m，30%。
φmax20m/m。
0.95 58.40
砂礫 (GS)
密
φ2～3cm以下の軽石，礫分50%程度。
下部において粘土を数cm挟む。
3.95 62.35
軽石混じり火山砂 (SPm)
暗茶褐灰～黒灰
密
阿蘇火砕流堆積物。
黒色スコリア軽石混じり。
下部で含水比高い。
GL-69.8mから礫分多く50%以上。含水比低い。
3cm以下灰色軽石。

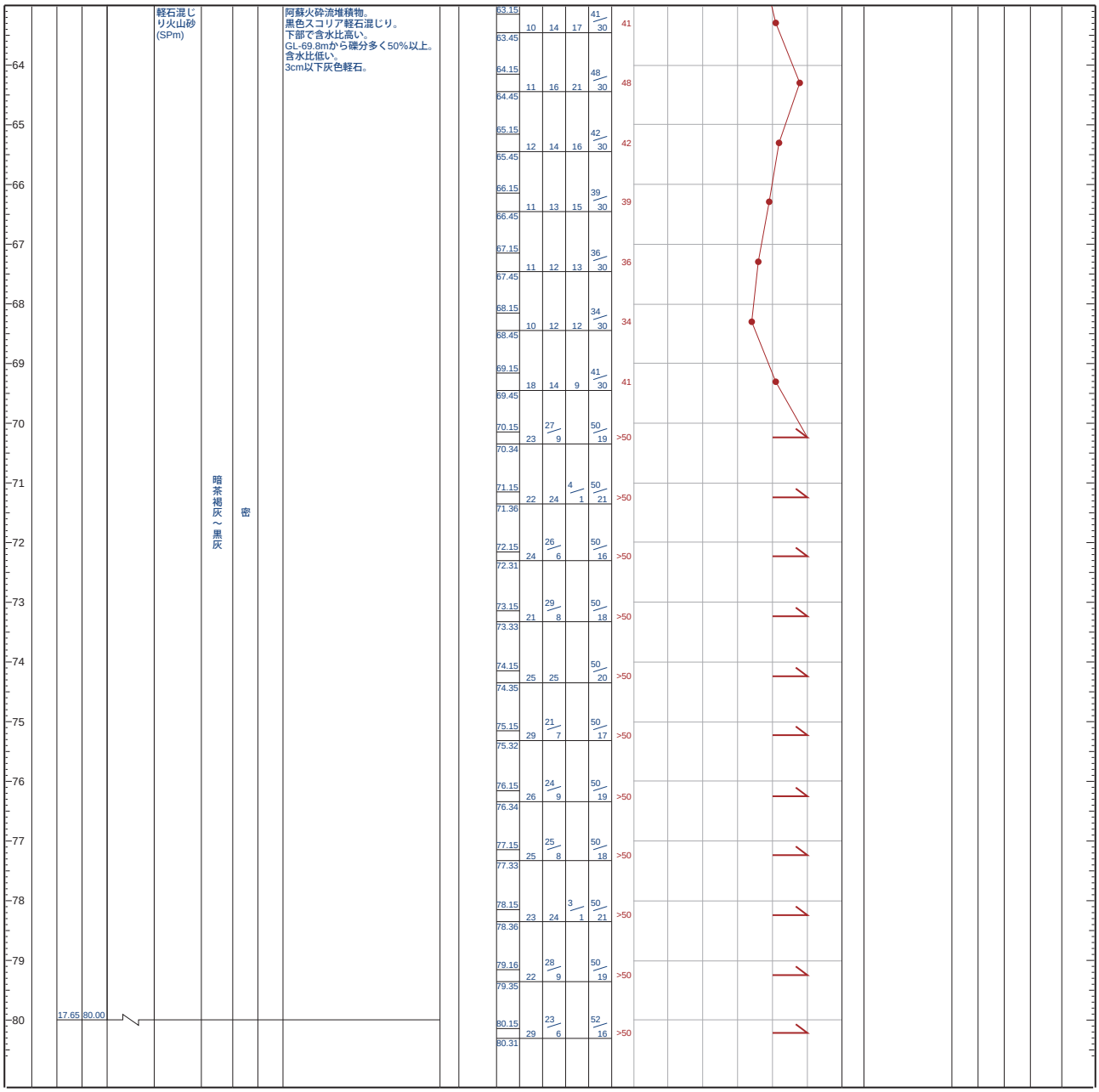
軽石混じり火山砂 (SPm)
暗茶褐灰～黒灰
密
阿蘇火砕流堆積物。
黒色スコリア軽石混じり。
下部で含水比高い。
GL-69.8mから礫分多く50%以上。
含水比低い。
3cm以下灰色軽石。
17.65
80.00
63.15
63.45
64.15
64.45
65.15
65.45
66.15
66.45
67.15
67.45
68.15
68.45
69.15
69.45
70.15
70.34
71.15
71.36
72.15
72.31
73.15
73.33
74.15
74.35
75.15
75.32
76.15
76.34
77.15
77.33
78.15
78.36
79.16
79.35
80.15
80.31
41
48
42
39
36
34
41
>50
>50
>50
>50
>50
>50
>50
>50
>50
>50

ボーリング柱状図

調　査　名　緑川下流部耐震箇所地質調査業務

事業・工事名　緑川下流部耐震箇所地質調査業務

ボーリングNO.

シートNO.

ボーリング名	浜戸川　3k/000	調査位置						北　緯	32° 41' 35.1000"
発注機関	建設省九州地方建設局熊本工事事務所			調査期間	平成9年08月28日 ～ 平成9年12月15日			東　経	130° 38' 54.5000"
調査業者名	明大工業株式会社	主任技師	古城　輝夫	現場代理人	市川　宏	コア鑑定者	市川　宏	ボーリング責任者	吉田　賢二
孔口標高	2.99 m	角度	上 180° 90° 下 0°	方向	0° 北 90° 東 180° 南 270° 西	地盤切配	水平 0° 鉛直 90°	試錐機	YBM式　YSO-1_型	ハンマー落下用具	
総掘進長	29.00 m	使用機種						エンジン	ヤンマーNS90	ポンプ	YBM式　SP-40型